High Mass Accuracy Analytical Applications of Fourier Transform Ion Cyclotron Resonance Mass Spectrometry

Rebecca Helen Wills

MSc Chemistry

Thesis submitted in partial fulfilment of the requirements for the degree of Doctor of Philosophy

Department of Chemistry

University of Warwick

January 2014

THE UNIVERSITY OF WARWICK

List of Tables

List of Figures

Abbreviations

APCI	Atmospheric pressure chemical ionization
CAD	Collision activated dissociation
CHEF	Correlated harmonic excitation field
CID	Collision induced dissociation
CRM	Charge residue mechanism (applied to ESI)
Cys	Cysteine
Cys(SO_3H)	Cysteine sulfonic acid (sulfonate)
Da	Daltons
DC	Direct current
ECD	Electron capture dissociation
EDM	Electric discharge machining
EI	Electron ionisation
EDD	Electron detachment dissociation
EID	Electron induced dissociation
ETD	Electron transfer dissociation
ESI	Electrospray ionization
FTICR	Fourier transform ion cyclotron resonance

FWHM	Full width at half maximum
GC-MS	Gas chromatography-mass spectrometry
Glu	Glutamic acid
Gly	Glycine
His	Histidine
IEM	Ion evaporation mechanism (applied to ESI)
IRMPD	Infrared multiphoton dissociation
IVR	Intramolecular vibrational energy redistribution
Leu	Leucine
LC-MS	Liquid chromatography-mass spectrometry
Mm	Millimetres
MALDI	Matrix assisted laser desorption ionization
MS/MS	Mass spectrometry/Mass spectrometry (tandem mass spectrometry)
m/z	Mass-to-charge ratio
nCI	Negative chemical ionisation
Nd:YAG	Neodymium-doped yttrium aluminium garnet
NRP	Non ribosomal peptide
NRPS	Non ribosomal peptide synthetase

NMR	Nuclear magnetic resonance
Oe	Oersted
ppm	Parts-per-million
PCA	Principal component analysis
PKS	Polyketide synthase
QIT	Quadrupole ion trap
RP	Resolving power
RF	Radio frequency
Ru	Ruthenium
Ser	Serine
SPE	Solid phase extraction
SPME	Solid phase micro extraction
T	Tesla
TOF	Time-of-flight
VSM	Vibrating sample magnetometer

List of symbols

α	Cell geometry factor
B	Magnetic field strength
e	Elementary charge (1.6×10^{-19} C)
E	Electric field
ε_0	Permittivity of free space
f	Frequency (Hz)
γ	Surface tension
θ	Angle between two vectors
λ	Wavelength
r or R	Radius
V_T	Trapping potential
υ	Velocity
ω	Angular frequency (rad s^{-1})
ω_c	Unperturbed cyclotron frequency
ω_+	Reduced cyclotron frequency
ω_-	Magnetron frequency
ω_z	Trapping frequency

Structures of the Amino Acids

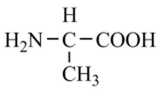

Alanine (A)

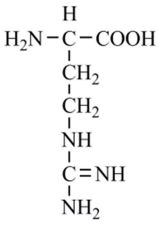

Arginine (R)

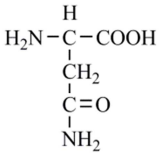

Asparagine (N)

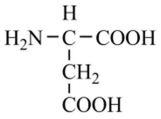

Aspartic acid (D)

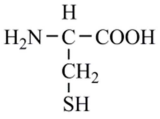

Cysteine (C)

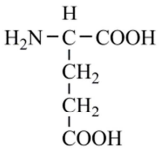

Glutamic acid (E)

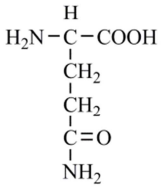

Glutamine (Q)

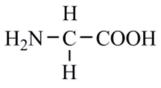

Glycine (G)

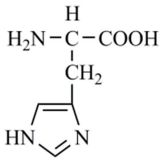

Histidine (H)

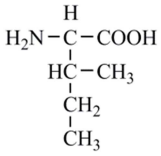

Isoleucine (I)

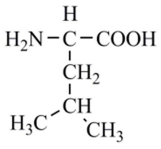

Leucine (L)

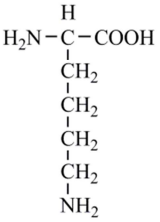

Lysine (K)

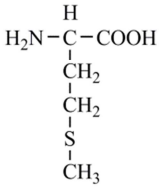

Methionine (M)

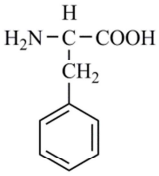

Phenylalanine (F)

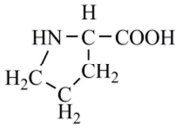

Proline (P)

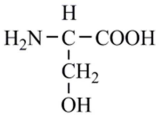

Serine (S)

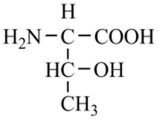

Threonine (T)

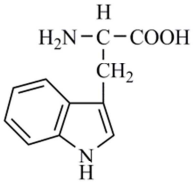

Tryptophan (W)

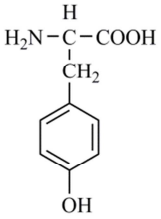

Tyrosine (Y)

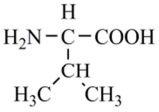

Valine (V)

Acknowledgments

First and foremost I would like to thank my supervisor, Professor Peter O'Connor, for giving me the opportunity to work in his group, and for all his advice and support throughout my PhD. Thank you for encouraging me to pursue so many different projects, especially the crazy ideas!

To my friends Andrea Lopez-Clavijo, Ruth McQuitty and Pilar Perez Hurtado - we made it through together, thank you for your support and friendship over the years. It has been a pleasure to get to know you and thank you Andrea and Pilar for introducing me to South American culture (even the salsa dancing!).

I would like to say a big thank you to Dr. Mark Barrow for providing training and assistance with the instrument, particularly when we were just starting out. Thank you for taking the time to answer my many questions, and for your invaluable advice and discussions.

Special thanks also to my friends and colleagues for helping make this an enjoyable experience: Juan Wei, Andrew Soulby, Yulin Qi, Huilin Li, Terry Lin, and Chris Wootton, and to Dr. David Kilgour and Dr. Maartje van Angthoven for taking the time to give me guidance with my many projects.

Thanks to my collaborators, Dr. Manuela Tosin, Dr. Abraha Habtemariam, Professor Julie Macpherson and Professor Peter Sadler for all their help and advice regarding my different projects, and for their very helpful feedback on papers. To my supervisory panel: Giovanni Costantini and Alessandro Troisi, thank you for your advice and help with viva preparations. Also thanks to the many people who have provided assistance particularly in the instrumentation work: Marcus Grant and Lee

Butcher, Alex Colburn, Dr. Martin Lees from the Physics department, and Dr. Alistair Ross from the Engineering department at the University of Cambridge. Also to Dr. Julia Smith at Bruker: thank you for your helpful discussions.

I have been fortunate to participate in various teaching activities throughout my PhD so a special thank you to Giovanni Costantini and Vas Stavros for helping me with laboratory demonstrating. Your advice and support helped me to recognise and improve my teaching abilities. Also special thanks to Nick Barker for encouraging me to take part in Outreach activities – what better way to spend a day out from the lab than making slime! It was fantastic to contribute to this program and teach so many eager young scientists.

Finally, and most importantly, to my parents, Nadine and Tony, and my brother Chris, I know I wouldn't have got this far without your love and support. You have kept me determined and motivated me to finish. Thank you for being there for me throughout this experience.

Declaration

I hereby declare that except where specific references are made to other sources, the work contained in this thesis is the original work of the named author. It has been composed by myself and has not been submitted, in whole or in part, for any other degree, diploma or other qualification.

Rebecca Wills

January 2014

Abstract

The performance capabilities of Fourier transform ion cyclotron resonance (FTICR) mass spectrometry are higher than any other type of mass spectrometer, making this technique suitable for a range of analytical applications. Here, FTICR mass spectrometry has been used for the structural analysis of polyketides and non-ribosomal peptides, and in the identification of peptide binding sites of ruthenium(II) arene anticancer complexes. In both these applications, methods have been developed involving complementary tandem mass spectrometry techniques, specifically collision activated dissociation (CAD), electron induced dissociation (EID), and electron capture dissociation. In particular, CAD and EID have been shown to be effective in the structural characterisation of polyketides, with a method developed for distinguishing between two isomers of the polyketide lasalocid A. This method has been optimised and extended for application to non-ribosomal peptides enabling detailed structural information to be obtained with very high accuracy. Using CAD and ECD has enabled the identification of amino acids involved in binding ruthenium(II) complexes. Binding to phenylalanine and glutamic acid was observed in this work for the first time; coordination by histidine and methionine was also observed and is in agreement with previous work. Overall, new methods for highly accurate structural characterisation and binding site identification have been successfully designed and implemented.

Chapter 1: Introduction

1.1 FTICR Mass Spectrometry as an Analytical Tool

Mass spectrometry has long been realized as a powerful analytical tool and, as such, can be used successfully in a wide range of applications, from small molecule structural characterization to the analysis of posttranslational modifications of proteins. The principle of a mass spectrometry experiment is to determine the mass of a molecule through measurement of its mass-to-charge (*m/z*) ratio, where *m* is a molecular weight measured in Da, and *z* is the elementary charge. By measuring the accurate mass of a molecule, the exact chemical composition can then be obtained. The *m/z* ratio of an analyte is determined by the behaviour of a charged particle in an electric field, or in a combination of electric and magnetic fields. In order to achieve this, a mass spectrometer is composed of three main parts: first, an ionisation source to transfer the analyte into the gas phase; secondly, a mass analyser to separate the ions based on their *m/z* ratio; and third, a detector. There are various types of mass analysers in use ranging from a simple quadrupole to an ion trap; the most sophisticated of which is a Fourier transform ion cyclotron resonance (FTICR) mass spectrometer.

FTICR mass spectrometry was first developed by Comisarow and Marshall[1] in 1974 and has the highest performance capabilities of any mass spectrometer in terms of resolving power and mass accuracy. The development of this technique has expanded the range of applications where mass spectrometry is advantageous over other methods. Examples of this include proteomics applications, where higher resolving powers enable the separation of peptide mixtures of large protein complexes, therefore increasing the accuracy of protein identification; natural product analysis, where the greater variety of tandem mass spectrometry techniques available with FTICR enable complementary, high mass accuracy data to be

obtained for the structural characterization of new compounds; and finally, in the analysis of complex mixtures, where a combination of high resolution and mass accuracy enable the identification of large numbers of compounds.

1.2 Ionization Techniques

1.2.1 Electrospray Ionisation (ESI)

Electrospray ionisation is a technique used to produce gaseous ions from a liquid under atmospheric pressure conditions and was developed by John Fenn[2-3] in the late 1980's based on work conducted by Dole in 1968.[4] It has become one of the most widely applicable ionisation techniques as it offers several advantages, including the detection of a wide range of masses without significant fragmentation, as well as preserving non-covalent interactions in the gas phase.[5]

There are three main stages in ESI, namely droplet formation, droplet shrinkage, and gaseous ion production. The solution containing the analyte of interest is pumped through a needle and a strong electric field (generally ~3-5 kV) is applied between the needle and the entrance to the instrument, in this case, the spray shield. The polarity of the voltage applied can be changed depending on whether positive mode or negative mode is required for analysis. The electrostatic field produced as a result of the potential difference between the needle capillary and the spray shield causes charge to accumulate at the tip of the needle, and is drawn out in a downfield direction, establishing a Taylor cone,[6] as illustrated in Figure 1.1.

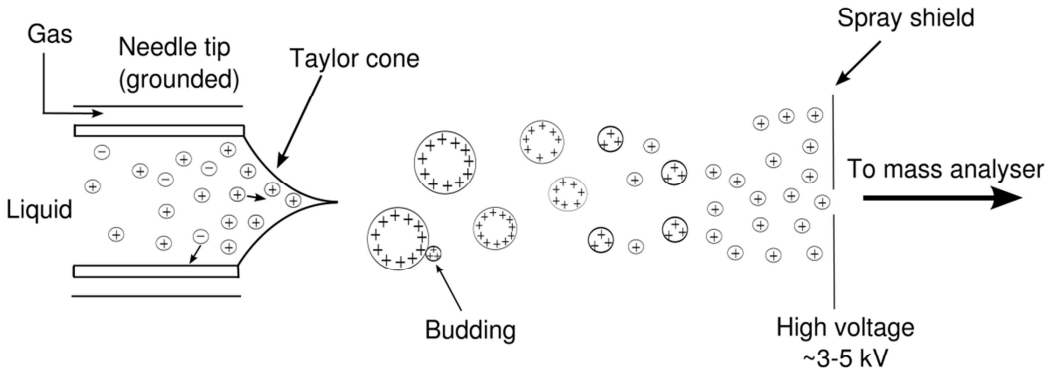

Figure 1.1: Illustration of electrospray ionisation process, adapted from references [6,7]

When the charge repulsion exceeds the surface tension of the liquid, a process known as "budding" occurs, resulting in the formation of highly charged droplets. Due to their charge, these droplets then migrate towards the entrance of the instrument. Droplet evaporation can be enhanced by the use of a nebulising gas, generally nitrogen, which is applied along the outside of the needle capillary.

There are two main mechanisms proposed for the shrinkage of the droplets before they enter the instrument.[7] The first, known as the charge residue mechanism (CRM),[4] involves evaporation of the solvent as the droplets move downstream, resulting in an increase in charge repulsion inside the droplet. At the point where the Coulombic repulsion exceeds the surface tension, known as the "Rayleigh Limit", droplet fission occurs, resulting in the formation of droplets with smaller radii. The Rayleigh limit can be defined by equation 1.1.

$$q_R = 8\pi(\gamma\varepsilon_0 R^3)^{1/2} \qquad (1.1)$$

This process continues until the production of droplets containing one analyte molecule, with one or more charges, has occurred. The second mechanism, known as the ion evaporation mechanism (IEM),[8] involves the desorption of a single analyte molecule into the gas phase, through Coulombic repulsion causing its ejection from the droplet. Both mechanisms can be used to explain the observed formation of ions from ESI; however, it is generally thought that IEM is applied to small (> 10 nm radius) droplets, whilst CRM applies more to larger biomolecules such as proteins.[7, 9-10]

Nanospray ionisation, or nanoESI, is a variation of ESI that uses much smaller needle tips, on the order of a few µm instead of ~100 µm, so that smaller droplets are produced.[11] A lower voltage, ~0.8-1.2 kV, is applied between the needle and the spray shield, and the sample is delivered at lower flow rates. This is particularly advantageous in biological analyses where sample volumes are often limited. Although smaller tips are more prone to clogging, reducing the amount of sample entering the instrument has the added benefit of reducing contamination in the source. For these reasons, it is often preferable to use nano-ESI in a number of applications.

1.2.2 Matrix Assisted Laser Desorption Ionisation (MALDI)

Matrix assisted laser desorption ionisation (MALDI) is, like ESI, an important ionisation technique which can be used to analyse non-volatile, high molecular weight compounds.[12] The compound of interest is mixed with a matrix, typically an organic acid, before being crystallised on a metal plate. The sample is irradiated with a laser, typically at wavelengths in the ultraviolet, such as a nitrogen laser (λ =

337 nm), causing ablation and creating a plume of analyte and matrix molecules, as illustrated in Figure 1.2.

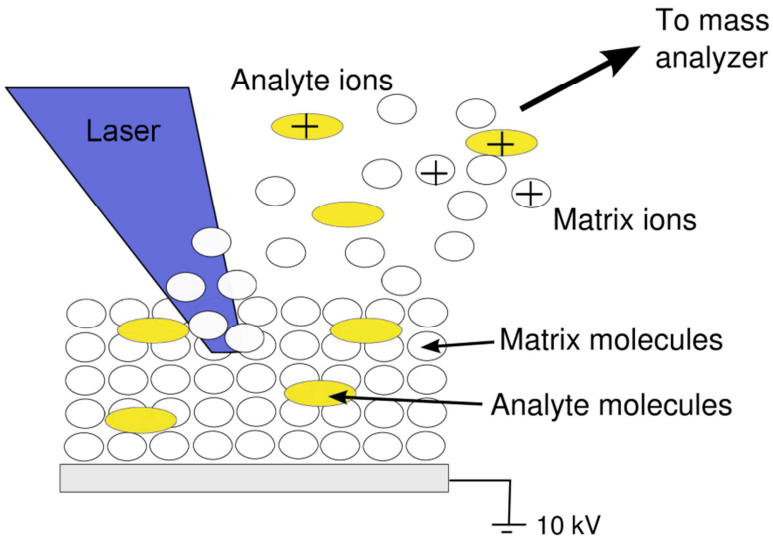

Figure 1.2: Illustration of ion formation using MALDI

Within the plume, ionisation of the analyte (A) molecules can occur; the most common mechanism by which this is thought to occur is through proton transfer[13] from the matrix (M), as illustrated by equations 1.2.

$$M + h\upsilon \rightarrow M^{+*}$$

$$M^{+*} + A \rightarrow [M\text{-}H]^{-} + [A+H]^{+} \qquad (1.2)$$

An alternative theory, known as the lucky survivor model,[14] suggests the analyte molecules preserve their charge states, together with associated counterions, from solution as they are incorporated with the matrix. The presence of matrix excess charges i.e. $[M+H]^{+}$ or $[M\text{-}H]^{-}$ in the clusters of molecules generated by laser irradiation can result in counterion neutralisation or analyte deprotonation

respectively, leading to the formation of mostly singly protonated species, as illustrated by equation 1.3.[14-16]

$$AH_n^{n+} + nX^- \rightarrow AH^+ + X^- + (n-1)HX \qquad (1.3)$$

Whilst the processes involved in MALDI are not completely understood, evidence for both mechanisms has been reported[16] showing neither mechanism can be applied to explain all results observed using MALDI. MALDI is now widely used for the analysis of biomolecules and polymers due to its simplicity and ease of use. One of the disadvantages of this ionisation technique lies in the generation of singly charged species, which limits the use of some tandem mass spectrometry techniques, such as electron capture dissociation (ECD), which require multiply charged species.

1.2.3 Electron Ionisation (EI)

Electrons produced by a heated filament are accelerated by an electric field to 70 eV and focussed into a continuous electron beam. The gaseous sample is passed through the beam in the perpendicular direction, whereby the close passage of highly energetic electrons causes fluctuations in the electric field around the sample molecules, consequently inducing ionisation and extensive fragmentation.[17-18] A schematic of the setup in an EI source is shown in Figure 1.3.

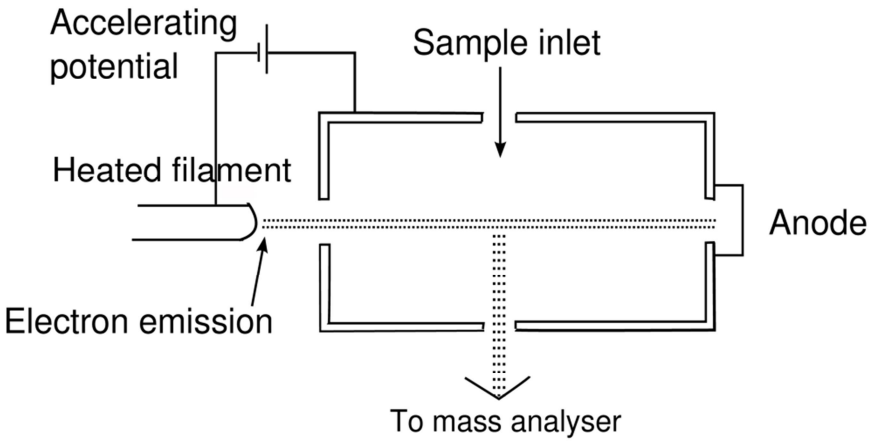

Figure 1.3: Schematic of an EI source, adapted from reference [17]

At energies of 70 eV, the de Broglie wavelength of the electrons closely matches the bond lengths of typical organic molecules (~ 0.15 nm), thereby maximising energy transfer. If the energy transferred is greater than the ionisation potential of the neutral molecule (M), ionisation occurs resulting in the formation of a radical cation,[17, 19] as illustrated in equation 1.4.

$$M + e^- \rightarrow M^{+\bullet} + 2e^- \qquad (1.4)$$

Approximately 10-20 eV is transferred to the molecules; since about 10-15 eV is required for ionisation for volatile, organic molecules, the excess energy results in extensive fragmentation, consequently providing product ions that can aid with structure elucidation. A disadvantage of this technique, however, is that the molecular ion of a compound is not always observed. Since the introduction of ESI and MALDI, which are gentler ionisation techniques and do not result in fragmentation, EI is generally used for the analysis of volatile, low molecular weight compounds, particularly in instruments coupled to gas chromatography systems.

1.3 Mass Analysers

Once the sample has been ionised, the ions can be separated according to their *m/z* and a mass spectrum produced. There are various types of mass analyser available for this purpose, including quadrupole, ion trap, time-of-flight, and FTICR analysers. Each differs according to its mode of operation, detectable mass range, sensitivity, cost, and two important performance capabilities: mass accuracy and resolving power.

1.3.1 Resolving Power and Mass Accuracy

Resolving power (RP) is important for separating closely spaced signals, such as in the analysis of multiply-charged ions, particularly in large proteins, and in the analysis of complex mixtures. The resolving power can be calculated by equation 1.5.

$$RP = \frac{m}{\Delta m} \qquad (1.5)$$

where *m* corresponds to the *m/z* of the peak of interest and *Δm* is the width of the peak. Generally, the full width at half maximum (FWHM) definition for peak width is used, where the width is measured at 50% of the height of the peak.

Mass accuracy, measured in parts-per-million (ppm), is a measure of how well the measured *m/z* correlates with the theoretical value[20] and can be calculated by equation 1.6.

$$Mass\ accuracy = \frac{m/z_{meas} - m/z_{theo}}{m/z_{theo}} \times 10^6 \qquad (1.6)$$

where m/z_{meas} and m/z_{theo} are the measured and theoretical values for the peak of interest respectively.

There are a number of characteristics that indicate the performance capabilities of different mass analysers, and are used to judge the best mass spectrometer for the type of analysis to be performed. Resolving power and mass accuracy are two examples of such characteristics; others include scan speed, sensitivity, and the detectable mass range. Quadrupoles are the simplest but are limited in terms of their resolving power and mass accuracy; on the other hand, FTICR mass spectrometers can achieve resolving powers on the order of millions, and mass accuracies of 1 ppm and below, making it suitable for a wide range of applications but a very expensive instrument. Since the FTICR mass analyser is the focus of this work, it will be discussed in detail in section 1.4.

1.3.2 Quadrupole Mass Analyser

Quadrupoles are the most common analyser in mass spectrometers and consist of two sets of two cylindrical rods lying parallel to each other, as shown in Figure 1.4.

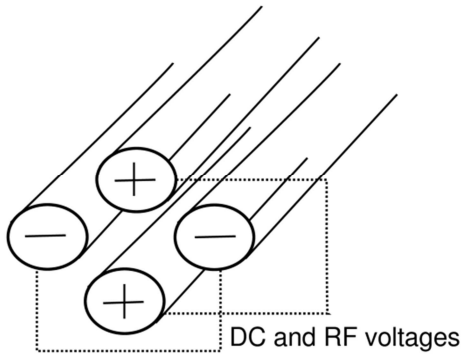

Figure 1.4: Schematic of a quadrupole

Ions are separated according to the stability of their trajectory through the oscillating electric field produced via a combination of direct current (DC) and radio frequency (RF) potentials applied to the rods. The motion of ions in a quadrupole can be described by the solutions to the Mathieu equation,[21-22] which determine regions of

stability and instability. These solutions can be used to describe the trajectories of ions in a quadrupole and to define the limits for a stable trajectory. The Mathieu stability diagram, illustrated in Figure 1.5, can be used to visualise the solutions to the Mathieu equation and therefore determine which ions will pass through the quadrupole and be detected.

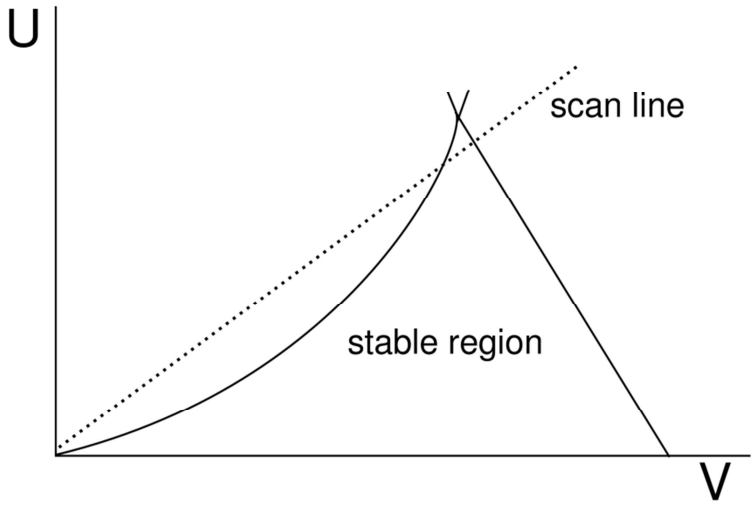

Figure 1.5: Illustration of a Mathieu stability diagram

The Mathieu stability diagram is prepared by plotting the two Mathieu parameters, a_u and q_u. These parameters are related to the DC (U) and RF (V) voltages respectively, and are defined by equations 1.7 and 1.8.

$$a_u = \frac{8eU}{mr_o^2\omega^2} \tag{1.7}$$

$$q_u = \frac{-4eV}{mr_o^2\omega^2} \tag{1.8}$$

where *u* represents either the x- or y-direction, *e* is the elementary charge, *m* is the mass, r_o is the radius of the ion path, and ω is the angular frequency.

The quadrupole can therefore be used either as a mass filter for selection of an ion with a particular *m/z*, or it can be used as a mass analyser and scan for a range of *m/z* values by varying the RF voltage. However, the achievable mass accuracies and resolving powers are limited at ~100 ppm and ~1000 Da, respectively.

1.3.3 Linear Ion Traps

Linear ion traps confine ions along the axis of a quadrupole by the application of a 2D radio frequency field, with additional DC voltages applied to two end trapping segments.[23] As well as acting as a mass analyser, linear ion traps are often used for storing ions as part of a hybrid instrument, or for isolating ions of a specific *m/z* for tandem mass spectrometry experiments.

1.3.4 Quadrupole Ion Trap (QIT) Mass Analyser

Quadrupole ion trap instruments originate from the work of Wolfgang Paul[24] and operate similarly to a quadrupole but instead of passing through, the ions are trapped in 3D for detection. A QIT consists of two endcap electrodes and a ring electrode in between. By applying oscillating RF voltages to the ring electrode and static DC voltages to the endcaps, a 3D quadrupolar electric field is created. By changing the electric field on the endcap, the ions can be sequentially ejected according to their mass through a small gap in one of the endcaps towards the detector. Although higher resolving powers are achievable with a quadrupole ion trap (~10,000 Da), mass accuracies are similar to those achievable with a quadrupole alone. The advantage of using an ion trap is the increase in sensitivity through the accumulation of ions for a specified time period before detection.

1.3.5 The Orbitrap

The Orbitrap[25-26] is an example of a modified Kingdon trap whereby ions are stored, not in a potential well, but through their angular momentum about a central electrode. The trap consists of a spindle contained within a barrel and it is this spindle to which the ions are attracted and rotate around, as illustrated in Figure 1.6.

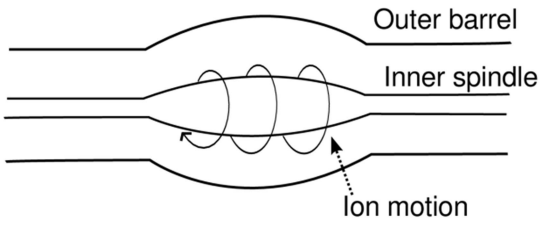

Figure 1.6: Schematic of the Orbitrap, illustrating ion rotation around a central spindle

The angular frequency (in the z-direction) of the rotation around the spindle is detected as an image current which is then processed using a Fourier transform to give a frequency spectrum and, ultimately, a mass spectrum. The Orbitrap can achieve resolving powers of ~2-300,000 and mass accuracies of 1 ppm with internal calibration making it the highest performing mass analyser next to FTICR instruments.

1.3.6 Time-of-Flight (TOF) Mass Analyser

In a time-of-flight, or TOF, analyser, the ions are accelerated by an electric field of a constant, known strength and therefore exit this region with the same kinetic energy.[27] The velocity of an ion depends on its *m/z* ratio, so the time taken to reach a detector at a known distance is measured. Since lighter ions have higher velocities,

these will reach the detector first, and the times (*t*) recorded can then be converted to values for *m/z* using equation 1.9.

$$t = \frac{d}{\sqrt{2U}}\sqrt{\frac{m}{q}} \qquad (1.9)$$

where *d* is the length of the flight tube and *U* is the acceleration voltage applied. A TOF mass analyser is commonly associated with MALDI ionisation; however, initial MALDI-TOF instruments demonstrated poor resolution, mainly due to the fact that the ions were accelerated as soon as they were produced through laser irradiation. Since this process lasts for a specified time period, ions of the same *m/z* value arrived at the detector at slightly different times through spreading out of the ion packet causing a distribution in kinetic energies of the ions. To overcome this, there are two solutions implemented in most TOF instruments; first, a reflectron was introduced into the instrument.[28] This effectively acts as a mirror by using an electric field to reflect the ion beam back to the detector whilst simultaneously improving the achievable resolving power. Ions of the same *m/z* but with higher kinetic energy will travel further into the reflectron than those with lower kinetic energy, therefore compensating for the difference in time taken for the ions to travel to the detector. Second, a technique known as delayed (or pulsed) ion extraction is used.[29-30] In this process, both the target plate and a second voltage plate separated by a few mm are initially held at the same voltage. After a delay of typically a few hundred nanoseconds, the voltage on the second plate is reduced by 2-3 kV generating an electric field to which all ions are drawn. The ions that are further away from this plate when the voltage is dropped are exposed to more of the potential than those that are already closer to the plate; consequently the initially slower moving ions will move faster in the field free region of the flight tube, compensating for their slower

initial velocity. As a result, all ions of the same *m/z* ratio will reach the detector at the same time, increasing both the resolution and the sensitivity. Resolving powers and mass accuracies vary for TOF instruments; the introduction of longer flight tubes and a reflectron has increased achievable resolving powers to ~15-20,000 Da with mass accuracies around 10 ppm. In linear mode, the sensitivity is generally better due to the shorter flight time; however, the lack of a reflectron reduces resolving powers to ~8-10,000 with mass accuracies increasing to 200 ppm. High resolution TOF instruments usually incorporate additional analysers such as a quadrupole thereby increasing resolving powers to ~20-40,000. An additional advantage of a time-of-flight analyser is the quicker scan speed which is on the order of milliseconds, as opposed to 1 second for ion traps, quadrupoles and FTICR instruments.

1.4 FTICR Mass Analyser

In an FTICR mass analyser ion detection occurs in an ICR cell, in which the ions are trapped radially by a magnetic field, and axially by an electric field. The behaviour of the ions in this combination of fields is the basis for FTICR mass spectrometry, and will be explained in detail in section 1.4.2.

1.4.1 The ICR Cell

The ICR analyser cell, or Penning trap, is at the core of the instrument, in that ions are trapped, excited, and detected here during the course of an experiment. The cell is positioned in the centre of a superconducting magnet and is composed of three pairs of plates, namely trapping, excitation, and detection plates.[31] The trapping

plates lie perpendicular to the magnetic field, whilst the excitation and detection plates lie in the plane of the field, as illustrated in Figure 1.7.

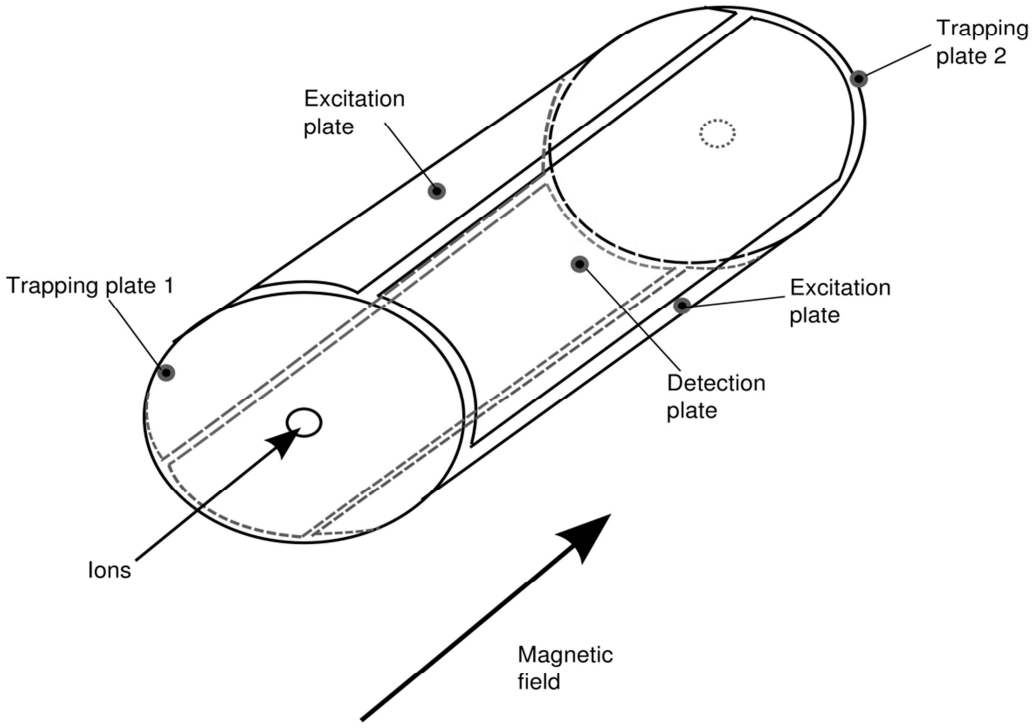

Figure 1.7: Schematic of a cylindrical ICR cell showing the trapping, excitation, and detection plates

Cell design is an important avenue of research in FTICR instrumentation, with the aim of improving the performance of these instruments through increasing attainable resolving powers and mass accuracies. Designs have moved on from the original cubic analyser cell,[32] to those based on a cylindrical geometry. Over the years the designs have been optimised so as to produce an "ideal" electrostatic potential for trapping the ions.[33] The open cylindrical cell,[34] Infinity cell,[35] compensated open cylindrical cell,[36-38] and the dynamically harmonised cell[39] are all examples of cell designs with different features for improving instrument performance.

1.4.2 Ion Motion

Once inside the ICR cell, an ion with mass *m*, charge *q*, and velocity *v*, moving in a magnetic field of magnitude *B*, experiences a force known as the Lorentz force, and as a result, moves in a circular orbit in the plane perpendicular to the direction of the magnetic field, as shown in Figure 1.8.

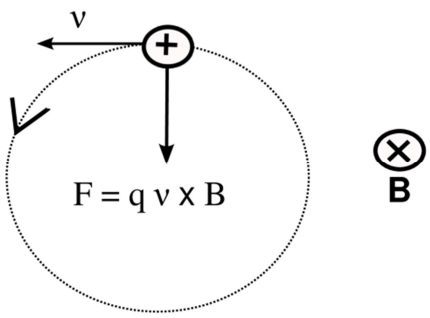

Figure 1.8: Illustration of the Lorentz force acting on a charged particle in a magnetic field

The magnitude of the force experienced by the ion is given by equation 1.10.

$$\vec{F} = q\vec{v}_{xy}\vec{B}sin\theta \qquad (1.10)$$

where θ is the angle between the axis of the ion's motion and the axis of the magnetic field strength, *B*. Equation 1.10 can be simplified to equation 1.11 due to the fact that the direction of ion motion and magnetic field are perpendicular.

$$\vec{F} = q\vec{v}_{xy}\vec{B} \qquad (1.11)$$

The Lorentz force is balanced by the centrifugal force, described by equation 1.12.

$$\vec{F} = ma = \frac{m\vec{v}^2}{r} \qquad (1.12)$$

Since the sum of the forces is equal to zero, equations 1.11 and 1.12 can be set as equal to each other (equation 1.13).

$$q\vec{v}_{xy}\vec{B} = \frac{m\vec{v}^2}{r} \qquad (1.13)$$

Rearrangement of equation 1.13 and substituting for the angular frequency, ω, where $v=\omega r$, yields an expression for the cyclotron frequency that characterises the circular motion of an ion in a magnetic field. The cyclotron frequency, which is related to the mass-to-charge ratio of the ion, is defined by equations 1.14 and 1.15.

$$\omega_c = \frac{qB}{m} \qquad (1.14)$$

$$f = \frac{qB}{2\pi m} \qquad (1.15)$$

In an FTICR experiment, the cyclotron frequency, ω_c, is measured so as to determine its mass-to-charge ratio, m/z, where $z = q/e$ and e is the elemental charge.

Equations 1.14 and 1.15 describe the cyclotron motion in the presence of a magnetic field only; in an FTICR experiment, an electric field is applied to the trapping plates in order to confine the ions in the axial (z) direction i.e. parallel to the magnetic field. As a result, the ions oscillate backwards and forwards along the z axis and are trapped in the ICR cell. The equation for the axial force in the z-direction is defined by equation 1.16.

$$F = \frac{md^2z}{dt^2} = q\vec{E} \qquad (1.16)$$

where $\vec{E}$ is the electric field. From this equation, it is possible to obtain an equation for the trapping frequency, ω_z, at which the ion oscillates along the z-axis, and this is defined by equation 1.17.

$$\omega_z = \sqrt{\frac{2qV_T\alpha}{ma^2}} \tag{1.17}$$

where V_T is the trapping potential applied to the plates, a is the distance between the trapping plates, and α is a coefficient dependent on the geometry of the trap.

The addition of a potential term in the z-direction also produces a radial force and so introduces another term to equation 1.11, leading to equation 1.18:

$$\vec{F} = q\left(\vec{v}_{xy} \times \vec{B}\right) + q\vec{E} \tag{1.18}$$

where $\vec{E}$ is the electric field, and $q\vec{E} = \frac{qV_T\alpha}{a^2}r$. The radial electric field produces an electric force that acts on the ion so as to push it away from the centre of the cell, thus opposing the Lorentz force from the magnetic field. The equation for ion motion can now be defined by equation 1.19:

$$Force = m\omega^2 r = qB\omega r - \frac{qV_T\alpha}{a^2}r \tag{1.19}$$

Equation 1.19 can be re-written in the form of a quadratic in ω, as shown in equation 1.20:

$$\omega^2 - \frac{qB\omega}{m} + \frac{qV_T\alpha}{ma^2} = 0 \tag{1.20}$$

The solutions of this quadratic equation correspond to two rotational frequencies in the plane perpendicular to the magnetic field i.e. the xy plane, as shown by equations 1.21 and 1.22:

$$\omega_+ = \frac{\omega_c}{2} + \sqrt{\left(\frac{\omega_c}{2}\right)^2 - \frac{{\omega_z}^2}{2}} \tag{1.21}$$

$$\omega_{-} = \frac{\omega_c}{2} - \sqrt{\left(\frac{\omega_c}{2}\right)^2 - \frac{{\omega_z}^2}{2}} \quad (1.22)$$

Where: $\omega_c = \frac{qB}{m}$ (1.14)

$$\omega_z = \sqrt{\frac{2qV_T\alpha}{ma^2}} \quad (1.17)$$

These resulting frequencies correspond to the reduced cyclotron frequency, ω_+ (1.21), and the magnetron frequency, ω_- (1.22). The magnetron frequency is a result of the contradictory forces acting on an ion from the magnetic and electric fields, causing the ions to experience a third type of motion, namely magnetron motion, which offsets the centre of the ion's cyclotron motion causing a shift in its cyclotron frequency.

1.4.3 Excitation and Detection

In order to detect the ions in the cell, they must first be excited into a larger radius of cyclotron motion, so as to pass closer to the detection plates. A radiofrequency (RF) pulse is applied to the two excitation plates; when the frequency of the pulse matches the cyclotron frequency of an ion, i.e. it is in resonance, the ion absorbs energy and spirals outwards into a larger orbit, as shown in Figure 1.9.

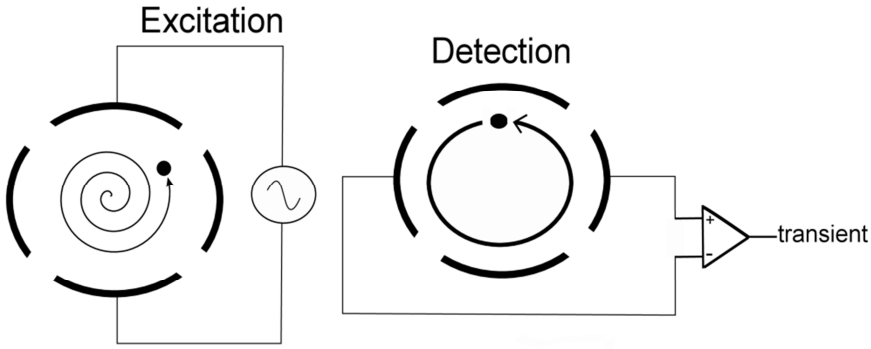

Figure 1.9: Illustration of excitation and detection processes in an FTICR experiment

The RF pulse is swept linearly through frequencies matching the *m/z* range of interest, thus exciting all ions in that range. Ions of the same *m/z* ratio are excited coherently and so orbit the cell as a tight packet at the same cyclotron frequency. Different types of excitation waveforms can be used for tandem mass spectrometry experiments whereby a single peak is selected for fragmentation. These waveforms form part of a pulse program, which defines each stage of an FTICR experiment, from an initial quench to remove all ions from the cell, to isolation and fragmentation, accumulation, and finally excitation and detection. A method for producing the optimal excitation waveform required with high selectivity was reported by Marshall *et al.*[40] and is known as stored waveform inverse Fourier transform, or SWIFT. The frequency domain excitation spectrum required is first specified so that the resonant frequencies of the selected ions only are excited. The inverse Fourier transform is taken to convert this frequency domain to a time domain excitation signal, and is therefore simply the reverse process for acquiring a mass spectrum in FTICR. SWIFT has been used to isolate individual isotope peaks[41-42] as well as in multiple stages of tandem mass spectrometry (MS^n) for the structural

elucidation of small molecules.[43] Other methods of excitation used for the selection of ions include correlated harmonic excitation field, or CHEF,[44] and an extension of this known as multi-CHEF.[45] In CHEF, single- and swept-frequency excitation fields are used to eject unwanted ions from the cell, and in multi-CHEF, this is extended from to include a set of known reference peaks which are isolated simultaneously with the precursor ion. These reference peaks can then continue to be detected as multiple stages of tandem mass spectrometry are performed, enabling accurate internal calibration of the product ions.

As the ions pass the two detector plates, an image charge is induced, which is then converted into an alternating current and recorded as a time domain signal known as a transient. A Fourier transform is applied to the transient to create a frequency domain spectrum, which is calibrated and converted to a mass spectrum using the relationship between frequency and *m/z* ratio. It is this non-destructive nature of FTICR mass spectrometry, and the fact that the ions can be detected for long periods of duration, that leads to the observation of ultra-high resolving power and mass accuracy.

1.4.4 Data Post-Processing

Once the data has been acquired, there are a number of post-processing functions that can be applied in order to enhance resolution further.

1.4.4.1 Apodisation

The time-domain signal, or transient, is acquired for a finite time period; consequently, the abrupt ending of the signal results in the generation of tails located on either side of the main peak in the frequency-domain spectrum. These tails can interfere with the identification of low-intensity peaks but can be reduced by

applying time-domain weight functions before Fourier transformation, a process known as apodisation.[46] There are several different weight functions that can be applied to the data, including Gaussian, sine-bell, and Hamming functions.[47] Application of one of these functions results in a reduction of the amplitude of peak-tails, but at the cost of broadening of the spectral peak thereby reducing resolution and signal-to-noise ratio. The extent of this effect varies from spectrum to spectrum, as it is dependent on the data acquisition time and the level of decay of the transient signal.[48]

1.4.4.2 Zero-filling

The use of the zero in FTICR mass spectrometry is two-fold; first, zeroes can be used to replace some of the data signal in order to filter out noise and improve the signal intensity. Second, zeros are generally added to the end of the time-domain data set in order to interpolate extra points aiding peak fitting algorithms to improve mass accuracy, by increasing the acquisition time of the signal.[47] The number of data points recorded in the time domain spectrum increases from N to 2N for one zero-fill thereby decreasing frequency point spacing resolution since point-resolution is proportional to acquisition time.

1.4.5 Instrument Developments

FTICR mass analysers are currently the best performing instruments in terms of achievable resolution and mass accuracy, although the mass range is limited to a few thousand *m/z* while high performing TOF analysers can detect in the tens of thousands. Resolving powers of ~500,000 can be obtained routinely but can be pushed to a few million in heterodyne mode, where a narrow *m/z* range is studied under high resolution conditions.[49] Although ultra-high resolution and mass accuracy are routinely achieved with FTICR mass spectrometers, the number of

unresolved peaks increases at higher *m/z* due to decreased resolving power and an increase in the number of possibilities of elemental compositions. The complex nature of current applications being explored has therefore resulted in a need for further improvements and optimisation of FTICR technology.[50] Developments in the hardware components contribute greatly to improvements in its performance; for example, increasing the magnetic field strength leads to a linear increase in achievable resolving power. The introduction of 14.5 T magnet[51] gave results with resolving powers two-fold better than that obtained with a 7 T magnet. Other features of the instrument have been improved over the years, including the vacuum system, to ensure detection occurs at a sufficiently low pressure (~ 10^{-10} mbar) and prevent sudden damping of the transient signal. The data acquisition system has also been improved to increase acquisition speeds and data storage space.[52]

1.5 Tandem Mass Spectrometry (MS/MS)

The principle of a tandem mass spectrometry experiment is to obtain structural information on a precursor compound through isolation, fragmentation, and subsequent analysis of the product ions detected. The process can be repeated a number of times by further selection of a specific fragment ion in each fragmentation spectrum, and subjecting it to dissociative processes, therefore yielding multistage mass spectrometry or MS^n experiments. There are a number of tandem MS techniques that can be used for this purpose, involving both neutral molecules and electrons.

1.5.1 Collision Activated Dissociation (CAD)

The most widely used tandem mass spectrometry technique is collision activated dissociation (CAD),[53] or collision induced dissociation (CID).[54-55] During CAD, the precursor ion is subjected to collisions with a neutral gas, such as argon. These ions become activated through the conversion of translational energy to vibrational energy thereby increasing the internal energy of the precursor. Since intramolecular vibrational energy redistribution (IVR) often occurs before fragmentation, the bonds with the lowest dissociation energy are preferentially broken, which, for peptides and proteins, corresponds to the peptide bond, forming the characteristic b- and y-ions,[56-58] as shown in Figure 1.10.

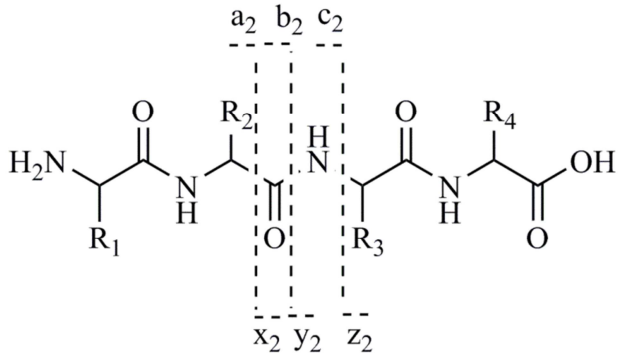

Figure 1.10: Illustration of the types of product ions formed during fragmentation in tandem mass spectrometry experiments

One of the main disadvantages of using CAD is the tendency for labile groups to be cleaved during the process making it an unreliable technique in the analysis of protein post-translational modifications. CAD still provides useful sequence information but the development of alternative tandem mass spectrometry techniques means it is often used to provide complementary information in addition to other

methods. One such technique is infrared multiphoton dissociation (IRMPD).[59] IRMPD involves the use of a laser, generally a CO_2 laser with a wavelength of 10.6 µm, which is directed at a sample so that the precursor ion absorbs one or more photons, causing the internal energy of the molecule to increase and fragment. IRMPD has been shown to produce significant fragmentation of large proteins, producing a number of additional sequence ions to CAD, and therefore improving the structural information obtainable on larger molecules.[41]

1.5.2 Sustained Off-Resonance Irradiation (SORI) - CAD

Sustained off-resonance irradiation (SORI)-CAD[60] is an alternative method for fragmenting molecules and can be performed in the ICR cell itself. The precursor ion is excited by the application of a pulse with a frequency slightly higher than its natural cyclotron frequency.[61] This causes the ions to repeatedly accelerate and decelerate as their cyclotron radii continuously expand and contract. A collision gas such as argon is then pulsed into the cell to cause dissociation of the analyte ions. The advantage of SORI-CAD is that the ions can be excited for longer periods of time (generally hundreds of milliseconds) and so more collisions can occur in this time thereby increasing the degree of fragmentation.

1.5.3 Electron Capture Dissociation (ECD)

The advent of techniques based on ion-electron interactions has broadened the applications where tandem mass spectrometry has significant advantages, such as in proteomics. Electron capture dissociation (ECD) in particular has been instrumental in this field due to its ability to provide detailed sequence information in proteins, complementary to CAD, as well as preserving post-translational modifications.[62] ECD involves the capture of an electron by a multiply-charged cation e.g. a polypeptide, subsequently forming a cation radical through neutralisation of a

charge, which results in bond cleavage; in the case of peptides, this bond is normally the N-C_α forming c and z$^\bullet$ ions. The exact mechanism of ECD is under heavy debate in the literature;[63-67] the technique was originally developed in the late 1990's by Zubarev *et al.*[67] who proposed that electron attachment occurs at a protonated site forming a hypervalent radical site, stabilised due to solvation of a proton by a backbone amide carbonyl. The energy released upon attachment of the electron (recombination energy) is sufficient to enable the ejection of a hydrogen radical with enough kinetic energy to transfer to the oxygen of an amide carbonyl. This mechanism, known as the Cornell, or hot hydrogen, mechanism is illustrated in Figure 1.11.

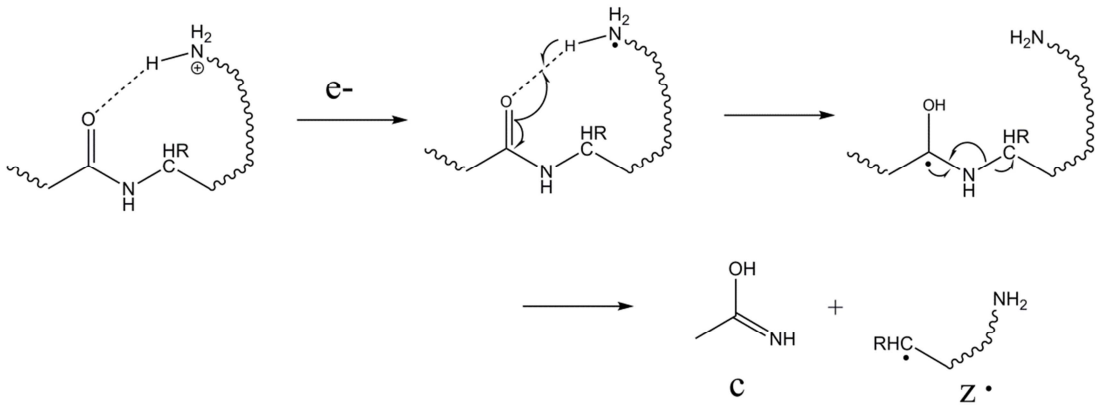

Figure 1.11: Illustration of the Cornell mechanism for ECD

An alternative mechanism was developed to explain where, for steric reasons, hydrogen radical transfer from a protonated site is unable to occur, but cleavage of the molecule is still observed. Syrstad and Turecek[66] proposed that electron capture occurs directly in an amide π* orbital whereby a number of electronic states of the charge reduced ion are sampled consecutively. If the ground state is reached, hydrogen transfer onto a solvated amide carbonyl group can occur, leading to

cleavage of the N-C_α bond. Simultaneously, Simons *et al.*[65, 68] reported a similar mechanism but proposed that the electron is most likely to attach to a Rydberg orbital localised on a positively charged site.[69] The electron can then undergo fast intramolecular transfer to a π^* amide orbital enabling cleavage of the N-C_α bond to occur. Consequently these collective results constitute the Utah-Washington mechanism for ECD, whereby an electron is captured directly into a Rydberg orbital and transferred to an amide π^* orbital stabilised by local intramolecular electrostatic potentials provided by protonated sites within the molecule, as shown in Figure 1.12.

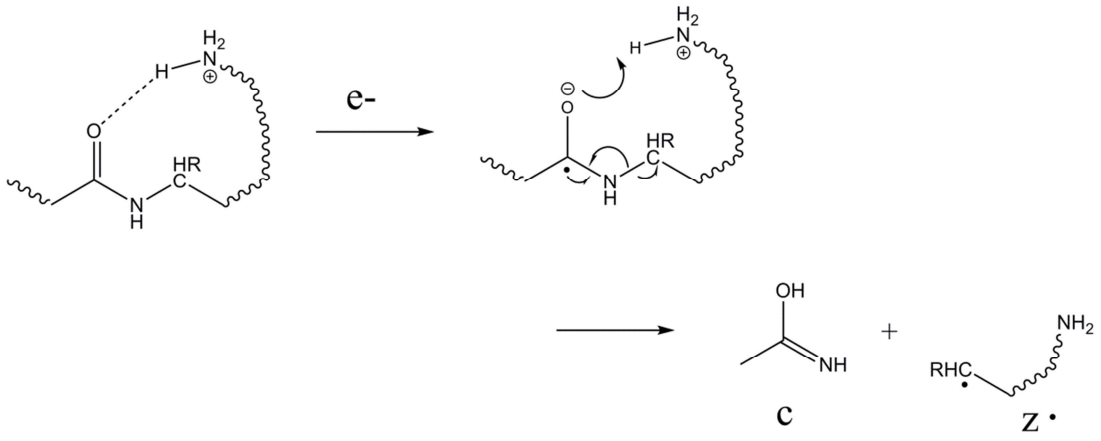

Figure 1.12: Illustration of the Utah-Washington mechanism for ECD

The unique fragment patterns able to be produced using ECD has led to the rapid development of a number of other electron-based dissociation techniques. Electron detachment dissociation (EDD)[70] can be applied to anions to cause fragmentation through electron ejection from the precursor ion. Electron transfer dissociation (ETD)[71] was developed for use in instruments other than FTICR mass spectrometers. In this case, electrons are transferred to the precursor ion via radical anions, which are produced in a negative chemical ionisation source and are generally molecules consisting of aromatic rings systems, such as anthracene ($C_{14}H_{10}$) or fluoranthene

($C_{16}H_{10}$). Transfer of an electron forms the radical cation species that leads to fragmentation analogous to that observed in ECD. ETD is therefore also advantageous in proteomics due to the preservation of labile groups during fragmentation, enabling analysis of protein post-translational modifications to be performed.[72]

Since ECD involves the capture of an electron and subsequent neutralisation of a charge site, molecules must carry a charge ≥ 2 in order for fragments to be detected. Therefore, this technique cannot be applied to molecules which can only carry a single positive charge, as is common with fatty acids and polyketides. As a result, ionisation methods like MALDI, which produce mainly singly charged species, cannot be used in conjunction with electron capture dissociation. There is, therefore, a drive to find tandem mass spectrometry techniques which are compatible with small, singly charged species, and that can produce extensive fragmentation of these molecules.

1.5.4 Electron Induced Dissociation (EID)

One of the first studies conducted on singly charged ions was reported in 1979 by Cody *et al.*[73] who used electrons to fragment substituted benzene radical cations. The technique was termed electron impact excitation of ions from organics (EIEIO) and the authors reported that similar fragmentation to CAD was observed when the molecules were fragmented using electrons with energies below the second ionisation energies of the cations. Wang and McLafferty took the technique further in 1990 and demonstrated its ability to fragment large biomolecules, like gramicidin S, using 70 eV electrons; again, they reported similar fragmentation patterns to CAD.[74]

Since then, several studies have reported on the fragmentation patterns obtained when singly charged molecules, such as biomolecules[75] and inorganic complexes,[76] are allowed to interact with electrons, a technique termed Electron Induced Dissociation (EID). More recently, Lioe and O'Hair compared EID spectra of singly protonated amino acids and their simple peptides, obtained using electron energies around 20 eV, to those obtained using CAD.[77] This approach is similar to hot ECD (hECD),[78] where electrons with high energies, typically around 10 eV, induce fragmentation in multiply charged molecules. The authors reported extensive fragmentation of the amino acids and peptides that was different and complementary to CAD. Generally, this has been the case reported in subsequent studies. Feketeova *et al.* demonstrated that EID produced more extensive fragmentation than CAD when applied to betaine[76] and to NaCl cluster cations,[79] and Kaczorowska and Cooper showed that EID was particularly effective in fragmenting polynuclear metal complexes,[80] and the metallo-porphyrin, octaethylporphyrin.[81]

The role of metals in EID has been investigated using tryptophan[82] and it has been shown that more fragments were produced than with CAD. This suggests that more electronic excited states can be accessed via an interaction between the metal ion and the electrons. Similar work undertaken by Mosely *et al.*[83] demonstrated that the charge carrying species of small, pharmaceutical-type molecules influenced the degree of fragmentation. They showed that sodium and potassium were retained by nearly all the product ions, and provided complementary data to the protonated and ammonium adducts. Work carried out by Kalli *et al.*[84] showed that radical ions unique to EID were formed when singly deprotonated peptides were irradiated with electrons. Differences were observed in the EID spectra of the amidated and the free

acid forms of substance P and LHRH, suggesting that the charge location may also have an impact on the fragmentation pattern observed.

1.6 Bruker solariX 12 T FTICR Mass Spectrometer

The majority of the work in this thesis was carried out on a Bruker solariX 12 T FTICR mass spectrometer (Bruker Daltonics, Coventry, UK). A schematic of this instrument is shown in Figure 1.13.

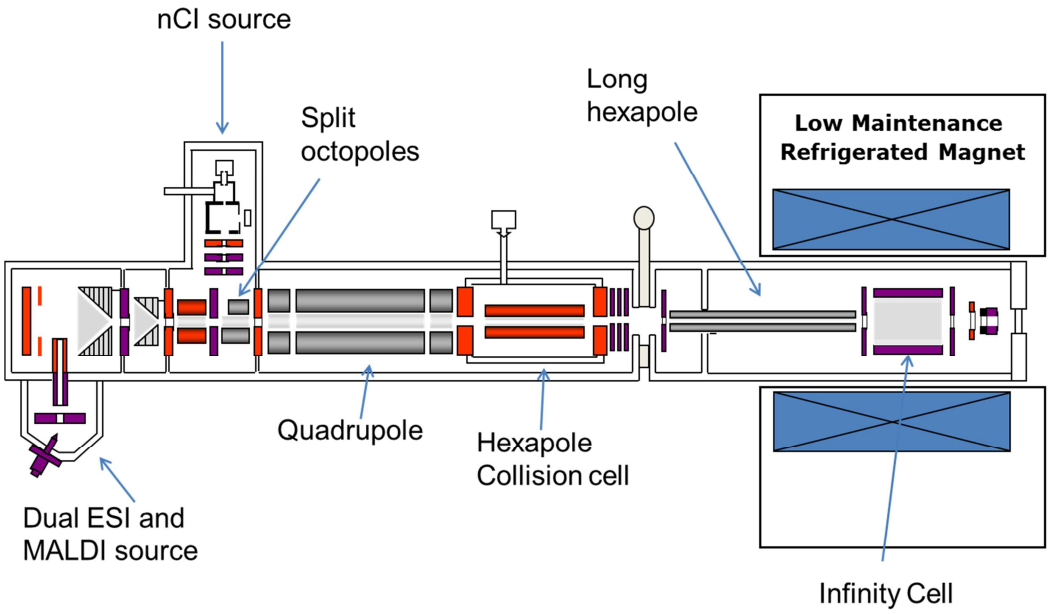

Figure 1.13: Schematic of the Bruker solariX FTICR mass spectrometer (reproduced and adapted from the Bruker solariX user guide with permission)

The instrument has a dual ESI and MALDI source for the generation of ions which are then transferred through a heated glass capillary, positioned perpendicular to the main axis of the instrument. A series of electrostatic and octapole ion optics guide the ions to the quadrupole and hexapole collision cell. Ions can be isolated by the quadrupole, before being transferred to the collision cell for fragmentation by CAD

or ETD, or for accumulation. For ETD, a negative chemical ionisation (nCI) source is located above the split octapoles for generation of the radical anions. The ions are transferred via a hexapole to the Infinity[35] ICR cell for detection. On the far side of the ICR cell, a hollow cathode is located for ECD and EID experiments inside the cell. The use of a hollow cathode further enables the positioning of an IR laser at the back of the instrument for IRMPD experiments. This instrument can routinely achieve 500,000 resolving power at *m/z* 400 and, with internal calibration, mass accuracies of <0.5 ppm.

1.7 Applications of FTICR-MS

The high performance capabilities of FTICR mass spectrometry make this instrument suitable for a number of different applications. The identification of thousands of components in complex mixtures is possible due to the ultra-high resolving powers achievable.[50] In proteomics, this enables the separation of overlapping isotopic distributions, and therefore charge state determination, for large, multiply charged biomolecules.[85] The variety of tandem mass spectrometry techniques available on an FTICR mass spectrometer, including CAD, ECD, EID and IRMPD enable detailed, complementary data to be obtained for small molecule structural analysis, as well as identifying modifications on peptides and proteins. High mass accuracy further supports the identification of elemental compositions with a high degree of confidence. The use of FTICR mass spectrometry in small molecule structural analysis and protein modifications is explored in chapters 2-4, and is introduced in the following sections.

1.7.1 Structural Characterization in Natural Product Analysis

Natural products have been a source of clinical drugs for a number of decades, with investigations into the discovery of novel therapeutic compounds peaking in the 1970s and '80s.[86] The increased resistance of bacterial strains to antibiotics has driven the need to develop new drugs;[87-88] natural products, such as polyketides and non-ribosomal peptides, in particular have displayed a remarkable range of pharmaceutical properties, and subsequently account for a significant number of clinical drugs currently available.[89-90] Polyketides include antibiotics (e.g. erythromycin A), anticancer drugs (e.g. epothilones), and cholesterol-lowering drugs (e.g. lovastatin). Non-ribosomal peptides also include antibiotics, such as tyrocidine, as well as antifungal, antiviral, and immunosuppressant drugs.[91]

The process of the discovery of natural product compounds, and its progression towards the development of new drugs, is challenging as it involves several stages, namely the extraction of the product from its source, concentration, fractionation, and purification yielding a single, bioactive compound.[86] Structural characterization is necessary to eliminate already known compounds from further investigation, a process known as "dereplication",[92-94] by comparing the chemical and mass spectral properties of the unknown with the known compounds. Traditionally, structural information has been obtained using a variety of different analytical techniques, including nuclear magnetic resonance (NMR), mass spectrometry, and chromatographic separation techniques such as gas chromatography (GC), and liquid chromatography (LC).[94] The timescale for the subsequent identification of the compound was considered to be a limiting factor in the discovery process, as structure determination would take on the order of weeks to months. Improvements in resolution of analytical techniques like mass spectrometry

have reduced this timescale significantly, meaning the identification of new compounds can be achieved at a faster rate than was previously possible.[92] High resolution mass spectrometry is generally used in the first instance to identify the molecular formula, which has the advantage that only micrograms of material is required, with NMR providing additional structural information.[86] As a result, combining both of these techniques has proved to be a powerful method for elucidating the structures of novel compounds.

In this work, a method using complementary tandem mass spectrometry techniques has been developed for the structural characterisation of polyketides and non-ribosomal peptides, which is explored in chapters 2 and 3.

1.7.2 Protein Binding Site Analysis of Anticancer Compounds

Cisplatin [$Pt(NH_3)_2Cl_2$] is one of the most widely used anticancer drugs due to its high success rate in the treatment of ovarian and testicular cancers.[95] However, on entering the blood plasma, cisplatin binds to proteins; some of these, such as human serum albumin, are thought to play a role in the distribution of the drug,[96] but with others, the binding is irreversible. This causes the deactivation of the drug and reduced urinary excretion, resulting in deposition of platinum in tissue.[97] It is believed that these interactions are the principal cause of the severe side effects observed, such as nephrotoxicity and ototoxicity.[98] Various papers report the results of binding studies carried out with cisplatin and a variety of proteins such as human serum albumin,[96] cytochrome c,[97] ubiquitin,[98] insulin,[99] transferrin,[100-101] and calmodulin.[102-103]

Complexes based on alternative metals to platinum are being developed; in particular, compounds based on ruthenium are promising and there are two

compounds, namely NAMI-A[104-105] and KP1019,[106] that are currently in phase 2 of clinical trials.[107] The major differences between ruthenium and platinum are the range of accessible oxidation states, coordination numbers, and geometries available. Potentially, ruthenium binding to biomolecules may be reversible, in contrast to platinum, which subsequently reduces the toxicity of the metal. Ruthenium is in the same group of the periodic table as iron (group VIII) and may mimic iron in its binding to biomolecules which, as tumour cells have a great demand for iron, would enable the drug to be delivered more effectively to the target site.[95, 108] Platinum also shows a lack of activity towards certain cancers, so developing different metal-based compounds might lead to effective treatment for other types of cancer.[109]

Mass spectrometry has proved to be a powerful tool for the elucidation of the binding sites of metal complexes. In particular, the use of FTICR-MS has been beneficial in this area due to the ultra-high resolving power and mass accuracy achievable, enabling clear isotope patterns to be distinguished. Metals like platinum and ruthenium have distinct isotope patterns,[110] enabling the identification of metal-containing species to be made with high mass accuracies, therefore ensuring that confident assignments are made.

1.8 Thesis Overview

In this thesis, a number of different applications of FTICR mass spectrometry have been investigated where high mass accuracy is demonstrated to be essential in order to achieve the objectives of the projects. Chapter 2 begins with the use of tandem mass spectrometry for the structural characterization of small molecules, specifically polyketides. By combining CAD and EID, a method has been developed that

enables detailed structural information to be obtained on these compounds and allows two isomers to be distinguished. In chapter 3 this method is extended so as to be applied to the larger class of natural products, the non-ribosomal peptides. As a test case, the method is focussed on the compound actinomycin D and combines multiple ion isolation with tandem mass spectrometry to produce detailed, accurately calibrated structural information. In chapter 4, tandem mass spectrometry is also used to develop a method for identifying the binding sites of potential ruthenium anticancer compounds on peptides and proteins. The importance of obtaining mass accuracies below 1 ppm has been demonstrated and the coordination of ruthenium to certain amino acids has been seen for the first time. The final chapters, 5 and 6, are further applications of FTICR mass spectrometry but are ongoing projects. Chapter 5 involves analysing mixtures where there are a large number of unknown peaks, and high resolving power and mass accuracy are necessary for the accurate identification of the different compounds. The mixture used is alcohol, with FTICR mass spectrometry used specifically to identify differences in genuine and counterfeit vodkas. Chapter 6 is an application involving MALDI and using carbon nanotubes as an alternative to a matrix for detecting peptides polymers. Overall, this thesis has demonstrated a number of applications involving FTICR mass spectrometry, in which a combination of high resolution and mass accuracy are necessary to achieve the end goal.

Chapter 2: Characterizing the Structures of Polyketides Using High Mass Accuracy Tandem Mass Spectrometry

This chapter has been partially reproduced from the following publication:

R.H.Wills, M.Tosin and P.B.O'Connor, Structural Characterization of Polyketides Using High Mass Accuracy Tandem Mass Spectrometry, *Anal. Chem*., **2012**, 84(20), 8863

2.1 Introduction

Understanding the biosynthetic pathways of natural products such as polyketides is of great interest for the drug discovery process as it can enable scientists to perform modifications in order to generate novel compounds with bioactive properties.[111] Type I polyketides are produced through the action of a series of enzymes that are organized into modules forming an assembly line, and are known as polyketide synthases (PKSs). These enzyme complexes are composed of individual domains, namely ketosynthase (KS), acyl transferase (AT), and acyl carrier protein (ACP), as shown in Figure 2.1 (A), and are coordinated within the complex so as to incorporate a small set of linear units into a chain through consecutive condensation reactions.[112]

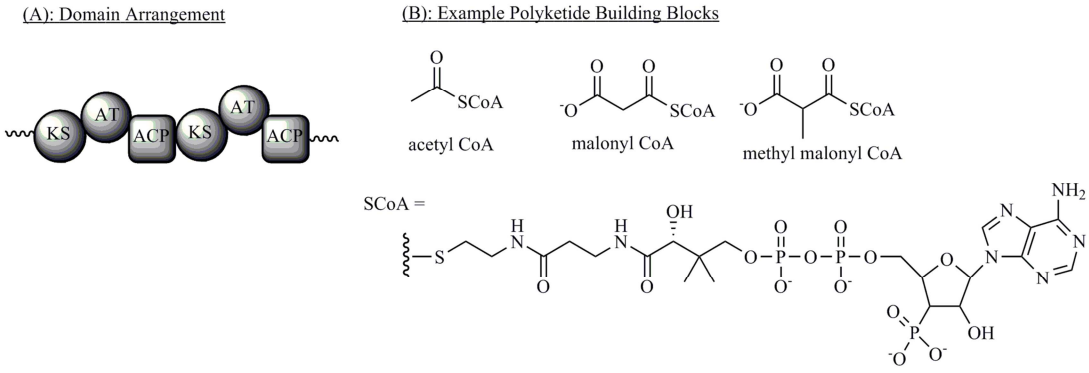

Figure 2.1: (A) Arrangement of the PKS domains, KS = ketosynthase, AT = acyl transferase, ACP = acyl carrier protein; (B) example building blocks in polyketide synthesis, adapted from reference [2]

Polyether ionophores are a group of polyketides that comprise a carboxylate group, and several tetrahydropyran (THP) or tetrahydrofuran (THF) rings. Amongst polyketides, polyether antibiotics constitute a unique class of compounds broadly used in veterinary medicine and in animal husbandry for their ability to complex inorganic cations and aid their transport across membrane barriers.[113-115] There is,

however, a growing concern about the presence of these compounds in the environment; specifically, the potential toxicity to organisms in aquatic environments and the contamination of drinking water. In order to quantify the amount of these antibiotics present in the environment, a reliable method of identification is needed.[116-118] Different tandem mass spectrometry techniques have been applied to assist in the structural characterisation of polyketides.[119-124] CAD[119-122] and IRMPD[120] have been used previously and produce few diagnostic ions for macrolides such as erythromycin A. This is due to the successive loss of water molecules being the dominant dissociation pathway under these conditions, resulting in little cleavage of the macrocycle itself. Similar studies have been conducted on polyether ionophores such as lasalocid,[113,125] tetronasin,[114] and monensin.[113] The ability of these compounds to complex metal ions has been utilised whereby the effect of adding different metal cations was investigated through a comparison of the CAD spectra obtained. The location of the charge has been found to vary according to whether a metal cation or a proton is bound, resulting in different fragmentation patterns being accessed.[113,119,120] The development of ion-electron fragmentation techniques has been advantageous in terms of providing complementary structural information to CAD and IRMPD; however, the use of odd-electron tandem mass spectrometry techniques, specifically electron induced dissociation (EID), has not, as yet, been explored as a method for characterising the structures of these molecules.

2.2 Experimental

2.2.1 Chemicals and Reagents

The polyketides erythromycin A, lasalocid A and *iso*-lasalocid A were provided after being isolated by fermentation of *S. erythraea* and *S. lasaliensis*, and extracted with ethyl acetate as previously reported.[126,115] The extracts were concentrated and then dissolved in 50% methanol and 50% Milli-Q water (Millipore Inc., Durham, UK) prior to analysis by ESI. Extracts containing intermediate mixtures were also provided after being extracted with ethyl acetate as previously described.[115] HPLC grade methanol was purchased from Fisher Scientific (Loughborough, UK), and lithium chloride was obtained from Sigma Aldrich (Gillingham, UK).

2.2.2 Analysis of Polyketides by ESI-MS

The extracts were analysed on a 12 T Bruker SolariX FTICR mass spectrometer (Bruker Daltonics, Billerica). The sodium and ammonium adducts of the polyketides occurred naturally in the cell extracts; the lithium adduct was produced by adding LiCl (1 mM) to the samples. The samples were injected directly into the source using a syringe pump with a flow rate of 200 μL/hour and sprayed from a solution of methanol/water (50:50). A nebuliser gas of nitrogen was used at a pressure of 1.2 bar, and a drying gas, also nitrogen, flowed at 4 L min^{-1} at temperature of 200 ºC. A voltage of -4500 V was applied to the glass capillary for analysis in positive mode, and an offset of 500 V was applied between the capillary and the spray shield at the entrance to the instrument. For CAD experiments, the precursor ion was isolated in the first quadrupole and fragmented in the collision cell with argon as the collision gas, and at energies of 18 V. For EID experiments, the precursor ion was isolated in the quadrupole and externally accumulated in the

collision cell for 2-5 seconds before being transferred to the ICR Infinity Cell.[35] The ions were then irradiated with electrons from a 1.7 A heated hollow cathode dispenser, biased with an offset potential of between 13 and 15 V, for 1 ms. Fifty scans were recorded for CAD experiments, and 100 were recorded for EID experiments; both used a dataset size of 4M. Trapping voltages were maintained at 0.5 V on the front plate and 0.6 V on the back plate for all experiments. In post-processing, one zero-fill was added and a sine-bell multiplication apodisation function was applied; finally the data was calibrated both internally and externally.

2.3 Results and Discussion

2.3.1 Fragmentation of Erythromycin A

In order to compare the fragmentation efficiency of EID to that of CAD, both techniques were initially performed on the molecule erythromycin A. Erythromycin A is a macrolide antibiotic, consisting of a 14-membered macrocycle with two sugars (D-desosamine and L-mycarose) attached, that has been in clinical use for the treatment of infections by Gram-positive bacteria since 1952. The main species observed in the ESI-MS spectrum of erythromycin A was that of the protonated molecule (*m/z* 734.47) and this was selected for fragmentation. Figure 2.2 shows the EID (A) and CAD (B) spectra obtained for erythromycin A, and Figures 2.2 (C) and (D) illustrate the fragments detected using both the techniques.

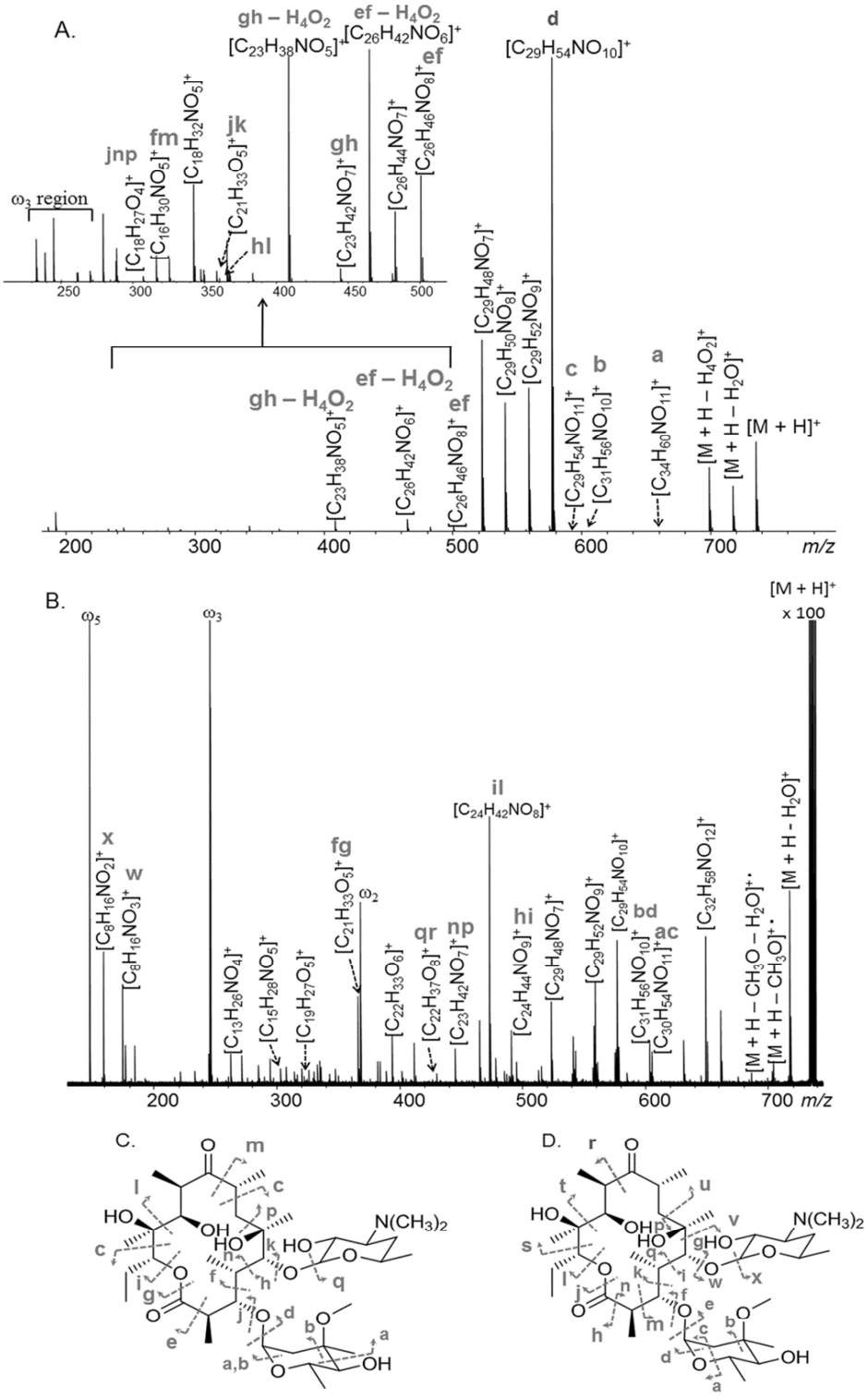

Figure 2.2: CAD (A) and EID (B) spectra of erythromycin A (precursor ion *m/z* 734.47), and identified fragments using CAD (C) and EID (D). Harmonics of these

peaks are marked ω_3 and ω_5. A full list of peak assignments can be found in Tables A-1 and A-2 of Appendix A

Table 2.1 lists the most abundant cleavages of erythromycin A observed in both EID and CAD, together with the proposed molecular formulae of each fragment and its associated mass error. The nomenclature system used here for fragment assignments is that each letter in the figure illustrations represents cleavage of that bond; the peaks are then assigned these letters depending on the bonds broken. For example, the peak at *m/*z 604.37 assigned "ac" in Table 2.1, indicates a product ion formed through cleavage at the bonds labelled "a" and "c", in the direction of the arrows shown in Figure 2.2 (D).

Table 2.1: Main fragment assignments of erythromycin A from CAD and EID (peaks used as internal calibrants are marked ▲)

Observed *m/z*	Proposed Formula	Mass Error / ppm	Fragment Cleavages
EID			
604.36912	$C_{30}H_{54}NO_{11}^{+}$	-0.03	ac
602.38994	$C_{31}H_{56}NO_{10}^{+}$	0.12	bd
▲576.37429	$C_{29}H_{54}NO_{10}^{+}$	0.12	e
514.33743	$C_{27}H_{48}NO_{8}^{+}$	0.14	f – C_2H_5O
512.29823	$C_{27}H_{44}O_{9}^{+\bullet}$	0.23	g – C_2H_8O
490.30105	$C_{24}H_{44}NO_{9}$	-0.02	hi
489.32988	$C_{25}H_{47}NO_{8}^{+\bullet}$	0.35	jk
486.34228	$C_{26}H_{48}NO_{7}^{+}$	-0.41	flm
464.30067	$C_{26}H_{42}NO_{6}^{+}$	0.02	hk – H_6O_3
472.29050	$C_{24}H_{42}NO_{8}^{+}$	0.02	il
444.29557	$C_{23}H_{42}NO_{7}^{+}$	-0.02	np
429.24843	$C_{22}H_{37}O_{8}^{+}$	0.14	qr
408.27474	$C_{23}H_{38}NO_{5}^{+}$	0.71	ij
404.26415	$C_{20}H_{38}NO_{7}^{+}$	-0.30	is
▲365.23224	$C_{21}H_{33}O_{5}^{+}$	-0.03	fg
360.23796	$C_{18}H_{34}NO_{6}^{+}$	-0.28	it
335.18521	$C_{19}H_{27}O_{5}^{+}$	-0.27	fguv
▲174.11250	$C_{8}H_{16}NO_{3}^{+}$	0.00	w
158.11760	$C_{8}H_{16}NO_{2}^{+}$	0.19	x
Mean Absolute Average		**0.04**	
Std Dev.		**0.25**	
CAD			
658.41557	$C_{34}H_{60}NO_{11}^{+}$	-0.79	a
602.38949	$C_{31}H_{56}NO_{10}^{+}$	-0.63	b
592.36878	$C_{29}H_{54}NO_{11}^{+}$	-0.61	c
▲576.37407	$C_{29}H_{54}NO_{10}^{+}$	-0.26	d
500.32154	$C_{26}H_{46}NO_{8}^{+}$	-0.50	ef – H_2O
444.29534	$C_{23}H_{42}NO_{7}^{+}$	-0.54	gh – H_2O
438.32128	$C_{25}H_{44}NO_{5}^{+}$	-0.27	fi – H_4O_2
▲365.23227	$C_{21}H_{33}O_{5}^{+}$	0.05	jk
360.23804	$C_{18}H_{34}NO_{6}^{+}$	-0.06	hl
316.21192	$C_{16}H_{30}NO_{5}^{+}$	0.22	fm
307.19048	$C_{18}H_{27}O_{4}^{+}$	0.29	jnp
158.11765	$C_{8}H_{16}NO_{2}^{+}$	-0.57	q
Mean Absolute Average		**-0.30**	
Std Dev.		**0.34**	

As shown in Table 2.1, when an internal calibration was performed, the mass accuracy for each proposed formulae for the fragments is well below 1 ppm, ensuring confident assignment. In order to achieve this, after an external calibration

was performed, a comparison with the CAD data was made and several peaks, present in both spectra, were chosen for internal calibration. As can be seen from the data in the supplementary tables of Appendix A, the assignments did not change on internal calibration, but the mass accuracy improved to well below 1 ppm. On this basis, the assignments of the product ions were made with greater accuracy so it is with greater confidence that the molecular formulae are presented and identification of the fragments made.

As shown in Figure 2.2 (A), the intensities of the fragments formed through EID are about 100-fold less intense than the precursor ion. Despite attempts to improve these intensities, including the use of a single frequency shot to improve the overlap of the ions with the electron beam,[127] no significant increase was detected. Similar results have been observed previously with Wolff *et al.*[7] and Yoo *et al.*[9] reporting intensities 50-100 fold and 50-200 fold lower than the precursors. Ly *et al.*[3] propose that the lower fragment intensities imply that the most frequent ion-electron interaction leads to the non-dissociative scattering of the electrons; however, a more likely explanation may be neutralisation of the fragments through interaction with the electrons.

Although similar fragments were detected using both CAD and EID, a greater number and variety of product ions were detected by EID. Fragmentation using CAD provides fewer ring cleavages and more neutral molecule losses, mainly water. EID results in fewer neutral losses and more cleavage of the macrocycle, therefore providing more information about the structure of the polyketide. It was thought that the charge would be located on the more basic amine group of the D-desosamine moiety, rather than one of the carbonyl oxygen atoms. However, since no fragmentation was observed in this ring, this is not likely to be the case. Studies

carried out by Gates *et al.*[121] used ^{18}O-labelling to demonstrate that the first water loss in CAD occurred from the carbonyl at the top of the macrocycle, indicating that this is the likely location of the proton.

CAD data for erythromycin A has been reported previously[120-122] with few characteristic ions detected and mainly neutral, small molecule loss occurring. The most abundant losses observed here were the same as those reported previously, including ions at *m/z* 716, corresponding to $[M+H-H_2O]^+$, and 698, corresponding to $[M+H-H_4O_2]^{+,}$ formed through the sequential loss of water, and at *m/z* 576, corresponding to "d" in Figure 2.2A, formed through the loss of the L-mycarose group. The data also shows cleavage of the intact D-desosamine sugar from the main ring, detected at *m/z* 158 ("q"), which has previously only been observed with IRMPD.[120] Some of the fragments observed in CAD were also observed using EID; however, EID resulted in more extensive fragmentation of the macrocycle, enabling complementary data to be obtained.

2.3.2 EID for Distinguishing Isomers: Lasalocid A and iso-Lasalocid A

Two polyether isomers, lasalocid A and *iso*-lasalocid A, isolated from cultures of *S.lasaliensis*[115] were both characterised by CAD and EID in order to determine if the greater fragment efficiency of EID could help distinguish the two polyether structures. Lasalocid A (Figure 2.3) features a tetrahydrofuran (THF) and a tetrahydropyran (THP) ring, whereas *iso*-lasalocid A (Figure 2.4) comprises two THF rings. Although investigations into the mechanism of formation of the two isomers have been previously conducted,[128-129] as yet, there is no report of a method using mass spectrometry that can distinguish the subtle structural differences between the two molecules. The main species observed in the ESI-MS spectra were that of the sodium and ammonium adducts; the protonated molecules were observed

but at low abundance. As the sodium adduct was clearly the dominant ion present, this was selected for both CAD and EID. Figure 2.3 shows the CAD (A) and EID (B) spectra of lasalocid A together with illustrations of the fragments detected by both techniques in Figures 2.3 (C) and (D).

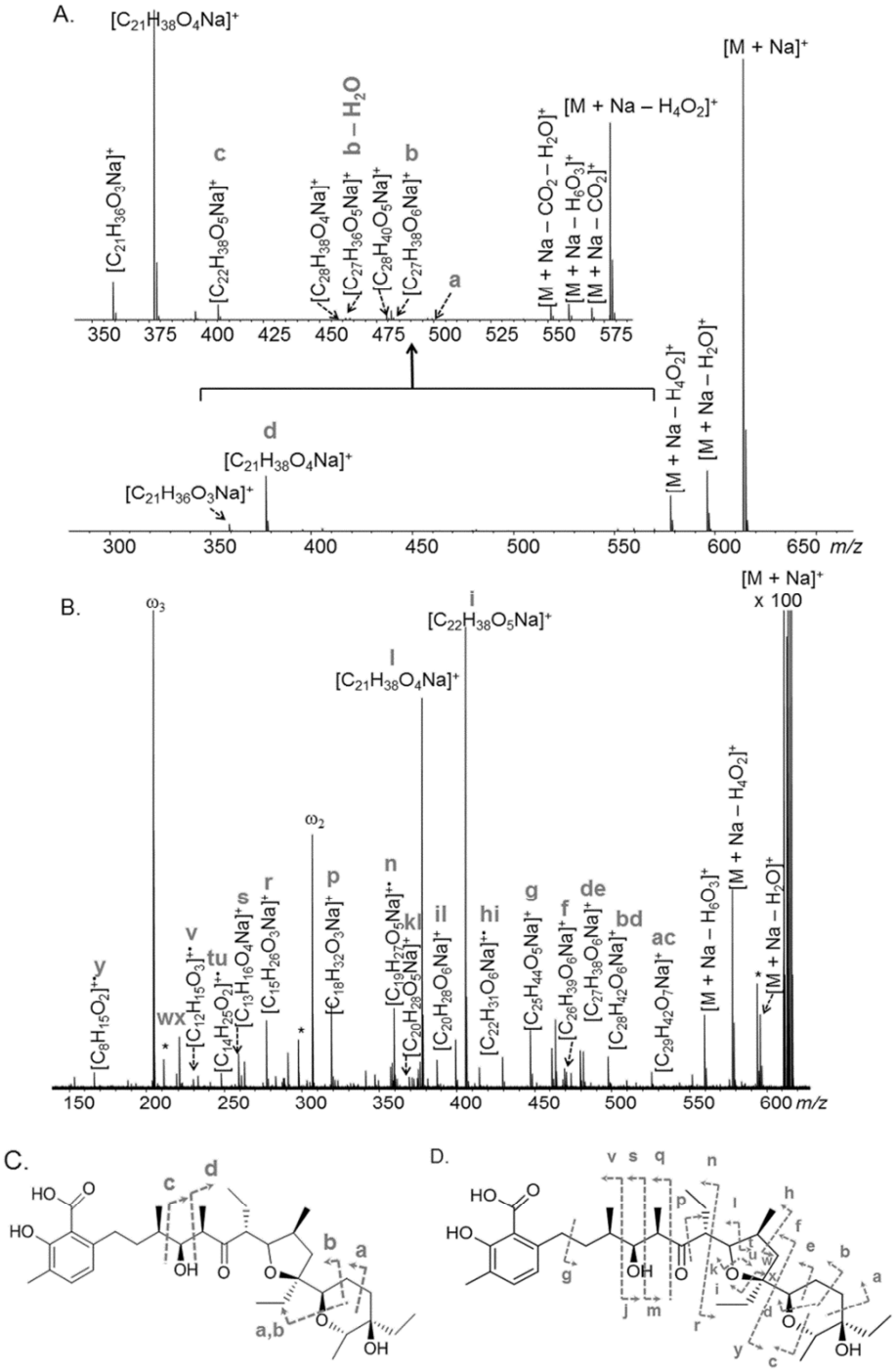

Figure 2.3: CAD (A) and EID (B) spectra of sodiated lasalocid A (precursor ion *m/z* 613.37) with illustrations of the detected fragments by CAD (C) and EID (D). Harmonics of these peaks are marked ω_2 and ω_3. A full list of peak assignments can be found in Tables A-3 and A-4 of Appendix A

CAD of lasalocid A resulted in very little fragmentation of the molecule compared with EID. Four major fragments were observed comprising two main chain cleavages and two cleavages of the tetrahydropyran ring, as illustrated in Figure 2.3(C). All other peaks observed were assigned as the loss of neutral molecules, mainly H_2O and CO_2, as was observed with erythromycin A. In contrast, EID provided a much more detailed fragment pattern with cleavages in both the THF and the THP rings occurring, as well as along the main chain. A number of complementary pairs were identified, mainly around the centre of the molecule, such as the pairs j and v, and m and s. Previous work[113,117,125] conducted on lasalocid A, where CAD was utilised, report a diagnostic ion at *m/z* 377, corresponding to the cleavage at "d" (Figure 2.3C), as well as the loss of several H_2O molecules, which is consistent with the data presented here.

The same experiments were conducted on *iso*-lasalocid A, and Figure 2.4 shows the EID and CAD spectra, together with illustrations of the fragments detected by each technique.

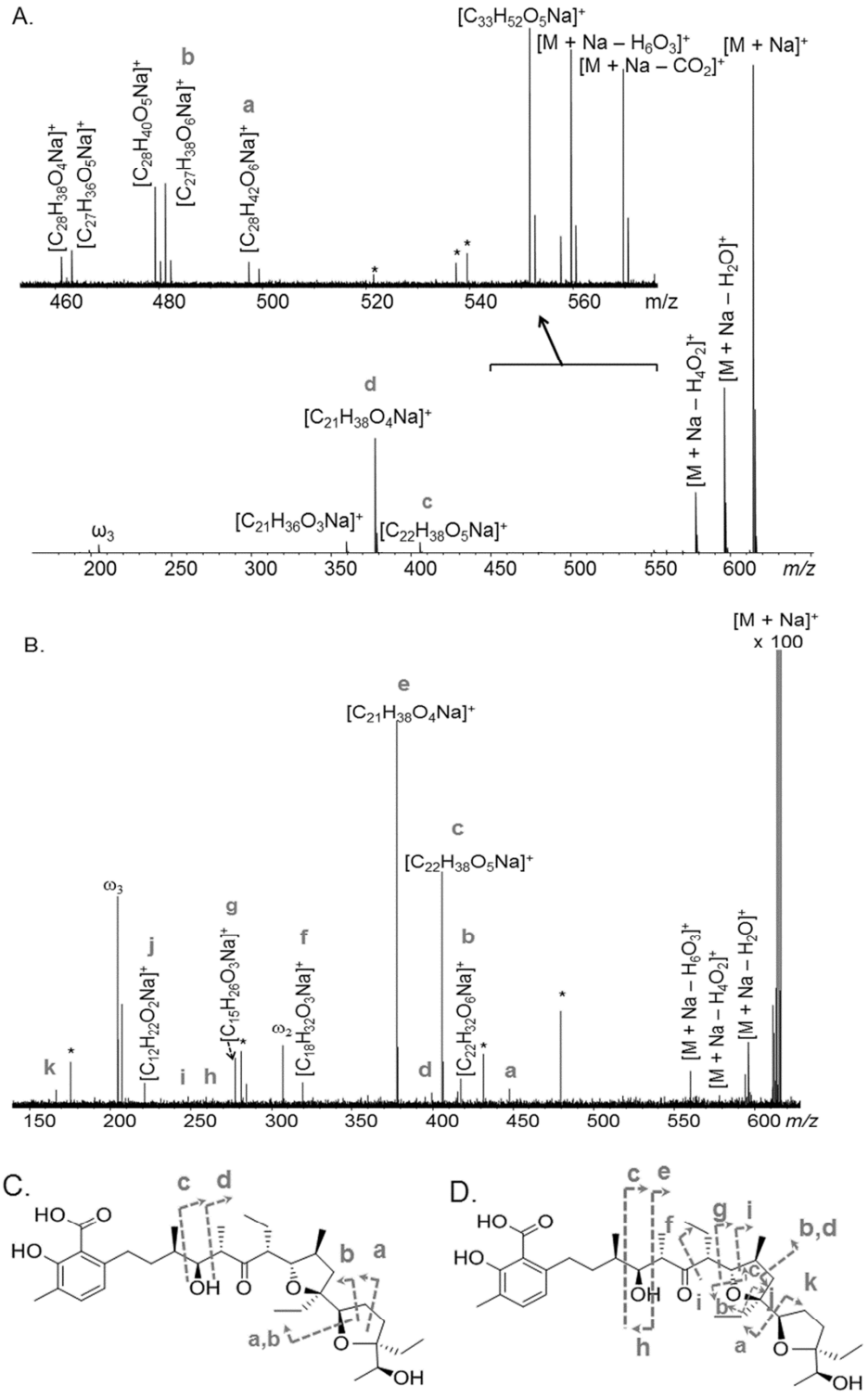

Figure 2.4: CAD (A) and EID (B) spectra of sodiated *iso*-lasalocid A (precursor ion *m/z* 613.37); fragments identified by CAD (C) and EID (D). Harmonics of these peaks are marked ω_3. A full list of peak assignments can be found in Tables A-5 and A-6 of Appendix A

As can be seen in both Figures 2.3 and 2.4, CAD did not provide much structural information on the two molecules so the more detailed EID spectra were analysed for key fragments that could be used to distinguish the two isomers. Differences were observed between the EID spectra of the two isomers; specifically of interest were the fragments resulting from cleavage of the THP ring of lasalocid A and the THF ring of *iso*-lasalocid A. Interestingly, cleavage of the terminal THF ring of *iso*-lasalocid A was not observed, whereas the THP ring of lasalocid A was cleaved to form three fragments. As this is where the structural difference between the two isomers occurs, it may be that this has a role in directing the fragmentation observed with EID. The terminal THF ring was only observed to fragment when MS^3 experiments were conducted as discussed below.

2.3.3 Effect of the Charge Carrier on the Fragmentation Pattern

Given that previous studies with CAD[113, 117,125] and EID[83] have shown the number and type of fragments vary according to which cation is coordinated by the molecule, different precursor ions were selected for fragmentation, namely the lithiated species (*m/z* 597.39). The protonated species (*m/z* 591.39) was not present in sufficient abundance to allow fragmentation with either CAD or EID, and the ammonium ion adduct (*m/z* 608.42) fragmented well with CAD but only to a limited extent with EID as shown in Figure 2.5.

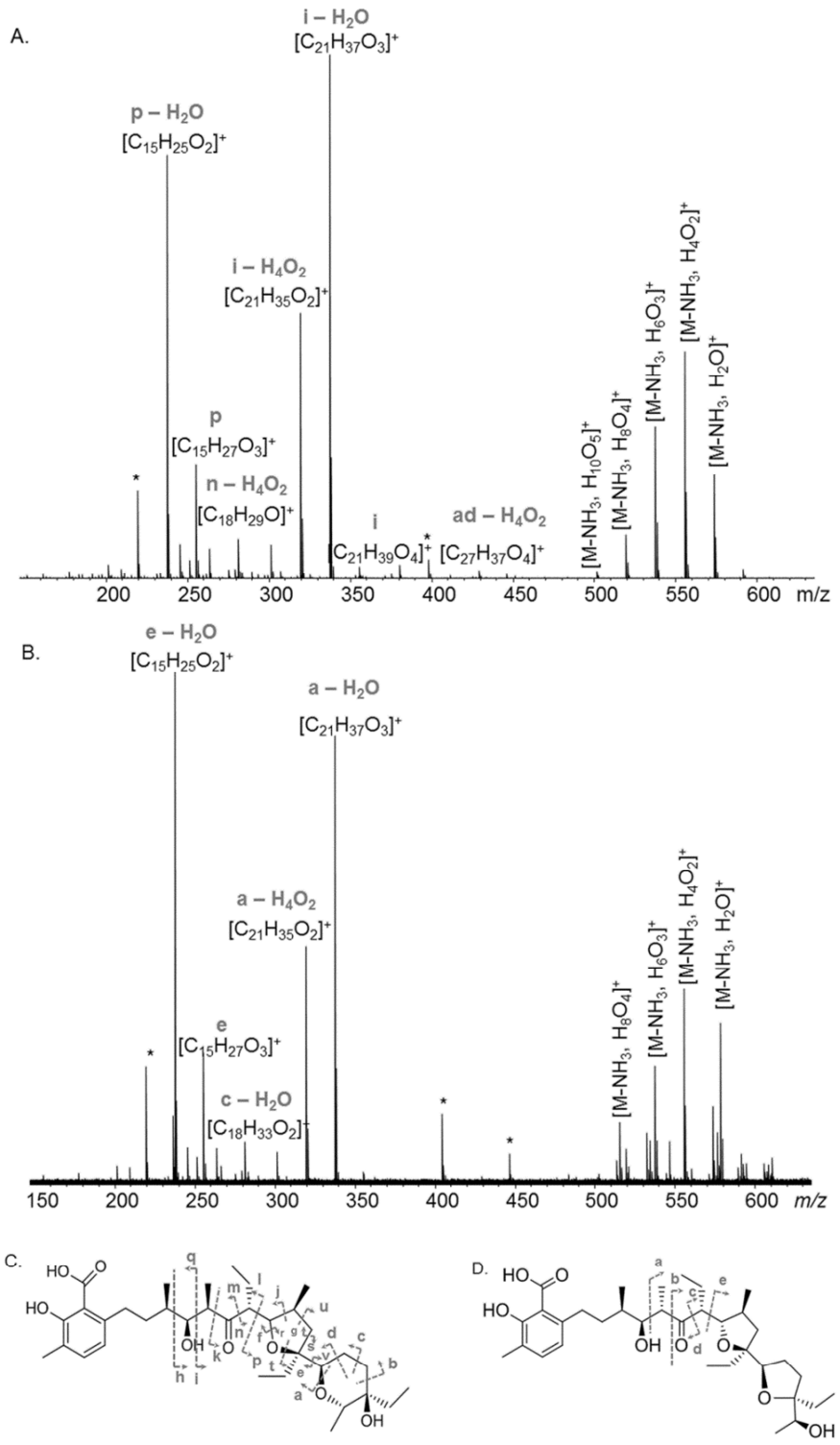

Figure 2.5: CAD spectra of Lasalocid A (A) and *iso*-Lasalocid A (B), NH_4^+ adduct (precursor ion *m/z* 608.42); illustrations of the corresponding fragments identified for Lasalocid A (C) and *iso*-lasalocid A (D). A full list of peak assignments can be found in Tables A-7 and A-8 of Appendix A

Figure 2.6 illustrates the fragments of the lithiated adduct of lasalocid A obtained by CAD (A) and EID (C), as well as the CAD (B) and EID (D) fragments of the lithiated adduct of *iso*-lasalocid A.

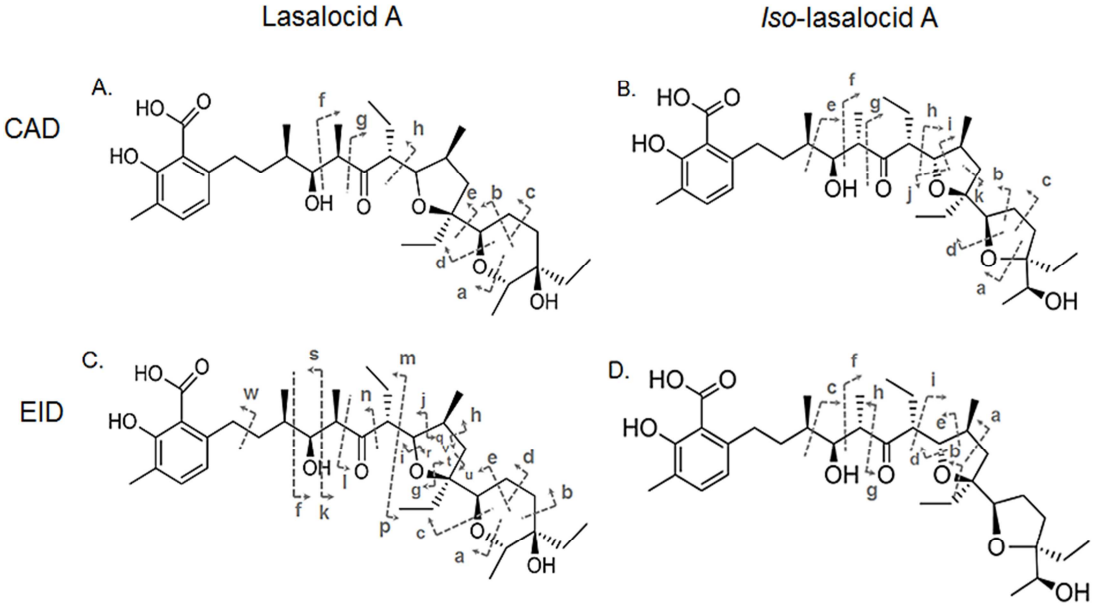

Figure 2.6: Illustrations of the CAD and EID fragments of Lasalocid A (A and C) and *iso*-lasalocid A (B and D) with the lithiated precursor ion (*m/z* 597.39) selected for fragmentation. A full list of peak assignments can be found in Tables A-9 to A-12 of Appendix A

The addition of the lithium ion to the molecules resulted in a similar EID fragmentation pattern as that observed for the sodium adduct, but provided a greater degree of fragmentation in CAD. The advantage of using the lithium adduct is that nearly all fragments retain the lithium ion, which has a readily identifiable isotope pattern, as shown in Figure 2.7, and, combined with the high resolution of FTICR-MS, means the fragments are easily distinguishable.

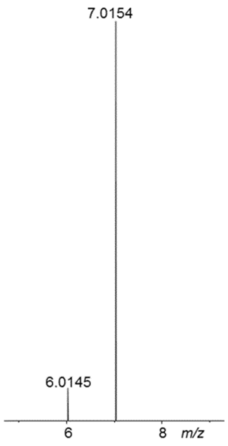

Figure 2.7: Natural abundance isotope pattern of lithium

For *iso*-lasalocid A, the CAD spectrum showed much greater cleavage of the molecule than obtained with the sodiated species. Interestingly, the EID spectra for the lithiated and sodiated adducts of *iso*-lasalocid A were almost identical, with no cleavage being observed in the terminal THF ring.

2.3.4 MS^3 experiments – CAD/EID of Lasalocid A and *iso*-Lasalocid A

Due to the intense nature of the fragment at *m/z* 361.29, (*m/z* 377.27 with sodium ion), corresponding to "f" in Figures 2.6A and B, MS^3 experiments were attempted in order to promote further cleavage of both isomers. CAD was performed on the lithiated species at *m/z* 597.39 and high collision energies (22.0 V) were used so as to increase the intensity of the product ion at *m/z* 361.29. This ion was then isolated in the ICR cell and fragmented further with EID. Figure 2.8 illustrates the CAD/EID spectra of lasalocid A and *iso*-lasalocid A.

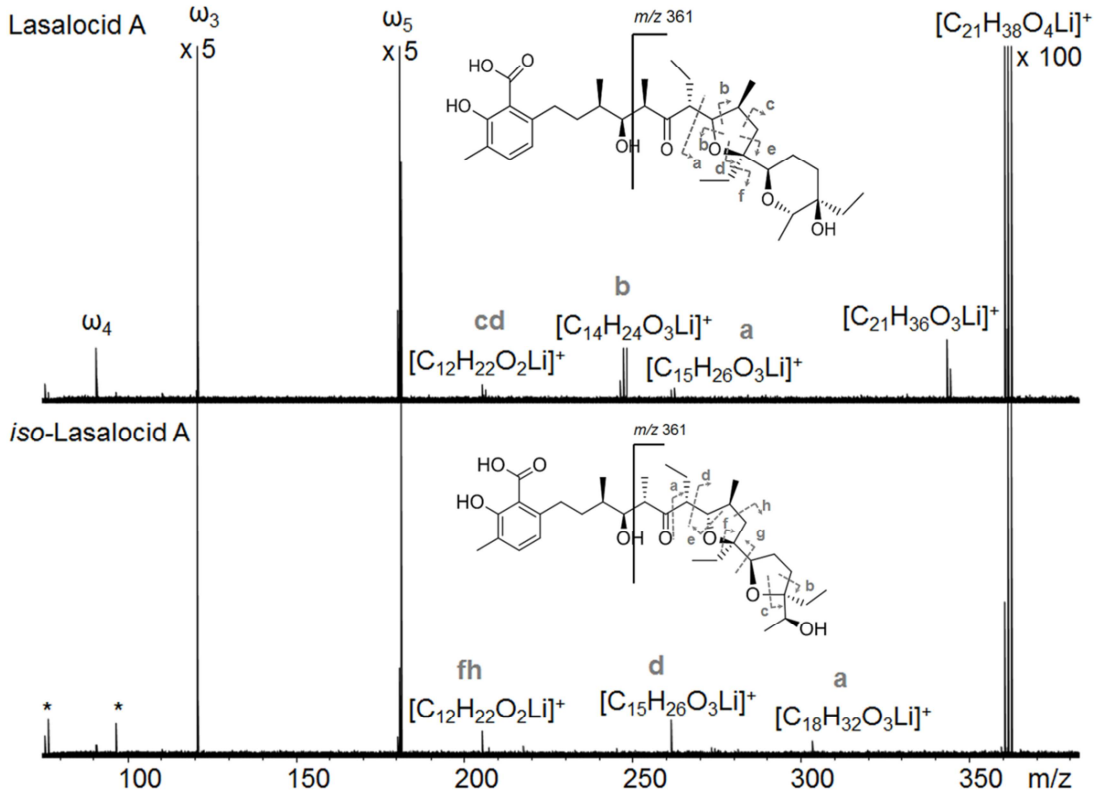

Figure 2.8: CAD/EID MS^3 spectra of lasalocid A and *iso*-lasalocid A. The lithiated adduct (*m/z* 597.39) was selected for CAD and the resulting product ion at *m/z* 361.29 was isolated and fragmented further using EID. A full list of peak assignments can be found in Tables A-13 and A-14 of Appendix A

The spectra show that for both lasalocid A and *iso*-lasalocid A, upon further fragmentation of the selected ion using EID, different fragment patterns were obtained for the two isomers. The intensities of the fragments shown in Figure 2.8 are approximately 1000 times lower than the precursor ion. This was expected due to the peaks in previous EID spectra already being 100-fold less intense than the precursor. Despite this, the use of CAD combined with EID was successful for producing further fragmentation of the peak at *m/z* 361 corresponding to $[C_{21}H_{38}O_4Li]^+$. This method was also applied to the equivalent sodiated fragment at

m/z 377 but no significant cleavage was observed. Again, as with the EID spectra of the entire molecule, different fragments were observed for each isomer. In this case, the THP ring of lasalocid A was not found to fragment, but the terminal THF ring of *iso*-lasalocid A was cleaved. As differences were detected in the spectra for the two molecules, this method can now be exploited in order to determine which isomer is present in the intermediate structures as the biosynthesis proceeds.

2.3.5 Structural Characterization of Biosynthetic Intermediates

The isolation and identification of intermediate species represents a significant obstacle, as they remain covalently tethered to the PKSs and NRPSs throughout the assembly of the natural product.[90] More recently, mass spectrometry has proved an extremely powerful tool for the detection of covalently-bound intermediates,[130] and the investigation of different active site occupancy.[131] However, the majority of enzyme-bound species remain undetectable due to their rapid elaboration, and novel approaches to biosynthetic studies are still needed in order to elucidate the molecular basis of the sophisticated PKS programming.

Recently, a chemical method for identifying the intermediate structures along the biosynthetic pathways of polyketides has also been developed.[115, 126, 132-133] This involves the capture and the off-loading of intermediates from polyketide synthases using synthetic mimics of malonate units that compete with the ACP domain for the growing polyketide chain (Figure 2.9); prematurely-truncated intermediates are generated and, unable to be "reloaded" onto the biosynthetic enzymes, they diffuse out of the active site.

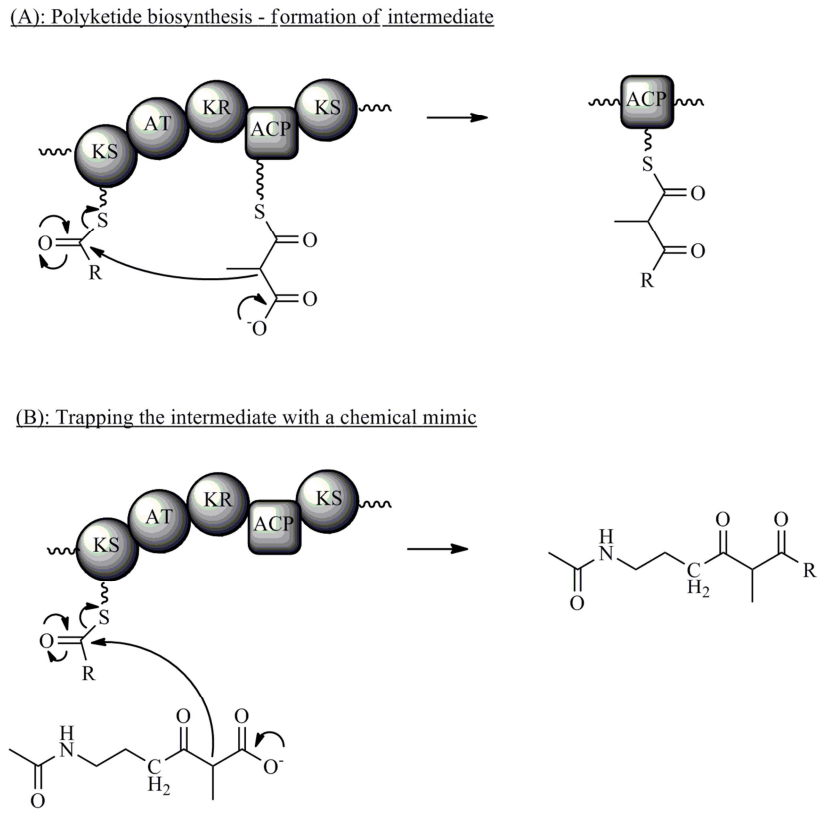

Figure 2.9: Standard chain growth mechanism for polyketide biosynthesis (A); use of competing malonate mimic to trap intermediate structure (B), adapted from reference [2]

Characterization of these intermediates can then be performed using high resolution tandem mass spectrometry techniques suitable for the analysis of small molecules, subsequently providing detailed insights into the biosynthetic pathways of these compounds.

This method of using multiple tandem mass spectrometry techniques has shown great potential for obtaining detailed structural information on polyketides, and can be applied to identifying the structures of intermediates formed throughout the biosynthetic process. The cell culture containing the off-loaded intermediates was analysed to determine if any structures could be identified. Figure 2.10(A)

shows the mass spectrum obtained for the extract of the intermediates for lasalocid A. The inset shows an expanded region of the spectrum in the expected *m/z* range of the intermediate, with the structure of the synthetic mimic used to off-load the intermediates shown in blue.

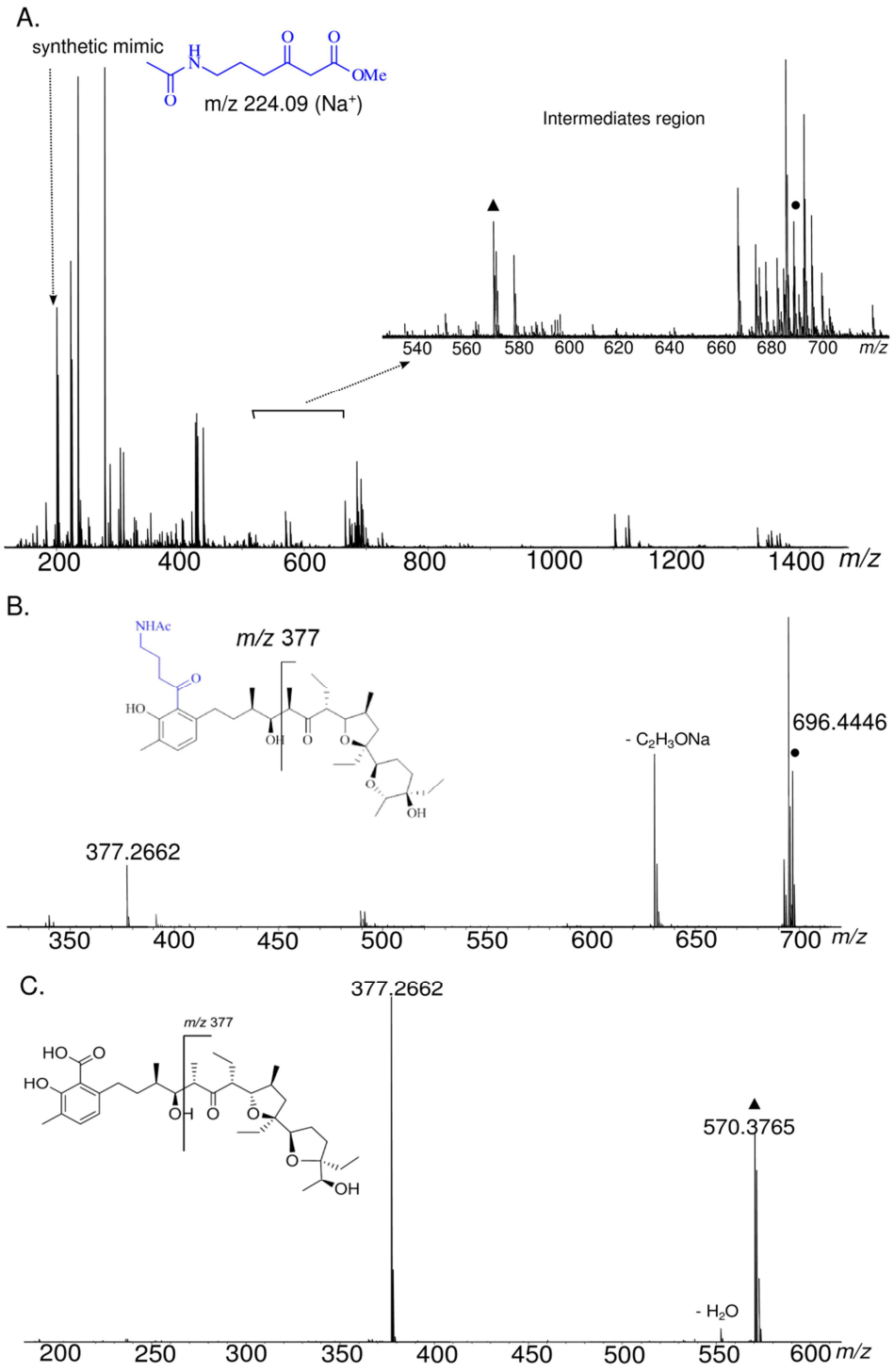

Figure 2.10: (A) Mass spectrum of the cell extract for lasalocid A, inset shows expanded region containing potential intermediate structures, and the chemical probe used to off-load the intermediates; (B) CAD spectrum of previously identified intermediate structure at *m/z* 694.44; (C) CAD spectrum of possible intermediate structure at *m/z* 570.37

As shown in Figure 2.10 (A), the synthetic mimic used to off-load the intermediates is identified as a major component at *m/z* 224.09 but there are a very large number of additional peaks in the mass spectrum, making identification of potential biosynthetic intermediates difficult. The structures of a few intermediates have been characterised previously using an LC-MS method[115] so these peaks were used as a starting point. Figure 2.10 (B) shows the CAD spectrum of a proposed intermediate that was identified at *m/z* 696.44 together with a possible structure. The main peak of interest is at *m/z* 377.62, which corresponds to one of the diagnostic ions identified for lasalocid A, as shown in section 2.3.2. A few other peaks were also detected but, as before, CAD does not provide detailed structural information of the compound showing the need to also use EID. In order to try and identify new intermediate structures, a few peaks in this *m/z* region were selected and fragmented using CAD. Figure 2.10 (C) shows one such spectrum and, although the fragmented peak was not very intense, the main fragment observed was also that of *m/z* 377.62, therefore it is likely that this peak also corresponds to a biosynthetic intermediate. The use of this diagnostic peak in CAD can provide the first-step in the identification of new intermediates for lasalocid A and other polyketides. More detailed structural information can then be provided by EID in order to elucidate the correct structure for the intermediate, with its additional advantage of being able to distinguish between lasalocid A and its isomer, *iso*-lasalocid A.

EID was attempted on the two ions in Figure 2.10 (B) and (C); however, given that EID spectra of lasalocid A have shown the product ions to be approximately 100 times less intense than the precursor ion, the intermediates shown here were not present in sufficient abundance to use this technique successfully. As EID is necessary to provide a greater amount of structural information on these

compounds, an additional analytical step is first required in order to purify and concentrate the mixtures containing the off-loaded intermediates. This has started to be investigated using liquid chromatography in order to purify the cell extract and separate the intermediate compounds before analysis by mass spectrometry but this is an ongoing method development step and needs refining before it can be applied to the analysis of these intermediates.

2.4 Conclusion

This study has demonstrated the effectiveness of combining CAD and EID as fragmentation techniques for singly charged polyketide molecules. Using EID results in more extensive fragmentation compared with CAD, and so enables detailed structural information to be obtained, especially when utilising the different adducts formed through coordination of metal cations. The ability of the technique to distinguish between isomers has been demonstrated for lasalocid A and *iso*-lasalocid A, with different fragmentation patterns observed in both EID and CAD/EID experiments. Further application of the technique to biosynthetic intermediates will help achieve structural elucidation of these molecules with a high degree of accuracy, enabling a detailed understanding of the biosynthetic pathways of these natural products.

Chapter 3: Characterizing the Structures of Non-Ribosomal Peptides Using Tandem Mass Spectrometry

This chapter has been partially reproduced from the following publication:

R.H.Wills and P.B.O'Connor, Characterizing the structure of Actinomycin D using multiple ion isolation and electron induced dissociation, accepted in JASMS, 2013.

3.1 Introduction

Non-ribosomal peptides, like type I polyktides, are biosynthesized by large multienzyme complexes known as non-ribosomal peptide synthetases (NRPSs), which consist of a series of modules divided into catalytic domains. The three main domains utilize a large variety of amino acids to assemble structurally and functionally diverse peptides with interesting pharmaceutical properties, and include A (adenylation), PCP or T (peptidyl carrier protein or thiolation), and C (condensation) domains, [112, 134-135] as illustrated in Figure 3.1.

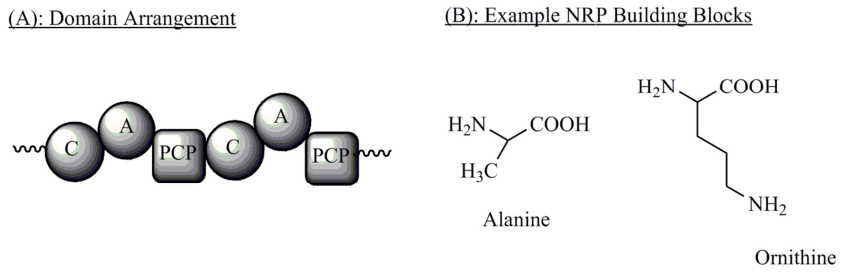

Figure 3.1: (A) Arrangement of the C-A-PCP domains comprising NRPS modules; (B) example building blocks for non-ribosomal peptide synthesis

This process is not limited to the 20 proteinogenic amino acids that constitute ribosomally-produced peptides; instead there are approximately 500 different building blocks, including modified amino acids, such as ornithine, fatty acids, and α-hydroxy acids. [134, 136] The large variation in monomer units can result in the formation of linear, cyclic, and branched peptides, which can be further modified by acylation, glycosylation or heterocyclic ring formation. As a result, non-ribosomal peptides are structurally diverse and have a range of biological activities, which can be exploited in the drug discovery process. [134-135, 137]

Sequencing non-ribosomal peptides is a challenging process, in that hundreds of possible building blocks are potentially present in a compound. These building blocks are often variations of the structures of the twenty standard amino acids, are often non-linear, include a non-standard backbone, and have modified structures; all of these factors complicate tandem mass spectra, making structural characterization difficult.[138] Several mass spectrometry based approaches have been reported for the sequencing of cyclic or non-ribosomal peptides,[138-141] including the use of multiple stages of tandem mass spectrometry.[138, 140] One of the difficulties faced with cyclic peptides is that fragmentation can occur through multiple ring-opening pathways, resulting in product ions that can originate from any of these different forms.[140] Multiple stages of tandem mass spectrometry therefore result in the successive deletion of amino acids, enabling the sequence to be constructed in the correct order.

The use of ion-electron interactions, specifically electron capture dissociation (ECD), has proved useful in the fragmentation of cyclic peptides,[63] through the observation of a radical cascade mechanism that results in the production of numerous fragments. Combining CAD and EID with the high resolution and mass accuracy of FTICR mass spectrometers, enables significant structural information to be obtained on a short timescale, making mass spectrometry a powerful tool for the analysis of these compounds.

Another advantage of using FTICR mass spectrometry is its ability to isolate ions of interest in the ICR cell itself, as well as externally. This enables the application of ion isolation techniques such as stored waveform inverse Fourier transform (SWIFT),[142] correlated harmonic excitation field (CHEF),[44] or multi-CHEF. The latter technique has been demonstrated for the accurate analysis of the peptide antibiotics rapamycin[45] and the muraymycins.[143] The compounds of interest

were isolated along with a set of reference peaks and fragmented by SORI-CAD (sustained off resonance irradiation),[60] in multiple MS^n stages, enabling structure elucidation through accurate mass assignments of the product ions. This technique has facilitated the assignment of the elemental formulae of unknown compounds.

3.2 Experimental

3.2.1 Chemicals and Reagents

Actinomycin D (Figure 3.2) and vancomycin were prepared in acetonitrile/water (50:50) at a concentration of 0.5 µM. The sodium, lithium, potassium, and silver adducts were produced by adding NaCl, LiCl, KOH, and $AgNO_3$ (1 mM) to the samples. D-Arginine was prepared in Milli-Q water (Millipore Inc., Durham, UK) at a concentration of 1 mM. Actinomycin D, vancomycin, and D-arginine were all purchased from Sigma Aldrich (Gillingham, UK). Acetonitrile, sodium chloride, lithium chloride, potassium hydroxide, and silver nitrate were all purchased from Fisher Scientific (Loughborough, UK).

3.2.2 Analysis by MS/MS

The samples were analysed on a 12 T Bruker SolariX FTICR mass spectrometer (Bruker Daltonics, Coventry, UK), using a nanospray ionization source. A capillary voltage of -900 V was applied, together with a drying gas flow rate of 2.5 L min^{-1} and temperature of 180 ºC, and a nebuliser gas pressure of 1.2 bar. For CAD experiments, the precursor ion was isolated in the first quadrupole and fragmented in the collision cell with argon at collision energies of 12 V, and an isolation window of 4 *m/z*. For EID experiments, the precursor ion was isolated in the quadrupole and externally accumulated in the collision cell for 2-5 seconds before being transferred

to the ICR Infinity cell.[35] The ions were then irradiated with electrons from a 1.7 A heated hollow cathode dispenser, biased with an offset potential of between 13 and 15 V, for 10-50 ms. In-cell isolation was conducted using multi-CHEF,[45] whereby the precursor ion and selected calibrant ions of D-arginine clusters were selected simultaneously, before being irradiated with electrons, using the same experimental parameters as for EID-only experiments. Trapping plate voltages of 0.5 V and 0.6 V were applied to the front and back trapping plates respectively, with dataset sizes of 4 MW and 100-150 scans recorded. Finally, post-processing functions of one zero-fill and sine-bell apodisation were applied.

3.3 Results and Discussion

3.3.1 CAD and EID of Actinomycin D

The structure of the non-ribosomal peptide actinomycin D, shown in Figure 3.2, is well characterized and, as such, was used as a test case for comparing structural data obtained using the complementary techniques CAD and EID.

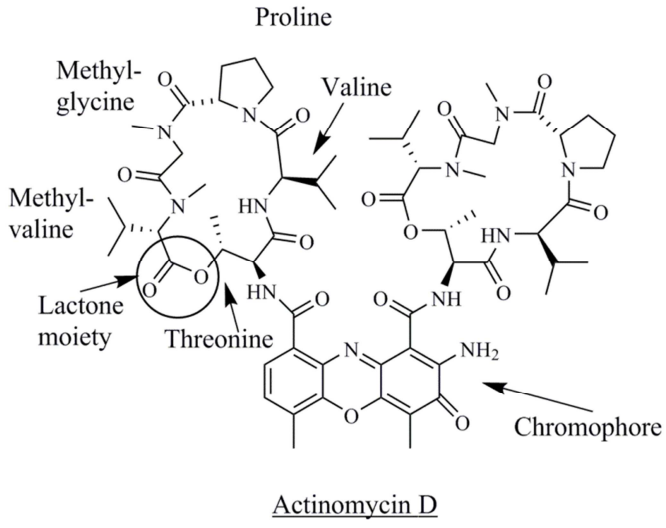

Figure 3.2: The structure of the non-ribosomal peptide, actinomycin D

This non-ribosomal peptide is composed of two identical peptidic rings and a chromophore composed of three aromatic rings. The sequence of the rings includes the amino acids valine, threonine and proline, with two modified amino acids, namely methyl glycine and methyl-valine, as well as a lactone moiety. Figure 3.3 shows the CAD (A) and EID (B) obtained for protonated actinomycin D (*m/z* 1255.63 Da), with Figures 3.3 (C) and (D) illustrating the main product ions assigned.

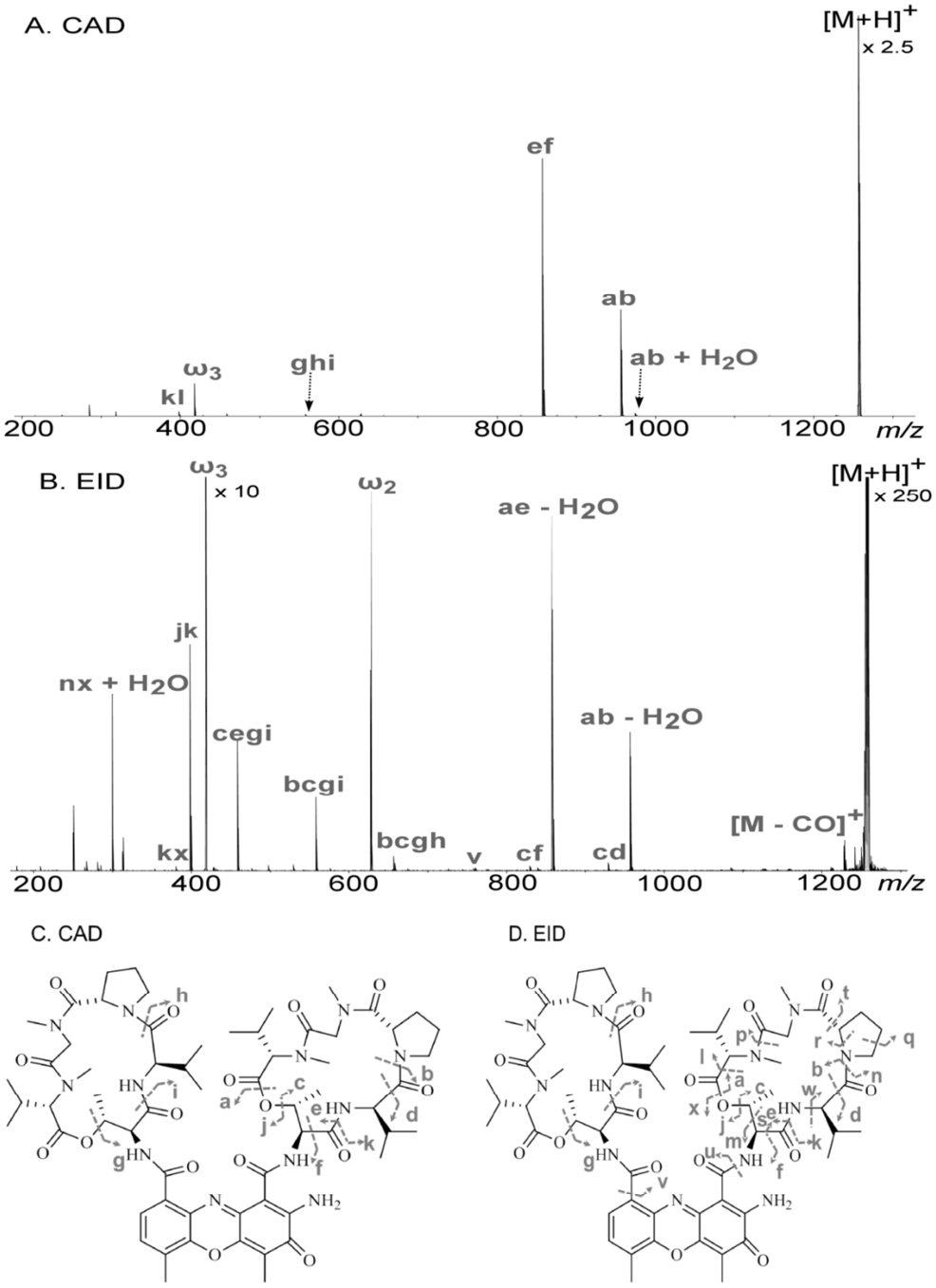

Figure 3.3: CAD (A) and EID (B) mass spectra of protonated actinomycin D (*m/z* 1255.63 Da), with illustrations of the fragments assigned from CAD (C) and EID (D). A full list of peak assignments can be found in Tables A-15 and A-16 of Appendix A

Fragmentation by CAD, as shown in Figure 3.3, is limited but some sequence information is obtained, which is in agreement with data reported previously.[144] The peptidic rings are identical, so the fragments illustrated could originate from either one. Barber *et al*.[144] suggested initial ring opening occurs at the lactone moiety, i.e. at the ester bond between the bridging oxygen and threonine side chain (highlighted in Figure 3.3C as "a"), resulting in the successive loss of amino acids. Ring opening at this linkage has been shown to occur preferentially in the presence of sodium ions, due to the strong interaction between Na^+ and the bridging oxygen, resulting in the formation of a linear acylium ion.[145] The main fragments detected here support this occurrence for the protonated molecule also, with additional peaks observed at *m/z* 974.46 ("ab"), 928.46 ("cd"), 875.39 ("ae"), and 829.39 ("cf"), which provide new diagnostic ions that could be used for identifying this cyclic structure.

EID has proved to be beneficial for structural characterization, in that a greater degree of fragmentation is generally observed compared to CAD. As shown in Table 3.1, sixteen extra peaks are observed, which are not restricted to the b/y ion formation observed in CAD through preferential cleavage of the amide bonds.

Table 3.1: Main fragment assignments of actinomycin D from CAD and EID (peaks used as internal calibrants are marked ▲)

Observed *m/z*	Proposed Formula	Mass Error / ppm	Fragment Cleavages
CAD			
974.46184	$C_{48}H_{64}N_9O_{13}^+$	0.03	ab
▲956.45129	$C_{48}H_{62}N_9O_{12}^+$	-	ab – H_2O
928.45644	$C_{47}H_{62}N_9O_{11}^+$	0.12	cd
875.39345	$C_{43}H_{55}N_8O_{12}^+$	0.06	ae
▲857.38288	$C_{43}H_{53}N_8O_{11}^+$	-	ae – H_2O
829.38784	$C_{42}H_{53}N_8O_{10}^+$	-0.10	cf
657.26635	$C_{34}H_{37}N_6O_8^+$	-0.60	bcgh
558.19828	$C_{29}H_{28}N_5O_7^+$	-0.07	bcgi
▲459.12992	$C_{24}H_{19}N_4O_6^+$	-	cegi
399.26020	$C_{19}H_{35}N_4O_5^+$	0.00	jk
EID			
1183.61508	$C_{59}H_{83}N_{12}O_{14}^+$	0.39	lm
1156.56816	$C_{57}H_{78}N_{11}O_{15}^+$	0.71	en
1127.54180	$C_{56}H_{75}N_{10}O_{15}^+$	0.90	eqr
1124.54153	$C_{56}H_{74}N_{11}O_{14}^+$	0.36	cp
1057.49868	$C_{52}H_{69}N_{10}O_{14}^+$	-0.23	ft
974.46146	$C_{48}H_{64}N_9O_{13}^+$	-0.36	ab
▲956.45126	$C_{48}H_{62}N_9O_{12}^+$	-	ab – H_2O
928.45676	$C_{47}H_{62}N_9O_{11}^+$	0.46	cd
875.39296	$C_{43}H_{55}N_8O_{12}^+$	-0.45	ae
▲857.38274	$C_{43}H_{53}N_8O_{11}^+$	-	ae - H_2O
829.38744	$C_{42}H_{53}N_8O_{10}^+$	-0.58	cf
803.37273	$C_{40}H_{51}N_8O_{10}^+$	0.57	fm
776.36116	$C_{39}H_{50}N_7O_{10}^+$	-0.27	u
675.27686	$C_{34}H_{39}N_6O_9^+$	-0.65	bcgh + H_2O
657.26677	$C_{34}H_{37}N_6O_8^+$	0.05	bcgh
576.19840	$C_{29}H_{30}N_5O_8^+$	-0.38	bcgi + H_2O
558.19840	$C_{29}H_{28}N_5O_7^+$	0.14	bcgi
508.27650	$C_{24}H_{38}N_5O_7^+$	-0.16	v
▲459.12998	$C_{24}H_{19}N_4O_6^+$	-	cegi
431.13515	$C_{23}H_{19}N_4O_5^+$	0.35	cfgi
399.26009	$C_{19}H_{35}N_4O_5^+$	-0.28	jk
381.24968	$C_{19}H_{33}N_4O_4^+$	0.13	kx
354.23861	$C_{18}H_{32}N_3O_4^+$	-0.34	lw
300.19169	$C_{14}H_{26}N_3O_4^+$	-0.30	nx + H_2O
282.18121	$C_{14}H_{24}N_3O_3^+$	-0.04	nx
169.09707	$C_8H_{13}N_2O_2^+$	-0.47	np
	Average (CAD)	**0.14**	
	(EID)	**0.37**	
	Std. Dev. (CAD)	**0.19**	
	(EID)	**0.21**	

The same nomenclature system for fragment assignments used in chapter 2 is used here. Each letter in the illustrations in the figures represents cleavage of that bond; the peaks are then assigned these letters depending on the bonds broken. For example, the peak at *m/*z 974.46 assigned "ab" in Table 3.1, indicates a product ion formed through cleavage at the bonds labelled "a" and "b", in the direction of the arrows shown in Figure 3.3 (D).

A technique such as EID that can cause greater fragmentation of a molecule will be extremely beneficial for the characterization of unknown compounds. One additional feature observed is that of complementary fragment pairs, for example the peaks and *m/z* 974 and 282. These peaks correspond to cleavages at "ab" and "nx", shown in Figure 3.3 (D), which helps improve the confidence of the peak assignments since the whole ion is being detected.

3.3.2 Changing the charge carrier in EID

It has been shown previously[82-83, 146] that changing the charge carrier from a proton to a metal cation, such as sodium or lithium, can affect the resulting fragmentation spectrum, with lithium in particular improving fragmentation in CAD. Figure 3.4 shows the EID spectra obtained for the sodium adduct of actinomycin D (A) and the lithium adduct (B), with illustrations of the fragments assigned in (C) and (D).

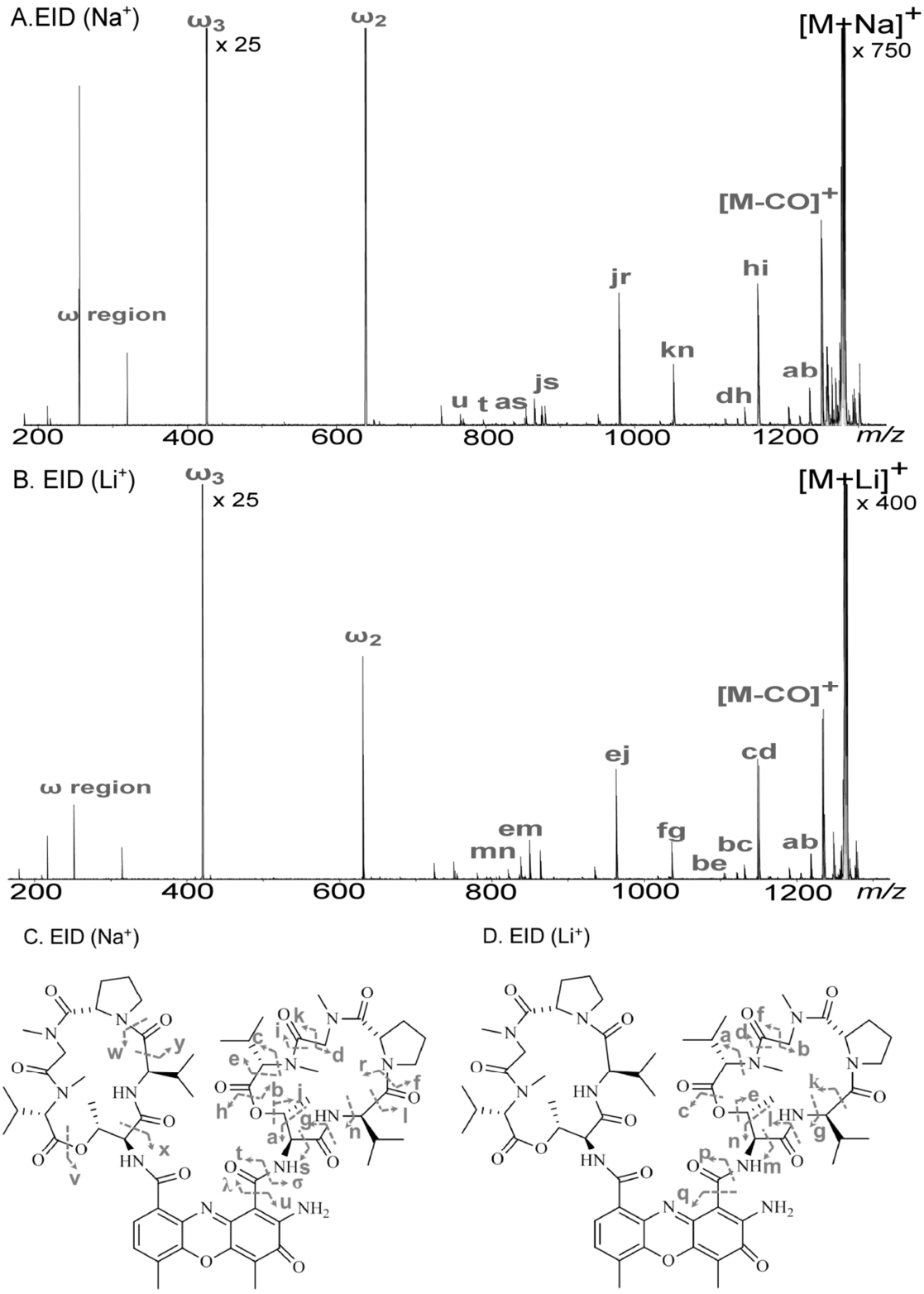

Figure 3.4: Comparison of EID spectra for Actinomycin D, with fragmentation of the sodium adduct, *m/z* 1277.62 Da (A), and lithium adduct, *m/z* 1261.64 Da (B),

with illustrations of the fragments detected (C and D). A full list of peak assignments can be found in Tables A-17 and A-18 of Appendix A

The sodium adduct was found to be more effective in producing fragments by EID, with cleavage of both peptide rings occurring, as well as cleavage of the chromophore (shown by cleavage site "u" in Figure 3.4). In addition to the main ring fragments, a number of small neutral losses were observed, including predominantly CO, H_2O, NH_3 and CH_2, therefore giving an indication of the functional groups attached to the main ring. Fragmentation of the lithium adduct was somewhat limited; the work conducted on polyketides demonstrated more effective fragmentation in EID with lithium than sodium. Non-ribosomal peptides are larger molecules than polyketides, so it is plausible that a larger charge carrier is required to direct fragmentation.

3.3.3 CAD and EID of Vancomycin

Vancomycin is an example of one of the larger peptide antibiotics with a mass of 1448 Da, and was fragmented by using both CAD and EID to determine whether there is a mass restriction for this method of structural characterization. Figure 3.5 shows the CAD spectra of (A) the lithium adduct, and (B) the sodium adduct of vancomycin, with the corresponding fragments shown in Figures 3.5 (C) and (D) respectively.

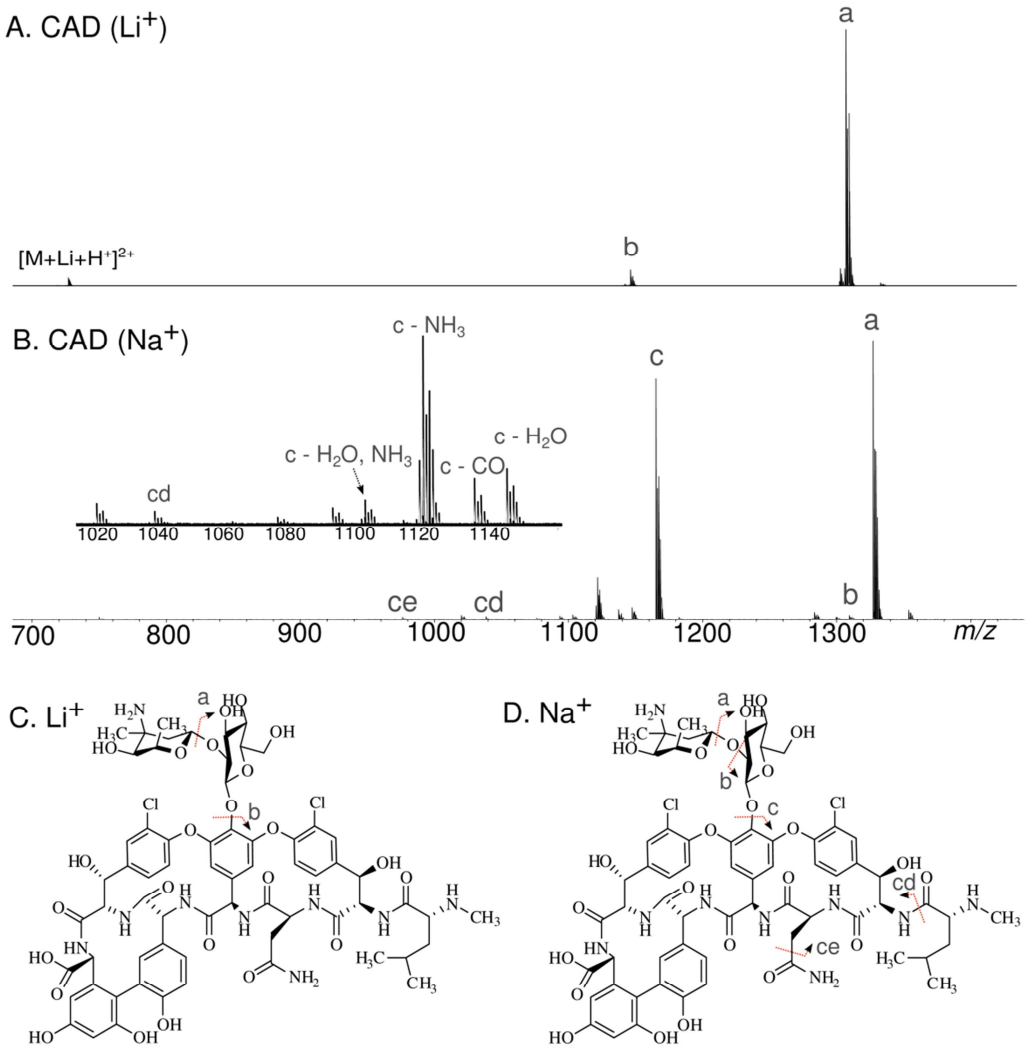

Figure 3.5: (A) CAD spectrum of the lithium adduct of vancomycin; (B) CAD spectrum of the sodium adduct of vancomycin, with inset illustrating an expanded region at *m/z* 1020 to 1140; (C) and (D) illustrations of the main fragments observed for the lithium adduct and sodium adduct respectively indicated by red arrows

As shown in Figure 3.5, fragmentation of the sodium adduct is more extensive than the lithium adduct, but both are still fairly limited in terms of providing structural information on this compound. To determine whether a larger charge carrier would aid further fragmentation of the resulting ion, potassium (K^+) and silver (Ag^+)

adducts were fragmented by CAD. Figure 3.6 shows the CAD spectrum of the potassium adduct of vancomycin with an illustration of the fragments observed.

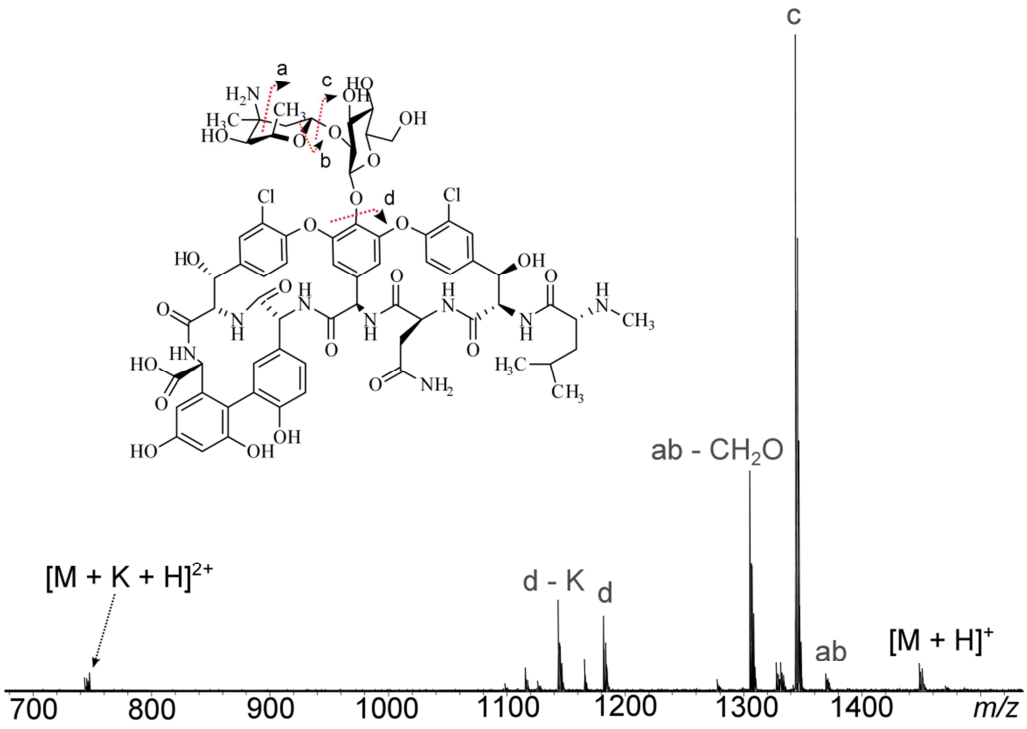

Figure 3.6: CAD spectrum of the potassium adduct of vancomycin, with the inset illustrating the main bond cleavage sites observed

Although the silver adduct was also fragmented by CAD, it did not provide any more detailed structural information than that obtained with the lithium, sodium and potassium adducts. As shown in Figure 3.6, use of a larger charge carrier such as potassium did not increase the degree of fragmentation observed; however, given similar fragments are observed with each carrier, this is more likely to be an indication of the difficulty in fragmenting the ring system of the molecule, particularly as the charge appears to be located in one of the sugar rings. This is indicated by the product ion formed by cleavage at "c" which was observed both with and without the potassium adduct, showing it had been cleaved with this sugar

ring. As this location of the charge carrier is removed from the rest of the molecule, cleavage within the main ring system is unlikely.

In addition, due to the increased size of vancomycin compared to actinomycin D, the 1+ species, $[M+K]^+$, was only present at low abundance, with the 2+ species, $[M+K+H]^{2+}$, being the dominant charge state through addition of a proton as well as the metal cation. Since the $[M+K]^+$ species was not present in sufficient abundance, EID could not be performed successfully. There are other alternative techniques to EID that may prove more successful in this case. Using ECD or hot ECD on the $[M+K+H]^{2+}$ species may cause fragmentation similar to that observed with ECD. Alternatively, the use of MS^3 techniques such as that utilised in chapter 2 on polyketides where EID is perfomed on the most abundant fragment observed in the CAD spectrum in order to fragment this part of the ion. IRMPD could also be used first in order to activate the ion for fragmentation by either of these techniques. Since fragmentation of vancomycin was difficult using EID and needed further investigation, the remaining experiments were conducted on actinomycin D only.

3.3.4 Combining EID and Multiple Ion Isolation for Internal Calibration

Although EID has proved to be a reliable technique for obtaining structural information on these types of compounds, there is a limitation to the method as demonstrated above. In order to achieve an accurate internal calibration for the product ions, a comparison of the peaks in both the CAD and EID spectra was made to identify a selection of peaks that could be used for internal calibration. Peak assignments following a lock mass calibration (using the precursor ion peak) revealed a number of fragments that were the result of a water loss, making them easily identifiable and usable as internal calibrants. Although this method has been

shown to work well, there are still many different possible combinations of elemental formulae for a given fragment, particularly when working with compounds that are generally >1 kDa in mass, making peak assignment more challenging. Additionally, when dealing with unknown structures, such neutral losses may not always be so easily identifiable, and therefore it may be difficult to find suitable peaks to use as internal calibrants.

In order to overcome the difficulties in internal calibration, multiple ion isolation was utilised, whereby the sample solution was mixed with a solution of an internal calibrant, in this case D-arginine, which, at a high enough concentration (~100 µM), generates clusters over a relevant mass range for the product ions. The calibrant peaks in the desired mass range were isolated as well as the actinomycin D precursor ion (both sodium and lithium adducts were used), and were detected with the product ions generated through performing EID. Although the arginine clusters are also exposed to the electron beam, and should therefore fragment, only a slight decrease in the relative intensities of these peaks (compared to the precursor ion peak) was observed with EID turned on, as shown in Figure 3.7.

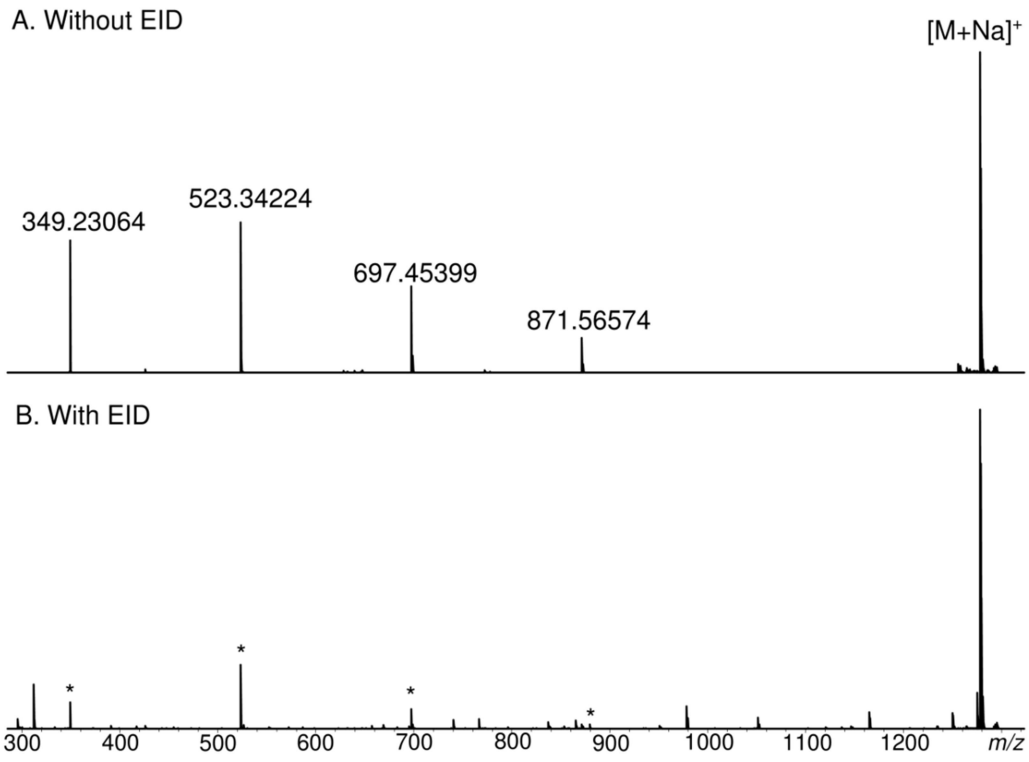

Figure 3.7: (A) Isolation of the arginine clusters and the sodiated precursor of actinomycin D without EID; (B) Isolation of the arginine clusters (*) with EID on

Dissociation therefore simply reduces the size of the clusters so there is no observed change in the *m/*z of these peaks making them ideal to use as internal calibrants. This method enables an accurate internal calibration to be performed and confident assignments to be made.

Figure 3.8 shows the EID spectra obtained for the sodium adduct (A) and lithium adduct (B) of actinomycin D, combined with multiple ion isolation, whereby four peaks of arginine clusters were isolated simultaneously and used as internal calibrants. Figures 3.8 (C) and (D) illustrate the fragments identified for both adducts.

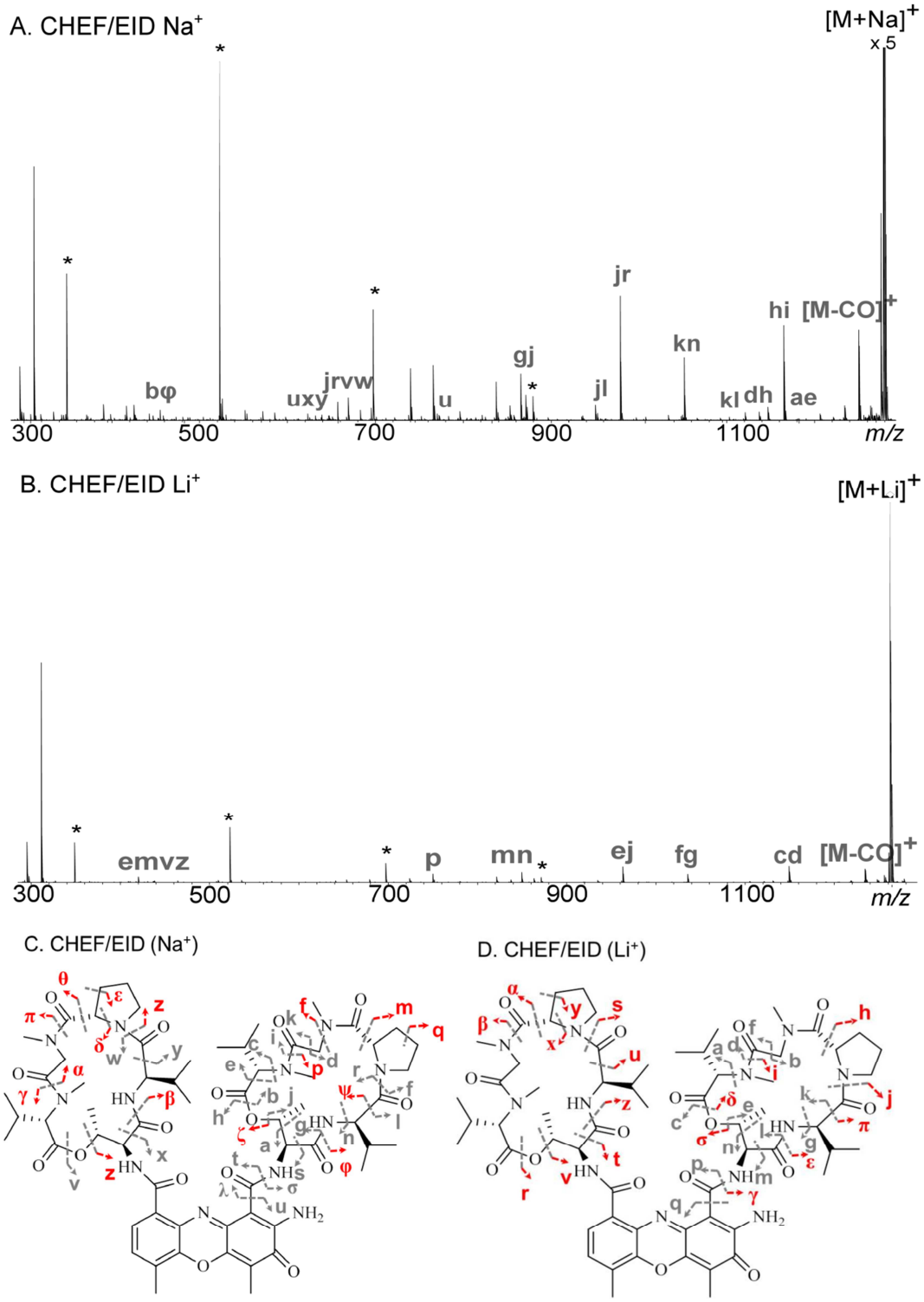

Figure 3.8: A comparison of EID spectra for the sodiated (A) and lithiated (B) actinomycin D, combined with multi-CHEF, with illustrations of the fragments identified; cleavages highlighted in red are new peaks detected using this method.

The peaks due to arginine clusters, used as internal calibrants, are marked with *. A full list of peak assignments can be found in Tables A-19 and A-20 of Appendix A

The fragments of actinomycin D shown in red in Figures 3.8 (A) and (B) indicate additional cleavages that were not observed when using EID alone. By combining EID with multiple ion isolation, a much greater degree of fragmentation of the peptide was achieved. This is presumably due to the increase in intensities of the product ion peaks relative to the precursor (discussed in section 3.3.5), whereby peaks that were most likely hidden in the baseline when EID was applied without multiple ion isolation (Figure 3.4) can now be observed. The sodium adduct, as before, produced a greater degree of fragmentation of both rings, enabling detailed structural characterization to be performed. The use of the arginine clusters as internal calibrants provided a reliable, accurate method for internal calibration, with mass accuracies of all peaks calculated to be well below 1 ppm. Table 3.2 provides a comparison of mass accuracy for a selection of peaks in the EID spectrum of the sodium adduct, with and without multiple ion isolation.

Table 3.2: A comparison of mass accuracies for a selection of assigned product ions, with and without the use of multiple ion isolation, for the sodium adduct of actinomycin D

Proposed Formula	Fragment Cleavage	Mass Error / ppm Without CHEF	Mass Error / ppm With CHEF
$C_{61}H_{86}N_{12}O_{14}Na^+$	ab	0.34	0.00
$C_{60}H_{83}N_{11}O_{15}Na^+$	cd	1.02	0.11
$C_{57}H_{79}N_{11}O_{15}Na^+$	fg	0.67	0.11
$C_{56}H_{75}N_{11}O_{15}Na^+$	hi	0.09	-0.28
$C_{55}H_{75}N_{11}O_{13}Na^+$	dj	0.50	-0.09
$C_{48}H_{61}N_9O_{12}Na^+$	jr	-0.01	-0.42
$C_{42}H_{54}N_8O_{10}Na^+$	js	-0.67	-0.35
$C_{39}H_{47}N_7O_{10}Na^+$	t	0.13	0.36
$C_{38}H_{49}N_7O_9Na^+$	u	0.22	-0.42
$C_{24}H_{37}N_5O_7Na^+$	λ	-0.57	-0.26
	Absolute Average	0.42	0.24
	Std. Dev.	0.32	0.14

It is clear to see that by using multiple ion isolation, a more accurate internal calibration is achieved, enabling the fragments assignments to be made with greater confidence. Both the absolute average and standard deviation of the mass accuracy values for the selected peaks in Table 3.2 are reduced by approximately half, showing the calibration is more consistent, and thereby providing a more reliable method for characterizing the structures of unknown compounds.

3.3.5 Improving Fragment Efficiency in EID

A further limitation currently associated with EID is the significantly lower peak intensities observed compared to the precursor ion. Low fragment intensities have been reported previously in EID experiments, with Wolff *et al.*[147] and Yoo *et al.*[148] reporting intensities 50-100 fold and 50-200 fold lower than the precursors. Although the signal-to-noise ratio in FTICR is such that the fragments are still identifiable in the noise, potentially there are many more peaks hidden in the noise

that may provide additional important structural information. This is illustrated by Figure 3.9, which shows an expanded region of the EID spectra of the sodiated adduct of actinomycin, both with and without multiple ion isolation.

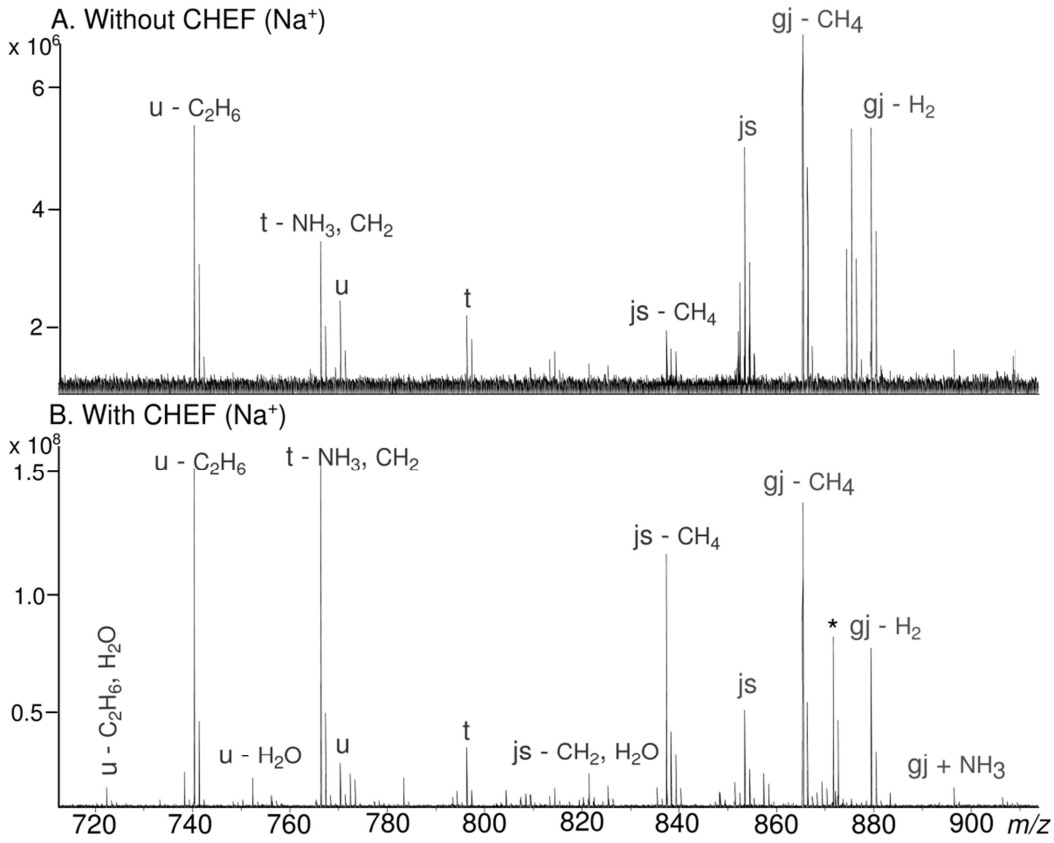

Figure 3.9: Expanded region *m/z* 720-900 of EID spectra of actinomycin D, without the use of multiple ion isolation (A); and with multiple ion isolation (B). The peaks due to arginine clusters, used as internal calibrants, are marked with *

Low product ion peak intensity is a feature of tandem mass spectrometry techniques involving electron interactions, the most reported of which is observed in electron capture dissociation (ECD). A number of factors have been proposed to account for the low fragment intensities including charge neutralisation, an increased number of

fragmentation pathways,[149] misalignment of the electron beam and ion cloud, and magnetron motion of the ions.[127] While charge neutralisation could account for some decrease in product ion intensity, it cannot explain the continual observation of the precursor signal.[149] A possible explanation for this occurrence is the generation of an electric field produced by space charge effects of the electron beam, that can trap a population of ions in a potential well and therefore prevent them from interacting with the electron beam.[150] Misalignment of the electron beam and ion cloud has been investigated,[127, 150] and manipulation of the ion cloud within the ICR cell has been shown to improve fragment efficiencies.[103, 127] SORI-CAD[60] causes radial oscillations of the ion cloud as they are activated for dissociation; combining this technique with ECD has been shown to increase fragment intensities as the ions are pushed into the electron beam.[127]

As can be seen in Figure 3.8B, an additional advantage of using multiple ion isolation with EID is that the intensities of the product ion peaks are increased by a factor of ~25 compared to those in Figure 3.8A. Instead of fragments that are on the order of a few hundred times less intense, with in-cell isolation, the peaks can be observed with small, or even no scaling of the spectrum. An increase in ECD efficiency has been demonstrated by using a single frequency shot[103, 127] at *m/*z 100 to improve the overlap between the ion and electron beams. In this case, multiple ion ejection occurs through using multi-CHEF to isolate the precursor ion. It is possible that this method of in-cell isolation simply improves the overlap between the ion cloud and the electron beam to such an extent that much more efficient fragmentation of the precursor can be achieved. This method therefore has potential for providing detailed structural information with a high degree of accuracy for characterising unknown compounds.

3.4 Conclusion

The tandem mass spectrometry techniques of CAD and EID have proved to be powerful tools for elucidating structural information on the non-ribosomal peptide, actinomycin D. Combining EID with the multiple ion isolation in the ICR cell improves this method two-fold; firstly, by providing an accurate internal calibration for confident assignment of the fragments, and secondly, by increasing the intensities of the fragment peaks, resulting in a greater degree of fragmentation of the precursor. The use of tandem mass spectrometry techniques for the analysis of natural products is becoming more prominent and, with such detailed structural information able to be obtained relatively easily, will be extremely valuable for aiding in the discovery of novel compounds.

Chapter 4: Insights into the Binding Sites of Organometallic Ruthenium(II) Complexes on Peptides

This chapter has been partially reproduced from the following publication:

R.H.Wills, A. Habtemariam, A.F.Lopez-Clavijo, M.P.Barrow, P.J.Sadler and P.B.O'Connor, Insights into the Binding Sites of Organometallic Ruthenium Anticancer Compounds on Peptides Using Ultra-High Resolution Mass Spectrometry, accepted in JASMS, 2014.

4.1 Introduction

Organometallic ruthenium(II) compounds, such as those in Figure 4.1, containing η^6-arene ligands have shown promising anticancer activity in vitro against a range of types of cancer cells, including cisplatin-resistant cells, as well as activity in vivo.[151-153] The arene stabilises the ruthenium(II) in its 2+ oxidation state,[154] and research has shown that increasing the size of the arene increases the cytotoxicity of the ruthenium(II) arene complex.[95, 151] The *N,N*-chelating ligand provides additional stabilisation for the compound, and the chloride ligand is substituted by an aqua ligand under physiological conditions, so as to facilitate the binding of the ruthenium(II) to the different biomolecules. In contrast to cisplatin, which is square planar with two chloride ligands, these ruthenium(II) compounds are pseudo-octahedral and, potentially, have only one free reactive coordination site available for binding. In order to assess the mode of binding of the compounds to peptides, these compounds were chosen as they carry variation in the chelating ligand. In this way, the role of steric and electronic properties in controlling a particular binding mode can be investigated.

The binding of ruthenium(II) compounds to proteins has started to be investigated[110, 155-163] but, as yet, these studies are not as extensive as for cisplatin. Such binding studies are important in order to fully understand their mechanism of action and to allow reversal of any side effects due to protein binding of ruthenium. The mode of action of ruthenium(II)-based drugs is thought to differ significantly from that of platinum-based drugs like cisplatin. While cisplatin binds to the DNA of cancer cells, research into the mechanism of ruthenium(II)-based drugs has started to suggest alternative targets, including proteins involved in cellular signalling pathways,[162, 164] and the histone proteins of nucleosome core particles.[165] Williams *et*

al.[155] have shown that ruthenium(II) arene complexes can bind to the methionine residue of the peptide substance P. Wang *et al*.[110] and McNae *et al*.[156] have also reported on binding to the imidazole nitrogen atom of histidine, whilst Casini *et al*.[160] report the binding to cysteine residues through the displacement of zinc from metallothionein-2.

Insulin is a small (~5.7 kDa) protein with two peptide chains connected through two disulfide bonds, with a third intramolecular disulfide bond in the A-chain. It is produced in the pancreas and is vital for the regulation of blood glucose levels. The interaction of cisplatin with insulin has been studied previously[99] and has shown that platinum binds preferentially to the two histidine residues, as well as the N-terminus of the B chain. Ruthenium(II) has been observed to bind to free cysteine in HSA;[161] insulin was therefore chosen in order to determine the binding sites in the presence of disulfide bonds. The sulfhydryl group of cysteine is easily oxidised to sulfenic acid (Cys-SOH), a species that is not uncommon in proteins, but is unstable and so readily reacts, either with a thiol to form a disulfide bond, or through further oxidation to form sulfinic acid (Cys-SO_2H) or sulfonic acid (Cys-SO_3H).[166-167] The conversion of cysteine to the sulfenic/sulfinic/sulfonic acids is an important post-translational modification that is involved in regulating protein function, specifically signal transduction pathways, in cells.[168-169] In order to investigate binding to cysteine in its oxidised form, the ruthenium(II) compounds were also reacted with oxidised insulin B-chain, where the two cysteine residues are in the form of cysteine sulfonic acid.

4.2 Experimental

4.2.1 Chemicals and Reagents

Angiotensin(II), bombesin, substance P, oxidised insulin B-chain, glutathione (oxidised and reduced), and insulin were purchased from Sigma Aldrich (Gillingham, UK) and dissolved in Milli-Q water (Millipore Inc., Durham, UK) to concentrations of 1 mM. The ruthenium(II) compounds (AH076 and AH078, Figure 4.1) were provided after synthesis as described in the literature.[154] Methanol, acetonitrile and formic acid were purchased from Fisher Scientific (Loughborough, UK). Hydrogen peroxide (30%) was purchased from Sigma Aldrich (Gillingham, UK).

4.2.2 Reaction of Ruthenium(II) Complexes with Peptides

Aqueous solutions of angiotensin(II), bombesin, oxidised insulin B-chain, glutathione, and insulin (1mM), and the ruthenium(II) compounds (1 mM) were prepared. Reaction mixtures were prepared using a starting volume of 100 μL of the peptide/protein solution and mixing with the ruthenium(II) compounds in molar ratios of 1:1, 1:2 and 1:10. The mixtures were then incubated at 37°C for 48 hours. Oxidation of glutathione was performed using hydrogen peroxide (30%) in a molar ratio of 1:1 and reacted at 37°C for 2 hours. Prior to analysis by mass spectrometry, the peptide/protein mixtures were diluted to a concentration of 0.5 μM in a solution of 50% methanol and 0.1% formic acid.

4.2.3 Analysis by ESI-MS

The samples were analysed on a Bruker solariX FTICR mass spectrometer (Bruker Daltonics, Coventry, UK). The samples were injected into the electrospray ionisation source using a syringe pump with a flow rate of 200 μL/hour. A drying

gas flow rate of 4 L min^{-1} and temperature of 220 ºC were used, with a nebuliser gas pressure of 1.2 bar. A voltage of -4500 V was applied to the capillary for analysis in positive mode, with an offset of 500 V applied to the spray shield. For CAD experiments, the precursor ion was isolated with a window of 4 *m/z* using the quadrupole, and fragmented in the collision cell using argon with collision energies between 11 and 13 V for peptides, and 20-22 V for proteins. The peptide ions were accumulated for 1 second, and protein ions accumulated for slightly longer at 1.5 seconds, with 4 MW datasets and 100 scans recorded per experiment. Trapping potentials of 0.5 V and 0.6 V were applied to the front and back trapping plates respectively. For ECD experiments, the precursor ion was isolated using the quadrupole and externally accumulated in the collision cell for 2-5 seconds before being transferred to the ICR Infinity cell.[35] The ions were then irradiated with electrons from a 1.7 A heated hollow cathode dispenser, biased with an offset potential of 1.4 V, for 80-100 ms. Datasets of 4 MW and 50 scans were recorded per experiment. All spectra were post-processed using one zero-fill and a sine-bell apodisation function. Internal calibration was performed on the spectra using the peptide precursor peaks with different numbers of charges; CAD spectra were calibrated using known b- and y-ion *m/z* values of the peptides, likewise ECD spectra were calibrated using known c- and z•-ion *m/z* values. Peak lists are included in Appendix B with calibrant values marked.

4.3 Results and Discussion

4.3.1 Compounds AH076 and AH078

The binding of two different ruthenium(II) $[(\eta^6\text{-arene})Ru(N,N)Cl]^+$ compounds where arene/*N*,*N* = biphenyl (bip)/bipyridine (bipy) for compound AH076, and biphenyl (bip)/*o*-phenylenediamine (*o*-pda) for compound AH078, shown in Figure 4.1, was initially investigated using three standard peptides, namely angiotensin(II), bombesin, and substance P.

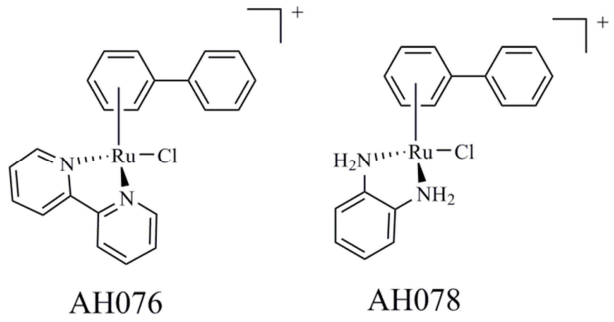

AH076 AH078

Figure 4.1 The ruthenium(II) complexes AH076 and AH078

Both ruthenium(II) complexes have a "piano-stool" geometry formed through the coordination of an arene (occupying three coordination sites), a chelating ligand, and a chloride ligand.[170] The FTICR mass spectra obtained for the products from reactions of the two complexes, AH076 and AH078, with the peptides showed a number of different peaks containing ruthenium, which were easily identified by the unique nature of the isotopic pattern of ruthenium. The adducts observed were dependent on the ratio of ruthenium(II) compound to peptide used. At low ratios

(1:1 and 1:2), the ruthenium(II) compounds lost both the arene and the chloride ligands, thus retaining only the chelating ligand and therefore providing the ruthenium with four vacant coordination sites to attach to the peptide (three from loss of the arene and one from loss of the chloride). At higher ratios of peptide to ruthenium(II) complex (1:10), multiple ruthenium(II) bound species were detected, most notable of which was the ruthenium(II) complex coordinated through loss of the chloride ligand only, therefore providing insight into the primary binding site on the peptide, which will be discussed in section 4.3.5.

4.3.2 Reaction of Angiotensin(II) with AH076 and AH078 (1:1)

Upon reaction between either AH076 or AH078 and angiotensin(II) (sequence DRVYIHPF) at a ratio of 1:1, the ruthenium retains its bidentate chelating ligand only; for AH076 this is denoted by Ru(bipy), and for AH078, the *o*-phenylenediamine chelating ligand is retained and is denoted by Ru(*o*-pda). In order to elucidate the binding sites on angiotensin(II), these adducts were fragmented using CAD. Figure 4.2 illustrates the CAD mass spectra obtained for the adducts formed between angiotensin(II) and AH076 (A) and AH078 (B).

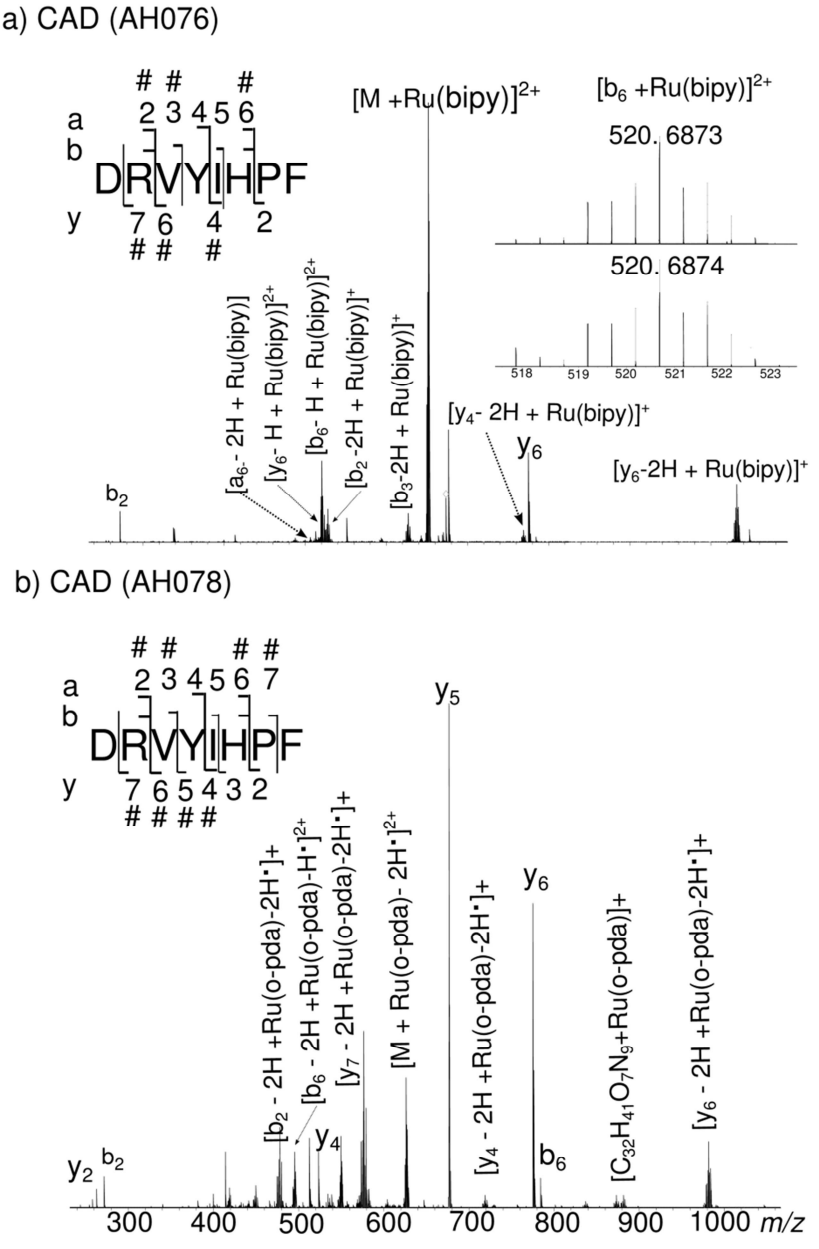

Figure 4.2: (a) CAD spectrum of angiotensin(II) after reaction with AH076, fragmented peak $[M+Ru(bipy)]^{2+}$ at *m/z* 651.8, with inset illustrating the sequence ions detected (# indicates a fragment containing ruthenium, either Ru(bipy) or Ru(o-pda)); (b) CAD spectrum of angiotensin(II) after reaction with AH078, fragmented peak $[M+Ru(o\text{-}pda)\text{-}2H^{\bullet}]^{2+}$ at *m/z* 626.7, with insets illustrating the sequence ions detected (# indicates a fragment containing ruthenium). A full list of peak assignments is provided in Tables B-1 and B-2 of Appendix B

Both CAD spectra suggest that ruthenium(II) is coordinated to histidine, as indicated by the b_6 fragment, as well as either arginine or aspartic acid, or even the N-terminus, as indicated by the presence of the b_2 fragments with Ru(*o*-pda) or Ru(bipy) bound. Also present are the b_3 ions together with the y-ion series from y_4 to y_7, all containing Ru(*o*-pda) or Ru(bipy). One peak in particular, at *m/z* 419.15, suggests the involvement of arginine in the coordination of AH078; this was assigned as the amino acids D, R, H, P and F with ruthenium(II) plus *o*-pda bound, implying that the metal is bound by both arginine and histidine subsequently bridging the two sides of the peptide, with the intervening amino acids V, Y, and I being cleaved by CAD.

Although the data indicate that Ru(bipy) and Ru(*o*-pda) are bound by arginine and histidine, through loss of the arene ligand, there are potentially two further vacant coordination sites for the ruthenium. The data do not suggest the involvement of any other amino acid side chains but one notable observation is the loss of hydrogen from the peptide during fragmentation by CAD. In Figure 4.2(a), there is either a loss of one or two protons from the b- and y- fragments. Since the precursor ion is simply the neutral peptide with Ru(bipy) coordinated, the charge is provided by the metal ion which therefore plays a role in directing fragmentation, primarily at the location at which it is bound.[171-172] Deprotonation of the peptide is consequently promoted by collisional activation and therefore should lead to a stable structure for the product ion with the metal bound. Ions such as Zn^{2+} and Ni^{2+} have been reported to interact weakly with amide oxygen atoms; an interaction that is strengthened by additional coordination to amino acid side chains and the amino group of the N-terminus. Zinc binding to angiotensin(II) has been reported to occur via coordination to histidine and two neighbouring amide oxygen atoms;

deprotonation subsequently occurs at the amide nitrogen of histidine resulting in a net negative charge on the amide oxygen creating a 2+ fragment ion.[171] Further deprotonation of another amide nitrogen can occur leading to the formation of a 1+ fragment ion, which was also observed here.

In Figure 4.2(b), for AH078 only, the ruthenium-containing fragments were assigned with an additional two-hydrogen-atom (denoted by 2H•) loss, which was not observed for the fragments of AH076. Since this loss was also observed in the precursor ion, removal of the two hydrogen atoms does not occur as a result of collisional activation and therefore must have an alternative explanation. Loss of the arene ligand from ruthenium has been observed in solution [151], and is thought to occur through oxidation of the chelating ligand, whereby an hydrogen atom is lost from each of the NH_2 groups subsequently forming a diimine. The observed hydrogen loss in the CAD spectrum is consistent with the formation of the diimine for AH078. Additionally, as the bipyridine chelating ligand of AH076 cannot undergo the same oxidation and subsequent hydrogen loss, and as the two compounds appear to be binding to the peptide in the same manner, it is unlikely that the hydrogen loss originates from the peptide itself through coordination of the ruthenium.

Although loss of the arene from AH078 may be coupled to oxidation of the *o*-pda chelating ligand, the same biphenyl ligand is lost in the reactions with AH076. Loss of the ligands other than the chloride from ruthenium complexes has been observed before. Meier *et al.*[162] have reported on the binding of ruthenium(II) compounds with bidentate pyrone chelating ligands which, on binding to methionine and ubiquitin, were lost in addition to the chloride ligand, providing the ruthenium with three potential coordination sites. They also report on the removal of ubiquitin

bound to these ruthenium(II) compounds by sulfur-containing species such as glutathione and cysteine.

4.3.3 Reaction of Bombesin with AH076 and AH078 (1:1)

Compound AH076 was reacted with bombesin (sequence p-EQRLGNQWAVGHLM-NH_2, where "p" signifies pyro-glutamic acid formed through cyclisation) and the resulting adduct, formed through loss of both the chloride and arene ligands, was fragmented with CAD, as shown in Figure 4.3(a).

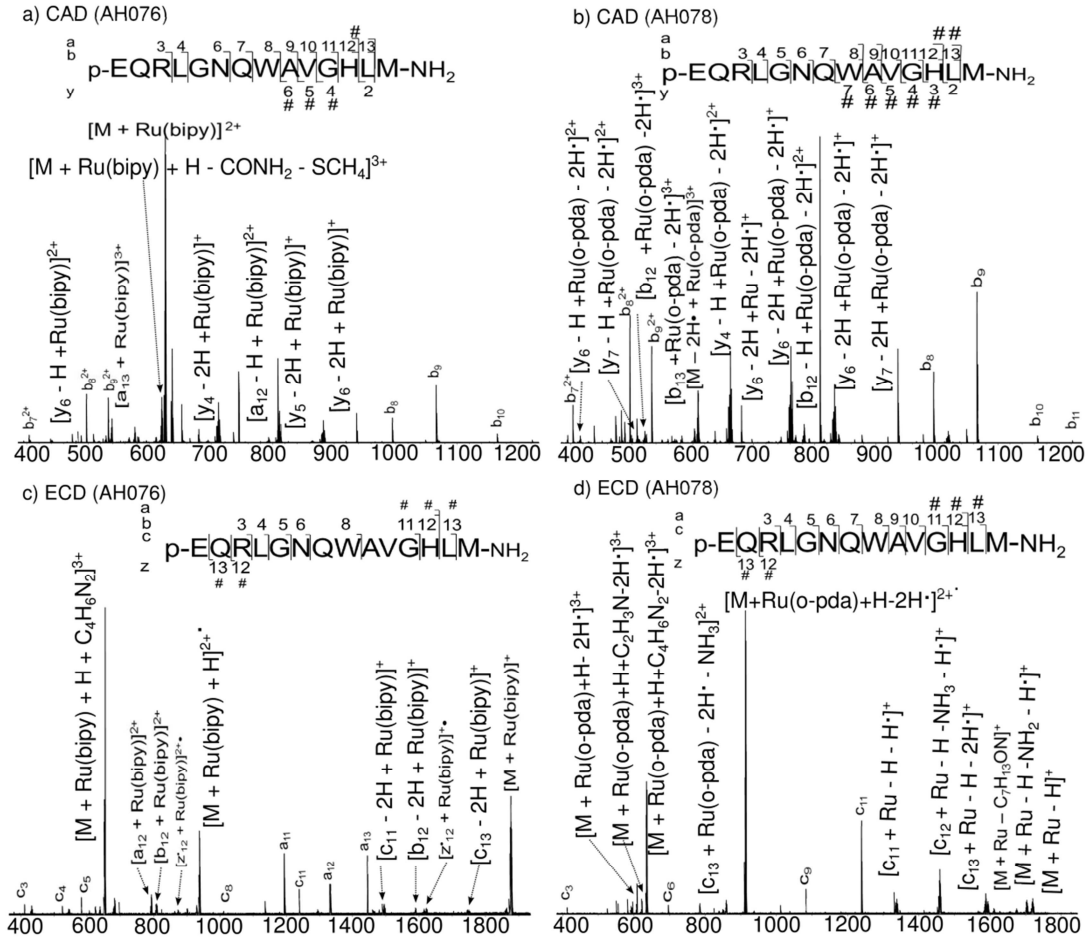

Figure 4.3: (a) CAD spectrum of bombesin after reaction with AH076, fragmented peak $[M+Ru(bipy)+H]^{3+}$ at *m/z* 625.9, with inset illustrating the fragments obtained (# indicates a fragment containing ruthenium); (b) CAD spectrum of bombesin after reaction with AH078, fragmented peak $[M+Ru(o\text{-}pda)\text{-}2H^{\bullet}]^{3+}$ at *m/z* 636.6; (c) ECD spectrum of bombesin after reaction with AH076, fragmented peak $[M+Ru(bipy)+H]^{3+}$ at *m/z* 653.3; (d) ECD spectrum of bombesin after reaction with AH078, fragmented peak $[M+Ru(o\text{-}pda)\text{-}2H^{\bullet}]^{3+}$ at *m/z* 636.6, with inset illustrating the sequence ions detected. A full list of peak assignments can be found in Tables B3 – B6 in Appendix B

The product ions detected using both techniques suggest ruthenium(II) is bound to histidine in the bombesin sequence. Histidine was expected to be involved in coordinating ruthenium(II) as the imidazole nitrogen (Nε) is known to be a strong binding site for ruthenium(II) arene complexes.[110] Since ruthenium(II) also has a high affinity for sulfur, methionine is likely to provide an additional binding site; a peak at *m/z* 594.92 Da was observed in Figure 4.3 (a), and was assigned as $[M+Ru(bipy)-CONH_2-SCH_4+H]^{3+}$ indicating losses of SCH_4 and $CONH_2$ from the peptide. This is consistent with binding at methionine and the amidated C-terminus, as has been reported previously,[162] providing two additional binding sites. CAD was also used to fragment the adduct formed after the reaction of bombesin with AH078. The spectrum, shown in Figure 4.3 (b), indicates similar binding as for AH076 with coordination at histidine, but no additional information on the binding sites was obtained.

4.3.4 Additional Information Obtained through ECD

ECD was also carried out on the adducts formed after reaction between the peptides and the ruthenium(II) complexes in order to determine if any further information on the binding sites could be elucidated using this complementary fragmentation technique. The ECD spectrum of angiotensin(II) and AH078, shown in Figure 4.4, simply showed the loss of the chelating ligand, *o*-pda, and the main species detected was simply the whole peptide with the addition of ruthenium(II), which could be bound anywhere in the peptide.

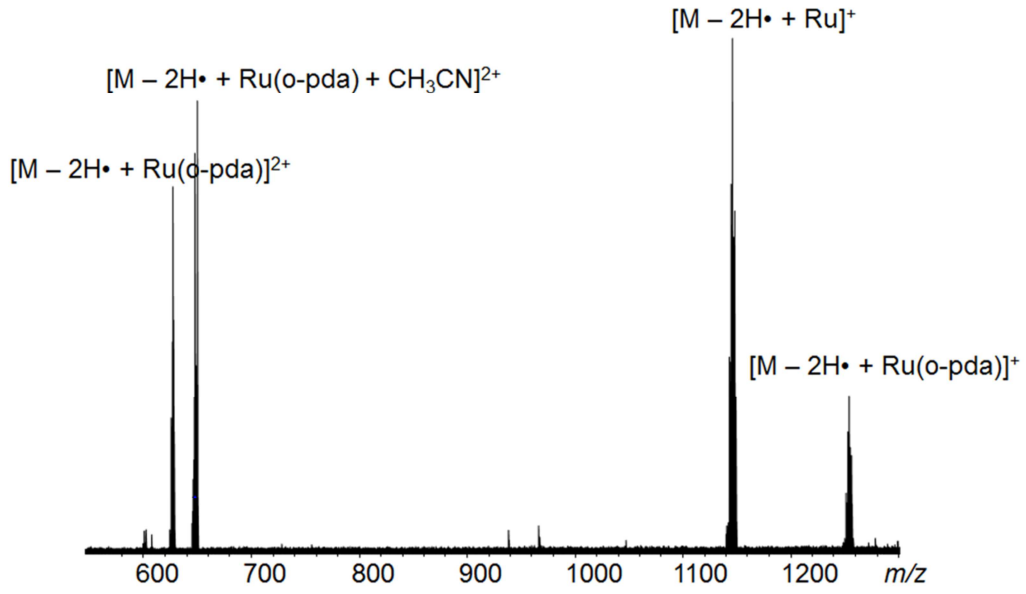

Figure 4.4: ECD spectrum of angiotensin(II) after reaction with AH078, fragmented peak $[M+Ru(o\text{-}pda)\text{-}2H^{\bullet}]^{2+}$ at *m/z* 647.3

Upon electron capture, the electron initially occupies an excited Rydberg orbital on a positively-charged site (typically n=6-7),[65] and drops to a low-lying electronic state through a cascade of either radiationless or radiative relaxation events on a timescale of 10^{-6} s. Since the addition of $\{(arene)Ru(N,N)\}^{2+}$ automatically provides the peptide with a 2+ charge, capture of an electron to a low-lying electronic state centred at the metal is a likely occurrence.[173-174] Thus, capture of the electron has simply resulted in a reduction of the charge on the ruthenium from 2+ to 1+, with no further backbone cleavage of the peptide.

The ECD spectra of bombesin and the two ruthenium(II) complexes were more useful, as shown in Figures 4.3(c) and (d). In this case, because the adduct had a 3+ charge, there was a bound proton in addition to the ruthenium; this protonated site could also provide a low-lying electronic state to capture the electron, enabling cleavage of the peptide backbone to be observed.[67, 175] Although the two spectra

were similar in that they suggested binding at histidine, the ECD spectrum of bombesin and AH078 (Figure 4.3 d) also revealed a peak at *m/*z 1593.62, which was identified as bombesin plus ruthenium(II) but minus a leucine residue. This may imply that ruthenium(II) is coordinated to both the histidine and the methionine so that, on fragmentation, the intervening Leu_{13} is removed whilst preserving the bound ruthenium and keeping the rest of the peptide together. This is consistent with the radical cascade mechanism for ECD proposed by Leymarie *et al.*[63] whereby the radical is propagated along the peptide backbone by odd-electron rearrangements, causing cleavage at multiple sites.

One other notable fragment in Figure 4.3(d) is the c_{11} ion, which was detected with the addition of the ruthenium(II) metal. The c_{11} ion does not contain either the histidine or the methionine residues so this suggests that the metal can be coordinated by other amino acids. Unfortunately this fragment constitutes the rest of the peptide, so it is unclear exactly where it is coordinated. However, this data does indicate that amino acids other than histidine and methionine are potentially involved in binding ruthenium(II). Since no other significant differences were observed between the mode of binding of AH076 and AH078, it appears that the chelating ligand does not have a significant effect on the compound coordination geometry. For this reason, the remaining experiments were conducted using AH076 only.

4.3.5 Reactions of Angiotensin(II) and Bombesin with AH076 (1:10)

The adducts observed in the reactions between angiotensin(II) and bombesin with AH076, where only loss of the chloride ligand was observed, were also fragmented using CAD in order to determine the primary binding site of the ruthenium(II) on the peptides. Figure 4.5 illustrates the CAD spectra obtained through fragmenting the adducts observed between (a) angiotensin(II) and AH076, and (b) bombesin and

AH076; the form of the ruthenium(II) compound attached is denoted {(bip)Ru(bipy)} in both cases.

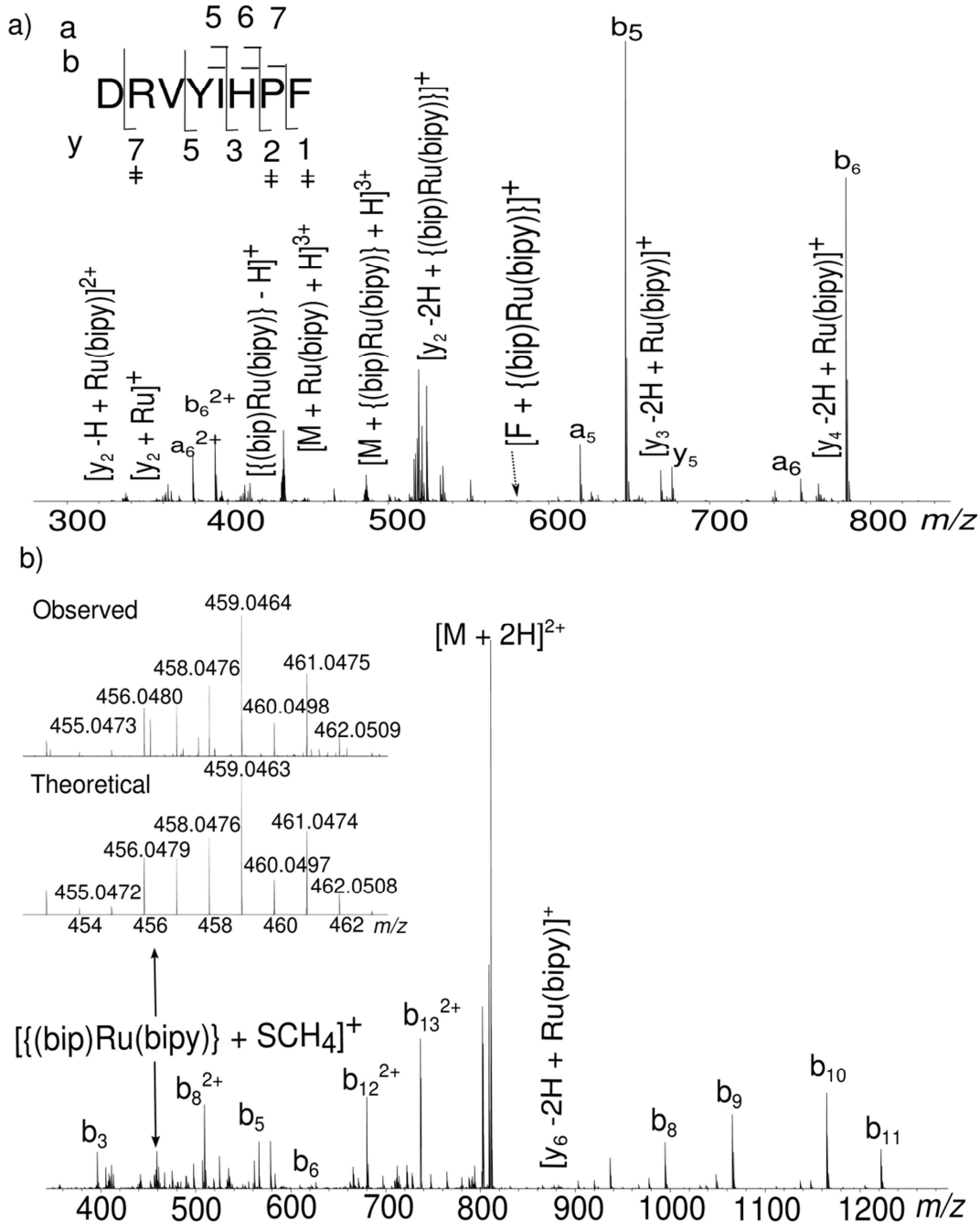

Figure 4.5: (a) CAD spectrum of angiotensin(II) and AH076, fragmented peak $[M+\{(bip)Ru(bipy)\}+H]^{3+}$ at *m/z* 586.6 (# indicates a fragment containing ruthenium); (b) CAD spectrum of bombesin and AH076, fragmented peak $[M+\{(bip)Ru(bipy)\}+2H]^{4+}$ at *m/z* 508.2; inset illustrates the observed and simulated isotopic distributions of the species at *m/z* 459.04 corresponding to the ruthenium

compound plus SCH_4 from the methionine side chain. A full list of peak assignments can be found in Tables B-7 and B-8 of Appendix B

The CAD spectrum of angiotensin(II) and AH076 showed similar fragments to that in Figure 4.2(a), where the arene had been lost in addition to the chloride ligand, showing that cleavage of the arene can still occur during the CAD process. Several fragments were detected that enabled the binding site of the ruthenium compound to be elucidated, namely the peak detected at *m/z* 576.12, which was assigned as the amino acid phenylalanine (F) plus {(bip)Ru(bipy)}. The observed isotope distribution and that of the simulated pattern are shown in Figures 4.6 (a) and (b).

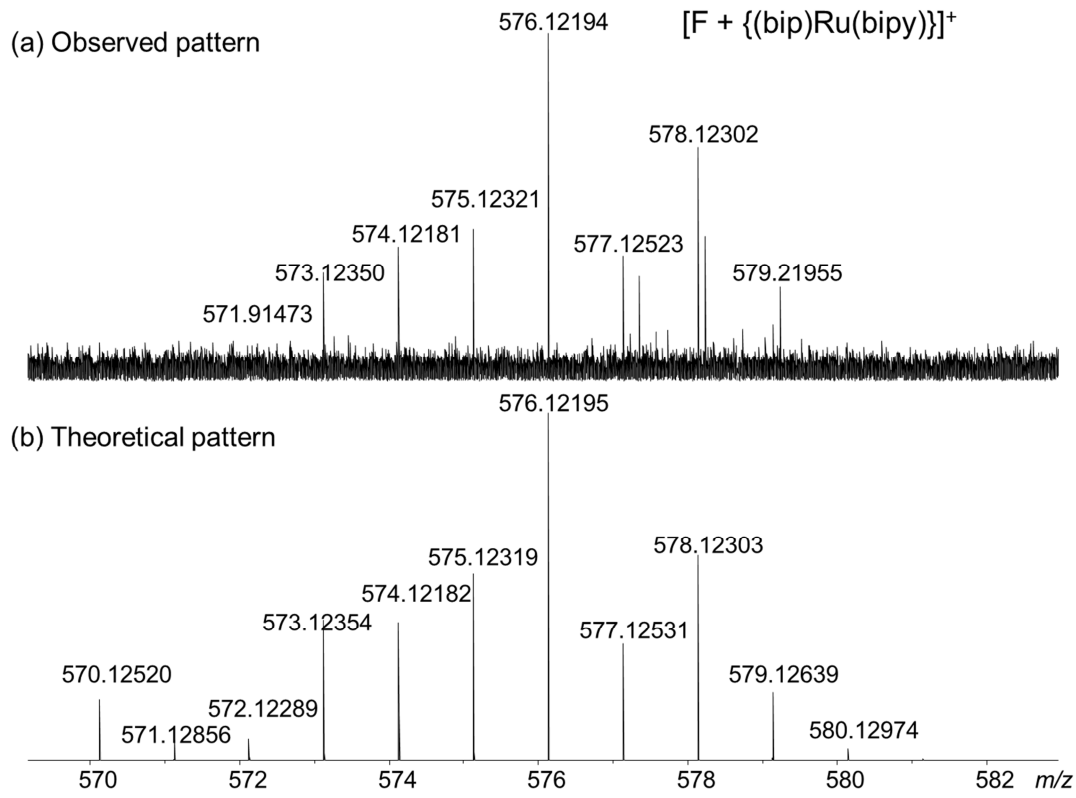

Figure 4.6: (a) Expanded region of the CAD spectrum of angiotensin(II) and AH076 showing the peak assigned as phenylalanine (F) plus {(bip)Ru(bipy)}; (b) the theoretical pattern expected from simulation of this species

Binding to phenylalanine is an observation that has been made for the first time here, and which is not observed when there are four coordination sites available, as discussed above. Since there is only one coordination site available, direct coordination between ruthenium and the aromatic ring of the phenylalanine side chain would be unlikely due to steric hindrance from the bulky biphenyl and bipyridine ligands, which are still attached. It is possible, therefore, that the aromatic ring of phenylalanine provides stabilisation through an interaction with one of the aromatic ligands (either biphenyl or bipyridine) in the form of π-stacking. This type of interaction has been observed previously[176] between the phenylalanine of substance P and a coumarin tag. Potentially, either aromatic ring of the arene and

chelating ligand could interact in this manner with the phenylalanine side chain; since this is not observed when the ruthenium retains only the chelating ligand, it is likely that it is the arene that is involved in this coordination.

The CAD spectrum for bombesin and AH076 also elucidated information about the ruthenium(II) binding site. Instead of peptides fragments, it is the side chain losses detected that show the primary binding site for ruthenium(II), in this case, to be the methionine side chain. The peak at *m/z* 459.05 was assigned as $[\{(bip)Ru(bipy)\} + SCH_4]^+$, which could only have originated from the methionine side chain. Detection also of the complementary fragment, $[M+3H-SCH_4]^{3+}$, at *m/z* 524.61, further supports this conclusion.

4.3.6 Summary of Peptide Binding with Ruthenium(II) Complexes

The initial work carried out on the reaction between peptides and two ruthenium(II) complexes provided a significant amount of information on their binding sites. To summarise these findings, the amino acids proposed to coordinate ruthenium(II), as well as the data supporting these conclusions is shown in Table 4.1.

Table 4.1: Key fragments detected from the reactions between the ruthenium(II) complexes and peptides indicating proposed binding sites

Proposed Binding Site	Supporting Data – Detected Fragments
Histidine (His)	Angiotensin(II) b_6 + Ru(bipy) [DRVYIHPF]
Methionine (Met)	SCH_4 + $[(bip)Ru(bipy)]^+$ SCH_4 loss from bombesin
Amidated C-terminus	$CONH_2$ loss from bombesin
Phenylalanine (Phe)	Phe + $[(bip)Ru(bipy)]^+$
Arginine (Arg)	Angiotensin(II) b_2 + Ru(bipy) [DRVYIHPF]
His and Arg	DR···[Ru(bipy)]···HPF
His and Met	p-EQRLGNQWAVGH···[Ru(bipy)]···M

The binding to histidine and methionine was expected as it has been observed in previous work;[110, 155, 162] of notable interest is the involvement of phenylalanine, which has been observed here for the first time.

4.3.7 Reaction of Insulin with AH076

The initial experiments involved two peptides, neither of which contain any cysteine residues (or disulfide bonds). Previous work[161] has indeed shown that ruthenium(II) can bind to a free cysteine, but not when it is oxidised and is present in a disulfide bond. Insulin has three disulfide bonds as well as histidine, arginine, and phenylalanine residues, so was chosen and was chosen so that the binding sites for ruthenium could be compared to those observed previously for cisplatin.[99] Figure

4.7 shows the CAD spectrum of insulin after reaction with AH076, together with an illustration of the fragments assigned, with both the non-ruthenium(II) bound (a) and ruthenium(II) bound fragments (b) shown in separate diagrams for clarity.

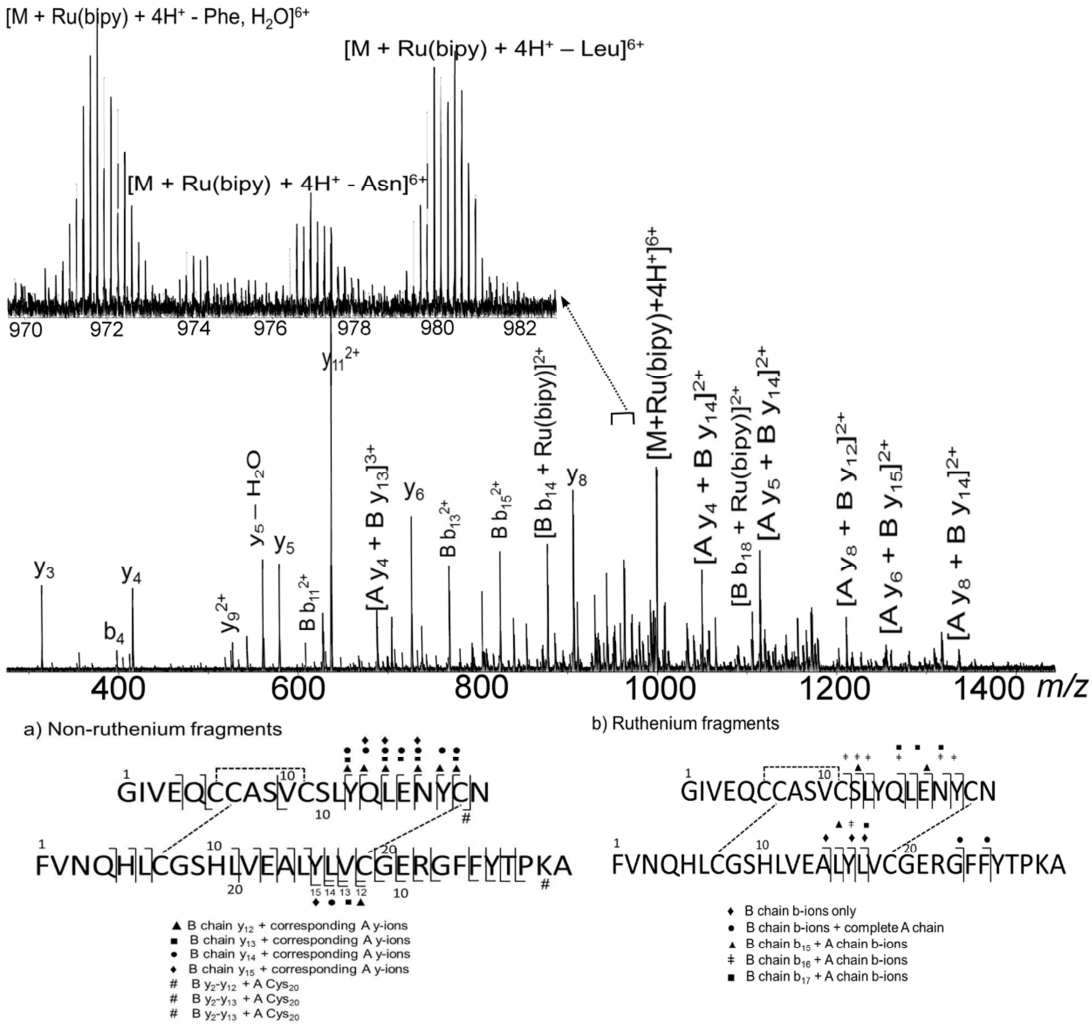

Figure 4.7: CAD spectrum of insulin after reaction with AH076, fragmented peak $[M+Ru(bipy)+4H]^{6+}$ at *m/z* 1007.6; inset illustrates a zoomed region of the spectrum to show the isotope pattern of the ruthenium fragments. Illustrations of the fragments obtained from the CAD spectrum of insulin after reaction with AH076, showing (a) the non-ruthenium bound fragments, and (b) fragments of insulin with

ruthenium bound. A full list of peak assignments can be found in Table B-9 of Appendix B

The ruthenium-containing product ions include several with an intact disulfide bond between A-chain Cys_7 and B-chain Cys_7, and there is no evidence in the CAD spectrum to suggest that this bond is broken on reaction of insulin with ruthenium. The non-ruthenium(II) bound product ions reflect the intact nature of the disulfide bonds between Cys_6 and Cys_{11} of the A-chain, and between Cys_{20} of the A chain and Cys_{19} of the B-chain, with mainly y-ions of the two chains detected, therefore indicating that the ruthenium is not bound in this region of the protein, specifically between amino acids Tyr_{14} and Asn_{21} of the A-chain, and between Tyr_{16} and Ala_{30} of the B-chain. A number of ruthenium(II)-containing fragments are observed, with 2+, 3+, 4+, 5+ and 6+ charges. The 2+ product ions consist of b-ions of the B-chain only, indicating it is unlikely that ruthenium(II) is bound by the A-chain. These fragments, the b_{14}, b_{16}, b_{17}, and b_{18} ions, are all observed with a $2H^{\bullet}$ loss which, unlike that observed with AH078, cannot originate from the chelating ligand and, as such, must originate from the peptide itself. The most likely binding site would be histidine at either His_5 or His_{10}; given that b_{14} is the first fragment observed, His_{10} is proposed as the main binding site, with additional coordination perhaps provided by glutamic acid at position 13. This conclusion is supported by the 5+ and 6+ fragments detected which have been assigned as the entire protein plus the ruthenium(II) compound, but with certain amino acids missing from the sequence. These losses, which include alanine, leucine, valine and phenylalanine, indicate that ruthenium(II) is bound to His_{10}, Glu_{13} and, possibly, Tyr_{15} of the B-chain, which would keep the protein intact whilst CAD cleaves these intervening amino acids

from the chain. The H• loss observed for the 2+ fragments could correspond to losses from the amide nitrogen atoms of the backbone, providing the remaining two binding sites. This coordination has been observed previously, where ruthenium(II) bound to the amide nitrogen of the backbone, in addition to the histidine side chain, causing loss of the hydrogen.[177]

4.3.8 Reaction of Oxidised Insulin B-chain with AH076

In order to determine if any more detailed information about ruthenium(II) binding to the insulin B chain could be elucidated, AH076 was reacted with the oxidised insulin B-chain, where the two cysteine residues are in the form of sulfonic acid (Cys-SO_3H). Figure 4.8 shows the CAD spectrum and fragments of the oxidised insulin B-chain after reaction with the ruthenium(II) complex AH076.

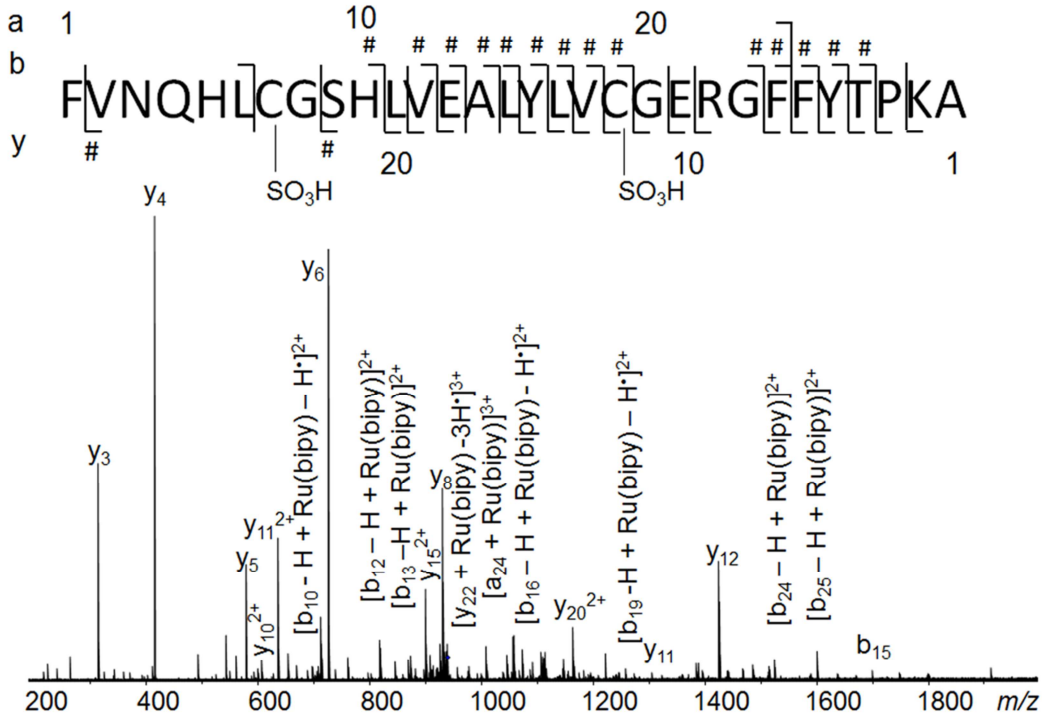

Figure 4.8: CAD spectrum of oxidised insulin B-chain after reaction with AH076, fragmented peak $[M+Ru(bipy)+2H]^{4+}$ at *m/z* 938.6; inset illustrates the fragments detected with # indicating a fragment containing ruthenium. A full list of peak assignments can be found in Table B-10 of Appendix B.

It can be seen that b-ions, starting at $b_{10,}$ contain ruthenium(II) and y-ions, up until y_{22}, do not, indicating that ruthenium(II) is bound within the part of the chain including Cys_7, Gly_8, Ser_9 and His_{10}. Since the b_6 ion was detected without ruthenium(II) bound, it minimises the possibility that His_5 is involved in binding. As the y_{22} does not include cysteine, it is proposed that His_{10} is the primary binding site, which is in agreement with Hong *et al.*[177] The importance of high mass accuracy in the assignment of the ruthenium(II)-containing fragments can be demonstrated by a peak at *m/z* 999.75. On first analysis, this was assigned as $[y_{24} + Ru(bipy) – OH]^{3+}$, which led to the unlikely implication that the ruthenium(II) could bind to cysteine

sulfonate, through displacement of the –OH group. This peak was assigned with a mass accuracy of 1.28 ppm which, although not unreasonable, is above average when examining all the other assignments. An alternative molecular formula was proposed in the form of $[a_{24} + Ru(bipy)]^{3+}$, which has an improved mass accuracy of -0.28 ppm and therefore can be assigned with a greater degree of confidence. The data does not indicate any other amino acids involved in binding, but an H• loss observed from the b-ions starting with b_{14} could indicate the involvement of glutamic acid, as was proposed for insulin. Glutamic acid binding was therefore investigated on a smaller scale using glutathione.

4.3.9 Reaction of Glutathione with AH076

Glutathione (GSH) is a tripeptide with sequence ECG, where glutamic acid and cysteine are connected through a gamma peptide linkage. GSH can be oxidised to form glutathione disulfide (GSSG), where two glutathione molecules are connected through a disulfide bond. The structures of both of these compounds are shown in Figure 4.8 and denoted (**1**) and (**2**) respectively. Compound AH076 was initially reacted with both GSH and GSSG in order to compare observations made for the binding sites in insulin. Figures 4.9(a) and (b) show the mass spectra obtained for the reactions of AH076 with GSH and GSSG respectively.

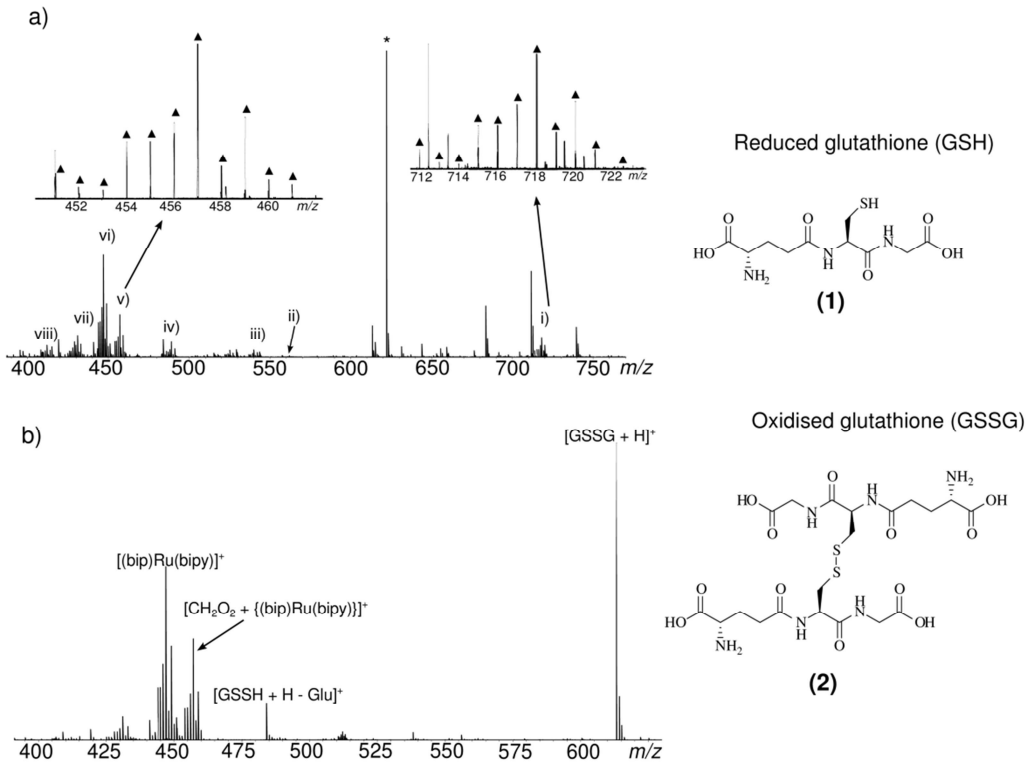

Figure 4.9: (a) reaction of glutathione (GSH) and AH076, with detected adducts containing ruthenium labelled i) – v), peaks labelled vi) - viii) are variations of complex AH076; * indicates an internal calibrant ion and ▲ indicates the isotope distributions of two of the adducts; (b) mass spectrum of the reaction between oxidised glutathione (GSSG) and AH076

As can be seen in Figure 4.9(a), on reaction of GSH with AH076, a number of ruthenium-containing adducts were detected, and these are summarised in Table 4.2.

Table 4.2: Ruthenium(II) adducts detected after reaction with glutathione (GSH)

Observed GSH–Ru adduct *m/z*	**Assignment**
(i) 718.12675	$[GSH + \{(bip)Ru(bipy)\} - H]^+$
(ii) 562.05797	$[GSH + (bip)Ru\} - H]^+$
(iii) 540.08508	$[Glu + \{(bip)Ru(bipy)\} - H^{\bullet} - H]^+$
(iv) 489.01624	$[Glu + Cys + Ru(bipy) - H^{\bullet} - H]^+$
(v) 457.04823	$[CH_2O_2 + \{(bip)Ru(bipy)\} - H]^+$

The adducts detected indicate, as was observed with angiotensin(II) and bombesin, that AH076 loses its ligands in different combinations. The major product detected was that at *m/z* 457.05 where the {(bip)Ru(bipy)} is bound to CH_2O_2 through loss of the chloride ligand. This is more likely to originate from the glutamic acid side chain than the C-terminus of the peptide, as a second adduct at *m/z* 540.08 was assigned as {(bip)Ru(bipy)} plus glutamic acid as a whole. This supports the observations of binding to glutamic acid, and potentially tyrosine, in insulin showing that in addition to nitrogen, ruthenium(II) has an affinity for –OH groups, with binding occurring through loss of $H^{\bullet}$. AH076 was also detected as Ru(bipy) bound to both glutamic acid and cysteine, indicating that with loss of the arene, ruthenium(II) is able to be coordinated by both amino acids.

Figure 4.8(B) shows the mass spectrum obtained after reaction between AH076 and oxidised glutathione (GSSG). This time, the sulfur atom of cysteine is in a disulfide bond, and so ruthenium(II) is unable to bind to the cysteine. The peak at *m/z* 613.16 corresponds to the unreacted oxidised glutathione, showing that the

majority is unable to react with the ruthenium(II). The major adduct observed is the same as for GSH, {(bip)Ru(bipy)} plus CH_2O_2; a peak at *m/z* 484.12 was also observed which corresponds to GSSG minus glutamic acid, supporting the conclusion that the CH_2O_2 originates from glutamic acid and not the C-terminus of the peptide.

In order to determine if AH076 could bind to cysteine when it is oxidised further to sulfonic acid, as was first thought with the oxidised insulin B-chain, glutathione was reacted with hydrogen peroxide in order to oxidise the cysteine side chain to sulfonic acid (Cys-SO_3H). The structure of this compound, (**3**), is shown in Figure 4.10 with the corresponding peaks detected in the mass spectra, showing the conversion of cysteine to the fully oxidised form.

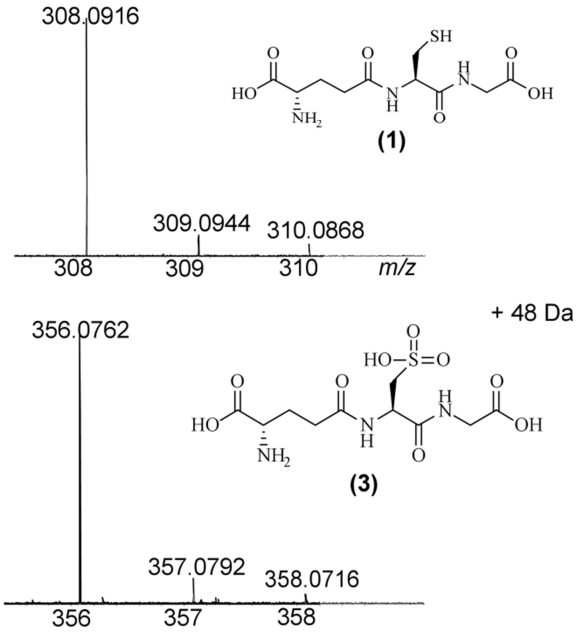

Figure 4.10: Oxidation of cysteine in GSH (**1**) to cysteine sulfonic acid (**3**); peaks at *m/z* 308.09 and 356.08 show the increase in 48 Da through addition of three oxygen atoms to the sulfur of cysteine

CAD was performed on glutathione both before and after reaction with H_2O_2 and determined that both the y_2 and b_2 fragments increase by 48 Da, showing the addition of three oxygen atoms to the sulfur of cysteine, forming cysteine sulfonic acid. Figure 4.11 shows the mass spectrum obtained after reaction between GSH (**3**) and AH076.

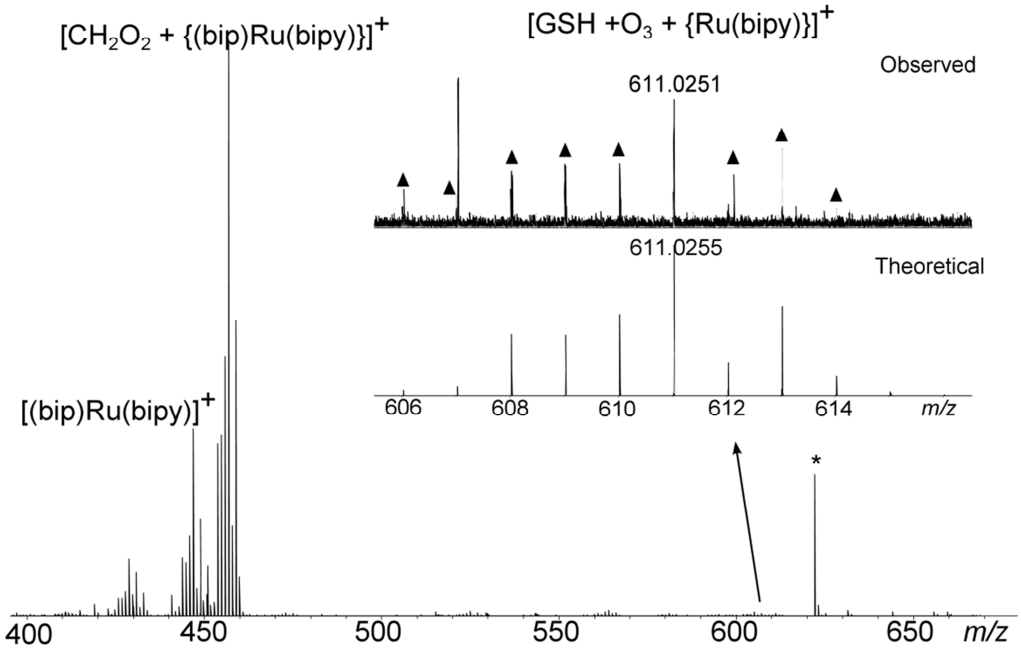

Figure 4.11: Mass spectrum of oxidised GSH (**3**) reacted with AH076; inset shows adduct at *m/z* 611.02 with ▲ indicating its isotope distribution as compared to the simulation. * indicates an internal calibrant ion

As before, the major adduct detected is the addition of CH_2O_2 to {(bip)Ru(bipy)}; however, a minor product was also observed at *m/z* 611.03, and was assigned as GSH (**3**) plus {Ru(bipy)} with a $2H^{\bullet}$ loss. Potentially, as a minor pathway, binding could occur through loss of the $H^{\bullet}$ from the –OH group of the sulfonic acid, as well

as from the –OH group of glutamic acid. This also indicates that ruthenium(II) is not binding to the oxidised cysteine through displacement of –OH, as was initially thought in the reaction with the oxidised insulin B-chain.

4.4 Conclusion

The products from reactions of two organometallic ruthenium(II) arene anticancer complexes has been investigated using FTICR mass spectrometry with the peptides angiotensin(II), bombesin, and glutathione, as well as insulin and the oxidised insulin B-chain. In particular, insights into ruthenium(II) binding sites have been gained using collision activated dissociation (CAD) and electron capture dissociation (ECD) to fragment the products. The amino acids primarily involved in coordination to ruthenium(II) have been identified as histidine, and methionine, with additional binding to arginine, phenylalanine, glutamic acid and, potentially, the nitrogen atoms of the backbone amides. Two different binding modes were assessed; at low ratios of ruthenium(II) to peptide, the ruthenium(II) compounds were observed to lose both the arene and the chloride ligands, providing the ruthenium with four possible binding sites. At higher ruthenium(II) to peptide ratios, an additional species was observed in which ruthenium(II) lost only its chloride ligand. Interestingly, ruthenium(II) appeared to preferentially coordinate to the phenylalanine residue of angiotensin(II) and not histidine as for the lower ratios; an observation that has been made for the first time. There was no evidence for the disruption of the disulfide bonds of insulin after reaction with ruthenium(II). Instead, the possible Ru(bipy) binding sites include histidine, glutamic acid, and tyrosine, which is in contrast to data obtained for cisplatin. Binding to His_{10} was further supported by reaction with the oxidised insulin B-chain, and binding to glutamic acid was investigated using

glutathione and its oxidised form, GSSG. The major product observed for both GSH and GSSG involved the addition of CH_2O_2 to {(bip)Ru(bipy)} indicating binding of ruthenium(II) to glutamic acid can occur. The use of high mass accuracy has been demonstrated in order to make peak assignments, and subsequently identify the binding sites of ruthenium(II) complexes, with a high degree of confidence.

Chapter 5: Further Applications of FTICR MS (ongoing project) - Analysis of Genuine and Counterfeit Vodka by FTICR-MS and GC-MS

5.1 Introduction

The incidence of counterfeit alcohol production is an increasing problem. An article in the Guardian newspaper published in February 2012, based on research conducted by the Institute of Engineering and Technology (IET), reported a 5-fold increase over a two year period. Vodka is one of the most commonly counterfeited spirits. It is produced through the fermentation and distillation of grain, followed by various filtering processes, such as through charcoal and carbon filters, to give it its characteristic neutral taste.[179] Illicit spirits can be produced by blending high quality distillates with ethanol from a cheaper raw material, adding synthetic volatile components to neutral alcohol, or through misleading labelling about the origin of the raw material; a common occurrence is for high quality alcohol to be replaced with a cheaper product. In some cases, industrial-strength alcohol has been detected, which has a high methanol content and can lead to severe health problems, and, in some cases, fatalities.[180]

The traditional approach to spirit authentication is to analyse the volatile components, particularly the products of the fermentation process known as congeners, which include fusel alcohols, fatty acids and their esters. Ethyl esters in particular contribute to the aroma and taste of alcohol, and are used to characterise whiskies, rums, and gins.[180] Analysis by gas chromatography is well reported for detecting differences in congener compositions between spirits;[181-189] however, in vodka, these compounds are only present in trace quantities,[190] making them difficult to detect. Therefore, efficient extraction techniques are first necessary to concentrate these compounds. Liquid-liquid extraction requires large volumes of sample and multiple extractions so is a laborious and time-consuming process. Solid phase

extraction (SPE) and solid phase micro extraction (SPME) are the preferred techniques;[191] SPME in particular is advantageous in terms of minimal sample preparation as a polymer coated silica fibre is used to sample the headspace and is therefore solvent-free.

Alternative techniques used to analyse vodka have also been investigated, including the use of conductivity measurements,[180] and ion chromatography.[192-193] Spirits are reduced to bottling strength with water. By detecting inorganic ions, such as chloride, nitrate, and phosphate, the ionic composition can be determined and matched to the quality of the product. Spectroscopic techniques are also developing considerably for the authentication of wine[194-196] and brandy,[194] through analysis of the sugar and ethanol contents and relating this specifically to origin. These analysis techniques are coupled with data analysis methods such as principal component analysis (PCA) so as to group the alcohols by differences in their chemical compositions.[196-197]

As yet, the use of high resolution mass spectrometry has not been explored as extensively for determining if a sample is counterfeit.[188, 198-199] Moller *et al*.[198] used ESI-MS to study the proof of origin of various whiskies and to identify specific chemical patterns, or fingerprinting mass spectra, that would indicate counterfeiting. This method is quicker to perform than GC-MS as there is no need for samples extraction and concentration;[200] however, GC is still suitable for analysis of low molecular weight, volatile compounds. A combination of these two techniques could potentially provide a powerful, accurate method for distinguishing counterfeit spirits from the genuine products. In this work, high resolution ESI-MS has been applied to distinguish counterfeit vodkas, in combination with method development for GC-MS to provide diagnostic ions and characteristic chemical patterns.

5.2 Experimental

5.2.1 Chemicals and Reagents

Genuine vodka samples were purchased from a local supermarket. Counterfeit vodka samples were provided by Worcestershire Scientific Services and West Yorkshire Scientific Services. Methanol, ethanol, hexane, and ammonium hydroxide were purchased from Fisher Scientific (Loughborough, UK).

5.2.2 Analysis by ESI-FTICR-MS

All vodka samples were diluted 1000-fold in 50% methanol, 50% Milli-Q water (Millipore Inc., Durham, UK) and 0.1% ammonium hydroxide and analysed directly in negative mode. The samples were analysed on a 12 T Bruker solariX FTICR mass spectrometer (Bruker Daltonics, Coventry, UK), using a nanospray ionization source. A positive voltage of 1000 V was applied to the capillary, a drying gas flow rate of 2.5 L min^{-1} and temperature of 180 ºC were used. Ions were accumulated for 0.01 s and 200 scans were recorded for each sample between *m/z* 95 and 2000. Trapping plate voltages of -0.5 V and -0.6 V were applied to the front and back plates respectively. Internal calibration was performed using the fatty acid/ester series, as highlighted in Table C-1, Appendix C. PCA analysis was performed using the using the software "Aabel", version 3.0.6, where the intensities of a selection of *m/z* values were used to create two principal components for each vodka sample (Table C-2, Appendix C).

5.2.3 Solid Phase Extraction (SPE)

The samples were prepared for analysis by GC-MS with solid phase extraction, using LiChrolut® EN (200 mg, 3 mL) SPE tubes (Merck Chemicals, Darmstadt, Germany). The tubes were washed with 2 mL of methanol followed by 2 mL of

ethanol/water (60:40). 2 mL of the vodka sample was applied to the tube and the compounds eluted with 1 mL of hexane which was analysed directly by GC-MS.

5.2.4 Analysis by GC-MS

The analysis was carried out in a Bruker Scion gas chromatograph (Bruker Daltonics, Coventry, UK) with a quadrupole mass spectrometer. 2 μL of the sample was injected with a split ratio of 1:5. The temperature of the injector was 250 ºC with helium as a carrier gas flowing at 1 mL min^{-1}, and the separation was performed using a Bruker BR-5ms fused silica column (15 m x 0.25 mm x 0.25 μm) with an oven temperature program of 50 ºC (2 minutes), ramping up to 290 ºC at a rate of 15 ºC/minute. The mass detector was operated in electron ionisation mode at 70 eV and scanned between *m/z* 50 and 300.

5.3 Results and Discussion

5.3.1 ESI-FTICR MS Analysis of Vodka

The vodka samples were analysed using negative mode FTICR mass spectrometry in order to examine the chemical pattern of the alcohols, and determine if differences could be observed between the genuine and counterfeit products. Since the major components of vodka used for authenticity analysis are fatty acids and their isomer ethyl esters, these were identified first and used as internal calibrants for each sample. Two different chemical patterns were observed for the vodka samples; most fell into the category represented by Figure 5.1(a), with a few resembling that shown in Figure 5.1(b).

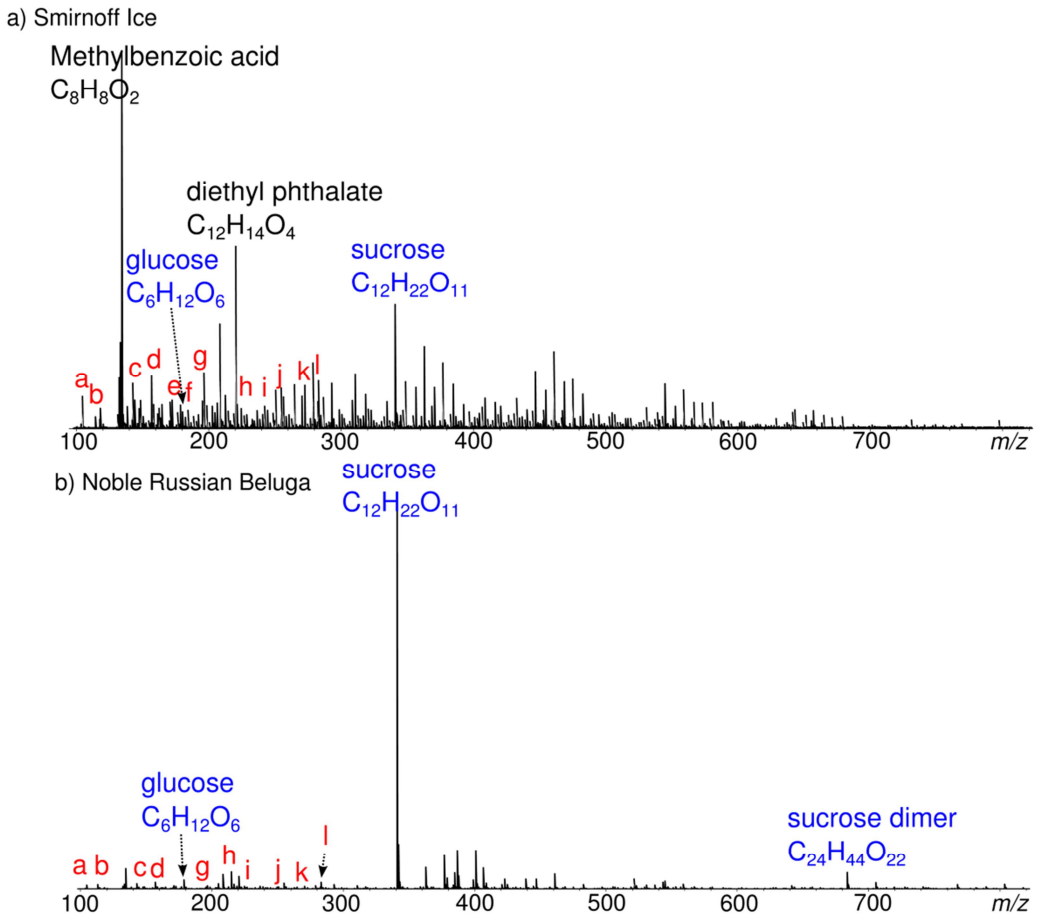

Figure 5.1: (a) (-)ESI mass spectrum of genuine Smirnoff Ice vodka, letters a-l represent fatty acid/ethyl ester compounds as listed in Table 5.1; (b) (-)ESI mass spectrum of genuine Noble Russian Beluga vodka

The mass spectra of the vodka samples represented by Figure 5.1(a) are dominated by a peak at *m/z* 135.08 which is assigned as 4-anisaldehyde ($C_8H_8O_2$). There are a large number of structures with this molecular formula, but this is proposed to be the most likely compound since it is a derivative of anethole, a flavouring compound that will be discussed later in the chapter. The other main peaks are assigned as fatty acids and/or esters, and are labelled in red. Since these compounds are isomers of each other, it is not possible to distinguish the fatty acid from the ester without

further analysis, but it is likely there is a mixture present. The assignments of these molecular formulae are shown in Table 5.1.

Table 5.1: Assignments of fatty acids/esters in vodka

Label	Observed *m/z*	Proposed Formula
a	101.06080	$C_5H_{10}O_2$
b	115.07645	$C_6H_{12}O_2$
c	143.10775	$C_8H_{16}O_2$
d	157.12340	$C_9H_{18}O_2$
e	171.13905	$C_{10}H_{20}O_2$
f	185.15470	$C_{11}H_{22}O_2$
g	199.17035	$C_{12}H_{24}O_2$
h	227.20165	$C_{14}H_{28}O_2$
i	241.21730	$C_{15}H_{30}O_2$
j	255.23295	$C_{16}H_{32}O_2$
k	269.24860	$C_{17}H_{34}O_2$
l	283.26425	$C_{18}H_{36}O_2$

The vodka samples represented by Figure 5.1(b) are dominated by a single peak at *m/z* 341, which is assigned as the sugar molecule sucrose. Assignments for as many peaks as possible between *m/z* 100 and 400 were made, in order to create a profile for each vodka sample in this region. The list of compounds assigned in this region can be found in Appendix C. Above this mass range, the compounds became harder to identify, since there were significantly more possibilities for each molecular formula even with a good internal calibration.

The MS profiles of the counterfeit samples do not appear to differ from the genuine products; however, subtle differences between the chemical profiles have been observed in the form of differing relative intensities of the key fatty acids/esters identified above, and a small number of flavouring compounds. Citric acid in particular was identified in most of the counterfeit samples, but not in any of the

genuine products. Figure 5.2 shows the ESI mass spectrum of a counterfeit vodka sample in which the intensity of the peak assigned as citric acid is significantly high.

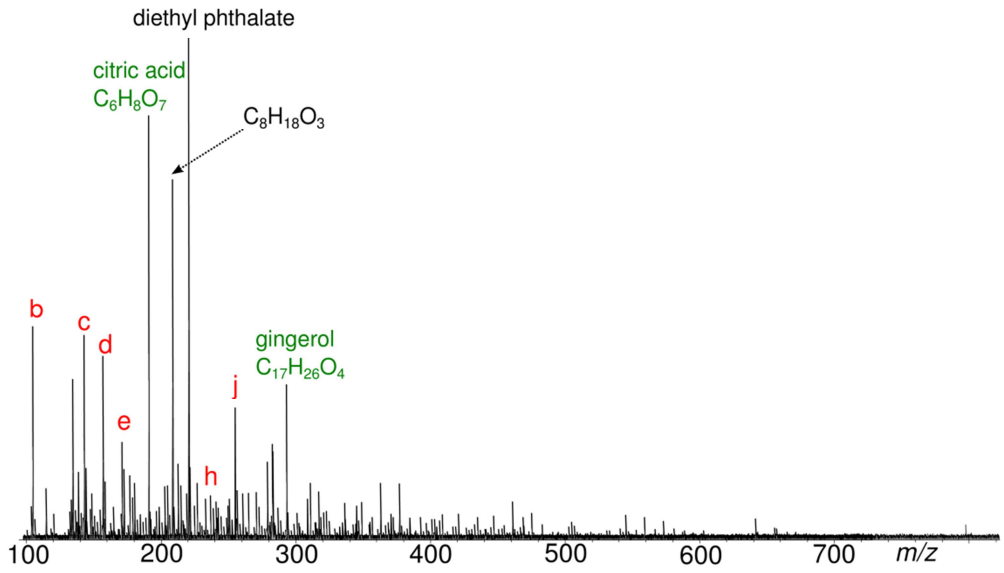

Figure 5.2: (-)ESI mass spectrum of a counterfeit vodka sample, highlighting citric acid and gingerol; letters in red indicate fatty acid/ester compounds

Citric acid is used as a flavouring and a food additive. It does not appear to be used in genuine vodka products, and, as such, could potentially be used as a marker for counterfeit samples. Another flavouring identified is that of gingerol. This compound is fairly intense in the sample shown in Figure 5.2, but it was also detected in all the vodka samples with a different relative intensity each time, so does not exclusively provide a marker for counterfeit products. The same was found for a third flavouring, vanillin, which was present in trace amounts in all of the vodka samples. This compound has been detected by GC-MS;[201] however, the low volatility of this compound makes the application of gas chromatography difficult and ESI-MS provides a better method of detection in this case.

Since the differences between genuine and counterfeit vodka samples are subtle, the full chemical profile analysed between *m/z* 100 and 400 were analysed using principal component analysis (PCA). PCA is a mathematical method used to identify groupings within data so should provide a simple way of determining differences between genuine and counterfeit vodka products.[202] The purpose of this method is to identify new variables, known as "principal components" (PCs), which account for most of the variability in the data. The first PC is computed as the direction through the data that describes the most variability; the second and subsequent PCs must be orthogonal to the previous PC and describe the remaining variability. Each sample is then given a score for each PC; scores are calculated from the original data multiplied by a coefficient that describes the PC. The scores for each PC are then plotted revealing any groupings between samples that were not obvious from the original data. In this work, the PCs were calculated from the identified *m/z* values for each vodka in the range 100-400, and the intensity of each identified peak. A full list of values for *m/z* and intensity for each sample can be found in appendix C, table C-1. The PCA plot for all 26 samples is shown in Figure 5.3.

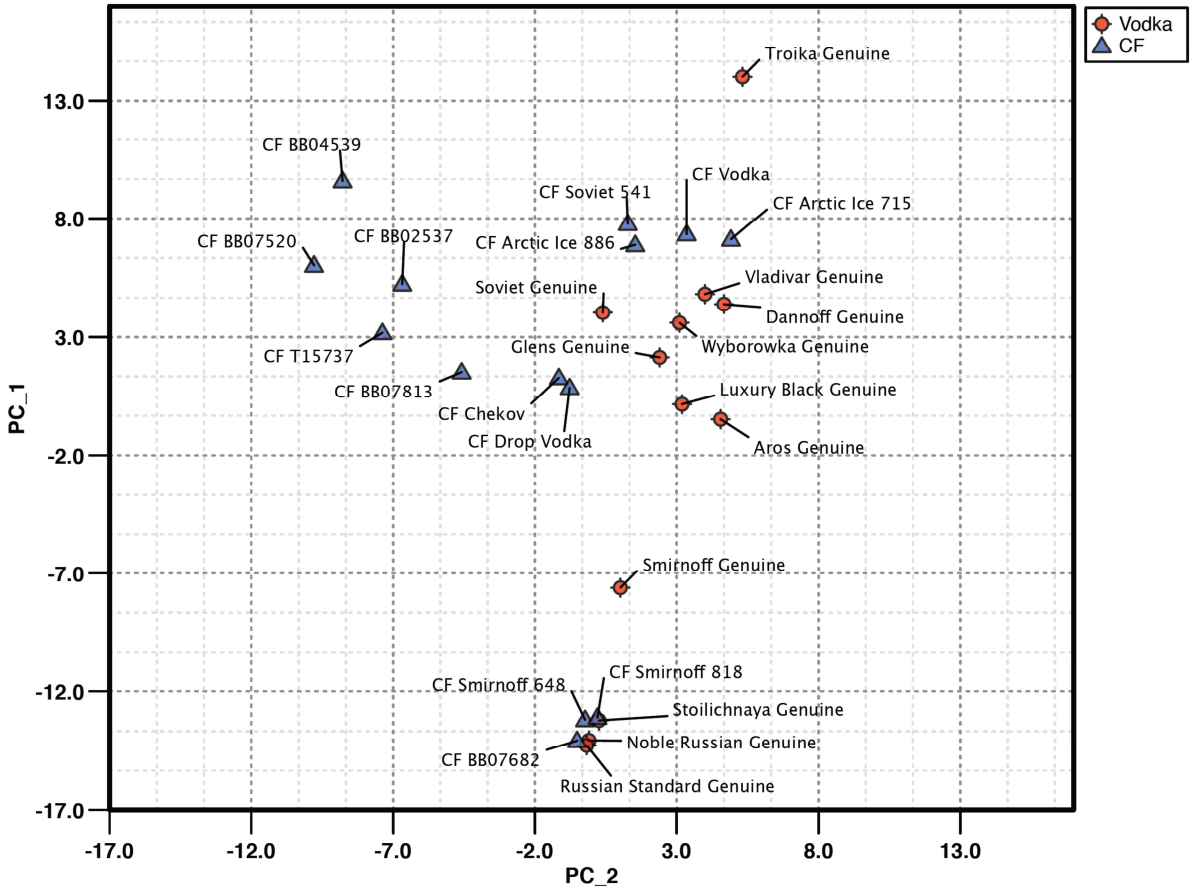

Figure 5.3: PCA plot of the ESI-MS data for each of the vodka samples, genuine samples are represented by a red diamond, counterfeit (CF) samples are represented by a blue triangle

The PCA plot does reveal groupings of the samples, with some significant distinction between genuine and counterfeit vodka products observed. There are two main groups of the genuine samples, reflecting the two chemical profiles observed in Figure 5.1. A couple of the samples, namely Smirnoff Ice and Troika, remain isolated from the others, reflecting further differences even within the genuine products. For the most part, the counterfeit samples are observed to lie separately from the genuine ones, showing that even with a small section of the chemical

profile of each vodka, differences are still detected. A few counterfeit samples are grouped with some of the genuine samples at the bottom of the plot. All of these vodkas had a chemical profile like that shown in Figure 5.1 (b), with a sucrose peak dominating the spectrum. This therefore makes it more difficult to identify counterfeit products since all other peaks are reduced significantly in intensity compared to this compound. In this case, liquid chromatography would be a useful technique to use in order to separate the signals for the different components that are suppressed by that of sucrose. This technique forms part of the further method development required in order to analyse the differences in genuine and counterfeit products, as discussed in the conclusion below.

A further interesting observation is that the PCA reflects, to some extent, the fact that the counterfeit samples were obtained from two different analytical companies located in different regions of the UK (Worcestershire and West Yorkshire). Five of the six samples with the codes starting "BB" and T1" lie to the left hand side of the plot away from the others, and these all originate from West Yorkshire. This observation has potential for locating the sources of counterfeit alcohol production since similarities should be observed between samples from the same batch as they will have been produced using the same method and with the same starting materials. The PCA plot, however, could change significantly by including more data so it is still necessary to identify compounds over the entire mass range, and use the entire chemical profile for detecting counterfeit products.

5.3.1 Analysis by GC-MS

A selection of the vodka samples were also analysed by GC-MS; however, due to the aqueous nature of the samples, as well as the need to pre-concentrate the volatile

components, a method involving solid phase extraction was first developed. The samples were extracted into hexane using SPE tubes and then analysed by GC-MS. In MS mode, fragmentation was performed using electron ionisation (EI) and the assignments made by matching to the NIST (National Institute of Standards and Technology) database. Figure 5.3 shows the chromatogram for a genuine sample of Smirnoff Ice vodka.

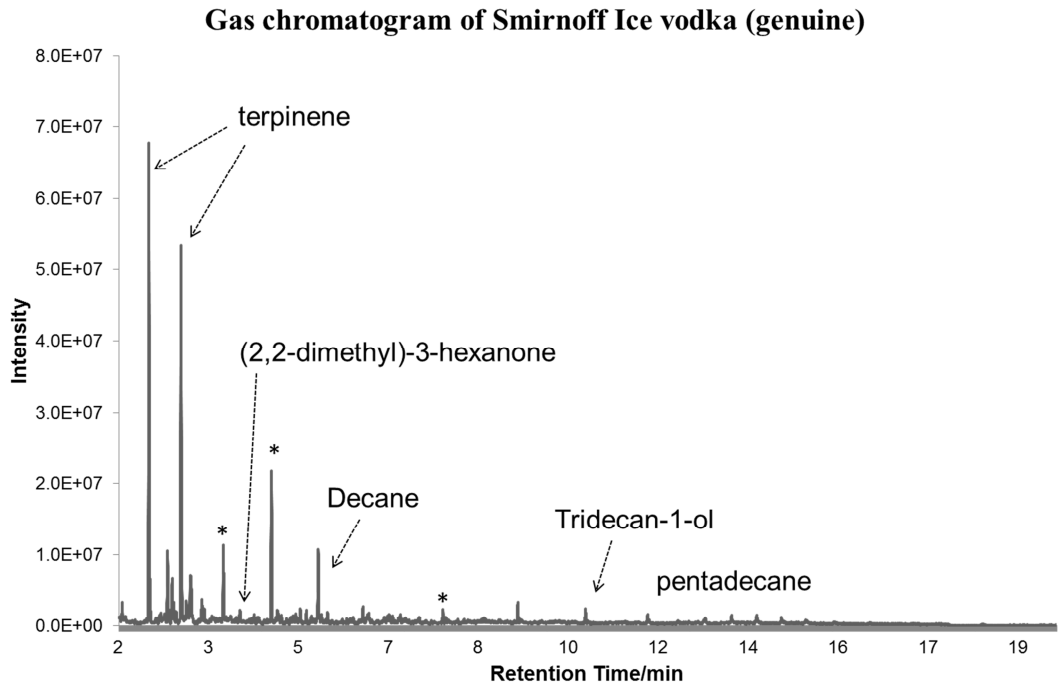

Figure 5.4: Gas chromatogram of genuine Smirnoff Ice vodka; * indicates long chain alkane compounds

The Figure shows the separation of a number of compounds; unfortunately the majority of these peaks were assigned as long chain alkanes such as decane and pentadecane. These compounds are unlikely to originate from the vodka; instead, it is likely they are from the SPE columns themselves and the hexane has stripped

these compounds from the packaging enabling them to be detected by GC-MS. A few useful compounds were identified in the chromatogram; terpinene is often used as a flavouring and constituted the most intense peaks in the spectrum. In order to determine if GC-MS could be used to identify compounds in the counterfeit samples, a counterfeit Smirnoff Ice sample was also analysed and the resulting spectrum is shown in Figure 5.5.

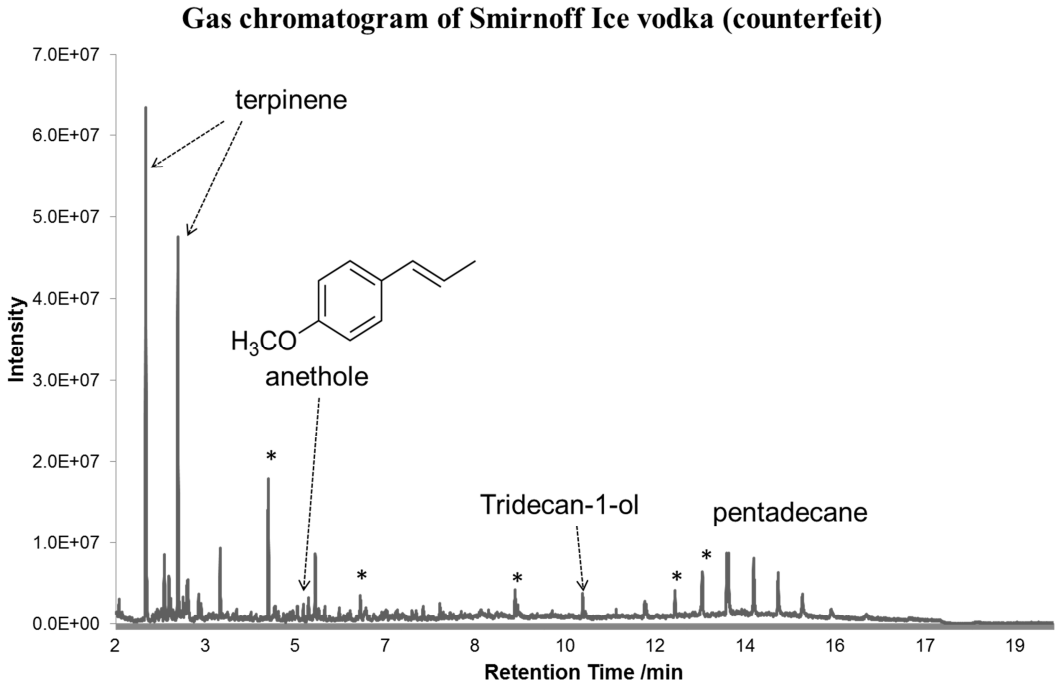

Figure 5.5: Gas chromatogram of counterfeit Smirnoff Ice vodka with structure of anethole shown; * indicates long chain alkane compounds

The chromatogram appears to be very similar to that of the genuine product, with the same long chain alkanes observed. One compound was assigned as anethole, which is also used as a flavouring, and was not observed in the genuine product. GC-MS has potential for identifying differences in the volatile, low molecular weight

components of vodka. However, an alternative sample preparation is first needed. SPME offers advantages over SPE,[179, 188] since it is used to sample the headspace, it is solvent-free and problems like that observed here, will be avoided. This will be a useful, complementary method to ESI-MS and should reveal more specific differences between genuine and counterfeit alcohol samples.

5.4 Conclusion and Future Work

Genuine and counterfeit vodka samples have been analysed by negative mode ESI mass spectrometry and GC-MS. The differences observed in the counterfeit samples arise through the addition of flavouring agents such as citric acid, a compound which is not present in any of the genuine vodka products. The low mass range (*m/z* 100-400) chemical profiles of 26 vodka samples were analysed and plotted using PCA in order to look for groupings in the data. The counterfeit samples were grouped separately for the most part; however, a selection of vodka samples contain mostly sucrose making all other compounds significantly less intense, and therefore distinguishing the counterfeit samples is more difficult. Further method development is required for these samples; in particular the use of reversed phase LC-MS should be explored in order to overcome the signal suppression observed in ESI-MS, and analyse the non-polar components of the vodka.

GC-MS was also used to analyse the samples; however, issues with sample preparation still need to be resolved. The use of a technique like SPME coupled with GC-MS would be ideal, as it would sample the headspace directly thereby detecting the volatile components without the need for any extraction techniques that could result in the loss of some compounds. This would therefore provide a further level

of analysis complementary to the chemical profiles obtained through ESI-MS. Additionally, the coupling of a GC to an FTICR mass spectrometer would take the existing analysis one step further since this coupling is achieved through the use of an atmospheric pressure chemical ionisation (APCI) source. In APCI ionisation, both protonated and radical species are formed enabling the detection of compounds that do not ionise easily by ESI and therefore providing another complementary technique for detailed analysis of these samples.

This initial work carried out shows that a combination of techniques involving GC and ESI-FTICR-MS show potential for providing a detailed analysis of alcohol samples with the aim of identifying counterfeit products. There are still significant method development steps that need to be explored since the current analyses on their own do not provide a definitive test for counterfeit vodka.

Chapter 6: Further Applications of FTICR MS (Ongoing Project) – Carbon Nanotubes as a Matrix Substitute in MALDI

6.1 Introduction

Since its development in the 1980s,[203] matrix-assisted laser desorption/ionisation (MALDI) mass spectrometry has proved to be an effective technique for the analysis of large molecules such as proteins[204] and polymers.[205] The analyte is mixed with a matrix, typically an organic acid such as as 2,5-dihydroxybenzoic acid (2,5-DHB), and irradiated with a laser. This method, however, is not ideal for the analysis of small (<1500 Da) molecules due to matrix interference effects, with the signal produced by the matrix and its clusters tending to dominate in this region of the mass spectrum. Furthermore, the matrix is co-crystallised with the analyte on the target plate, and can form an inhomogeneous layer resulting in the detection of "hot spots".[206] Consequently, matrix-free approaches are being investigated in order to expand the mass range of molecules for which MALDI is applicable.

Liquid matrices such as 3-nitrobenzyl alcohol (3-NBA) are an alternative[207] but issues with high chemical background noise have been encountered. The use of particles suspended in a liquid has turned out to be a more promising avenue of research. Tanaka *et al.*[12] developed an "ultra-fine metal plus liquid matrix" whereby cobalt particles were suspended in glycerol, and found to improve the detection of proteins with molecular weights up to 25 kDa. Alternative surfaces have been investigated, such as porous silicon, to trap the analytes before irradiation. This method is known as desorption ionisation on silicon (DIOS)[208] and was reported to effectively minimise matrix effects in MALDI spectra of peptides. Graphite particles suspended in glycerol have been successful for the analysis of proteins and peptides,[209-210] a method which is known as graphite surface-assisted laser desorption ionisation, or graphite SALDI.[209] Other SALDI materials investigated include silicon,[211] titanium,[212] carbon,[213] and electrospun nanofibres.[214]

Carbon nanotubes were first discovered in 1991[215] and have gained considerable interest in a number of applications including MALDI mass spectrometry.[216-218] Xu *et al.*[216] prepared carbon nanotubes as a particle suspension in a liquid matrix, as was reported with graphite,[209-210] and, after solvent evaporation, deposited peptide samples on top. Shin *et al.*[217] used vertically aligned carbon nanotube arrays grown on a stainless steel plate and applied the peptide samples directly. Both methods were reported to be efficient in the analysis of peptides, with good signal-to-noise ratios achieved, and low background noise observed. Chen *et al.*[218] used a citrate buffer to modify the surfaces of carbon nanotubes in order to provide a proton source for peptides, thereby reducing the intensity of alkali cation adducts which tend to dominate these spectra.

Carbon nanotubes can be arranged in a number of different geometries, including 3D forests,[219-220] which are investigated in this work. The potential advantages of using carbon nanotubes are that sample preparation is reduced, there is minimal interference from a matrix and, unlike DIOS, the samples have not been observed to degrade over time. Therefore, these materials show potential for the detection of small molecules where signal suppression due to the matrix is a significant problem.

6.2 Experimental

6.2.1 Chemicals and Reagents

PEG-1000 (polydispersity index 1.101), substance P (MW 1347.63 Da), 2,5-dihydroxybenzoic acid, and sodium hydroxide were purchased from Sigma Aldrich

(Gillingham, UK). Carbon nanotube forests were grown by chemical vapour deposition[219] and provided by the electrochemistry group, University of Warwick.

6.2.2 Analysis by MALDI-TOF Mass Spectrometry

2,5-dihydroxybenzoic acid, PEG-1000 and substance P were dissolved in Milli-Q water (Millipore, Durham, UK) at a concentration of 20 μM. Sodium hydroxide (10 mM) was added to produce sodium adducts of the analytes. The sample and matrix were mixed in a 1:1 ratio and 1 μL was deposited onto a MTP 384 ground steel MALDI plate (Bruker Daltonics, Coventry, UK) and dried in air. For analysis on nanotubes, 1 μL of the analyte was deposited directly onto the carbon nanotube forests and dried in air. The samples were analysed on a Bruker Ultraflex MALDI-TOF/TOF instrument (Bruker Daltonics, Coventry, UK) with a nitrogen laser (λ = 337 nm) at 50 Hz and 200 laser shots per spot. Source voltages of 25 kV and 21.5 kV were applied to the target plate and second voltage respectively, with 9 kV applied to the focusing lens. Delayed ion extraction of 10 ns was used with detection in reflectron mode between *m/z* 120-2000.

6.2.3 Analysis by FTICR Mass Spectrometry

The samples were prepared as described in section 6.2.2 and analysed using a Bruker solariX (Bruker Daltonics, Coventry, UK) with a Nd:YAG laser (λ = 355 nm). An offset of 100 V was applied to the target plate for analysis in positive mode. A dataset of 4 MW was recorded over *m/z* 300-5000, with an ion accumulation time of 5 seconds and 32 scans. A 2000 μm laser spot was used with 200 shots fired per scan. Trapping plate potentials of 0.4 and 0.3 V were applied to the front and back trapping plates respectively.

6.3 Results and Discussion

Samples of PEG-1000 and substance P were dissolved in water and mixed with the matrix 2,5-dihydroxybenzoic acid (DHB) and analysed by MALDI-TOF, as shown in Figure 6.1.

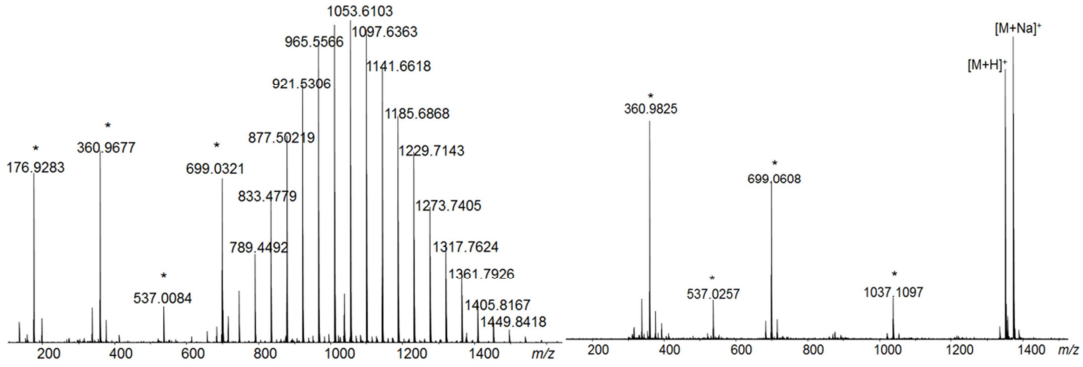

Figure 6.1: MALDI-TOF spectra of (a) PEG-1000 (Na^+ adduct) and (b) substance P (H^+ and Na^+ adducts) mixed with the matrix 2,5-DHB; * represents an unidentified peak. A full list of peak assignments can be found in Tables D-1 and D-2 of Appendix D

As shown in Figure 6.1, both samples can be observed by MALDI but there are a significant number of additional peaks observed particularly in the low molecular weight region below *m/*z 800. This is the region of the spectrum that suffers interference from the matrix and which is likely to be improved through the use of a matrix-free method. The same samples were deposited directly onto the carbon nanotubes and analysed by MALDI-TOF in order to determine if a signal could be detected. Figure 6.2 illustrates the spectra obtained for PEG-1000 (a), and substance P (b).

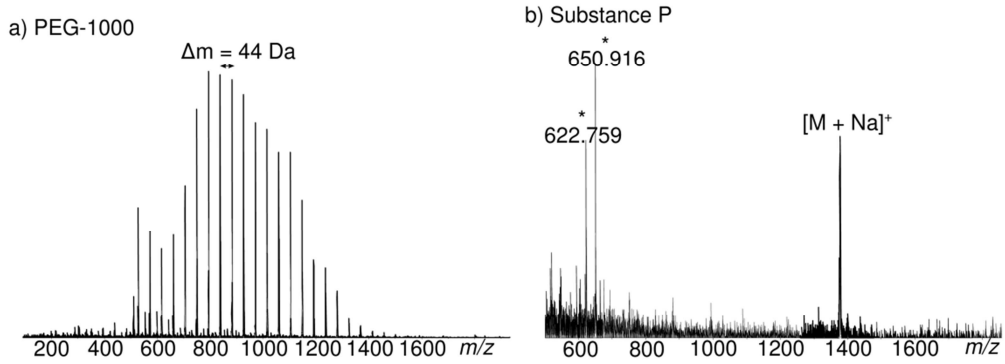

Figure 6.2: MALDI-TOF spectra of (a) PEG-1000 (Na^+ adducts), and (b) substance P (Na^+ adduct) deposited on carbon nanotube forests; * represents an unidentified peak

As shown in Figure 6.2, both compounds were detected using MALDI without a matrix, and through simple deposition of the samples onto the nanotubes. The signal for substance P was less intense than that of PEG, and showed some chemical noise in the lower *m/z* region which could not be identified. Both samples could only be observed when sodium was added to the samples; the protonated species were not detected. This is in agreement with Shin *et al.*[217] who reported the detection of sodium and potassium adducts but not the protonated form. The sensitivity specification of the Ultraflex instrument states a signal-to-noise ratio of 50:1 for 250 attomoles of a mass of 1570 Da in reflectron mode. Since the amount of substance P deposited on the plate is in the picomole region, the signal-to-noise observed should be significantly higher than this. A signal-to-noise ratio of 478.5 was observed with the matrix (i.e. in Figure 6.1b) but only a ratio of 78.9 was observed when detected off the nanotubes. On the other hand, the signal-to-noise ratios for PEG-1000 were

approximately equal. The efficiency of detection from the nanotubes therefore seems to be sample-dependent and will need to be investigated further.

The distribution of the PEG-1000 sample shown in Figure 6.2a is significantly distorted compared to that in Figure 6.1a. The *m/z* values are also different by 4 Da. A similar effect was also observed for substance P in that the expected *m/z* differed by about 6 Da. This is expected due to the fact that a different target plate had to be used for experiments involving the nanotubes. The nanotubes themselves are grown on a plate a few mm thick and this has to be attached to the plate for MALDI analysis. Since there is not room in the source of the MALDI-TOF instrument to accommodate the nanotubes on a standard MTP 384 MALDI plate, the samples were fastened to a plate that had grooves cut into it in which the nanotube samples could fit. This meant that the distance between the plate and the detector was different to that of the samples on the MTP 384 and, as a result, the time-of-flight, and consequently the *m/z* observed, changed significantly. Re-calibration of the instrument is therefore necessary for use of the nanotube samples, and should improve the distribution of the polymer spectra.

Signal detection appears to be affected by the density of the carbon nanotube forests. Shin *et al.*[217] showed that with vertically aligned nanotubes, a signal could not be obtained when the density of the packing was increased. The results in Figure 6.2 are from a low density nanotube forest, so, in order to compare results, a relatively higher density nanotube forest was also used and Figure 6.3 shows the spectrum obtained for PEG.

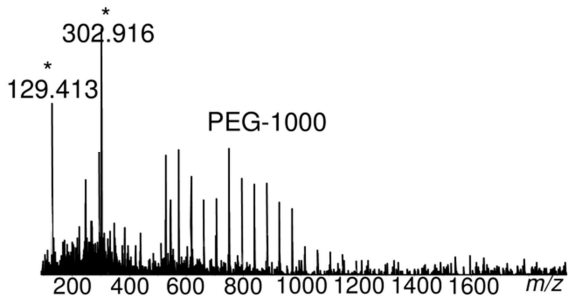

Figure 6.3: MALDI-TOF spectrum of PEG deposited on a high density carbon nanotube forest; * represents unidentified peaks

As shown in Figure 6.3, the signal for PEG is a lot lower with a signal-to-noise ratio of 43.5, and several unidentified peaks are present in the low *m/z* region of the spectrum. This is consistent with previous results from Shin, and is proposed to be due to enhanced cooling of the nanotube tips through more dense packing, thus decreasing desorption of the sample from the surface.[217]

Since a signal was detected for both samples on a TOF instrument, the same samples were analysed using MALDI-FTICR mass spectrometry. Figure 6.4 shows the spectrum obtained for PEG on a low density carbon nanotube forest.

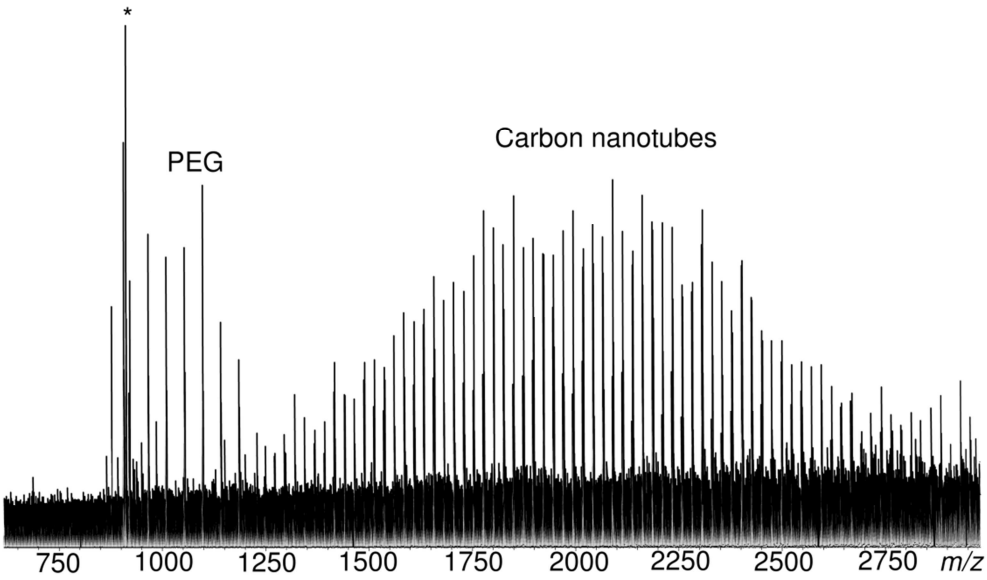

Figure 6.4: MALDI-FTICR mass spectrum of PEG-1000 deposited on a carbon nanotube forest; * represents an unidentified peak

When analysed by FTICR mass spectrometry, a carbon nanotube distribution was observed over a large mass region. PEG could be detected but the signal of both distributions was weak as a low laser power was used. As the laser power was increased, the PEG distribution disappeared entirely and the signal from the carbon nanotubes became more intense, as shown in Figure 6.5.

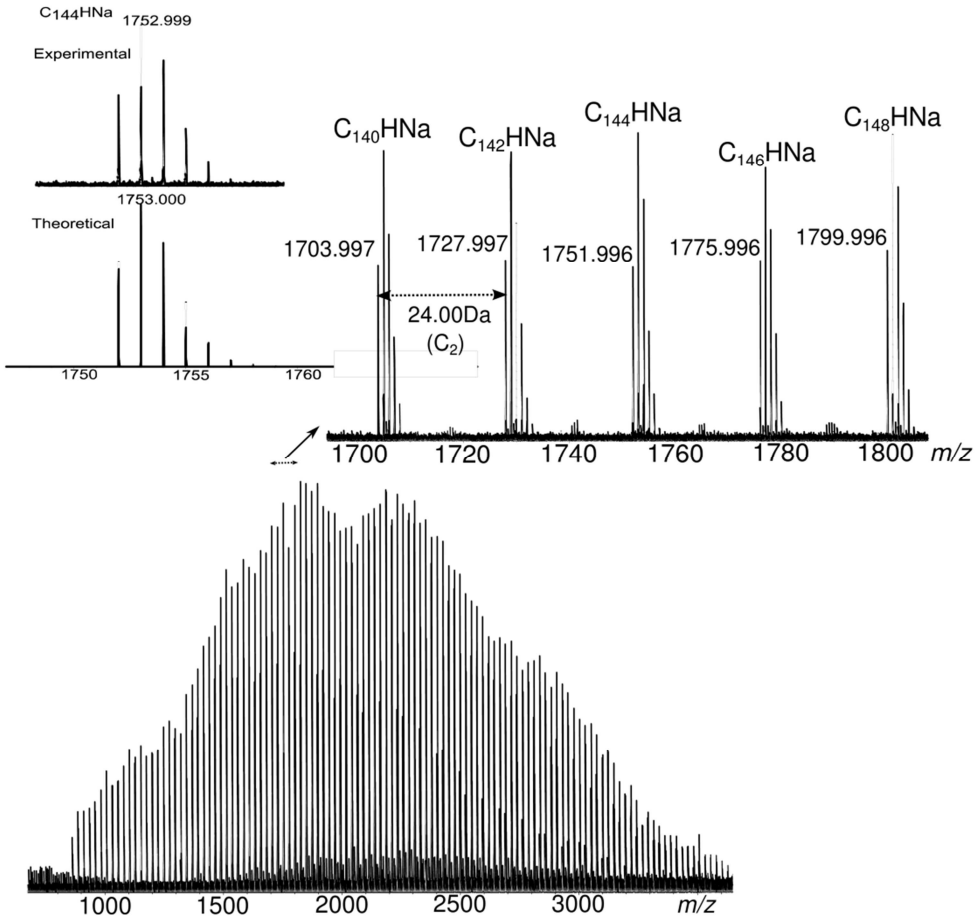

Figure 6.5: MALDI-FTICR mass spectrum showing carbon nanotube distribution; inset (right) proposes molecular formulae for a selection of peaks, showing difference of C_2 between adjacent peaks and addition of sodium adducts; inset (left) shows a comparison between the experimental and theoretical isotope distributions of the assigned peak at *m/z* 1751.99

On analysis of the spectrum, differences of 24.00 Da were observed between adjacent isotope distributions showing the addition of C_2 each time. The molecular formulae for the peaks show a carbon series, increasing by two carbon atoms each time, with one hydrogen and one sodium atom attached. It is therefore likely that the addition of sodium to the samples promotes the formation of adducts with the

nanotubes as well, thereby enabling their detection in the instrument instead of the samples. This nanotube distribution was observed in every spectrum; PEG could only just be observed at low laser powers, as shown in Figure 6.4, but substance P was not detected at all. The two instruments use different lasers for MALDI – the TOF has a nitrogen laser, and the FTICR has a Nd:YAG laser. The difference in the wavelength of these lasers may be the reason why the nanotubes are only observed in FTICR spectra.

The detection of carbon nanotubes has been observed before,[214] and the use of glycerol has been suggested to prevent detachment of the nanotubes from a target plate. However, glycerol and its associated adducts have also been detected in the low mass region of the spectrum,[209-210] so it is not ideal for producing matrix-free spectra. An alternative approach that has been investigated is the modification of the surface of carbon nanotubes in suspension, through oxidation and chemical functionalization so as to introduce carboxyl groups onto the nanotube surface.[218, 221-222] The presence of these functional groups improves the solubility of the nanotubes in water, and therefore enables a more homogeneous layer to be deposited onto the target plate. Surface modifications also enable the carbon nanotubes to act as a proton source, thereby reducing cation adducts and increasing the range of samples for which they may be suitable. Therefore, in order to minimise the detection of carbon nanotube distributions in MALDI spectra, additional sample preparation is first required.

6.4 Conclusion

Carbon nanotubes have shown potential as a substitute for a matrix in MALDI. A good signal was observed for both PEG and substance P, deposited onto a low density carbon nanotube forest, when analysed on a TOF instrument. A higher density nanotube forest reduced the signal intensity, potentially due to enhanced cooling through closer packing, resulting in decreased desorption of the analyte. Analysis using FTICR mass spectrometry resulted in the detection of a sodium adduct distribution of the nanotubes themselves. PEG could be detected at low laser powers but the large mass range covered by the nanotube distribution suppresses the signal of peptides like substance P. Modification of the carbon nanotube surfaces is one possible approach to preventing the nanotubes from being detected in the MALDI mass spectra, as well as providing a proton source for compounds. This would need to be investigated before analysis of other samples can be completed due to the interference of the nanotube distribution in the spectra.

Chapter 7: Conclusions and Future Work

7.1 Conclusions

This thesis contains a number of different analytical applications of Fourier transform ion cyclotron resonance mass spectrometry. The main applications chapters demonstrate the role FTICR mass spectrometry can play in biological applications, namely natural product structure characterisation and identifying the binding sites of anticancer drugs on proteins, due to the high mass accuracies possible.

Natural products, particularly polyketides and non-ribosomal peptides, are becoming increasingly important as sources of clinical drugs, and efficient methods for their structural characterisation are essential. This work has demonstrated the combined use of two tandem mass spectrometry techniques, one of which is unique to FTICR, to provide detailed, complementary structural information on examples of these classes of compounds. In particular, the use of CAD and EID in multistage mass spectrometry has been shown to be effective in distinguishing between two polyketide isomers, lasalocid A and iso-lasalocid A, which is necessary to elucidate the biosynthetic pathways of these compounds. This method has started to be applied to identifying intermediate structures in the biosynthesis process, but developments in sample preparation are necessary to improve signal intensities for tandem mass spectrometry experiments, before they can be implemented. The use of CAD and EID has also been applied to non-ribosomal peptides; EID in particular was found to be useful in providing detailed structural information on the compound actinomycin D. Multiple ion isolation was investigated in order to provide an accurate internal calibration for the fragment ions produced by EID; in doing so, the use of in-cell isolation proved to increase the intensities of the product ions, enabling many more fragments to be detected than with external isolation. The combination

of CAD, EID, and multiple ion isolation has therefore been developed as a method for providing detailed, complementary, accurately calibrated structural information for natural products.

The identification of anticancer drug binding sites on proteins is essential for understanding the mode of action of these drugs, as well as investigating potential side effects these compounds may cause. The use of high mass accuracy tandem mass spectrometry has shown to provide insights into the binding of potential ruthenium(II) arene anticancer complexes, by studying their interaction with peptides and proteins. In this case, CAD alone was used to determine the binding sites, as ECD, in most cases, resulted in capture of an electron at the ruthenium metal and caused cleavage of the complex from the peptide. Peptide binding of two ruthenium(II) complexes revealed binding at histidine and methionine; an observation that was expected based on previous work. However, binding at phenylalanine and glutamic acid was also observed here for the first time. Binding to insulin and the oxidised insulin B-chain supported evidence of histidine binding, with glutamic acid binding being investigated further by reaction with glutathione. This project in particular demonstrated the need for sub-ppm mass accuracy when identifying molecular formulae. An assignment made with a mass accuracy above 1 ppm indicated potential binding to cysteine sulfonic acid, which is an unlikely occurrence. Re-assignment of this peak revealed an a-ion with a mass accuracy below 1 ppm, indicating this is the more likely of the two. Instruments which can only achieve 1 ppm mass accuracy would not have made this distinction, therefore demonstrating how FTICR is a powerful analytical tool in biological applications.

Two further applications of FTICR mass spectrometry have also been investigated and are ongoing projects. First, the use of FTICR mass spectrometry

and GC-MS have been used for identifying differences in genuine and counterfeit vodkas. The negative mode ESI mass spectra were obtained and the chemical profiles analysed between *m/z* 100 and 400. PCA was used to look for groupings of the samples; for the most part, the counterfeit samples were grouped separately to the genuine products. The main differences between the samples arise from the addition of flavouring agents; citric acid was detected in most of the counterfeit samples, but not in any of the genuine products showing its potential as a marker for identifying counterfeit vodka. GC-MS was also used to investigate differences in the volatile components of the vodkas; however, improved sample preparation techniques are first needed, such as the use of solid phase microextraction. The flavouring compound anethole was observed in the gas chromatogram of a counterfeit sample and not in the genuine product, which again may be a potential marker for detecting illicit vodka.

The second ongoing project investigated carbon nanotubes as a substitute for a matrix in MALDI, in order to minimise matrix interference effects commonly observed in the low mass region. PEG and substance P were successfully detected on a MALDI-TOF instrument; analysis by FTICR resulted in the observation of a strong signal belonging to the carbon nanotubes themselves. There are various approaches reported for preventing detection of the nanotubes, most successful of which appears to be modification of the carbon surface through oxidation. Investigation into this is outside the scope of this project; however, carbon nanotubes do show potential in MALDI analysis.

Overall, the importance of high mass accuracy has been demonstrated in this work in the design and implementation of tandem mass spectrometry methods for structure characterisation and binding site identification. Improvements in

FTICR instrumentation will ensure high mass accuracies are routinely achieved, which should see this technique continue to play an important role in analytical applications in the future.

7.2 Future Work

7.2.1 Natural Product Analysis

A method involving the use of high mass accuracy tandem mass spectrometry, specifically the techniques of CAD and EID, has been developed to characterise the structures of natural products. The ultimate goal is to apply this method to characterise the structures of intermediates formed throughout the biosynthetic pathway of polyketides, such as lasalocid A, and non-ribosomal peptides, such as actinomycin D. As yet, the intermediates captured are not present in sufficient abundances for this method to work successfully, so further sample preparation steps are first required. This will involve purification and separation of the crude cell extract mixtures which contain the intermediate structures, so may involve the use of liquid chromatography coupled with FTICR mass spectrometry in order to increase the abundance of the compounds. Once this has been achieved, this method can be applied to characterising these structures and elucidating the biosynthetic processes involved.

7.2.2 Drug Binding Site Analysis

The use of high mass accuracy tandem mass spectrometry has been applied to successfully identify the binding sites of ruthenium anticancer drugs on peptides and proteins. These preliminary experiments can be scaled up so that ultimately, the mechanisms and modes of action of these compounds in vivo can be understood.

The two ruthenium complexes studied here are two of several complexes that have been synthesised and exhibit anticancer activity, and consist of different arene and chelating ligands attached to the ruthenium. The observed loss of the arene in this work can be investigated further so that the effect different ligands have on the observed peptide and protein binding can be studied. Since these experiments have involved peptides and small proteins, the use of liquid chromatography coupled to FTICR mass spectrometry should be investigated for the elucidation of binding sites on much larger proteins, where a bottom-up proteomics approach may be necessary.

7.2.3 Counterfeit Vodka Analysis

The use of ESI-FTICR-MS and gas chromatography to identify counterfeit samples showed potential but there are a number of alternative analysis techniques and sample preparation steps that need to be explored first, in order to optimise the developing method. Solid phase extraction resulted in detection of long chain alkanes from the tubes themselves. A more efficient method to use would be that of solid phase micro extraction (SPME) whereby the headspace is sampled to analyse the volatile components directly. Additional analysis with LC-MS would overcome the signal suppression observed in the ESI-FTICR-MS analysis of some vodka samples which contained high levels of sucrose. Combining gas chromatography with FTICR mass spectrometry has also started to be investigated. The GC can be coupled to an atmospheric pressure chemical ionisation (APCI) source and used to analyse the vodka samples by GC-APCI-FTICR mass spectrometry. This technique is not widely used and may be a more efficient method for combining the separation of GC with the high resolving power and mass accuracy of FTICR mass spectrometry to identify counterfeit spirits.

7.2.4 Carbon Nanotubes in MALDI

Mass spectra of small molecules using carbon nanotubes as a matrix substitute were observed; however, serious contamination from the nanotubes themselves was encountered. Methods to improve the spectra have already been reported in the literature but these mainly involve the modification of the nanotubes through oxidation and chemical functionalization. This route could be explored in order to achieve MALDI-FTICR spectra without the use of a matrix.

Bibliography

1. Comisarow, M. B.; Marshall, A. G., Fourier transform ion cyclotron resonance spectroscopy. *Chem. Phys. Lett.* **1974,** *25*, 282-283.

2. Yamashita, M.; Fenn, J. B., Electrospray ion source. Another variation on the free-jet theme. *J. Phys. Chem.* **1984,** *88*, 4451-4459.

3. Fenn, J. B.; Mann, M.; Meng, C. K.; Wong, S. F.; Whitehouse, C. M., Electrospray ionization for mass spectrometry of large biomolecules. *Science* **1989,** *246*, 64-71.

4. Dole, M.; Mack, L.; Hines, R.; Mobley, R.; Ferguson, L.; Alice, M., Molecular beams of macroions. *J. Chem. Phys.* **1968,** *49*, 2240.

5. Loo, J. A., Studying noncovalent protein complexes by electrospray ionization mass spectrometry. *Mass Spectrom. Rev.* **1997,** *16*, 1-23.

6. Gaskell, S. J., Electrospray: principles and practice. *J. Mass Spectrom.* **1997,** *32*, 677-688.

7. Crotti, S.; Seraglia, R.; Traldi, P., Some thoughts on electrospray ionization mechanisms. *Eur. J. Mass Spectrom.* **2011,** *17*, 85-99.

8. Thomson, B.; Iribarne, J., Field induced ion evaporation from liquid surfaces at atmospheric pressure. *J. Chem. Phys.* **1979,** *71*, 4451.

9. Fenn, J., Ion formation from charged droplets: Roles of geometry, energy, and time. *J. Am. Soc. Mass Spectrom.* **1993,** *4*, 524-535.

10. Konermann, L.; Ahadi, E.; Rodriguez, A. D.; Vahidi, S., Unraveling the mechanism of electrospray ionization. *Anal. Chem.* **2012,** *85*, 2-9.

11. Wilm, M.; Mann, M., Analytical properties of the nanoelectrospray ion source. *Anal. Chem.* **1996,** *68*, 1-8.

12. Tanaka, K.; Waki, H.; Ido, Y.; Akita, S.; Yoshida, Y.; Yoshida, T.; Matsuo, T., Protein and polymer analyses up to m/z 100 000 by laser ionization time-of-flight mass spectrometry. *Rapid Commun. Mass Spectrom.* **1988,** *2*, 151-153.

13. Karas, M.; Bachmann, D.; Bahr, U.; Hillenkamp, F., Matrix-assisted ultraviolet laser desorption of non-volatile compounds. *Int. J. Mass Spectrom. Ion Processes* **1987,** *78*, 53-68.

14. Karas, M.; Krüger, R., Ion formation in MALDI: The cluster ionization mechanism. *Chem. Rev.* **2003,** *103*, 427-440.

15. Karas, M.; Glückmann, M.; Schäfer, J., Ionization in matrix-assisted laser desorption/ionization: singly charged molecular ions are the lucky survivors. *J. Mass Spectrom.* **2000,** *35*, 1-12.

16. Jaskolla, T.; Karas, M., Compelling evidence for Lucky Survivor and gas phase protonation: the unified MALDI analyte protonation mechanism. *J. Am. Soc. Mass Spectrom.* **2011,** *22*, 976-988.

17. de Hoffmann, E. a. S., V., *Mass spectrometry: principles and applications*. Second ed.; Wiley: 2002.

18. McLafferty, F. W., *Interpretation of mass spectra*. University Science Books: 1993.

19. Gross, J. H., *Mass spectrometry*. Wiley Online Library: 2004.

20. Brenton, A. G.; Godfrey, A. R., Accurate mass measurement: Terminology and treatment of data. *J. Am. Soc. Mass Spectrom.* **2010,** *21*, 1821-1835.

21. Mathieu, É., Mémoire sur le mouvement vibratoire d'une membrane de forme elliptique. *Journal de mathématiques pures et appliquées* **1868**, 137-203.

22. March, R. E., An introduction to quadrupole ion trap mass spectrometry. *J. Mass Spectrom.* **1997,** *32*, 351-369.

23. Douglas, D. J.; Frank, A. J.; Mao, D., Linear ion traps in mass spectrometry. *Mass Spectrom. Rev.* **2005,** *24*, 1-29.

24. Paul, W., Electromagnetic traps for charged and neutral particles (Nobel lecture). *Angew. Chem. Int. Ed. (English)* **1990,** *29*, 739-748.

25. Hu, Q.; Noll, R. J.; Li, H.; Makarov, A.; Hardman, M.; Graham Cooks, R., The Orbitrap: a new mass spectrometer. *J. Mass Spectrom.* **2005,** *40*, 430-443.

26. Scigelova, M.; Makarov, A., Orbitrap mass analyzer – Overview and applications in proteomics. *Proteomics* **2006,** *6*, 16-21.

27. Wolff, M.; Stephens, W., A pulsed mass spectrometer with time dispersion. *Rev. Sci. Instrum.* **1953,** *24*, 616.

28. Mamyrin, B.; Karataev, V.; Shmikk, D.; Zagulin, V., The mass-reflectron, a new non-magnetic time-of-flight mass spectrometer with high resolution. *Zh. Eksp. Teor. Fiz* **1973,** *64*, 82-89.

29. Vestal, M. L.; Juhasz, P.; Martin, S. A., Delayed extraction matrix-assisted laser desorption time-of-flight mass spectrometry. *Rapid Commun. Mass Spectrom.* **1995,** *9*, 1044-1050.

30. Brown, R. S.; Lennon, J. J., Mass resolution improvement by incorporation of pulsed ion extraction in a matrix-assisted laser desorption/ionization linear time-of-flight mass spectrometer. *Anal. Chem.* **1995,** *67*, 1998-2003.

31. Amster, I. J., Fourier transform mass spectrometry. *J. Mass Spectrom.* **1996,** *31*, 1325-1337.

32. Comisarow, M., Cubic trap. *Adv. Mass Spectrom* **1980,** *8*, 1698.

33. Guan, S.; Marshall, A. G., Ion traps for Fourier transform ion cyclotron resonance mass spectrometry: principles and design of geometric and electric configurations. *Int. J. Mass Spectrom. Ion Processes* **1995,** *146–147*, 261-296.

34. Gabrielse, G.; Haarsma, L.; Rolston, S. L., Open-endcap penning traps for high-precision experiments. *Int. J. Mass Spectrom. Ion Processes* **1989,** *88*, 319-332.

35. Caravatti, P.; Allemann, M., The 'Infinity cell': A new trapped-ion cell with radiofrequency covered trapping electrodes for Fourier transform ion cyclotron resonance mass spectrometry. *Org. Mass Spectrom.* **1991,** *26*, 514-518.

36. Rempel, D.; Grese, R.; Gross, M., A scaling technique for studying the dynamics of high mass ions in Fourier transform mass spectrometry: a preliminary report. *Int. J. Mass Spectrom. Ion Processes* **1990,** *100*, 381-395.

37. Tolmachev, A. V.; Robinson, E. W.; Wu, S.; Kang, H.; Lourette, N. M.; Pasa-Tolic, L.; Smith, R. D., Trapped-ion cell with improved DC potential harmonicity for FT-ICR MS. *J. Am. Soc. Mass Spectrom.* **2008,** *19*, 586-597.

38. Brustkern, A. M.; Rempel, D. L.; Gross, M. L., An electrically compensated trap designed to eighth order for FT-ICR mass Spectrometry. *J. Am. Soc. Mass Spectrom.* **2008,** *19*, 1281-1285.

39. Nikolaev, E. N.; Boldin, I. A.; Jertz, R.; Baykut, G., Initial experimental characterization of a new ultra-high resolution FTICR cell with dynamic harmonization. *J. Am. Soc. Mass Spectrom.* **2011,** *22*, 1125-1133.

40. Marshall, A. G.; Wang, T. C. L.; Ricca, T. L., Tailored excitation for Fourier transform ion cyclotron mass spectrometry. *J. Am. Chem. Soc.* **1985,** *107*, 7893-7897.

41. O'Connor, P. B.; Speir, J. P.; Senko, M. W.; Little, D. P.; McLafferty, F. W., Tandem mass spectrometry of carbonic anhydrase (29 kDa). *J. Mass Spectrom.* **1995,** *30*, 88-93.

42. O'Connor, P. B.; McLafferty, F. W., High-resolution ion isolation with the ion cyclotron resonance capacitively coupled open cell. *J. Am. Soc. Mass Spectrom.* **1995,** *6,* 533-535.

43. Wu, Q., Multistage accurate mass spectrometry: A "Basket in a Basket" approach for structure elucidation and its application to a compound from combinatorial synthesis. *Anal. Chem.* **1998,** *70,* 865-872.

44. de Koning, L. J.; Nibbering, N. M. M.; van Orden, S. L.; Laukien, F. H., Mass selection of ions in a Fourier transform ion cyclotron resonance trap using correlated harmonic excitation fields (CHEF). *Int. J. Mass Spectrom. Ion Processes* **1997,** *165–166,* 209-219.

45. Kruppa, G.; Schnier, P. D.; Tabei, K.; Van Orden, S.; Siegel, M. M., Multiple ion isolation applications in FT-ICR MS: Exact-mass MSn internal calibration and purification/interrogation of protein−drug complexes. *Anal. Chem.* **2002,** *74,* 3877-3886.

46. Aarstol, M.; Comisarow, M. B., Apodization of FT-ICR spectra. *Int. J. Mass Spectrom. Ion Processes* **1987,** *76,* 287-297.

47. Marshall, A. G.; Verdun, F. R., *Fourier transforms in NMR, optical, and mass spectrometry*. Elsevier: 1989.

48. Qi, Y.; Li, H.; Wills, R.; Perez-Hurtado, P.; Yu, X.; Kilgour, D. A.; Barrow, M.; Lin, C.; O'Connor, P., Absorption-mode Fourier transform mass spectrometry: The effects of apodization and phasing on modified protein spectra. *J. Am. Soc. Mass Spectrom.* **2013,** *24,* 828-834.

49. Barrow, M. P.; Burkitt, W. I.; Derrick, P. J., Principles of Fourier transform ion cyclotron resonance mass spectrometry and its application in structural biology. *Analyst* **2005,** *130,* 18-28.

50. Kaiser, N.; Quinn, J.; Blakney, G.; Hendrickson, C.; Marshall, A., A novel 9.4 Tesla FTICR mass spectrometer with improved sensitivity, mass resolution, and mass range. *J. Am. Soc. Mass Spectrom.* **2011,** *22*, 1343-1351.

51. Schaub, T. M.; Hendrickson, C. L.; Horning, S.; Quinn, J. P.; Senko, M. W.; Marshall, A. G., High-performance mass spectrometry: Fourier transform ion cyclotron resonance at 14.5 Tesla. *Anal. Chem.* **2008,** *80*, 3985-3990.

52. Marshall, A. G., Milestones in fourier transform ion cyclotron resonance mass spectrometry technique development. *Int. J. Mass Spectrom.* **2000,** *200*, 331-356.

53. Senko, M. W.; Speir, J. P.; McLafferty, F. W., Collisional activation of large multiply charged ions using fourier transform mass spectrometry. *Anal. Chem.* **1994,** *66*, 2801-2808.

54. Jennings, K. R., Collision-induced decompositions of aromatic molecular ions. *Int. J. Mass Spectrom. Ion Phys.* **1968,** *1*, 227-235.

55. Bordas-Nagy, J.; Jennings, K. R., Collision-induced decomposition of ions. *Int. J. Mass Spectrom. Ion Processes* **1990,** *100*, 105-131.

56. Roepstorff, P.; Fohlman, J., Proposal for a common nomenclature for sequence ions in mass-spectra of peptides. *Biomed. Mass Spectrom.* **1984,** *11*, 601-601.

57. Johnson, R. S.; Martin, S. A.; Biemann, K.; Stults, J. T.; Watson, J. T., Novel fragmentation process of peptides by collision-induced decomposition in a tandem mass spectrometer: differentiation of leucine and isoleucine. *Anal. Chem.* **1987,** *59*, 2621-2625.

58. Johnson, R. S.; Martin, S. A.; Biemann, K., Collision-induced fragmentation of $(M + H)^+$ ions of peptides. Side chain specific sequence ions. *Int. J. Mass Spectrom. Ion Processes* **1988,** *86*, 137-154.

59. Little, D. P.; Speir, J. P.; Senko, M. W.; O'Connor, P. B.; McLafferty, F. W., Infrared multiphoton dissociation of large multiply charged ions for biomolecule sequencing. *Anal. Chem.* **1994,** *66*, 2809-2815.

60. Gauthier, J. W.; Trautman, T. R.; Jacobson, D. B., Sustained off-resonance irradiation for collision-activated dissociation involving Fourier transform mass spectrometry. Collision-activated dissociation technique that emulates infrared multiphoton dissociation. *Anal. Chim. Acta* **1991,** *246*, 211-225.

61. Sleno, L.; Volmer, D. A., Ion activation methods for tandem mass spectrometry. *J. Mass Spectrom.* **2004,** *39*, 1091-1112.

62. Cooper, H. J.; Hakansson, K.; Marshall, A. G., The role of electron capture dissociation in biomolecular analysis. *Mass Spectrom. Rev.* **2005,** *24*, 201-222.

63. Leymarie, N.; Costello, C. E.; O'Connor, P. B., Electron capture dissociation initiates a free radical reaction cascade. *J. Am. Chem. Soc.* **2003,** *125*, 8949-8958.

64. O'Connor, P. B.; Lin, C.; Cournoyer, J. J.; Pittman, J. L.; Belyayev, M.; Budnik, B. A., Long-lived electron capture dissociation product ions experience radical migration via hydrogen abstraction. *J. Am. Soc. Mass Spectrom.* **2006,** *17*, 576-585.

65. Simons, J., Mechanisms for S-S and N-C(alpha) bond cleavage in peptide ECD and ETD mass spectrometry. *Chem. Phys. Lett.* **2010,** *484*, 81-95.

66. Syrstad, E. A.; Turecek, F., Toward a general mechanism of electron capture dissociation. *J. Am. Soc. Mass Spectrom.* **2005,** *16*, 208-224.

67. Zubarev, R. A.; Kelleher, N. L.; McLafferty, F. W., Electron capture dissociation of multiply charged protein cations. A nonergodic process. *J. Am. Chem. Soc.* **1998,** *120*, 3265-3266.

68. Anusiewicz, I.; Berdys-Kochanska, J.; Skurski, P.; Simons, J., Simulating electron transfer attachment to a positively charged model peptide. *J. Phys. Chem. A* **2005,** *110*, 1261-1266.

69. Świerszcz, I.; Skurski, P.; Simons, J., Dipole and coulomb forces in electron capture dissociation and electron transfer dissociation mass spectroscopy. *J. Phys. Chem. A* **2012,** *116*, 1828-1837.

70. Budnik, B. A.; Haselmann, K. F.; Zubarev, R. A., Electron detachment dissociation of peptide di-anions: an electron-hole recombination phenomenon. *Chem. Phys. Lett.* **2001,** *342*, 299-302.

71. Syka, J. E. P.; Coon, J. J.; Schroeder, M. J.; Shabanowitz, J.; Hunt, D. F., Peptide and protein sequence analysis by electron transfer dissociation mass spectrometry. *P Natl Acad Sci USA* **2004,** *101*, 9528-9533.

72. Wiesner, J.; Premsler, T.; Sickmann, A., Application of electron transfer dissociation (ETD) for the analysis of posttranslational modifications. *Proteomics* **2008,** *8*, 4466-4483.

73. Cody, R. B.; Freiser, B. S., Electron-impact excitation of ions from organics - alternative to collision-induced dissociation. *Anal. Chem.* **1979,** *51*, 547-551.

74. Wang, B. H.; McLafferty, F. W., Electron-impact excitation of ions from larger organic-molecules. *Org. Mass Spectrom.* **1990,** *25*, 554-556.

75. Ly, T.; Yin, S.; Loo, J. A.; Julian, R. R., Electron-induced dissociation of protonated peptides yields backbone fragmentation consistent with a hydrogen-deficient radical. *Rapid Commun. Mass Spectrom.* **2009,** *23*, 2099-2101.

76. Feketeova, L.; O'Hair, R. A. J., Electron-induced dissociation of doubly protonated betaine clusters: controlling fragmentation chemistry through electron energy. *Rapid Commun. Mass Spectrom.* **2009,** *23*, 3259-3263.

77. Lioe, H.; O'Hair, R. A. J., Comparison of collision-induced dissociation and electron-induced dissociation of singly protonated aromatic amino acids, cystine and related simple peptides using a hybrid linear ion trap-FT-ICR mass spectrometer. *Anal. Bioanal. Chem.* **2007,** *389*, 1429-1437.

78. Kjeldsen, F.; Haselmann, K. F.; Budnik, B. A.; Jensen, F.; Zubarev, R. A., Dissociative capture of hot (3-13 eV) electrons by polypeptide polycations: an efficient process accompanied by secondary fragmentation. *Chem. Phys. Lett.* **2002,** *356*, 201-206.

79. Feketeova, L.; O'Hair, R. A. J., Comparison of collision- versus electron-induced dissociation of sodium chloride cluster cations. *Rapid Commun. Mass Spectrom.* **2009,** *23*, 60-64.

80. Kaczorowska, M. A.; Cooper, H. J., Electron induced dissociation: A mass spectrometry technique for the structural analysis of trinuclear oxo-centred carboxylate-bridged iron complexes. *J. Am. Soc. Mass Spectrom.* **2010,** *21*, 1398-1403.

81. Kaczorowska, M. A.; Cooper, H. J., Electron induced dissociation (EID) tandem mass spectrometry of octaethylporphyrin and its iron(III) complex. *Chem. Commun.* **2011,** *47*, 418-420.

82. Feketeova, L.; Wong, M. W.; O'Hair, R. A. J., The role of metal cation in electron-induced dissociation of tryptophan. *Eur. Phys. J. D* **2010,** *60*, 11-20.

83. Mosely, J. A.; Smith, M. J. P.; Prakash, A. S.; Sims, M.; Bristow, A. W. T., Electron-induced dissociation of singly charged organic cations as a tool for structural characterization of pharmaceutical type molecules. *Anal. Chem.* **2011,** *83*, 4068-4075.

84. Kalli, A.; Grigorean, G.; Håkansson, K., Electron induced dissociation of singly deprotonated peptides. *J. Am. Soc. Mass Spectrom.* **2011,** *22*, 2209-2221.

85. Bogdanov, B.; Smith, R. D., Proteomics by FTICR mass spectrometry: Top down and bottom up. *Mass Spectrom. Rev.* **2005,** *24*, 168-200.

86. Koehn, F. E.; Carter, G. T., The evolving role of natural products in drug discovery. *Nat. Rev. Drug Discovery* **2005,** *4*, 206-220.

87. Finking, R.; Marahiel, M. A., Biosynthesis of nonribosomal peptides. *Annu. Rev. Microbiol.* **2004,** *58*, 453-488.

88. Butler, M. S.; Buss, A. D., Natural products — The future scaffolds for novel antibiotics? *Biochem. Pharmacol.* **2006,** *71*, 919-929.

89. Newman, D. J.; Cragg, G. M., Natural products as sources of new drugs over the last 25 years. *J. Nat. Prod.* **2007,** *70*, 461-477.

90. Weissman, K. J., Introduction to polyketide biosynthesis. In *Complex Enzymes in Microbial Natural Product Biosynthesis, Part B: Polyketides, Aminocoumarins and Carbohydrates*, Hopwood, D. A., Ed. 2009; Vol. 459, pp 3-16.

91. Marahiel, M. A., Protein templates for the biosynthesis of peptide antibiotics. *Chem. Biol.* **1997,** *4*, 561-567.

92. Feng, X.; Siegel, M. M., FTICR-MS applications for the structure determination of natural products. *Anal. Bioanal. Chem.* **2007,** *389*, 1341-1363.

93. Konishi, Y.; Kiyota, T.; Draghici, C.; Gao, J.-M.; Yeboah, F.; Acoca, S.; Jarussophon, S.; Purisima, E., Molecular formula analysis by an MS/MS/MS technique to expedite dereplication of natural products. *Anal. Chem.* **2006,** *79*, 1187-1197.

94. Shin, Y. G.; van Breemen, R. B., Analysis and screening of combinatorial libraries using mass spectrometry. *Biopharm. Drug Dispos.* **2001,** *22*, 353-372.

95. Ang, W. H.; Dyson, P. J., Classical and non-classical ruthenium-based anticancer drugs: Towards targeted chemotherapy. *Eur. J. Inorg. Chem.* **2006**, 4003-4018.

96. Ivanov, A. I.; Christodoulou, J.; Parkinson, J. A.; Barnham, K. J.; Tucker, A.; Woodrow, J.; Sadler, P. J., Cisplatin binding sites on human albumin. *J. Biol. Chem.* **1998,** *273*, 14721-14730.

97. Zhao, T.; King, F. L., A mass spectrometric comparison of the interactions of cisplatin and transplatin with myoglobin. *J. Inorg. Biochem.* **2010,** *104*, 186-192.

98. Gibson, D.; Costello, C. E., A mass spectral study of the binding of the anticancer drug cisplatin to ubiquitin. *Eur. Mass Spectrom.* **1999,** *5*, 501-510.

99. Moreno-Gordaliza, E.; Canas, B.; Palacios, M. A.; Gomez-Gomez, M. M., Top-down mass spectrometric approach for the full characterization of insulin-cisplatin adducts. *Anal. Chem.* **2009,** *81*, 3507-3516.

100. Allardyce, C. S.; Dyson, P. J.; Coffey, J.; Johnson, N., Determination of drug binding sites to proteins by electrospray ionisation mass spectrometry: the interaction of cisplatin with transferrin. *Rapid Commun. Mass Spectrom.* **2002,** *16*, 933-935.

101. Khalaila, I.; Allardyce, C. S.; Verma, C. S.; Dyson, P. J., A mass spectrometric and molecular modelling study of cisplatin binding to transferrin. *ChemBioChem* **2005,** *6*, 1788-1795.

102. Li, H. L.; Zhao, Y.; Phillips, H. I. A.; Qi, Y. L.; Lin, T. Y.; Sadler, P. J.; O'Connor, P. B., Mass spectrometry evidence for cisplatin as a protein cross-linking reagent. *Anal. Chem.* **2011,** *83*, 5369-5376.

103. Li, H.; Lin, T.-Y.; Van Orden, S. L.; Zhao, Y.; Barrow, M. P.; Pizarro, A. M.; Qi, Y.; Sadler, P. J.; O'Connor, P. B., Use of top-down and bottom-up Fourier transform ion cyclotron resonance mass spectrometry for mapping calmodulin sites modified by platinum anticancer drugs. *Anal. Chem.* **2011,** *83*, 9507-9515.

104. Rademaker-Lakhai, J. M.; van den Bongard, D.; Pluim, D.; Beijnen, J. H.; Schellens, J. H. M., A phase I and pharmacological study with imidazolium-trans-

DMSO-imidazole-tetrachlororuthenate, a novel ruthenium anticancer agent. *Clin. Cancer Res.* **2004,** *10*, 3717-3727.

105. Alessio, E.; Mestroni, G.; Bergamo, A.; Sava, G., Ruthenium antimetastatic agents. *Curr. Top. Med. Chem.* **2004,** *4*, 1525-1535.

106. Jakupec, M. A.; Galanski, M.; Arion, V. B.; Hartinger, C. G.; Keppler, B. K., Antitumour metal compounds: more than theme and variations. *Dalton Trans.* **2008**, 183-194.

107. Groessl, M.; Tsybin, Y. O.; Hartinger, C. G.; Keppler, B. K.; Dyson, P. J., Ruthenium versus platinum: interactions of anticancer metallodrugs with duplex oligonucleotides characterised by electrospray ionisation mass spectrometry. *J. Biol. Inorg. Chem.* **2010,** *15*, 677-688.

108. Kratz, F.; Hartmann, M.; Keppler, B.; Messori, L., The binding-properties of 2 anticancer ruthenium(III) complexes to apotransferrin. *J. Biol. Chem.* **1994,** *269*, 2581-2588.

109. Yan, Y. K.; Melchart, M.; Habtemariam, A.; Sadler, P. J., Organometallic chemistry, biology and medicine: ruthenium arene anticancer complexes. *Chem. Commun.* **2005**, 4764-4776.

110. Wang, F. Y.; Bella, J.; Parkinson, J. A.; Sadler, P. J., Competitive reactions of a ruthenium arene anticancer complex with histidine, cytochrome c and an oligonucleotide. *J. Biol. Inorg. Chem.* **2005,** *10*, 147-155.

111. Wilkinson, B.; Micklefield, J., Mining and engineering natural-product biosynthetic pathways. *Nat. Chem. Biol.* **2007,** *3*, 379-386.

112. Fischbach, M. A.; Walsh, C. T., Assembly-line enzymology for polyketide and nonribosomal peptide antibiotics: logic, machinery, and mechanisms. *Chem. Rev.* **2006,** *106*, 3468-3496.

113. Volmer, D. A.; Lock, C. M., Electrospray ionization and collision-induced dissociation of antibiotic polyether ionophores. *Rapid Commun. Mass Spectrom.* **1998,** *12*, 157-164.

114. Fonseca, T.; Lopes, N. P.; Gates, P. J.; Staunton, J., Fragmentation studies on tetronasin by accurate-mass electrospray tandem mass spectrometry. *J. Am. Soc. Mass Spectrom.* **2004,** *15*, 325-335.

115. Tosin, M.; Smith, L.; Leadlay, P. F., Insights into lasalocid A ring formation by chemical chain termination in vivo. *Angew Chem Int Edit* **2011,** *50*, 11930-11933.

116. Cha, J. M.; Yang, S.; Carlson, K. H., Rapid analysis of trace levels of antibiotic polyether ionophores in surface water by solid-phase extraction and liquid chromatography with ion trap tandem mass spectrometric detection. *J. Chromatogr. A* **2005,** *1065*, 187-198.

117. Harris, J. A.; Russell, C. A. L.; Wilkins, J. P. G., The characterisation of polyether ionophore veterinary drugs by HPLC-electrospray MS. *Analyst* **1998,** *123*, 2625-2628.

118. Martinez-Villalba, A.; Moyano, E.; Galceran, M. T., Fast liquid chromatography/multiple-stage mass spectrometry of coccidiostats. *Rapid Commun. Mass Spectrom.* **2009,** *23*, 1255-1263.

119. Cerny, R. L.; Macmillan, D. K.; Gross, M. L.; Mallams, A. K.; Pramanik, B. N., Fast-atom-bombardment and tandem mass-spectrometry of macrolide antibiotics. *J. Am. Soc. Mass Spectrom.* **1994,** *5*, 151-158.

120. Crowe, M. C.; Brodbelt, J. S.; Goolsby, B. J.; Hergenrother, P., Characterization of erythromycin analogs by collisional activated dissociation and infrared multiphoton dissociation in a quadrupole ion trap. *J. Am. Soc. Mass Spectrom.* **2002,** *13*, 630-649.

121. Gates, P. J.; Kearney, G. C.; Jones, R.; Leadlay, P. F.; Staunton, J., Structural elucidation studies of erythromycins by electrospray tandem mass spectrometry. *Rapid Commun. Mass Spectrom.* **1999,** *13*, 242-246.

122. Kearney, G. C.; Gates, P. J.; Leadlay, P. F.; Staunton, J.; Jones, R., Structural elucidation studies of erythromycins by electrospray tandem mass spectrometry II. *Rapid Commun. Mass Spectrom.* **1999,** *13*, 1650-1656.

123. Kim, Y. H.; Yoo, J. S.; Lee, C. H.; Goo, Y. M.; Kim, M. S., Application of fast atom bombardment combined with tandem mass spectrometry to the structural elucidation of O-demethylabierixin and related polyether antibiotics. *J. Mass Spectrom.* **1996,** *31*, 855-860.

124. Volmer, D. A.; Hui, J. P. M., Study of erythromycin A decomposition products in aqueous solution by solid-phase microextraction liquid chromatography tandem mass spectrometry. *Rapid Commun. Mass Spectrom.* **1998,** *12*, 123-129.

125. Lopes, N. P.; Gates, P. J.; Wilkins, J. P. G.; Staunton, J., Fragmentation studies on lasalocid acid by accurate mass electrospray mass spectrometry. *Analyst* **2002,** *127*, 1224-1227.

126. Tosin, M.; Demydchuk, Y.; Parascandolo, J. S.; Per, C. B.; Leeper, F. J.; Leadlay, P. F., In vivo trapping of polyketide intermediates from an assembly line synthase using malonyl carba(dethia)-N-acetyl cysteamines. *Chem. Commun.* **2011,** *47*, 3460-3462.

127. Gorshkov, M. V.; Masselon, C. D.; Nikolaev, E. N.; Udseth, H. R.; Pasa-Tolic, L.; Smith, R. D., Considerations for electron capture dissociation efficiency in FTICR mass spectrometry. *Int. J. Mass Spectrom.* **2004,** *234*, 131-136.

128. Migita, A.; Shichijo, Y.; Oguri, H.; Watanabe, M.; Tokiwano, T.; Oikawa, H., Stereo-controlled synthesis of prelasalocid, a key precursor proposed in the

biosynthesis of polyether antibiotic lasalocid A. *Tetrahedron Lett.* **2008,** *49*, 1021-1025.

129. Smith, L.; Hong, H.; Spencer, J. B.; Leadlay, P. F., Analysis of specific mutants in the lasalocid gene cluster: evidence for enzymatic catalysis of a disfavoured polyether ring closure. *ChemBioChem* **2008,** *9*, 2967-2975.

130. Bumpus, S. B.; Evans, B. S.; Thomas, P. M.; Ntai, I.; Kelleher, N. L., A proteomics approach to discovering natural products and their biosynthetic pathways. *Nat. Biotechnol.* **2009,** *27*, 951-U120.

131. Hong, H.; Leadlay, P. F.; Staunton, J., The changing patterns of covalent active site occupancy during catalysis on a modular polyketide synthase multienzyme revealed by ion-trap mass spectrometry. *Febs J* **2009,** *276*, 7057-7069.

132. Tosin, M.; Spiteller, D.; Spencer, J. B., Malonyl carba(dethia)- and malonyl oxa(dethia)-coenzyme A as tools for trapping polyketide intermediates. *ChemBioChem* **2009,** *10*, 1714-1723.

133. Tosin, M.; Betancor, L.; Stephens, E.; Li, W. M. A.; Spencer, J. B.; Leadlay, P. F., Synthetic Chain Terminators Off-Load Intermediates from a Type I Polyketide Synthase. *ChemBioChem* **2010,** *11*, 539-546.

134. Strieker, M.; Tanovic, A.; Marahiel, M. A., Nonribosomal peptide synthetases: structures and dynamics. *Curr. Opin. Struct. Biol.* **2010,** *20*, 234-240.

135. Felnagle, E. A.; Jackson, E. E.; Chan, Y. A.; Podevels, A. M.; Berti, A. D.; McMahon, M. D.; Thomas, M. G., Nonribosomal peptide synthetases involved in the production of medically relevant natural products. *Mol. Pharm.* **2008,** *5*, 191-211.

136. Schwarzer, D.; Finking, R.; Marahiel, M. A., Nonribosomal peptides: from genes to products. *Nat. Prod. Rep.* **2003,** *20*, 275-287.

137. Konz, D.; Marahiel, M. A., How do peptide synthetases generate structural diversity? *Chem. Biol.* **1999,** *6*, R39-R48.

138. Bandeira, N.; Ng, J.; Meluzzi, D.; Linington, R.; Dorrestein, P.; Pevzner, P., De novo sequencing of nonribosomal peptides. In *Research in Computational Molecular Biology*, Vingron, M.; Wong, L., Eds. Springer Berlin Heidelberg: 2008; Vol. 4955, pp 181-195.

139. Eckart, K.; Schwarz, H.; Tomer, K. B.; Gross, M. L., Tandem mass spectrometry methodology for the sequence determination of cyclic peptides. *J. Am. Chem. Soc.* **1985,** *107*, 6765-6769.

140. Ngoka, L. C. M.; Gross, M. L., Multistep tandem mass spectrometry for sequencing cyclic peptides in an ion-trap mass spectrometer. *J. Am. Soc. Mass Spectrom.* **1999,** *10*, 732-746.

141. Barber, M.; Bell, D. J.; Morris, M. R.; Tetler, L. W.; Monaghan, J. J.; Morden, W. E.; Bycroft, B. W.; Green, B. N., An investigation of the tyrothricin complex by tandem mass spectrometry. *Int. J. Mass Spectrom. Ion Processes* **1992,** *122*, 143-151.

142. Wang, T. C. L.; Ricca, T. L.; Marshall, A. G., Extension of dynamic range in Fourier transform ion cyclotron resonance mass spectrometry via stored waveform inverse Fourier transform excitation. *Anal. Chem.* **1986,** *58*, 2935-2938.

143. McDonald, L. A.; Barbieri, L. R.; Carter, G. T.; Kruppa, G.; Feng, X. D.; Lotvin, J. A.; Siegel, M. M., FTMS structure elucidation of natural products: Application to muraymycin antibiotics using ESI multi-CHEF SORI-CID FTMSn, the top-down/bottom-up approach, and HPLC ESI capillary-skimmer CID FTMS. *Anal. Chem.* **2003,** *75*, 2730-2739.

144. Barber, M.; Bell, D.; Morris, M.; Tetler, L.; Woods, M.; Bycroft, B. W.; Monaghan, J. J.; Morden, W. E.; Green, B. N., Study of an actinomycin complex by mass-spectrometry mass-spectrometry. *Talanta* **1988,** *35*, 605-611.

145. Ngoka, L. C. M.; Gross, M. L.; Toogood, P. L., Sodium-directed selective cleavage of lactones: a method for structure determination of cyclodepsipeptides. *Int. J. Mass Spectrom.* **1999,** *182–183*, 289-298.

146. Wills, R. H.; Tosin, M.; O'Connor, P. B., Structural characterization of polyketides using high mass accuracy tandem mass spectrometry. *Anal. Chem.* **2012,** *84*, 8863-8870.

147. Wolff, J. J.; Laremore, T. N.; Aslam, H.; Linhardt, R. J.; Amster, I. J., Electron-induced dissociation of glycosaminoglycan tetrasaccharides. *J. Am. Soc. Mass Spectrom.* **2008,** *19*, 1449-1458.

148. Yoo, H. J.; Hakansson, K., Determination of double bond location in fatty acids by manganese adduction and electron induced dissociation. *Anal. Chem.* **2010,** *82*, 6940-6946.

149. McFarland, M. A.; Chalmers, M. J.; Quinn, J. P.; Hendrickson, C. L.; Marshall, A. G., Evaluation and optimization of electron capture dissociation efficiency in Fourier transform ion cyclotron resonance mass spectrometry. *J. Am. Soc. Mass Spectrom.* **2005,** *16*, 1060-1066.

150. Hendrickson, C. L.; Hadjarab, F.; Laude Jr, D. A., Electron beam potential depression as an ion trap in Fourier transform ion cyclotron resonance mass spectrometry. *Int. J. Mass Spectrom. Ion Processes* **1995,** *141*, 161-170.

151. Bugarcic, T.; Habtemariam, A.; Deeth, R. J.; Fabbiani, F. P. A.; Parsons, S.; Sadler, P. J., Ruthenium(II) arene anticancer complexes with redox-active diamine ligands. *Inorg. Chem.* **2009,** *48*, 9444-9453.

152. Aird, R. E.; Cummings, J.; Ritchie, A. A.; Muir, M.; Morris, R. E.; Chen, H.; Sadler, P. J.; Jodrell, D. I., In vitro and in vivo activity and cross resistance profiles of novel ruthenium (II) organometallic arene complexes in human ovarian cancer. *Br. J. Cancer* **2002,** *86*, 1652-1657.

153. Morris, R. E.; Aird, R. E.; Murdoch, P. D.; Chen, H. M.; Cummings, J.; Hughes, N. D.; Parsons, S.; Parkin, A.; Boyd, G.; Jodrell, D. I.; Sadler, P. J., Inhibition of cancer cell growth by ruthenium(II) arene complexes. *J. Med. Chem.* **2001,** *44*, 3616-3621.

154. Habtemariam, A.; Melchart, M.; Fernandez, R.; Parsons, S.; Oswald, I. D. H.; Parkin, A.; Fabbiani, F. P. A.; Davidson, J. E.; Dawson, A.; Aird, R. E.; Jodrell, D. I.; Sadler, P. J., Structure-activity relationships for cytotoxic ruthenium(II) arene complexes containing N,N-, N,O-, and O,O-chelating ligands. *J. Med. Chem.* **2006,** *49*, 6858-6868.

155. Williams, J. P.; Brown, J. M.; Campuzano, I.; Sadler, P. J., Identifying drug metallation sites on peptides using electron transfer dissociation (ETD), collision induced dissociation (CID) and ion mobility-mass spectrometry (IM-MS). *Chem. Commun.* **2010,** *46*, 5458-5460.

156. McNae, I. W.; Fishburne, K.; Habtemariam, A.; Hunter, T. M.; Melchart, M.; Wang, F. Y.; Walkinshaw, M. D.; Sadler, P. J., Half-sandwich arene ruthenium(II)-enzyme complex. *Chem. Commun.* **2004**, 1786-1787.

157. Piccioli, F.; Sabatini, S.; Messori, L.; Orioli, P.; Hartinger, C. G.; Keppler, B. K., A comparative study of adduct formation between the anticancer ruthenium(III) compound HInd *trans*-[$RuCl_4(Ind)_2$] and serum proteins. *J. Inorg. Biochem.* **2004,** *98*, 1135-1142.

158. Hartinger, C. G.; Casini, A.; Duhot, C.; Tsybin, Y. O.; Messori, L.; Dyson, P. J., Stability of an organometallic ruthenium-ubiquitin adduct in the presence of glutathione: Relevance to antitumour activity. *J. Inorg. Biochem.* **2008,** *102*, 2136-2141.

159. Casini, A.; Gabbiani, C.; Michelucci, E.; Pieraccini, G.; Moneti, G.; Dyson, P. J.; Messori, L., Exploring metallodrug-protein interactions by mass spectrometry:

comparisons between platinum coordination complexes and an organometallic ruthenium compound. *J. Biol. Inorg. Chem.* **2009,** *14*, 761-770.

160. Casini, A.; Karotki, A.; Gabbiani, C.; Rugi, F.; Vasak, M.; Messori, L.; Dyson, P. J., Reactivity of an antimetastatic organometallic ruthenium compound with metallothionein-2: relevance to the mechanism of action. *Metallomics* **2009,** *1*, 434-441.

161. Hu, W. B.; Luo, Q.; Ma, X. Y.; Wu, K.; Liu, J. A.; Chen, Y.; Xiong, S. X.; Wang, J. P.; Sadler, P. J.; Wang, F. Y., Arene control over thiolate to sulfinate oxidation in albumin by organometallic ruthenium anticancer complexes. *Chem. Eur. J.* **2009,** *15*, 6586-6594.

162. Meier, S. M.; Hanif, M.; Kandioller, W.; Keppler, B. K.; Hartinger, C. G., Biomolecule binding vs. anticancer activity: Reactions of Ru(arene) (thio)pyr-(id)one compounds with amino acids and proteins. *J. Inorg. Biochem.* **2012,** *108*, 91-95.

163. Casini, A.; Mastrobuoni, G.; Ang, W. H.; Gabbiani, C.; Pieraccini, G.; Moneti, G.; Dyson, P. J.; Messori, L., ESI–MS Characterisation of Protein Adducts of Anticancer Ruthenium(II)-Arene PTA (RAPTA) Complexes. *ChemMedChem* **2007,** *2*, 631-635.

164. Chatterjee, S.; Kundu, S.; Bhattacharyya, A.; Hartinger, C.; Dyson, P., The ruthenium(II)–arene compound RAPTA-C induces apoptosis in EAC cells through mitochondrial and p53–JNK pathways. *J. Biol. Inorg. Chem.* **2008,** *13*, 1149-1155.

165. Wu, B.; Ong, M. S.; Groessl, M.; Adhireksan, Z.; Hartinger, C. G.; Dyson, P. J.; Davey, C. A., A ruthenium antimetastasis agent forms specific histone protein adducts in the nucleosome core. *Chem. Eur. J.* **2011,** *17*, 3562-3566.

166. Wang, Y.; Vivekananda, S.; Men, L.; Zhang, Q., Fragmentation of protonated ions of peptides containing cysteine, cysteine sulfinic acid, and cysteine sulfonic acid. *J. Am. Soc. Mass Spectrom.* **2004,** *15*, 697-702.

167. Claiborne, A.; Yeh, J. I.; Mallett, T. C.; Luba, J.; Crane, E. J.; Charrier, V.; Parsonage, D., Protein-sulfenic acids: diverse roles for an unlikely player in enzyme catalysis and redox regulation. *Biochemistry* **1999,** *38*, 15407-15416.

168. Chang, Y.-C.; Huang, C.-N.; Lin, C.-H.; Chang, H.-C.; Wu, C.-C., Mapping protein cysteine sulfonic acid modifications with specific enrichment and mass spectrometry: An integrated approach to explore the cysteine oxidation. *Proteomics* **2010,** *10*, 2961-2971.

169. Winterbourn, C. C.; Hampton, M. B., Thiol chemistry and specificity in redox signaling. *Free Radic. Biol. Med.* **2008,** *45*, 549-561.

170. Williams, J. P.; Lough, J. A.; Campuzano, I.; Richardson, K.; Sadler, P. J., Use of ion mobility mass spectrometry and a collision cross-section algorithm to study an organometallic ruthenium anticancer complex and its adducts with a DNA oligonucleotide. *Rapid Commun. Mass Spectrom.* **2009,** *23*, 3563-3569.

171. Hu, P.; Loo, J. A., Gas-phase coordination properties of Zn2+, Cu2+, Ni2+, and Co2+ with histidine-containing peptides. *J. Am. Chem. Soc.* **1995,** *117*, 11314-11319.

172. Loo, J. A.; Hu, P.; Smith, R. D., Interaction of angiotensin peptides and zinc metal ions probed by electrospray ionization mass spectrometry. *J. Am. Soc. Mass Spectrom.* **1994,** *5*, 959-965.

173. Kleinnijenhuis, A. J.; Mihalca, R.; Heeren, R. M. A.; Heck, A. J. R., Atypical behavior in the electron capture induced dissociation of biologically relevant transition metal ion complexes of the peptide hormone oxytocin. *Int. J. Mass Spectrom.* **2006,** *253*, 217-224.

174. Mosely, J. A.; Murray, B. S.; Parker, D., Electron-capture dissociation and collision-induced dissociation of lanthanide metal-ligand complexes and lanthanide metal-ligand complexes bound to phosphopeptides. *Eur. J. Mass Spectrom.* **2009,** *15*, 145-155.

175. Zubarev, R. A.; Horn, D. M.; Fridriksson, E. K.; Kelleher, N. L.; Kruger, N. A.; Lewis, M. A.; Carpenter, B. K.; McLafferty, F. W., Electron capture dissociation for structural characterization of multiply charged protein cations. *Anal. Chem.* **2000,** *72*, 563-573.

176. Belyayev, M. A.; Cournoyer, J. J.; Lin, C.; O'Connor, P. B., The effect of radical trap moieties on electron capture dissociation spectra of Substance P. *J. Am. Soc. Mass Spectrom.* **2006,** *17*, 1428-1436.

177. Hong, J.; Miao, Y.; Miao, R.; Yang, G.; Tang, H.; Guo, Z.; Zhu, L., Binding sites of $[Ru(bpy)_2(H_2O)_2](BF_4)_2$ with sulfur- and histidine-containing peptides studied by electrospray ionization mass spectrometry and tandem mass spectrometry. *J. Mass Spectrom.* **2005,** *40*, 91-99.

178. http://www.theiet.org/policy/media/press-releases/20120203.cfm.

179. Ng, L.-K.; Hupé, M.; Harnois, J.; Moccia, D., Characterisation of commercial vodkas by solid-phase microextraction and gas chromatography/mass spectrometry analysis. *J. Sci. Food Agric.* **1996,** *70*, 380-388.

180. Lachenmeier, D. W.; Schmidt, B.; Bretschneider, T., Rapid and mobile brand authentication of vodka using conductivity measurement. *Microchim. Acta* **2008,** *160*, 283-289.

181. Ng, L.-K., Analysis by gas chromatography/mass spectrometry of fatty acids and esters in alcoholic beverages and tobaccos. *Anal. Chim. Acta* **2002,** *465*, 309-318.

182. Savchuk, S. A.; Nuzhnyi, V. P.; Kolesov, G. M., Factors affecting the accuracy of the determination of diethyl phthalate in vodka, ethanol, and samples of illegal alcoholic products. *J. Anal. Chem.* **2006,** *61*, 1198-1203.

183. MacNamara, K.; Lee, M.; Robbat Jr, A., Rapid gas chromatographic analysis of less abundant compounds in distilled spirits by direct injection with ethanol–water venting and mass spectrometric data deconvolution. *J. Chromatogr. A* **2010,** *1217*, 136-142.

184. Bauer-Christoph, C.; Wachter, H.; Christoph, N.; Rßmann, A.; Adam, L., Assignment of raw material and authentication of spirits by gas chromatography, hydrogen- and carbon-isotope ratio measurements I. Analytical methods and results of a study of commercial products. *Zeitschrift für Lebensmitteluntersuchung und - Forschung A* **1997,** *204*, 445-452.

185. Pino, J.; Martí, M. P.; Mestres, M.; Pérez, J.; Busto, O.; Guasch, J., Headspace solid-phase microextraction of higher fatty acid ethyl esters in white rum aroma. *J. Chromatogr. A* **2002,** *954*, 51-57.

186. Fitzgerald, G.; James, K. J.; MacNamara, K.; Stack, M. A., Characterisation of whiskeys using solid-phase microextraction with gas chromatography–mass spectrometry. *J. Chromatogr. A* **2000,** *896*, 351-359.

187. Ferreira do Nascimento, R.; Cardoso, D. R.; Lima Neto, B. S.; Franco, D. W., Determination of acids in Brazilian sugar cane spirits and other alcoholic beverages by HRGC-SPE. *Chromatographia* **1998,** *48*, 751-757.

188. Pino, J. A., Characterization of rum using solid-phase microextraction with gas chromatography–mass spectrometry. *Food Chem.* **2007,** *104*, 421-428.

189. Park, Y. J.; Kim, K. R.; Kim, J. H., Gas chromatographic organic acid profiling analysis of brandies and whiskeys for pattern recognition analysis. *J. Agric. Food Chem.* **1999,** *47*, 2322-2326.

190. Simpkins, W. A., Congener profiles in the detection of illicit spirits. *J. Sci. Food Agric.* **1985,** *36*, 367-376.

191. Field, J. A.; Monohan, K., In-vial derivatization and empore disk elution for the quantitative determination of the carboxylic acid metabolites of dacthal in groundwater. *Anal. Chem.* **1995,** *67*, 3357-3362.

192. Lachenmeier, D.; Attig, R.; Frank, W.; Athanasakis, C., The use of ion chromatography to detect adulteration of vodka and rum. *Eur. Food Res. Technol.* **2003,** *218*, 105-110.

193. Arbuzov, V. N.; Savchuk, S. A., Identification of vodkas by ion chromatography and gas chromatography. *J. Anal. Chem.* **2002,** *57*, 428-433.

194. Palma, M.; Barroso, C. G., Application of FT-IR spectroscopy to the characterisation and classification of wines, brandies and other distilled drinks. *Talanta* **2002,** *58*, 265-271.

195. Picque, D.; Lieben, P.; Corrieu, G.; Cantagrel, R.; Lablanquie, O.; Snakkers, G., Discrimination of cognacs and other distilled drinks by mid-infrared spectropscopy. *J. Agric. Food Chem.* **2006,** *54*, 5220-5226.

196. Lehtonen, P. J.; Keller, L. A.; Ali-Mattila, E. T., Multi-method analysis of matured distilled alcoholic beverages for brand identification. *Zeitschrift für Lebensmitteluntersuchung und -Forschung A* **1999,** *208*, 413-417.

197. Cordella, C.; Moussa, I.; Martel, A.-C.; Sbirrazzuoli, N.; Lizzani-Cuvelier, L., Recent developments in food characterization and adulteration detection: technique-oriented perspectives. *J. Agric. Food Chem.* **2002,** *50*, 1751-1764.

198. Moller, J. K. S.; Catharino, R. R.; Eberlin, M. N., Electrospray ionization mass spectrometry fingerprinting of whisky: immediate proof of origin and authenticity. *Analyst* **2005,** *130*, 890-897.

199. de Souza, P. P.; Augusti, D. V.; Catharino, R. R.; Siebald, H. G. L.; Eberlin, M. N.; Augusti, R., Differentiation of rum and Brazilian artisan cachaça via electrospray ionization mass spectrometry fingerprinting. *J. Mass Spectrom.* **2007,** *42*, 1294-1299.

200. Biasoto, A. C. T.; Catharino, R. R.; Sanvido, G. B.; Eberlin, M. N.; da Silva, M. A. A. P., Flavour characterization of red wines by descriptive analysis and ESI mass spectrometry. *Food Quality and Preference* **2010,** *21*, 755-762.

201. Savchuk, S. A.; Vlasov, V. N.; Appolonova, S. A.; Arbuzov, V. N.; Vedenin, A. N.; Mezinov, A. B.; Grigor'yan, B. R., Application of chromatography and spectrometry to the authentication of alcoholic beverages. *J. Anal. Chem.* **2001,** *56*, 214-231.

202. Davies, T.; Fearn, T., Back to basics: the principles of principal component analysis. *Spectroscopy Europe* **2004,** *16*, 20.

203. Karas, M.; Hillenkamp, F., Laser desorption ionization of proteins with molecular masses exceeding 10,000 daltons. *Anal. Chem.* **1988,** *60*, 2299-2301.

204. Chan, T. W. D.; Duan, L.; Sze, T. P. E., Accurate mass measurements for peptide and protein mixtures by using matrix-assisted laser desorption/ionization Fourier transform mass spectrometry. *Anal. Chem.* **2002,** *74*, 5282-5289.

205. Jackson, C.; Larsen, B.; McEwen, C., Comparison of most probable peak values as measured for polymer distributions by MALDI mass spectrometry and by size exclusion chromatography. *Anal. Chem.* **1996,** *68*, 1303-1308.

206. Peterson, D. S., Matrix-free methods for laser desorption/ionization mass spectrometry. *Mass Spectrom. Rev.* **2007,** *26*, 19-34.

207. Yau, P. Y.; Dominic Chan, T. W.; Cullis, P. G.; Colburn, A. W.; Derrick, P. J., Threshold fluences for production of positive and negative ions in matrix-assisted

laser desorption/ionisation using liquid and solid matrices. *Chem. Phys. Lett.* **1993,** *202*, 93-100.

208. Wei, J.; Buriak, J. M.; Siuzdak, G., Desorption-ionization mass spectrometry on porous silicon. *Nature* **1999,** *399*, 243-246.

209. Sunner, J.; Dratz, E.; Chen, Y.-C., Graphite surface-assisted laser desorption/ionization time-of-flight mass spectrometry of peptides and proteins from liquid solutions. *Anal. Chem.* **1995,** *67*, 4335-4342.

210. Dale, M. J.; Knochenmuss, R.; Zenobi, R., Graphite/liquid mixed matrices for laser desorption/ionization mass spectrometry. *Anal. Chem.* **1996,** *68*, 3321-3329.

211. Jokinen, V.; Aura, S.; Luosujärvi, L.; Sainiemi, L.; Kotiaho, T.; Franssila, S.; Baumann, M., Surface assisted laser desorption/ionization on two-layered amorphous silicon coated hybrid nanostructures. *J. Am. Soc. Mass Spectrom.* **2009,** *20*, 1723-1730.

212. Lo, C.-Y.; Lin, J.-Y.; Chen, W.-Y.; Chen, C.-T.; Chen, Y.-C., Surface-assisted laser desorption/ionization mass spectrometry on titania nanotube arrays. *J. Am. Soc. Mass Spectrom.* **2008,** *19*, 1014-1020.

213. Han, M.; Sunner, J., An activated carbon substrate surface for laser desorption mass spectrometry. *J. Am. Soc. Mass Spectrom.* **2000,** *11*, 644-649.

214. Lu, T.; Olesik, S. V., Electrospun nanofibers as substrates for surface-assisted laser desorption/ionization and matrix-enhanced surface-assisted laser desorption/ionization mass spectrometry. *Anal. Chem.* **2013**.

215. Iijima, S., Helical microtubules of graphitic carbon. *Nature* **1991,** *354*, 56-58.

216. Xu, S. Y.; Li, Y. F.; Zou, H. F.; Qiu, J. S.; Guo, Z.; Guo, B. C., Carbon nanotubes as assisted matrix for laser desorption/ionization time-of-flight mass spectrometry. *Anal. Chem.* **2003,** *75*, 6191-6195.

217. Shin, S. J.; Choi, D.; Kwak, H.; Lim, G. I.; Choi, Y. S., Matrix-free laser desorption/ionization on vertically aligned carbon nanotube arrays. *B. Kor. Chem..Soc.* **2006,** *27*, 581.

218. Chen, W.-Y.; Wang, L.-S.; Chiu, H.-T.; Chen, Y.-C.; Lee, C.-Y., Carbon nanotubes as affinity probes for peptides and proteins in MALDI MS analysis. *J. Am. Soc. Mass Spectrom.* **2004,** *15*, 1629-1635.

219. Miller, T. S.; Ebejer, N.; Güell, A. G.; Macpherson, J. V.; Unwin, P. R., Electrochemistry at carbon nanotube forests: sidewalls and closed ends allow fast electron transfer. *Chem. Commun.* **2012,** *48*, 7435-7437.

220. Futaba, D. N.; Hata, K.; Yamada, T.; Hiraoka, T.; Hayamizu, Y.; Kakudate, Y.; Tanaike, O.; Hatori, H.; Yumura, M.; Iijima, S., Shape-engineerable and highly densely packed single-walled carbon nanotubes and their application as super-capacitor electrodes. *Nat. Mater.* **2006,** *5*, 987-994.

221. Ren, S.-f.; Guo, Y.-l., Oxidized carbon nanotubes as matrix for matrix-assisted laser desorption/ionization time-of-flight mass spectrometric analysis of biomolecules. *Rapid Commun. Mass Spectrom.* **2005,** *19*, 255-260.

222. Pan, C.; Xu, S.; Hu, L.; Su, X.; Ou, J.; Zou, H.; Guo, Z.; Zhang, Y.; Guo, B., Using oxidized carbon nanotubes as matrix for analysis of small molecules by MALDI-TOF MS. *J. Am. Soc. Mass Spectrom.* **2005,** *16*, 883-892.

Appendices

Appendix A

Appendix A contains the supplementary data tables for chapters 2 and 3, detailing tandem mass spectrometry data for the structural characterisation of polyketides and non-ribosomal peptides.

Table A-1: Fragment ions produced by CAD of Erythromycin A (precursor ion *m/z* 734.48); peaks used for internal calibration are marked by ▲

Observed *m/z* (ext cal)	Observed m/z (int cal)	Theoretical m/z	Proposed formula	Mass Error (ext cal) / ppm	Mass error (int cal) / ppm	Fragment Cleavage
734.47682	▲ 734.46863	734.46895	$C_{37}H_{68}NO_{13}^+$	10.72	-	$[M+H]^+$
716.46591	▲ 716.45798	716.45795	$C_{37}H_{66}NO_{12}^+$	11.11	-	$[M+H-H_2O]^+$
698.45518	▲ 698.44749	698.44739	$C_{37}H_{64}NO_{11}^+$	11.15	-	$[M+H-H_4O_2]^+$
684.43880	684.43130	684.43174	$C_{36}H_{62}NO_{11}^+$	10.32	-0.64	$[M+H-CH_4O]^+$
680.44376	680.43631	680.43682	$C_{37}H_{62}NO_{10}^+$	10.20	-0.75	$[M+H-H_6O_3]^+$
666.42843	666.42117	666.42117	$C_{36}H_{60}NO_{10}^+$	10.89	0.00	$[M+H-CH_8O_3]^+$
658.42272	658.41557	658.41609	$C_{34}H_{60}NO_{11}^+$	10.07	-0.79	a
640.37547	640.36855	-	unassigned	-	-	-
602.39591	602.38949	602.38987	$C_{31}H_{56}NO_{10}^+$	10.03	-0.63	b
592.37507	592.36878	592.36914	$C_{29}H_{54}NO_{11}^+$	10.01	-0.61	c
590.35958	590.35331	590.35349	$C_{29}H_{52}NO_{11}^+$	10.32	-0.30	c – H_2
576.38016	▲ 576.37407	576.37422	$C_{29}H_{54}NO_{10}^+$	10.31	-	d
558.36898	558.36312	558.36366	$C_{29}H_{52}NO_9^+$	9.53	-0.97	d – H_2O
540.35761	540.35197	540.35309	$C_{29}H_{50}NO_8^+$	8.36	-2.07	d – H_4O_2
522.34760	522.34218	522.34253	$C_{29}H_{48}NO_7^+$	9.71	-0.67	d – H_6O_3
500.32668	500.32154	500.32179	$C_{26}H_{46}NO_8^+$	9.77	-0.50	ef
482.31604	482.31111	482.31123	$C_{26}H_{44}NO_7^+$	9.97	-0.25	ef – H_2O
480.30044	480.29553	480.29558	$C_{26}H_{42}NO_7^+$	10.12	-0.10	ef – H_4O
464.30531	464.30060	464.30066	$C_{26}H_{42}NO_6^+$	10.02	-0.13	ef – H_4O_2
444.29981	444.29534	444.29558	$C_{23}H_{42}NO_7^+$	9.52	-0.54	gh
438.32569	438.32128	438.32140	$C_{23}H_{42}NO_7^+$	9.79	-0.27	fi
426.28924	426.28497	426.28501	$C_{23}H_{40}NO_6^+$	9.92	-0.09	gh – H_2O
420.31497	420.31077	420.31084	$C_{25}H_{42}NO_4^+$	9.83	-0.17	fi – H_2O

408.27851	408.27445	408.27445	$C_{23}H_{38}NO_5^+$	9.94	0.00	gh – H_4O_2
401.25732	401.25334	-	unassigned	-	-	-
393.23101	393.22713	-	unassigned	-	-	-
383.24660	383.24282	-	unassigned	-	-	-
365.23584	▲ 365.23227	365.23225	$C_{21}H_{33}O_5^+$	9.83	-	jk
360.24156	360.23804	360.23806	$C_{18}H_{34}NO_6^+$	9.72	-0.06	hl
347.22514	347.22177	347.22169	$C_{21}H_{31}NO_4^+$	9.94	0.23	jk – H_2O
342.23084	342.22752	342.22750	$C_{18}H_{32}NO_5^+$	9.76	0.06	hl – H_2O
325.20408	325.20095	325.20095	$C_{18}H_{29}O_5^+$	9.62	0.00	hl-H_2O, -NH_3
316.21496	316.21192	316.21185	$C_{16}H_{30}NO_5^+$	9.84	0.22	fm
307.19342	307.19048	307.19039	$C_{18}H_{27}O_4^+$	9.86	0.29	jnp
284.18837	284.18567	284.18563	$C_{15}H_{26}NO_4^+$	9.64	0.14	fm – CH_4O
279.18513	279.18249	-	$C_{13}H_{27}O_6^{2+}$	-	-	ω_2
270.17740	270.17458	-	$C_{29}H_{50}NO_8^{2+}$	-	-	ω_2
261.67619	261.17179	-	$C_{29}H_{48}NO_7^{2+}$	-	-	ω_2
250.16384	250.16151	-	unassigned	-	-	-
244.82811	244.82582	-	$C_{37}H_{68}NO_{13}^{3+}$	-	-	ω_3
238.82440	238.82208	-	$C_{37}H_{66}NO_{12}^{3+}$	-	-	ω_3
232.82062	232.81846	-	$C_{37}H_{64}NO_{11}^{3+}$	-	-	ω_3
192.12827	192.12651	-	$C_{29}H_{54}NO_{10}^{3+}$	-	-	ω_3
186.12446	186.11227	-	$C_{29}H_{52}NO_9^{3+}$	-	-	ω_3
180.12056	180.11892	-	$C_{29}H_{50}NO_8^{3+}$	-	-	ω_3
174.11711	174.11553	-	$C_{29}H_{48}NO_7^{3+}$	-	-	ω_3
158.11907	158.11765	158.11756	$C_8H_{16}NO_2^+$	9.55	0.57	q
Mean Absolute Average				**9.98**	**-0.33**	
Standard Deviation				**0.49**	**0.50**	

Table A-2: Fragment ions produced by EID of Erythromycin A (precursor ion *m/z* 734.48); peaks used for internal calibration are marked by ▲

Observed *m/z* (ext cal)	**Observed m/z (int cal)**	**Theoretical m/z**	**Proposed formula**	**Mass Error (ext cal) / ppm**	**Mass error (int cal) / ppm**	**Fragment Cleavage**
734.46862	▲ 734.46833	734.46852	$C_{37}H_{68}NO_{13}^+$	0.14	-	$[M+H]^+$
716.45845	▲ 716.45806	716.45795	$C_{37}H_{66}NO_{12}^+$	0.70	-	$[M+H-H_2O]^+$
703.45105	703.45060	703.45013	$C_{36}H_{65}NO_{12}^{+\bullet}$	1.31	0.67	$[M+H-CH_3O]^{+\bullet}$
685.44003	685.43949	685.43956	$C_{36}H_{63}NO_{11}^{+\bullet}$	0.69	-0.10	$[M+H-CH_5O_2]^{+\bullet}$
674.4118	674.41121	674.411	$C_{34}H_{60}NO_{12}^+$	1.19	0.31	$[M+H-C_3H_8O]^+$
660.43248	660.43183	660.43174	$C_{34}H_{62}NO_{11}^+$	1.12	0.14	$[M+H-C_3H_6O_2]^+$

648.39613	648.39542	648.39535	$C_{32}H_{58}NO_{12}^{+}$	1.2	0.11	$[M+H-C_5H_{10}O]^{+}$
644.40121	644.40049	644.40044	$C_{33}H_{58}NO_{11}^{+}$	1.19	0.08	$[M+H-C_4H_{10}O_2]^{+}$
630.38569	630.38491	630.38479	$C_{32}H_{56}NO_{11}^{+}$	1.43	0.19	$[M+H-C_5H_{12}O_2]^{+}$
604.37000	604.36912	604.36914	$C_{30}H_{54}NO_{11}^{+}$	1.42	-0.03	ac
602.39082	602.38994	602.38987	$C_{31}H_{56}NO_{10}^{+}$	1.58	0.12	bd
584.38007	584.37913	584.37931	$C_{31}H_{54}NO_{9}^{+}$	1.30	-0.31	bd – H_2O
576.37525	▲ 576.37429	576.37422	$C_{29}H_{54}NO_{10}^{+}$	1.79	-	e
575.36735	575.36638	575.3664	$C_{29}H_{53}NO_{10}^{+\bullet}$	1.65	-0.03	e – H
574.35967	574.35870	574.35837	$C_{29}H_{52}NO_{10}^{+}$	2.26	0.57	e – H_2
560.34395	560.34294	560.34292	$C_{28}H_{50}NO_{10}^{+}$	1.84	0.04	e – CH_2
558.36474	558.36372	558.36366	$C_{29}H_{52}NO_{9}^{+}$	1.93	0.11	e – H_2O
557.3569	557.35588	557.35583	$C_{29}H_{51}NO_{9}^{+\bullet}$	1.92	0.09	e – H_3O
556.3491	556.34808	556.34801	$C_{29}H_{50}NO_{9}^{+}$	1.96	0.13	e – H_4O
542.36984	542.36878	542.36874	$C_{29}H_{50}NO_{8}^{+}$	2.03	0.07	e – H_2O_2
540.35421	540.35315	540.35309	$C_{29}H_{50}NO_{8}^{+}$	2.07	0.11	e – H_4O_2
539.34616	539.34510	539.34527	$C_{29}H_{49}NO_{8}^{+\bullet}$	1.65	-0.32	e – H_5O_2
522.34359	522.34248	522.34253	$C_{29}H_{48}NO_{7}^{+}$	2.03	-0.10	e – H_6O_3
514.33863	514.33751	514.33744	$C_{27}H_{48}NO_{8}^{+}$	2.31	0.14	f – C_2H_5O
512.29923	512.29810	512.29798	$C_{27}H_{44}O_{9}^{+\bullet}$	2.44	0.23	g – C_2H_8O
494.28857	494.28742	494.28742	$C_{27}H_{42}O_{8}^{+\bullet}$	2.33	0	g – H_2O
490.30221	490.30105	490.30106	$C_{24}H_{44}NO_{9}^{+}$	2.35	-0.02	hi
489.33095	489.32979	489.32962	$C_{25}H_{47}NO_{8}^{+\bullet}$	2.72	0.35	jk
488.28665	488.28548	488.28541	$C_{24}H_{42}NO_{9}^{+}$	2.54	0.14	hi – H_2
486.34349	486.34232	486.34252	$C_{26}H_{48}NO_{7}^{+}$	1.99	-0.41	flm
484.32813	484.32696	484.32688	$C_{26}H_{46}NO_{7}^{+}$	2.58	0.17	flm – H_2
477.28586	477.28468	477.28468	$C_{27}H_{41}O_{7}^{+}$	2.47	0	g – $C_2H_{10}O_3$
472.29168	472.29050	472.28915	$C_{24}H_{42}NO_{8}^{+}$	5.36	2.86	jk – CH_5
468.33313	468.33193	468.33196	$C_{26}H_{46}NO_{6}^{+}$	2.5	-0.06	hi – H_2O
464.30187	464.30067	464.30066	$C_{26}H_{42}NO_{6}^{+}$	2.61	0.02	hk – H_6O_3
444.29678	444.29557	444.29558	$C_{23}H_{42}NO_{7}^{+}$	2.70	-0.02	il
429.24958	429.24835	429.24829	$C_{22}H_{37}O_{8}^{+}$	3.01	0.14	np
411.23896	411.23773	411.23639	$C_{22}H_{35}O_{7}^{+}$	6.25	3.26	np – H_2O
408.27598	408.27474	408.27445	$C_{23}H_{38}NO_{5}^{+}$	3.75	0.71	ij
404.26539	404.26415	404.26427	$C_{20}H_{38}NO_{7}^{+}$	2.77	-0.3	is
401.2546	401.25336	401.25337	$C_{21}H_{37}O_{7}^{+}$	3.07	-0.02	np – CO
393.22836	393.22713	393.22717	$C_{22}H_{33}O_{6}^{+}$	3.03	-0.1	np – H_4O_2
388.27065	388.26942	388.26936	$C_{20}H_{38}NO_{6}^{+}$	3.32	0.15	is – O
383.24402	383.24279	383.24282	$C_{21}H_{35}O_{6}^{+}$	3.13	-0.08	np – CH_2O_2
381.22833	381.22710	381.22717	$C_{21}H_{33}O_{6}^{+}$	3.04	-0.18	np – CH_4O_2
375.2628	375.26156	375.26154	$C_{19}H_{37}NO_{6}^{+\bullet}$	3.36	0.05	is – CHO

367.23599	367.23480	-	$C_{37}H_{68}NO_{13}^{2+\bullet}$	-	-	ω_2
365.23347	▲ 365.23224	365.23225	$C_{21}H_{33}O_5^+$	3.34	-	fg
360.23919	360.23796	360.23806	$C_{18}H_{34}NO_6^+$	3.14	-0.28	it
349.23862	349.23740	349.23734	$C_{21}H_{33}O_4^+$	3.67	0.17	fg – O
347.22286	347.22165	347.22169	$C_{21}H_{31}O_4^+$	3.37	-0.12	fg – H_2O
342.22873	342.22752	342.2275	$C_{18}H_{32}NO_5^+$	3.59	0.06	is – H_2O
335.18642	335.18521	335.1853	$C_{19}H_{27}O_5^+$	3.34	-0.27	fguv
334.22363	334.22243	334.22241	$C_{16}H_{32}NO_6^+$	3.65	0.06	is – C_2H_2
332.24437	332.24316	332.24315	$C_{17}H_{34}NO_5^+$	3.67	0.03	is – CO
325.20214	325.20094	325.20095	$C_{18}H_{29}O_5^+$	3.66	-0.03	fg – C_3H_4
316.21303	316.21184	316.21185	$C_{16}H_{30}NO_5^+$	3.73	-0.03	is – C_2H_4O
315.18137	315.18018	-	unassigned	-	-	-
307.19155	307.19038	307.19039	$C_{18}H_{27}O_4^+$	3.78	-0.03	fg – C_3H_6O
302.19732	302.19616	302.1962	$C_{15}H_{28}NO_5^+$	3.71	-0.13	is – C_3H_6O
293.68408	293.68293	-	$C_{30}H_{53}NO_{10}^{2+}$	-	-	ω_2
289.1809	289.17976	289.17982	$C_{18}H_{25}O_3^+$	3.73	-0.21	fg – C_3H_6O
284.67875	284.67761	-	$C_{30}H_{51}NO_9^{2+}$	-	-	ω_2
279.16027	279.15915	-	unassigned	-	-	-
275.67349	275.67237	-	$C_{30}H_{49}NO_8^{2+}$	-	-	ω_2
270.68132	270.68022	-	$C_{29}H_{51}NO_8^{2+}$	-	-	ω_2
261.67596	261.67487	-	$C_{29}H_{49}NO_7^{2+}$	-	-	ω_2
260.18676	260.18568	260.18563	$C_{13}H_{26}NO_4^+$	4.34	0.19	is – $C_5H_8O_2$
258.20753	258.20645	258.20637	$C_{14}H_{28}NO_3^+$	4.49	0.31	is – $C_4H_6O_3$
251.16533	251.16427	-	unassigned	-	-	-
232.65499	232.65395	-	$C_{26}H_{43}NO_6^{2+}$	-	-	ω_2
221.15452	221.1536	-	unassigned	-	-	-
195.13888	195.13797	-	unassigned	-	-	-
193.12311	193.12221	-	unassigned	-	-	-
183.61868	183.86856	-	unassigned	-	-	-
181.12314	181.12228	-	unassigned	-	-	
176.12895	176.1281	176.12812	$C_8H_{18}NO_3^+$	4.71	-0.11	w + H_2
174.11330	▲ 174.1125	174.11247	$C_8H_{16}NO_3^+$	4.77	-	w
158.11836	158.1176	158.11756	$C_8H_{16}NO_2^+$	5.06	0.19	x
Mean Absolute Average				**2.78**	**0.14**	
Standard Deviation				**1.18**	**0.57**	

Table A-3: Fragment ions produced by CAD of Lasalocid A, Na^+ adduct (*m/z* 613.37); peaks used for internal calibration are marked by ▲

Observed m/z (locked mass 613.3)	Observed m/z (int cal)	Theoretical m/z	Proposed formula	Mass Error (ext cal) / ppm	Mass error (int cal) / ppm	Fragment Cleavage
613.37109	613.37041	613.37109	$C_{34}H_{54}O_8Na^+$	-	-1.11	$[M+Na]^+$
595.36121	▲595.36052	595.36053	$C_{34}H_{52}O_7Na^+$	1.14	-	$[M+Na-H_2O]^+$
577.35119	577.35048	577.34996	$C_{34}H_{50}O_6Na^+$	2.13	-0.02	$[M+Na-H_4O_2]^+$
569.38251	569.38180	569.38126	$C_{33}H_{54}O_6Na^+$	2.20	0.90	$[M+Na-CO_2]^+$
559.34060	559.33988	559.33940	$C_{34}H_{48}O_5Na^+$	2.15	0.95	$[M+Na-H_6O_3]^+$
551.37184	551.37112	551.37070	$C_{33}H_{52}O_5Na^+$	2.07	0.86	$[M+Na-CO_2, H_2O]^+$
497.28838	497.28765	497.28736	$C_{28}H_{42}O_6Na^+$	2.05	0.76	a
481.25706	481.25632	481.25606	$C_{27}H_{38}O_6Na^+$	2.08	0.58	b
479.27758	479.27701	479.27680	$C_{28}H_{40}O_5Na^+$	1.62	0.54	$a - H_2O$
463.24657	463.24583	463.24550	$C_{27}H_{36}O_5Na^+$	2.30	0.44	$a - H_2O, CH_4$
461.26716	461.26643	461.26623	$C_{28}H_{38}O_4Na^+$	2.02	0.71	$a - H_4O_2$
405.26190	▲405.26118	405.26115	$C_{22}H_{38}O_5Na^+$	1.85	-	c
395.26499	395.26428	-	unassigned	-	-	-
377.26691	▲377.26621	377.26623	$C_{21}H_{38}O_4Na^+$	1.80	-	d
359.25632	359.25562	359.25567	$C_{21}H_{36}O_3Na^+$	1.80	-0.14	$d - H_2O$
204.46073	204.46024	-	$C_{34}H_{54}O_8Na^{3+}$	-	-	ω_3
198.45649	198.456801	-	$C_{34}H_{52}O_7Na^{3+}$	-	-	ω_3
192.45376	192.45329	-	$C_{34}H_{50}O_6Na^{3+}$	-	-	ω_3
125.75704	125.75672	-	$C_{21}H_{38}O_4Na^{3+}$	-	-	ω_3
Mean Absolute Average				**1.94**	**0.45**	
Standard Deviation				**0.30**	**0.60**	

Table A-4: Fragment ions produced by EID of Lasalocid A, Na^+ adduct (*m/z* 613.37); peaks used for internal calibration are marked by ▲

Observed *m/z* (locked mass 613.3)	Observed m/z (int cal)	Theoretical m/z	Proposed formula	Mass Error (locked) / ppm	Mass error (int cal) / ppm	Fragment Cleavage
613.37109	▲613.37119	613.37109	$C_{34}H_{54}O_8Na^+$	0.00	0.16	$[M+Na]^+$
595.36020	▲595.36043	595.36053	$C_{34}H_{52}O_7Na^+$	-0.55	-0.17	$[M+Na-H_2O]^+$

593.39632	593.39631	-	unassigned	-	-	-
585.37662	585.37640	585.37618	$C_{33}H_{54}O_7Na^+$	0.75	0.38	$[M+Na-CO]^+$
583.32440	583.32415	583.32414	$C_{32}H_{48}O_8Na^+$	0.45	0.02	$[M+Na-C_2H_6]^+$
577.35005	577.35005	577.34996	$C_{34}H_{50}O_6Na^+$	0.16	0.16	$[M+Na-H_4O_2]^+$
575.33425	575.33431	575.33431	$C_{34}H_{48}O_6Na^+$	-0.10	0.00	$[M+Na-H_6O_2]^+$
569.38145	569.38121	569.38126	$C_{33}H_{54}O_6Na^+$	0.33	-0.09	$[M+Na-CO_2]^+$
567.36624	567.36645	567.36561	$C_{33}H_{53}O_6Na^+$	1.11	1.48	$[M+Na-CH_2O_2]^+$
559.33939	559.33934	559.33940	$C_{34}H_{48}O_5Na^+$	-0.02	-0.11	$[M+Na-H_6O_3]^+$
554.36024	554.36028	-	unassigned	-	-	-
551.37087	551.37080	551.37070	$C_{33}H_{52}O_5Na^+$	0.31	0.18	$[M+Na-CH_2O_3]^+$
543.33168	543.33160	-	unassigned	-	-	-
525.28232	525.28219	525.28227	$C_{29}H_{42}O_7Na^+$	0.10	-0.15	ac
515.35007	515.35003	515.34957	$C_{33}H_{48}O_3Na^+$	0.97	0.89	$[M+Na-CH_6O_5]^+$
509.28739	509.28723	509.28736	$C_{29}H_{42}O_6Na^+$	0.06	-0.26	ad
497.28749	497.28730	497.28736	$C_{28}H_{42}O_6Na^+$	0.26	-0.12	bd
481.25626	481.25603	481.25606	$C_{27}H_{38}O_6Na^+$	0.42	-0.06	de
479.27694	479.27672	479.27680	$C_{28}H_{40}O_5Na^+$	0.29	-0.17	bd – H_2O
473.30288	473.30259	-	unassigned	-	-	-
470.26496	470.26388	470.26389	$C_{26}H_{39}O_6Na^{+\bullet}$	2.28	-0.02	f
469.25646	469.25622	469.25606	$C_{26}H_{38}O_6Na^+$	0.85	0.34	f – H
468.28694	468.28688	-	unassigned	-	-	-
463.24574	463.24549	463.24550	$C_{27}H_{36}O_5Na^+$	0.52	-0.02	de – H_2O
461.26650	461.26630	461.26623	$C_{28}H_{38}O_4Na^+$	0.59	0.15	bd – H_4O_2
451.24567	451.24542	451.24550	$C_{26}H_{36}O_5Na^+$	0.38	-0.18	f – H_3O
447.30818	447.30814	447.30810	$C_{25}H_{44}O_5Na^+$	0.18	0.09	g
429.26393	429.26363	-	unassigned	-	-	-
414.20163	414.20131	414.20128	$C_{22}H_{31}O_6Na^{+\bullet}$	0.84	0.07	hi
405.26148	▲405.26115	405.26115	$C_{22}H_{38}O_5Na^+$	0.81	0.00	j
399.21455	399.21422	399.21420	$C_{22}H_{32}O_5Na^+$	0.88	0.05	hk
389.26663	389.26621	-	unassigned	-	-	-
387.17816	387.17781	387.17781	$C_{20}H_{28}O_6Na^+$	0.90	0.00	il
381.20389	381.20361	381.20363	$C_{22}H_{30}O_4Na^+$	0.68	-0.05	hk – H_2O
377.26659	▲377.26623	377.26623	$C_{21}H_{38}O_4Na^+$	0.95	0.00	m
376.25881	376.25839	376.25841	$C_{21}H_{37}O_4Na^+$	1.06	-0.05	m – H
375.25085	375.25050	375.25058	$C_{21}H_{36}O_4Na^+$	0.72	-0.21	m – H_2
374.20881	374.20877	-	unassigned	-	-	-
372.19098	372.19070	-	unassigned	-	-	-
371.18328	371.18296	371.18290	$C_{20}H_{28}O_5Na^+$	1.02	0.16	kl
369.16772	369.16735	369.16725	$C_{20}H_{26}O_5Na^+$	1.27	0.27	kl – H_2
361.23520	361.23479	-	unassigned	-	-	-

358.17538	358.17510	358.17507	$C_{19}H_{27}O_5Na^{+\bullet}$	0.87	0.08	n
357.16796	357.16731	357.16725	$C_{19}H_{26}O_5Na^{+}$	1.99	0.17	n – H
347.21969	347.21931	347.21928	$C_{19}H_{32}O_4Na^{+}$	1.18	0.09	-
341.17278	341.17240	341.17233	$C_{19}H_{26}O_4Na^{+}$	1.32	0.21	n – OH
319.22477	319.22438	319.22437	$C_{18}H_{32}O_3Na^{+}$	1.25	0.03	p
306.68557	306.68547	-	$C_{34}H_{54}O_8Na^{2+}$	-	-	ω_2
305.20911	305.20869	-	unassigned	-	-	-
303.22985	303.22952	303.22945	$C_{18}H_{32}O_2Na^{+}$	1.32	0.23	p – O
297.68011	297.68001	-	unassigned	-	-	-
291.19347	291.19308	291.19307	$C_{16}H_{28}O_3Na^{+}$	1.37	0.03	p – C_2H_4
288.13363	288.13323	288.13321	$C_{15}H_{21}O_4Na^{+\bullet}$	1.46	0.07	q
287.12573	287.12537	287.12538	$C_{15}H_{20}O_4Na^{+}$	1.22	-0.03	q – H
283.16056	283.16046	-	unassigned	-	-	-
277.17785	277.17746	277.17742	$C_{15}H_{26}O_3Na^{+}$	1.55	0.14	r
263.16224	263.16179	263.16177	$C_{14}H_{24}O_3Na^{+}$	1.79	0.08	r – CH_2
261.18293	261.18256	261.18250	$C_{15}H_{26}O_2Na^{+}$	1.65	0.23	r – O
259.09452	259.09413	259.09408	$C_{13}H_{16}O_4Na^{+}$	1.70	0.19	s
248.17510	248.17471	248.17468	$C_{14}H_{25}O_2Na^{+\bullet}$	1.69	0.12	tu
241.08397	241.08357	241.08352	$C_{13}H_{14}O_3Na^{+}$	1.87	0.21	s – H_2O
233.15164	233.15125	233.15120	$C_{13}H_{22}O_2Na^{+}$	1.89	0.21	s – H_4O
230.09180	230.09139	230.09134	$C_{12}H_{15}O_3Na^{+\bullet}$	2.00	0.22	v
221.15163	221.15126	221.15120	$C_{12}H_{22}O_2Na^{+}$	1.94	0.27	wx
219.10201	219.10161	-	unassigned	-	-	-
211.16968	211.16932	-	unassigned	-	-	-
204.46055	204.46044	-	$C_{34}H_{54}O_8Na^{3+}$	-	-	ω_3
166.09683	166.09651	166.09643	$C_8H_{15}O_2Na^{+\bullet}$	2.41	0.48	y
Mean Absolute Average				**1.16**	**0.28**	
Standard Deviation				**1.07**	**0.98**	

Table A-5: Fragment ions produced by CAD of *iso*-Lasalocid A, Na^+ adduct (precursor ion *m/z* 613.37); peaks used for internal calibration are marked by ▲

Observed *m/z* (locked mass 613.3)	**Observed m/z (int cal)**	**Theoretical m/z**	**Proposed formula**	**Mass Error (ext cal) / ppm**	**Mass error (int cal) / ppm**	**Fragment Cleavage**
613.37109	613.37069	613.37109	$C_{34}H_{54}O_8Na^{+}$	-	-0.65	$[M+Na]^+$
595.36092	▲ 595.36052	595.36053	$C_{34}H_{52}O_7Na^{+}$	0.66	-	$[M+Na-H_2O]^+$
577.35041	577.35002	577.34996	$C_{34}H_{50}O_6Na^{+}$	0.78	0.10	$[M+Na-H_4O_2]^+$
569.38172	569.38133	569.38126	$C_{33}H_{54}O_6Na^{+}$	0.81	0.12	$[M+Na-CO_2]^+$

559.33977	559.33938	559.33940	$C_{34}H_{48}O_5Na^+$	0.66	-0.04	$[M+Na-H_6O_3]^+$
551.37113	551.37074	551.37070	$C_{33}H_{52}O_5Na^+$	0.78	0.07	$[M+Na-CO_2, H_2O]^+$
497.28783	497.28745	497.28736	$C_{28}H_{42}O_6Na^+$	0.95	0.18	a
481.25651	481.25613	481.25606	$C_{27}H_{38}O_6Na^+$	0.94	0.15	b
479.27688	479.27686	479.27680	$C_{28}H_{40}O_5Na^+$	0.17	0.13	a – H_2O
463.24586	463.24548	463.24550	$C_{27}H_{36}O_5Na^+$	0.78	-0.04	a – H_2O, CH_4
461.26686	461.26616	461.26623	$C_{28}H_{38}O_4Na^+$	1.37	-0.15	a – H_4O_2
447.08503	447.08466	-	unassigned	-	-	-
405.26152	▲405.26117	405.26115	$C_{22}H_{38}O_5Na^+$	0.91	-	c
377.26655	▲377.26622	377.26623	$C_{21}H_{38}O_4Na^+$	0.85	-	d
359.25599	359.25566	359.25567	$C_{21}H_{36}O_3Na^+$	0.89	-0.03	d – H_2O
353.26662	353.26629	-	unassigned	-	-	-
337.27412	337.27375	337.27372	$C_{21}H_{37}O_3^+$	1.19	0.09	d – OH, Na
319.26354	319.26321	319.26316	$C_{21}H_{35}O_2^+$	1.19	0.16	d – OH,Na, H_2O
237.18519	237.18494	-	unassigned	-	-	-
219.17463	219.17440	-	unassigned	-	-	-
204.46054	204.46032	-	$C_{34}H_{54}O_8Na^{3+}$	-	-	ω_3
198.45689	198.45597	-	$C_{34}H_{52}O_7Na^{3+}$	-	-	ω_3
192.45323	192.45302	-	$C_{34}H_{50}O_6Na^{3+}$	-	-	ω_3
125.75686	125.75646	-	$C_{21}H_{38}O_4Na^{3+}$	-	-	ω_3
Mean Absolute Average				**0.86**	**0.01**	
Standard Deviation				**0.28**	**0.21**	

Table A-6: Fragment Ions produced by EID of *iso*-Lasalocid A, Na^+ adduct (precursor ion *m/z* 613.37); peaks used for internal calibration are marked by ▲

Observed *m/z* (locked mass 613.3)	**Observed m/z (int cal)**	**Theoretical m/z**	**Proposed formula**	**Mass Error (locked) / ppm**	**Mass error (int cal) / ppm**	**Fragment Cleavage**
613.37109	▲613.37105	613.37109	$C_{34}H_{54}O_8Na^+$	-	-	$[M+Na]^+$
595.36080	▲595.36058	595.36053	$C_{34}H_{52}O_7Na^+$	0.45	-	$[M+Na-H_2O]^+$
593.39581	593.39572	-	unassigned	-	-	-
577.35075	577.35056	577.34996	$C_{34}H_{50}O_6Na^+$	1.37	1.04	$[M+Na-H_4O_2]^+$
559.33949	559.33931	559.33940	$C_{34}H_{48}O_5Na^+$	0.16	-0.16	$[M+Na-H_6O_3]^+$
479.20260	479.20229	-	unassigned	-	-	-
473.30288	473.30284	-	unassigned	-	-	-
447.27454	447.27419	447.27412	$C_{26}H_{39}O_6^+$	0.94	0.16	a

431.14284	431.14247	-	unassigned	-	-	-
415.20932	415.20893	415.20911	$C_{22}H_{32}O_6Na^+$	0.51	-0.43	b
414.20143	414.20104	414.20128	$C_{22}H_{31}O_6Na^{+\bullet}$	0.36	-0.58	b - H
405.26154	▲405.26115	405.26115	$C_{22}H_{38}O_5Na^+$	0.96	-	c
403.13174	403.13135	-	unassigned	-	-	-
399.21478	399.21438	399.21420	$C_{22}H_{32}O_5Na^+$	1.45	0.45	d
377.26665	▲377.26623	377.26623	$C_{21}H_{38}O_4Na^+$	1.11	-	e
359.25598	359.25556	-	unassigned	-	-	-
319.22480	319.22436	319.22437	$C_{18}H_{32}O_3Na^+$	1.35	-0.03	f
281.05156	281.05113	-	unassigned	-	-	-
277.17784	277.17741	277.17742	$C_{15}H_{26}O_3Na^+$	1.52	-0.03	g
259.09456	259.09414	259.09408	$C_{13}H_{16}O_4Na^+$	1.85	0.23	h
248.17504	248.17462	248.17468	$C_{14}H_{25}O_2Na^{+\bullet}$	1.45	-0.24	i
221.15160	221.15120	221.15120	$C_{12}H_{22}O_2Na^+$	1.81	0	j
204.46074	204.46036	-	$C_{34}H_{54}O_8Na^{3+}$	-	-	ω_3
166.09677	166.09644	166.09643	$C_8H_{15}O_2Na^{+\bullet}$	2.05	0.06	k
Mean Absolute Average				**1.16**	**0.04**	
Standard Deviation				**0.58**	**0.42**	

Table A-7: Fragment ions produced by CAD of Lasalocid A, $NH4^+$ adduct (precursor ion *m/z* 608.42); peaks used for internal calibration are marked by ▲

Observed m/z (int cal)	Theoretical m/z	Proposed formula	Mass error (int cal) / ppm	Fragment Cleavage
591.38910	591.38915	$C_{34}H_{55}O_8^+$	-0.08	$[M\text{-}NH_3]^+$
▲573.37863	573.37858	$C_{34}H_{53}O_7^+$	-	$[M\text{-}NH_3,H_2O]^+$
▲555.36804	555.36802	$C_{34}H_{51}O_6^+$	-	$[M\text{-}NH_3,\text{-}H_4O_2]^+$
▲537.35749	537.35745	$C_{34}H_{49}O_5^+$	-	$[M\text{-}NH_3,\text{-}H_6O_3]^+$
519.34691	519.34689	$C_{34}H_{47}O_4^+$	0.04	$[M\text{-}NH_3,\text{-}H_8O_4]^+$
501.33636	501.33632	$C_{34}H_{45}O_3^+$	0.08	$[M\text{-}NH_3,\text{-}H_{10}O_5]^+$
483.32565	483.32576	$C_{34}H_{43}O_2^+$	-0.23	$[M\text{-}NH_3,\text{-}H_{12}O_6]^+$
469.29488	469.29485	$C_{29}H_{41}O_5^+$	0.06	ab – H_2O
459.27402	-	unassigned	-	-
455.27908	455.27920	$C_{28}H_{39}O_5^+$	-0.26	ac – H_2O
451.28436	451.28429	$C_{29}H_{39}O_4^+$	0.16	ab – H_4O_2
446.14937	-	unassigned	-	-
443.27966	443.27920	$C_{27}H_{39}O_5^+$	1.04	ad – H_2O
441.26356	441.26355	$C_{27}H_{37}O_5^+$	0.02	ad – H_2O, H_2
433.27388	433.27385	$C_{29}H_{37}O_3^+$	0.07	ab – H_6O_3

429.26362	429.26355	$C_{26}H_{37}O_5^+$	0.16	e
427.28456	427.28429	$C_{27}H_{39}O_4^+$	0.63	ad –H_2O, O
425.26852	425.26864	$C_{27}H_{37}O_4^+$	-0.28	ad – H_4O_2
411.25306	411.25299	$C_{26}H_{35}O_4^+$	0.17	e – H_4O_2
409.27378	409.27372	$C_{27}H_{37}O_3^+$	0.15	ad – H_4O_2, O
398.14592	-	unassigned	-	-
380.13529	-	unassigned	-	-
375.28942	-	unassigned	-	-
371.22159	371.22169	$C_{23}H_{31}O_4^+$	-0.27	fg – H_2O
365.26885	365.26864	$C_{22}H_{37}O_4^+$	0.57	h – H_2O
355.28418	355.28429	$C_{21}H_{39}O_4^+$	-0.31	i
▲337.27364	337.27372	$C_{21}H_{37}O_3^+$	-0.24	i – H_2O
335.25791	335.25807	$C_{21}H_{35}O_3^+$	-0.48	i – H_2O, H_2
335.20043	335.20056	$C_{23}H_{27}O_2^+$	-0.39	fg – H_4O_2
331.19026	331.19039	$C_{20}H_{27}O_4^+$	-0.39	fj – H_2O
325.23725	325.23734	$C_{19}H_{33}O_4^+$	-0.28	k
319.26306	319.26316	$C_{21}H_{35}O_2^+$	-0.31	i – H_4O_2
317.24750	317.24751	$C_{21}H_{33}O_2^+$	-0.03	i – H_4O_2, H_2
313.17970	313.17982	$C_{20}H_{25}O_3^+$	-0.38	fj – H_4O_2
307.22675	307.22677	$C_{19}H_{31}O_3^+$	-0.07	k – H_2O
305.17496	-	unassigned	-	-
301.25254	301.25259	$C_{21}H_{33}O^+$	-0.17	i – H_6O_3
301.17979	301.17982	$C_{19}H_{25}O_3^+$	-0.10	l – H_2O, O
299.16420	299.16417	$C_{19}H_{23}O_3^+$	0.10	l – H_4O_2
297.09820	-	unassigned	-	-
293.13829	293.13835	$C_{16}H_{21}O_5^+$	-0.20	m
289.21615	289.21615	$C_{19}H_{29}O_2^+$	0	k – H_4O_2
281.24749	281.24751	$C_{18}H_{33}O_2^+$	-0.07	n – O
279.23187	279.23186	$C_{18}H_{31}O_2^+$	0.04	n – H_2O
275.12781	275.12779	$C_{16}H_{19}O_4^+$	0.07	m – H_2O
263.23697	263.23694	$C_{18}H_{31}O^+$	0.11	n – H_2O, O
261.22133	261.22129	$C_{18}H_{29}O^+$	0.15	n – H_4O_2
259.24208	-	unassigned	-	-
255.19548	255.19547	$C_{15}H_{27}O_3^+$	0.04	p
251.20059	251.20056	$C_{16}H_{27}O_2^+$	0.12	m – H_6O_3
245.22641	-	unassigned	-	-
▲237.18494	237.18491	$C_{15}H_{25}O_2^+$	0.13	p – H_2O
233.19005	-	unassigned	-	-
219.17440	-	unassigned	-	-
219.10164	219.10157	$C_{13}H_{15}O_3^+$	0.32	q – H_2O

211.16932	-	unassigned	-	-
209.19005	-	unassigned	-	-
207.17442	-	unassigned	-	-
201.16384	-	unassigned	-	-
199.13292	199.13287	$C_{11}H_{19}O_3^+$	0.25	rs
197.15368	197.15361	$C_{12}H_{21}O_2^+$	0.36	tu
195.17442	-	unassigned	-	-
191.17951	-	unassigned	-	-
185.12563	-	unassigned	-	-
183.13804	183.13796	$C_{11}H_{19}O_2^+$	0.44	rs – O
179.12190	-	unassigned	-	-
177.16386	-	unassigned	-	-
169.12240	-	unassigned	-	-
163.14824	-	unassigned	-	-
161.13260	-	unassigned	-	-
155.14318	-	unassigned	-	-
153.12754	-	unassigned	-	-
151.11187	-	unassigned	-	-
141.09113	141.09101	$C_8H_{13}O_2^+$	0.85	v – H_2
137.13261	-	unassigned	-	-
Mean Absolute Average			**0.04**	
Standard Deviation			**0.33**	

Table A-8: Fragment ions produced by CAD of *iso*-Lasalocid A, $NH4^+$ adduct (precursor ion *m/z* 608.42); peaks used for internal calibration are marked by ▲.

Observed m/z (int cal)	Theoretical m/z	Proposed formula	Mass error (int cal) / ppm	Fragment Cleavage
591.38958	591.38915	$C_{34}H_{55}O_8^+$	0.73	$[M\text{-}NH_3]^+$
▲573.37875	573.37858	$C_{34}H_{53}O_7^+$	-	$[M\text{-}NH_3,H_2O]^+$
▲555.36801	555.36802	$C_{34}H_{51}O_6^+$	-	$[M\text{-}NH_3,\text{-}H_4O_2]^+$
▲537.35742	537.35745	$C_{34}H_{49}O_5^+$	-	$[M\text{-}NH_3,\text{-}H_6O_3]^+$
519.34685	519.34689	$C_{34}H_{47}O_4^+$	-0.08	$[M\text{-}NH_3,\text{-}H_8O_4]^+$
404.18715	-	unassigned	-	-
337.27364	337.27372	$C_{21}H_{37}O_3^+$	-0.24	a – H_2O
319.26308	319.26316	$C_{21}H_{35}O_2^+$	-0.25	a – H_4O_2
315.20680	-	unassigned	-	-

301.25262	301.25259	$C_{21}H_{33}O^+$	0.10	a – H_6O_3
289.21653	289.21615	$C_{19}H_{29}O_2^+$	1.31	b – H_4O_2
281.24756	281.24751	$C_{18}H_{33}O_2^+$	0.18	c – O
279.23184	279.23186	$C_{18}H_{31}O_2^+$	-0.07	c – H_2O
275.12766	275.12779	$C_{16}H_{19}O_4^+$	-0.47	d – H_2O
263.23696	263.23694	$C_{18}H_{31}O^+$	0.08	c – H_2O, O
255.19550	255.19547	$C_{15}H_{27}O_3^+$	0.12	e
251.20062	251.20056	$C_{16}H_{27}O_2^+$	0.24	
245.22644	-	unassigned	-	-
237.18494	237.18491	$C_{15}H_{25}O_2^+$	0.13	e – H_2O
219.17439	-	unassigned	-	-
209.19003	-	unassigned	-	-
177.11219	-	unassigned	-	-
Mean Absolute Average			**0.14**	
Standard Deviation			**0.46**	

Table A-9: Fragment ions produced by CAD of Lasalocid A, Li^+ adduct (precursor ion *m/z* 597.39); peaks used for internal calibration are marked by ▲.

Observed m/z (int cal)	Theoretical m/z	Proposed formula	Mass error (int cal) / ppm	Fragment Cleavage
▲579.38665	579.38683	$C_{34}H_{52}O_7Li^+$	-	$[M+Li-H_2O]^+$
561.37601	561.37627	$C_{34}H_{50}O_6Li^+$	-0.46	$[M+Li-H_4O_2]^+$
553.40753	553.40757	$C_{33}H_{54}O_6Li^+$	-0.07	$[M+Li-CO_2]^+$
543.36561	543.36570	$C_{34}H_{48}O_5Li^+$	-0.17	$[M+Li-H_6O_3]^+$
535.39675	535.39700	$C_{33}H_{52}O_5Li^+$	-0.47	$[M+Li-CO_2,H_2O]^+$
▲525.35508	525.35514	$C_{34}H_{46}O_4Li^+$	-	$[M+Li-H_8O_4]^+$
517.38678	517.38644	$C_{33}H_{50}O_4Li^+$	0.66	$[M+Li-CO_2,H_4O_2]^+$
499.37597	499.37587	$C_{33}H_{48}O_3Li^+$	0.20	$[M+Li-CO_2,H_6O_3]^+$
497.36042	497.36022	$C_{33}H_4O_3Li^+$	0.40	$[M+Li-CO_2,H_6O_3, H_2]^+$
486.68660	-	unassigned	-	-
483.29302	483.29292	$C_{33}H_{46}O_3Li^+$	0.21	ab
481.31356	481.31365	$C_{28}H_{42}O_6Li^+$	-0.19	cd
465.28253	465.28235	$C_{27}H_{38}O_6Li^+$	0.39	bd – H_2
463.30310	463.30309	$C_{28}H_{40}O_{45}Li^+$	0.02	cd – H_2O
457.32899	-	unassigned	-	-
447.27186	447.27179	$C_{27}H_{36}O_5Li^+$	0.16	bd – H_2O, H_2

445.29257	445.29253	$C_{28}H_{38}O_4Li^+$	0.09	cd – H_4O_2
▲437.32411	437.32382	$C_{27}H_{42}O_4Li^+$	-	bd – O_2
429.26141	429.26122	$C_{27}H_{34}O_4Li^+$	0.44	bd – H_4O_2, H_2
427.28224	427.28196	$C_{28}H_{36}O_3Li^+$	0.66	cd – H_4O_2
421.29263	421.29252	$C_{26}H_{38}O_4Li^+$	0.26	e – HO_2
419.31354	-	unassigned	-	-
415.33960	-	unassigned	-	-
406.15216	-	unassigned	-	-
403.28240	-	unassigned	-	-
401.30287	-	unassigned	-	-
397.32923	-	unassigned	-	-
389.28775	389.28743	$C_{27}H_{42}O_4Li^+$	0.82	f – H_2
384.28043	-	unassigned	-	-
375.30841	375.30816	$C_{22}H_{40}O_4Li^+$	0.67	f - O
▲361.29241	361.29251	$C_{21}H_{38}O_4Li^+$	-0.28	g
343.28202	343.28202	$C_{21}H_{36}O_3Li^+$	0.00	g – H_2O
337.29271	-	unassigned	-	-
331.24580	331.24556	$C_{19}H_{32}O_4Li^+$	0.72	h
313.23525	313.23499	$C_{19}H_{30}O_3Li^+$	0.83	h – H_2O
307.18827	307.18804	$C_{19}H_{24}O_3Li^+$	0.75	i
298.19947	-	$C_{34}H_{54}O_8Li^{2+}$	-	ω_2
289.69454	-	$C_{34}H_{52}O_7Li^{2+}$	-	ω_2
280.68916	-	$C_{34}H_{50}O_6Li^{2+}$	-	ω_2
271.68387	-	$C_{34}H_{48}O_5Li^{2+}$	-	ω_2
267.69942	-	$C_{33}H_{52}O_5Li^{2+}$	-	ω_2
247.18836	-	unassigned	-	-
245.20906	-	unassigned	-	-
232.64205	-	$C_{27}H_{38}O_6Li^{2+}$	-	ω_2
223.63666	-	$C_{27}H_{36}O_5Li^{2+}$	-	ω_2
222.64701	-	$C_{28}H_{38}O_4Li^{2+}$	-	ω_2
199.13626	-	$C_{34}H_{54}O_8Li^{3+}$	-	ω_3
193.13255	-	$C_{34}H_{52}O_7Li^{3+}$	-	ω_3
187.12880	-	$C_{34}H_{50}O_6Li^{3+}$	-	ω_3
180.64668	-	$C_{21}H_{38}O_4Li^{2+}$	-	ω_2
154.43674	-	$C_{19}H_{24}O_3Li^{2+}$	-	ω_2
149.35180	-	$C_{34}H_{54}O_8Li^{4+}$	-	ω_4
144.84905	-	unassigned	-	-
140.34625	-	$C_{34}H_{52}O_7Li^{4+}$	-	ω_4
135.84350	-	$C_{34}H_{48}O_5Li^{4+}$	-	ω_4
133.85122	-	$C_{33}H_{52}O_5Li^{4+}$	-	ω_4

120.32230	-	$C_{21}H_{38}O_4Li^{3+}$	-	ω_3
Mean Absolute Average		**0.27**		
Standard Deviation		**0.40**		

Table A-10: Fragment ions produced by EID of Lasalocid A, Li^+ adduct (precursor ion *m/z* 597.39); peaks used for internal calibration are marked by ▲

Observed m/z (int cal)	Theoretical m/z	Proposed formula	Mass error (int cal) / ppm	Fragment Cleavage
595.38132	595.38175	$C_{34}H_{52}O_8Li^+$	-0.72	$[M+Li–H_2]^+$
▲579.38683	579.38683	$C_{34}H_{52}O_7Li^+$	-	$[M+Li-H_2O]^+$
561.37640	561.37627	$C_{34}H_{50}O_6Li^+$	0.23	$[M+Li-H_4O_2]^+$
543.36484	543.36570	$C_{34}H_{48}O_5Li^+$	-1.58	$[M+Li-H_6O_3]^+$
530.24634	-	unassigned	-	-
509.30793	509.30851	$C_{29}H_{42}O_7Li^+$	-1.14	ae – H_2
481.31334	481.31365	$C_{28}H_{42}O_6Li^+$	-0.64	cd
463.30303	463.30309	$C_{28}H_{40}O_{45}Li^+$	-0.13	cd – H_2O
457.32861	-	unassigned	-	-
447.27169	447.27179	$C_{27}H_{36}O_5Li^+$	-0.22	bd – H_2O, H_2
445.29225	445.29253	$C_{28}H_{38}O_4Li^+$	-0.63	cd – H_4O_2
398.22748	398.22752	$C_{22}H_{31}O_6Li^{+\bullet}$	-0.10	gh
389.28737	389.28743	$C_{22}H_{38}O_5Li^+$	-0.15	f
383.24035	383.24043	$C_{22}H_{32}O_5Li^+$	-0.21	hi
371.20388	371.20404	$C_{20}H_{28}O_6Li^+$	-0.43	gj
▲361.29246	361.29251	$C_{21}H_{38}O_4Li^+$	-	k
343.28183	343.28202	$C_{21}H_{36}O_3Li^+$	-0.55	k – H_2O
337.29244	-	unassigned	-	-
332.25347	332.25334	$C_{19}H_{33}O_4Li^{+\bullet}$	0.39	l
325.19853	325.19856	$C_{19}H_{26}O_4Li^+$	-0.09	m – H_2
307.18793	307.18800	$C_{19}H_{24}O_3Li^+$	-0.23	m – H_2, H_2O
303.25061	303.25060	$C_{18}H_{32}O_3Li^+$	0.03	n - H
289.69309	-	unassigned	-	-
287.25567	287.25569	$C_{18}H_{32}O_2Li^+$	-0.07	n - OH
275.21894	-	unassigned	-	-
261.20344	261.20368	$C_{15}H_{26}O_3Li^+$	-0.92	p - H
▲247.18801	247.18803	$C_{14}H_{24}O_3Li^+$	-	qr

245.20884	245.20886	$C_{15}H_{26}O_2Li^+$	-0.08	p - OH
243.12040	243.12031	$C_{13}H_{16}O_4Li^+$	0.37	s
237.65130	-	unassigned	-	-
232.20096	232.20091	$C_{14}H_{25}O_2Li^{+\bullet}$	0.22	qt - H
225.10971	-	unassigned	-	-
205.17747	205.17744	$C_{12}H_{22}O_2Li^+$	0.15	tv
199.13526	-	$C_{34}H_{54}O_8Li^{3+}$	-	ω_3
189.14610	189.14614	$C_{11}H_{18}O_2Li^+$	-0.21	tu – H_2
172.07061	172.07062	$C_9H_9O_3Li^{+\bullet}$	-0.06	w
149.35101	-	$C_{34}H_{54}O_8Li^{4+}$	-	ω_4
119.48152	-	$C_{34}H_{54}O_8Li^{5+}$	-	ω_5
Mean Absolute Average			**-0.27**	
Standard Deviation			**0.47**	

Table A-11: Fragment ions produced by CAD of *iso*-Lasalocid A, Li^+ adduct (precursor ion *m/z* 597.39); peaks used for internal calibration are marked by ▲.

Observed m/z (int cal)	Theoretical m/z	Proposed formula	Mass error (int cal) / ppm	Fragment Cleavage
▲579.38673	579.38683	$C_{34}H_{52}O_7Li^+$	-	$[M+Li-H_2O]^+$
561.37621	561.37627	$C_{34}H_{50}O_6Li^+$	-0.11	$[M+Li-H_4O_2]^+$
553.40736	553.40757	$C_{33}H_{54}O_6Li^+$	-0.38	$[M+Li-CO_2]^+$
543.36566	543.36570	$C_{34}H_{48}O_5Li^+$	-0.07	$[M+Li-H_6O_3]^+$
535.39674	535.39700	$C_{33}H_{52}O_5Li^+$	-0.49	$[M+Li-CO_2,H_2O]^+$
517.38638	517.38644	$C_{33}H_{50}O_4Li^+$	-0.12	$[M+Li-CO_2,H_4O_2]^+$
499.37587	499.37587	$C_{33}H_{48}O_3Li^+$	0	$[M+Li-CO_2,H_6O_3]^+$
483.29302	483.29292	$C_{33}H_{46}O_3Li^+$	0.21	ab
481.31367	481.31365	$C_{28}H_{42}O_6Li^+$	0.04	cd
465.28243	465.28235	$C_{27}H_{38}O_6Li^+$	0.17	bd – H_2
463.30312	463.30309	$C_{28}H_{40}O_{45}Li^+$	0.06	cd – H_2O
457.32894	-	unassigned	-	-
447.27184	447.27179	$C_{27}H_{36}O_5Li^+$	0.11	bd – H_2O, H_2
445.29255	445.29253	$C_{28}H_{38}O_4Li^+$	0.04	cd – H_4O_2
▲437.32394	437.32382	$C_{27}H_{42}O_4Li^+$	-	bd – O_2
421.21977	-	unassigned	-	-
415.16882	-	unassigned	-	-
401.15319	-	unassigned	-	-
397.32907	-	unassigned	-	-

389.28741	389.28743	$C_{22}H_{38}O_5Li^+$	-0.05	e – H_2
383.27694	-	unassigned	-	-
375.30818	375.30818	$C_{22}H_{40}O_4Li^+$	0	e - O
▲361.29246	361.29251	$C_{21}H_{38}O_4Li^+$	-	f
343.28201	343.28202	$C_{21}H_{36}O_3Li^+$	-0.03	f – H_2O
337.29258	-	unassigned	-	-
331.24561	331.24556	$C_{19}H_{32}O_4Li^+$	0.15	g
313.23503	313.23499	$C_{19}H_{30}O_3Li^+$	0.13	g – H_2O
309.26112	-	unassigned	-	-
298.69887	-	$C_{34}H_{54}O_8Li^{2+}$	-	ω_2
289.69359	-	unassigned	-	-
283.10656	-	unassigned	-	-
271.09022	-	unassigned	-	-
261.20377	261.20368	$C_{15}H_{26}O_3Li^+$	0.34	h
252.14190	-	unassigned	-	-
247.18813	247.18803	$C_{14}H_{24}O_3Li^+$	0.40	ij
245.20906	245.20886	$C_{15}H_{26}O_2Li^+$	0.82	h - O
243.09533	-	unassigned	-	-
239.14665	239.14655	$C_{11}H_{20}O_5Li^+$	0.42	jk
236.12825	-	unassigned	-	-
233.10558	-	unassigned	-	-
227.10039	-	unassigned	-	-
199.13560	-	$C_{34}H_{54}O_8Li^{3+}$	-	ω_3
193.13188	-	$C_{34}H_{52}O_7Li^{3+}$	-	ω_3
187.12823	-	$C_{34}H_{50}O_6Li^{3+}$	-	ω_3
180.64642	-	$C_{21}H_{38}O_4Li^{2+}$	-	ω_2
170.04255	-	unassigned	-	-
120.43199	-	$C_{21}H_{38}O_4Li^{3+}$	-	ω_3
96.21726	-	noise	-	-
Mean Absolute Average			**0.08**	
Standard Deviation			**0.28**	

Table A-12: Fragment ions produced by EID of *iso*-Lasalocid A, Li^+ adduct (precursor ion *m/z* 597.39); peaks used for internal calibration are marked by ▲.

Observed m/z (int cal)	Theoretical m/z	Proposed formula	Mass error (int cal) / ppm	Fragment Cleavage
▲579.38653	579.38683	$C_{34}H_{52}O_7Li^+$	-	$[M+Li-H_2O]^+$

557.22609	-	unassigned	-	-
541.27305	-	unassigned	-	-
513.24205	-	unassigned	-	-
499.22644	-	unassigned	-	-
485.21081	-	unassigned	-	-
415.16887	-	unassigned	-	-
▲399.23549	399.23539	$C_{22}H_{32}O_6Li^+$	0.25	ab
389.28745	389.28743	$C_{22}H_{38}O_5Li^+$	0.05	c + H_2
385.21982	385.21974	$C_{21}H_{30}O_6Li^+$	0.21	ab – CH_2
383.24032	383.24043	$C_{22}H_{32}O_5Li^+$	-0.29	ad
371.20430	371.20404	$C_{20}H_{28}O_6Li^+$	0.70	be
▲361.29258	361.29251	$C_{21}H_{38}O_4Li^+$	-	f
343.28206	343.28202	$C_{21}H_{36}O_3Li^+$	0.12	f – H_2O
337.29263	-	unassigned	-	-
303.25060	303.25060	$C_{18}H_{32}O_3Li^+$	0	g
298.69900	-	$C_{34}H_{54}O_8Li^{2+}$	-	ω_2
275.21947	275.21930	$C_{16}H_{28}O_3Li^+$	0.62	h – H_4O_2, H_2
▲261.20365	261.20368	$C_{15}H_{26}O_3Li^+$	-0.11	i
236.12821	-	unassigned	-	-
199.13526	-	$C_{34}H_{54}O_8Li^{3+}$	-	ω_3
166.41079	-	unassigned	-	-
119.48049	-	$C_{34}H_{54}O_8Li^{5+}$	-	ω_5
Mean Absolute Average			**0.20**	
Standard Deviation			**0.35**	

Table A-13: Fragment ions produced by CAD/EID of Lasalocid A, Li^+ adduct (precursor ion *m/z* 597.39 fragmented by CAD, followed by *m/z* 361.29 fragmented by EID); peaks used for internal calibration are marked by ▲.

Observed m/z (int cal)	Theoretical m/z	Proposed formula	Mass error (int cal) / ppm	Fragment Cleavage
361.29203	361.29251	$C_{21}H_{38}O_4Li^+$	-1.33	$[M+Li]^+$
▲ 343.28202	343.28195	$C_{21}H_{26}O_3Li^+$	-	$[M+Li-H_2O]^+$
331.24499	331.24551	$C_{19}H_{32}O_4Li^+$	-1.57	f
▲261.20358	261.20365	$C_{15}H_{26}O_3Li^+$	-	a

247.18805	247.18803	$C_{14}H_{24}O_3Li^+$	0.08	b
▲ 205.17748	205.17746	$C_{12}H_{22}O_2Li^+$	-	cd
189.14614	189.14614	$C_{11}H_{18}O_2Li^+$	0.00	de – H_2
180.64633	-	$C_{21}H_{38}O_4Li^{2+}$	-	ω_2
120.43177	-	$C_{21}H_{38}O_4Li^{3+}$	-	ω_3
90.32330	-	$C_{21}H_{38}O_4Li^{4+}$	-	ω_4
Mean Absolute Average			**-0.94**	
Standard Deviation			**0.73**	

Table A-14: Fragment ions produced by CAD/EID of *iso*-Lasalocid A, Li^+ adduct (precursor ion *m/z* 597.39 fragmented by CAD, followed by *m/z* 361.29 fragmented by EID); peaks used for internal calibration are marked by ▲.

Observed m/z (int cal)	Theoretical m/z	Proposed formula	Mass error (int cal) / ppm	Fragment Cleavage
361.29265	361.29251	$C_{21}H_{38}O_4Li^+$	0.39	$[M+Li]^+$
▲ 303.25057	303.25064	$C_{18}H_{32}O_3Li^+$	-	a
273.20347	273.20365	$C_{16}H_{26}O_3Li^+$	-0.66	bc – H_2
▲261.20373	261.20365	$C_{15}H_{26}O_3Li^+$	-	d
245.20875	245.20874	$C_{15}H_{26}O_2Li^+$	0.04	def
217.17747	217.17746	$C_{13}H_{22}O_2Li^+$	0.05	g
▲ 205.17748	205.17746	$C_{12}H_{22}O_2Li^+$	-	fh
180.14598	-	$C_{21}H_{38}O_4Li^{2+}$	-	ω_2
120.43090	-	$C_{21}H_{38}O_4Li^{3+}$	-	ω_3
96.21726	-	noise	-	-
90.32318	-	$C_{21}H_{38}O_4Li^{4+}$	-	ω_4
Mean Absolute Average			**-0.05**	
Standard Deviation			**0.38**	

Table A-15: CAD fragments of Actinomycin D (H^+); $[M+H]^+$ *m/z* 1255.63575

Expt. *m/z*	Theo. *m/z*	Proposed Formula	Mass Error (ppm)	Fragment Cleavage
▲1227.64075	1227.64084	$C_{61}H_{87}N_{12}O_{15}^+$	-	$[M+H - CO]^+$
974.46184	974.46181	$C_{48}H_{64}N_9O_{13}^+$	0.03	ab
▲956.45129	956.45124	$C_{48}H_{62}N_9O_{12}^+$	-	ab – H_2O

928.45644	928.45633	$C_{47}H_{62}N_9O_{11}^+$	0.12	cd
875.39345	875.9340	$C_{43}H_{55}N_8O_{12}^+$	0.06	ae
▲857.38288	857.38283	$C_{43}H_{53}N_8O_{11}^+$	-	ae – H_2O
829.38784	829.38792	$C_{42}H_{53}N_8O_{10}^+$	-0.10	cf
657.26635	657.26674	$C_{34}H_{37}N_6O_8^+$	-0.60	bcgh
558.19828	558.19832	$C_{29}H_{28}N_5O_7^+$	-0.07	bcgi
▲459.12992	459.12991	$C_{24}H_{19}N_4O_6^+$	-	cegi
428.69598	-	ω_2	-	-
418.55413	-	ω_3	-	-
399.26020	399.26020	$C_{19}H_{35}N_4O_5^+$	0.00	jk
251.13211	-	ω_5	-	-
	Mean Absolute Average		**0.12**	
	Standard Deviation		**0.18**	

Table A-16: EID fragments of Actinomycin D (H^+); $[M+H]^+$ *m/z* 1255.63575

Expt. *m/z*	**Theo. *m/z***	**Proposed Formula**	**Mass Error (ppm)**	**Fragment Cleavage**
1227.64165	1227.64084	$C_{61}H_{87}N_{12}O_{15}^+$	0.66	$[M+H - CO]^+$
1211.64618	1211.64592	$C_{61}H_{85}N_{12}O_{14}^+$	0.21	$[M+H – CO_2]^+$
1209.63127	1209.63027	$C_{61}H_{83}N_{12}O_{14}^+$	0.83	$[M+H –CO_2 –H_2O]^+$
1183.61508	1183.61462	$C_{59}H_{83}N_{12}O_{14}^+$	0.39	lm
1156.56816	1156.56734	$C_{57}H_{78}N_{11}O_{15}^+$	0.71	en
1142.55421	1142.55437	$C_{59}H_{74}N_{12}O_{12}^+$	-0.14	$[M+H-H_8O_4-C_3H_5]^+$
1127.54180	1127.54079	$C_{56}H_{75}N_{10}O_{15}^+$	0.90	eqr
1124.54153	1124.54112	$C_{56}H_{74}N_{11}O_{14}^+$	0.36	cp
1098.56477	-	unassigned	-	-
1084.54778	-	unassigned	-	-
1057.49868	1057.49892	$C_{52}H_{69}N_{10}O_{14}^+$	-0.23	ft
1025.51443	-	unassigned	-	-
1012.51443	-	unassigned	-	-
974.46146	974.46181	$C_{48}H_{64}N_9O_{13}^+$	-0.36	ab
972.44299	-	unassigned	-	-
▲956.45126	956.45124	$C_{48}H_{62}N_9O_{12}^+$	-	ab – H_2O

938.44101	-	unassigned	-	-
928.45676	928.45633	$C_{47}H_{62}N_9O_{11}^+$	0.46	cd
875.39296	875.39340	$C_{43}H_{55}N_8O_{12}^+$	-0.45	ae
▲857.38274	857.38283	$C_{43}H_{53}N_8O_{11}^+$	-	ae - H_2O
839.37237	839.37227	$C_{43}H_{51}N_8O_{10}^+$	0.12	ae – H_4O_2
829.38744	829.38792	$C_{42}H_{53}N_8O_{10}^+$	-0.58	cf
825.35741	825.35662	$C_{42}H_{49}N_8O_{10}^+$	0.96	ae – H_4O_2 –CH_2
813.39406	813.39300	$C_{42}H_{53}N_8O_9^+$	1.30	ae – H_2O –CO_2
803.37273	803.37227	$C_{40}H_{51}N_8O_{10}^+$	0.57	fm
776.36116	776.36137	$C_{39}H_{50}N_7O_{10}^+$	-0.27	u
774.34555	774.34572	$C_{39}H_{48}N_7O_{10}^+$	-0.22	u – H_2
760.33055	760.33007	$C_{38}H_{46}N_7O_{10}^+$	0.63	u – H_2 –CH_2
758.31444	758.31442	$C_{38}H_{44}N_7O_{10}^+$	0.03	u – CH_2 -$2H_2$
744.29930	744.29877	$C_{37}H_{42}N_7O_{10}^+$	0.71	u – $2CH_2$ -$2H_2$
726.28858	726.28820	$C_{37}H_{40}N_7O_9^+$	0.52	u – $2CH_2$ -$2H_2$ –H_2O
686.29370	686.29329	$C_{35}H_{40}N_7O_8^+$	0.60	u – $3CH_2$ -H_2 –H_2O -CO
675.27686	675.27730	$C_{34}H_{39}N_6O_9^+$	-0.65	bcgh + H_2O
657.26677	657.26674	$C_{34}H_{37}N_6O_8^+$	0.05	bcgh
655.25031	655.25109	$C_{34}H_{35}N_6O_8^+$	-1.19	bcgh – H_2
645.26695	645.26674	$C_{33}H_{37}N_6O_8^+$	0.33	bcgh - C
627.81997	-	ω_2	-	-
576.19840	576.20889	$C_{29}H_{30}N_5O_8^+$	-0.38	bcgi + H_2O
▲558.19840	558.19832	$C_{29}H_{28}N_5O_7^+$	-	bcgi
556.18206	556.18267	$C_{29}H_{26}N_5O_7^+$	-1.10	bcgi – H_2
546.19773	-	unassigned	-	-
542.20350	542.20341	$C_{29}H_{28}N_5O_6^+$	0.17	bcgi - O
530.20344	530.20341	$C_{28}H_{28}N_5O_6^+$	0.06	bcgi - CO
514.20801	514.20850	$C_{28}H_{28}N_5O_5^+$	-0.95	bcgi – CO_2
508.27650	508.27658	$C_{24}H_{38}N_5O_7^+$	-0.16	v
498.32874	-	unassigned	-	-
477.14075	477.14048	$C_{24}H_{21}N_4O_7^+$	0.57	cegi + H_2O
▲459.12998	459.12991	$C_{24}H_{19}N_4O_6^+$	-	cegi
433.15064	433.15065	$C_{23}H_{21}N_4O_5^+$	-0.02	cegi + H_2 -CO
431.13515	431.13500	$C_{23}H_{19}N_4O_5^+$	0.35	cfgi
428.70063	-	ω_2	-	-
418.56138	-	ω_3	-	-

399.26009	399.26020	$C_{19}H_{35}N_4O_5^+$	-0.28	jk
381.24968	381.24963	$C_{19}H_{33}N_4O_4^+$	0.13	kx
354.23861	354.23873	$C_{18}H_{32}N_3O_4^+$	-0.34	lw
318.82712	-	ω_2	-	-
313.91508	-	ω_3	-	-
300.19169	300.19178	$C_{14}H_{26}N_3O_4^+$	-0.30	nx + H_2O
285.80253	-	ω_3	-	-
282.18121	282.18122	$C_{14}H_{24}N_3O_3^+$	-0.04	nx
268.16553	268.16557	$C_{13}H_{22}N_3O_3^+$	-0.15	nx – CH_2
169.09707	169.09715	$C_8H_{13}N_2O_2^+$	-0.47	np
	Mean Absolute Average		**0.45**	
	Standard Deviation		**0.32**	

Table A-17: EID fragments of Actinomycin D (Na^+); $[M+Na]^+$ *m/z* 1277.61770

Expt. *m/z*	**Theo. *m/z***	**Proposed Formula**	**Mass Error (ppm)**	**Fragment Cleavage**
1249.62374	1249.62278	$C_{61}H_{86}N_{12}O_{15}Na^+$	0.77	$[M+H - CO]^+$
1233.62829	1233.62787	$C_{61}H_{86}N_{12}O_{14}Na^+$	0.34	ab
1220.59748	1220.59623	$C_{60}H_{83}N_{11}O_{15}Na^+$	1.02	cd
1205.59618	1205.59657	$C_{59}H_{82}N_{12}O_{14}Na^+$	-0.32	ae
1180.56572	1180.56493	$C_{57}H_{79}N_{11}O_{15}Na^+$	0.67	fg
▲1164.53373	1164.53363	$C_{56}H_{75}N_{11}O_{15}Na^+$	-	hi
▲1146.52297	1146.52307	$C_{56}H_{73}N_{11}O_{14}Na^+$	-	hi – H_2O
1136.53958	1136.53872	$C_{55}H_{75}N_{11}O_{14}Na^+$	0.76	dh
1120.54436	1120.54380	$C_{55}H_{75}N_{11}O_{13}Na^+$	0.50	dj
1051.45018	1051.44957	$C_{50}H_{64}N_{10}O_{14}Na^+$	0.58	kn
1049.50844	1049.50669	$C_{52}H_{70}N_{10}O_{12}Na^+$	1.67	jm
1033.43653	1033.43900	$C_{50}H_{62}N_{10}O_{13}Na^+$	-2.39	kn – H_2O
▲978.43318	978.43319	$C_{48}H_{61}N_9O_{12}Na^+$	-	jr
950.43770	950.43827	$C_{47}H_{61}N_9O_{11}Na^+$	-0.60	jl – H_2
934.44378	934.44336	$C_{47}H_{61}N_9O_{10}Na^+$	0.45	jl – H_2O
896.39034	896.39132	$C_{43}H_{55}N_9O_{11}Na^+$	-1.09	gj + NH_3
879.36479	879.36478	$C_{43}H_{52}N_8O_{11}Na^+$	0.01	gj – H_2

865.34907	865.34913	$C_{42}H_{50}N_8O_{11}Na^+$	-0.07	gj – CH_4
853.38494	853.38551	$C_{42}H_{54}N_8O_{10}Na^+$	-0.67	js
837.35420	837.35421	$C_{41}H_{50}N_8O_{10}Na^+$	-0.01	js – CH_4
825.35420	825.35421	$C_{40}H_{50}N_8O_{10}Na^+$	-0.01	as
821.35941	821.35930	$C_{41}H_{50}N_8O_9Na^+$	0.13	js – CH_2 –H_2O
796.32756	796.32766	$C_{39}H_{47}N_7O_{10}Na^+$	-0.13	t
770.34857	770.34840	$C_{38}H_{49}N_7O_9Na^+$	0.22	u
766.27997	766.28071	$C_{37}H_{41}N_7O_{10}Na^+$	-0.97	t – CH_3 –H_2 –NH_3
740.30069	740.30145	$C_{36}H_{43}N_7O_9Na^+$	-1.03	u – C_2H_6
683.24275	683.24360	$C_{33}H_{36}N_6O_9Na^+$	-1.24	jrvw – CH_2
657.26443	657.26433	$C_{32}H_{38}N_6O_8Na^+$	0.15	uxy – CH_2
530.25822	530.25852	$C_{24}H_{37}N_5O_7Na^+$	-0.57	λ
504.27896	504.27926	$C_{23}H_{39}N_5O_6Na^+$	-0.59	σ
447.22044	-	unassigned	-	-
	Mean Absolute Average		**0.63**	
	Standard Deviation		**0.55**	

Table A-18: EID fragments of Actinomycin D (Li^+); $[M+Li]^+$ *m/z* 1261.64393

Expt. *m/z*	**Theo. *m/z***	**Proposed Formula**	**Mass Error (ppm)**	**Fragment Cleavage**
1247.62815	1247.62839	$C_{61}H_{85}N_{12}O_{16}Li^+$	-0.19	$[M+H – CH_2]^+$
▲1233.64950	1233.64913	$C_{61}H_{86}N_{12}O_{15}Li^+$	-	$[M+H – CO]^+$
1217.65446	1217.65421	$C_{61}H_{86}N_{12}O_{14}Li^+$	0.21	$[M+H – CO_2]^+$
1204.62130	1204.62247	$C_{60}H_{83}N_{11}O_{15}Li^+$	-0.97	ab
1189.62270	-	unassigned	-	-
1174.59207	-	unassigned	-	-
1164.59303	-	unassigned	-	-
▲1148.55956	1148.55998	$C_{56}H_{75}N_{11}O_{15}Li^+$	-	cd
▲1130.54941	1130.54942	$C_{56}H_{73}N_{11}O_{14}Li^+$	-	cd – H_2O
1120.56370	1120.56507	$C_{55}H_{75}N_{11}O_{14}Li^+$	-1.22	bc
1104.57073	1104.57015	$C_{55}H_{75}N_{11}O_{13}Li^+$	0.53	be
1086.55903	1086.55959	$C_{55}H_{83}N_{11}O_{12}Li^+$	-0.52	be – H_2O

1059.47571	-	unassigned	-	-
1035.47576	1035.47591	$C_{50}H_{64}N_{10}O_{14}Li^+$	-0.14	fg
1017.46607	1017.46524	$C_{50}H_{62}N_{10}O_{13}Li^+$	0.82	fg – H_2O
▲962.45961	962.45953	$C_{48}H_{61}N_9O_{12}Li^+$	-	ej
934.46489	934.46461	$C_{47}H_{61}N_9O_{11}Li^+$	0.30	ek – H_2
918.47035	918.46959	$C_{47}H_{61}N_9O_{10}Li^+$	0.83	ek – CH_2
880.41758	880.41756	$C_{43}H_{55}N_9O_{11}Li^+$	0.02	eg
863.39104	863.39110	$C_{43}H_{52}N_8O_{11}Li^+$	-0.07	el – H_2
849.37557	849.37545	$C_{42}H_{50}N_8O_{11}Li^+$	0.14	el – CH_4
837.41172	837.41183	$C_{42}H_{54}N_8O_{10}Li^+$	-0.13	em
821.38081	821.38053	$C_{41}H_{50}N_8O_{10}Li^+$	0.34	em – CH_4
809.38036	809.38045	$C_{40}H_{54}N_8O_{10}Li^+$	-0.11	mn
797.38062	797.38045	$C_{39}H_{50}N_8O_{10}Li^+$	0.21	p + NH_3
780.35410	780.35390	$C_{39}H_{47}N_7O_{10}Li^+$	0.26	p
754.37446	754.37463	$C_{38}H_{49}N_7O_9Li^+$	-0.23	p – CH_2O
750.30707	750.30702	$C_{37}H_{41}N_7O_{10}Li^+$	0.07	p – NH_3 –CH_3
724.32763	724.32776	$C_{36}H_{43}N_7O_9Li^+$	-0.18	q – C_2H_4
653.29010	-	unassigned	-	-
630.83735	-	ω_2	-	-
514.28480	-	unassigned	-	-
431.24756	-	unassigned	-	-
420.56211	-	ω_3	-	-
298.17595	-	unassigned	-	-
252.33934	-	ω	-	-
		Mean Absolute Average	**0.36**	
		Standard Deviation	**0.33**	

Table A-19: Multiple ion isolation and EID fragments of Actinomycin D (Na^+); $[M+Na]^+$ *m/z* 1277.61770

Expt. *m/z*	**Theo. *m/z***	**Proposed Formula**	**Mass Error (ppm)**	**Fragment Cleavage**
1249.62249	1249.62278	$C_{61}H_{86}N_{12}O_{15}Na^+$	-0.23	$[M+H - CO]^+$
1233.62787	1233.62787	$C_{61}H_{86}N_{12}O_{14}Na^+$	0.00	ab

1220.59637	1220.59623	$C_{60}H_{83}N_{11}O_{15}Na^+$	0.11	cd
1205.59668	1205.59657	$C_{59}H_{82}N_{12}O_{14}Na^+$	0.09	ae
1189.56510	1189.56527	$C_{58}H_{78}N_{12}O_{14}Na^+$	-0.14	ae – CH_4
1180.56506	1180.56493	$C_{57}H_{79}N_{11}O_{15}Na^+$	0.11	fg
1164.53330	1164.53363	$C_{56}H_{75}N_{11}O_{15}Na^+$	-0.28	hi
1146.52274	1146.52307	$C_{56}H_{73}N_{11}O_{14}Na^+$	-0.29	hi – H_2O
1136.53848	1136.53872	$C_{55}H_{75}N_{11}O_{14}Na^+$	-0.21	dh
1120.54370	1120.54380	$C_{55}H_{75}N_{11}O_{13}Na^+$	-0.09	dj
1118.52751	1118.52815	$C_{55}H_{73}N_{11}O_{13}Na^+$	-0.57	dj – H_2
1109.52732	1109.52782	$C_{54}H_{74}N_{10}O_{14}Na^+$	-0.45	kl
1107.51161	1107.51217	$C_{54}H_{74}N_{10}O_{14}Na^+$	-0.51	kl – H_2
1102.53281	1102.53324	$C_{55}H_{73}N_{11}O_{12}Na^+$	-0.39	dj – H_2O
1092.51214	1092.51250	$C_{53}H_{71}N_{11}O_{13}Na^+$	-0.33	ad
1075.48514	1075.48595	$C_{53}H_{68}N_{10}O_{13}Na^+$	-0.75	ad – NH_3
1065.50165	1065.50160	$C_{52}H_{70}N_{10}O_{13}Na^+$	0.05	hm
1051.44924	1051.44957	$C_{50}H_{64}N_{10}O_{14}Na^+$	-0.31	kn
1049.50658	1049.50669	$C_{52}H_{70}N_{10}O_{12}Na^+$	-0.10	jm
1047.49069	1047.49104	$C_{52}H_{68}N_{10}O_{12}Na^+$	-0.33	jm – H_2
1033.43861	1033.43900	$C_{50}H_{62}N_{10}O_{13}Na^+$	-0.38	kn – H_2O
1017.44441	1017.44409	$C_{50}H_{62}N_{10}O_{12}Na^+$	0.31	kn – H_2O_2
1007.45962	1007.45974	$C_{49}H_{64}N_{10}O_{12}Na^+$	-0.12	np - O
1005.44423	1005.44409	$C_{49}H_{62}N_{10}O_{12}Na^+$	0.14	np – H_2O
996.44324	996.44375	$C_{48}H_{63}N_9O_{13}Na^+$	-0.51	jr + H_2O
993.44384	993.44409	$C_{48}H_{62}N_{10}O_{13}Na^+$	-0.25	np – CH_2O
978.43278	978.43319	$C_{48}H_{61}N_9O_{12}Na^+$	-0.42	jr
968.44919	968.44884	$C_{47}H_{63}N_9O_{12}Na^+$	0.36	jr – H_2O -CO
961.40666	961.40664	$C_{48}H_{58}N_8O_{12}Na^+$	0.02	ar – H_2O –NH_3
956.45163	-	unassigned	-	-
952.45365	952.45393	$C_{47}H_{63}N_9O_{11}Na^+$	-0.29	jl
950.43785	950.43827	$C_{47}H_{61}N_9O_{11}Na^+$	-0.44	jl – H_2
936.42234	936.42262	$C_{46}H_{59}N_9O_{11}Na^+$	-0.30	jl – CH_2
934.44301	934.44336	$C_{47}H_{61}N_9O_{10}Na^+$	-0.37	jl – H_2O
921.41148	-	unassigned	-	-
918.41221	918.41206	$C_{46}H_{57}N_9O_{10}Na^+$	0.16	jl – H_2O –CH_4
917.41571	917.41681	$C_{47}H_{58}N_8O_{10}Na^+$	-1.20	jl – H_2O –NH_3
906.44836	906.44845	$C_{46}H_{61}N_9O_9Na^+$	-0.10	jl – H_2O -CO

896.39099	896.39132	$C_{43}H_{55}N_9O_{11}Na^+$	-0.37	gj + NH_3
893.41666	-	unassigned	-	-
879.36439	879.36478	$C_{43}H_{52}N_8O_{11}Na^+$	-0.44	gj – H_2
▲871.56574	871.56565	$(D\text{-}Arg)_5$	-	-
868.34293	-	unassigned	-	-
865.34888	865.34913	$C_{42}H_{50}N_8O_{11}Na^+$	-0.29	gj – CH_4
853.38521	853.38551	$C_{42}H_{54}N_8O_{10}Na^+$	-0.35	js
851.36958	851.36986	$C_{42}H_{52}N_8O_{10}Na^+$	-0.33	js – H_2
848.32234	848.32258	$C_{42}H_{47}N_7O_{11}Na^+$	-0.28	gj – NH_3
837.35392	837.35421	$C_{41}H_{50}N_8O_{10}Na^+$	-0.35	js – CH_4
835.37434	835.37495	$C_{42}H_{52}N_8O_9Na^+$	-0.73	js – H_2O
825.35380	825.35421	$C_{40}H_{50}N_8O_{10}Na^+$	-0.50	as
821.35925	821.35930	$C_{41}H_{50}N_8O_9Na^+$	-0.06	js – CH_2 –H_2O
820.32749	820.32766	$C_{41}H_{47}N_7O_{10}Na^+$	-0.21	js – NH_3 –CH_4
814.33782	-	unassigned	-	-
809.37095	-	unassigned	-	-
804.33238	804.33275	$C_{41}H_{47}N_7O_9Na^+$	-0.46	js – H_2O –NH_3 –CH_2
796.32737	796.32766	$C_{39}H_{47}N_7O_{10}Na^+$	-0.36	t
794.31177	794.31201	$C_{39}H_{45}N_7O_{10}Na^+$	-0.30	t – H_2
783.30693	-	unassigned	-	-
770.34808	770.34840	$C_{38}H_{49}N_7O_9Na^+$	-0.42	u
766.28045	766.28071	$C_{37}H_{41}N_7O_{10}Na^+$	-0.34	t – CH_3 –H_2 –NH_3
752.33749	752.33783	$C_{38}H_{47}N_7O_8Na^+$	-0.45	u – H_2O
740.30118	740.30145	$C_{36}H_{43}N_7O_9Na^+$	-0.36	u – C_2H_6
738.28553	738.28580	$C_{36}H_{41}N_7O_9Na^+$	-0.37	u – C_2H_6 –H_2
733.29528	733.29563	$C_{38}H_{42}N_6O_8Na^+$	-0.48	u – H_2O –NH_3 –H_2
722.29055	722.29088	$C_{36}H_{41}N_7O_8Na^+$	-0.46	u – C_2H_6 –H_2O
712.26990	712.27015	$C_{34}H_{39}N_7O_9Na^+$	-0.35	jrvw + NH_3
708.34767	708.34800	$C_{37}H_{47}N_7O_6Na^+$	-0.47	u – H_2O -CO
701.25391	-	unassigned	-	-
▲697.45397	697.45398	$(D\text{-}Arg)_4$	-	-
695.24337	695.24360	$C_{34}H_{36}N_6O_9Na^+$	-0.33	jrvw – H_2
683.24336	683.24360	$C_{33}H_{36}N_6O_9Na^+$	-0.35	jrvw – CH_2
669.26411	669.26433	$C_{33}H_{38}N_6O_8Na^+$	-0.33	uxy
667.24853	667.24868	$C_{33}H_{36}N_6O_8Na^+$	-0.22	uxy – H_2
657.26407	657.26433	$C_{32}H_{38}N_6O_8Na^+$	-0.40	uxy – CH_2

653.26939	-	unassigned	-	-
651.25354	651.25377	$C_{33}H_{36}N_6O_7Na^+$	-0.35	uxy – H_2O
639.25358	639.25377	$C_{32}H_{36}N_6O_7Na^+$	-0.30	uzα
635.25871	635.25885	$C_{33}H_{36}N_6O_6Na^+$	-0.22	uxy – H_2O_2
625.27427	625.27450	$C_{32}H_{38}N_6O_6Na^+$	-0.37	uxy – CO_2
623.25868	623.25885	$C_{32}H_{36}N_6O_6Na^+$	-0.27	uzα – H_2O
621.24308	621.24320	$C_{32}H_{34}N_6O_6Na^+$	-0.19	uzα – H_2O –H_2
612.20634	612.20648	$C_{30}H_{31}N_5O_8Na^+$	-0.23	gjβγ
611.25864	611.25885	$C_{31}H_{36}N_6O_6Na^+$	-0.34	uzα – CH_2O
598.19071	598.19083	$C_{29}H_{29}N_5O_8Na^+$	-0.20	gjβγ – CH_2
595.22741	595.22755	$C_{30}H_{32}N_6O_6Na^+$	-0.24	uvα – C_2H_6
586.22704	586.22722	$C_{29}H_{33}N_5O_7Na^+$	-0.31	uxδε
580.18016	580.18027	$C_{29}H_{27}N_5O_7Na^+$	-0.19	jrvβ
572.21139	572.21157	$C_{28}H_{31}N_5O_7Na^+$	-0.31	uxθ
570.19579	570.19592	$C_{28}H_{29}N_5O_7Na^+$	-0.23	uxθ – CH_2
568.21667	568.21665	$C_{29}H_{31}N_5O_6Na^+$	0.04	uxδε – H_2O
566.20092	566.20100	$C_{29}H_{29}N_5O_6Na^+$	-0.14	uxδε – H_2O –H_2
554.20089	554.20100	$C_{28}H_{29}N_5O_6Na^+$	-0.20	uxσ – H_2O
552.18527	552.18535	$C_{28}H_{27}N_5O_6Na^+$	-0.14	uxσ – H_2O –H_2
540.22160	540.22174	$C_{28}H_{31}N_5O_5Na^+$	-0.26	uxδε – H_2O -CO
536.19041	536.19044	$C_{28}H_{27}N_5O_5Na^+$	-0.06	uxσ – H_4O_2
530.25838	530.25852	$C_{24}H_{37}N_5O_7Na^+$	-0.26	λ
526.20597	526.20609	$C_{27}H_{29}N_5O_5Na^+$	-0.23	uxπ – H_2O
▲523.34225	523.34230	$(D\text{-}Arg)_3$	-	-
512.19042	512.19044	$C_{26}H_{27}N_5O_5Na^+$	-0.04	uxπ – CH_2
508.19530	508.19553	$C_{27}H_{27}N_5O_4Na^+$	-0.45	uxπ – H_4O_2
504.27896	504.27926	$C_{23}H_{39}N_5O_6Na^+$	-0.59	σ
502.22723	-	unassigned	-	-
498.17478	-	unassigned	-	-
489.17431	-	unassigned	-	-
486.26855	486.26869	$C_{23}H_{37}N_5O_5Na^+$	-0.29	σ – H_2O
481.11178	481.11186	$C_{24}H_{18}N_4O_6Na^+$	-0.17	gjvβ
471.12753	471.12751	$C_{23}H_{20}N_4O_6Na^+$	0.04	jsvβ
455.13255	455.13259	$C_{23}H_{20}N_4O_5Na^+$	-0.09	jszβ
453.11687	453.11695	$C_{23}H_{18}N_4O_5Na^+$	-0.18	jszβ – H_2
447.22132	-	unassigned	-	-

443.16892	-	unassigned	-	-
437.12195	437.12203	$C_{23}H_{18}N_4O_4Na^+$	-0.18	jszβ – H_2O
425.99279	-	ω_3	-	-
421.24211	421.24214	$C_{19}H_{34}N_4O_5Na^+$	-0.07	bφ
413.12193	-	unassigned	-	-
409.12710	-	unassigned	-	-
403.23152	403.23158	$C_{19}H_{32}N_4O_4Na^+$	-0.15	bφ – H_2O
399.26020	399.26020	$C_{19}H_{35}N_4O_5^+$	0.00	bφ - Na
391.19517	391.19519	$C_{17}H_{28}N_4O_5Na^+$	-0.05	bφ – C_2H_6
377.25231	377.25231	$C_{18}H_{34}N_4O_3Na^+$	0.00	bφ – CO_2
375.23666	375.23666	$C_{18}H_{32}N_4O_3Na^+$	0.00	bφ – CO_2 –H_2
373.18461	373.18463	$C_{17}H_{26}N_4O_4Na^+$	-0.05	bφ – H_2O –C_2H_6
370.07986	-	unassigned	-	-
▲349.23064	349.23063	$(D\text{-}Arg)_2$	-	-
344.10056	-	unassigned	-	-
334.13735	334.13734	$C_{14}H_{21}N_3O_5Na^+$	0.03	ψζ – CH_2
320.15809	320.15808	$C_{14}H_{23}N_3O_4Na^+$	0.03	fζ
308.15810	-	unassigned	-	-
300.19183	300.19178	$C_{14}H_{26}N_3O_4^+$	0.17	fζ – Na + H_2
276.16829	276.16825	$C_{13}H_{23}N_3O_2Na^+$	0.14	fζ – CO_2
251.10670	-	unassigned	-	-
		Mean Absolute Average	**0.27**	
		Standard Deviation	**0.18**	

Table A-20: Multiple ion isolation and EID fragments of Actinomycin D (Li^+); $[M+Li]^+$ *m/z* 1261.64393

Expt. *m/z*	**Theo. *m/z***	**Proposed Formula**	**Mass Error (ppm)**	**Fragment Cleavage**
1233.64903	1233.64913	$C_{61}H_{86}N_{12}O_{15}Li^+$	-0.08	$[M+H – CO]^+$
1217.65426	1217.65421	$C_{61}H_{86}N_{12}O_{14}Li^+$	0.04	$[M+H – CO_2]^+$
1203.61450	1203.61477	$C_{60}H_{82}N_{11}O_{15}Li^+$	-0.22	ab
1189.62270	-	unassigned	-	-
1148.55988	1148.55998	$C_{56}H_{75}N_{11}O_{15}Li^+$	-0.09	cd

1130.54915	1130.54942	$C_{56}H_{73}N_{11}O_{14}Li^+$	-0.24	cd – H_2O
1120.56505	1120.56507	$C_{55}H_{75}N_{11}O_{14}Li^+$	-0.02	bc
1104.57017	1104.57015	$C_{55}H_{75}N_{11}O_{13}Li^+$	0.02	be
1086.55917	1086.55959	$C_{55}H_{73}N_{11}O_{12}Li^+$	-0.39	be – H_2O
1035.47571	1035.47591	$C_{50}H_{64}N_{10}O_{14}Li^+$	-0.19	fg
1017.46506	1017.46534	$C_{50}H_{62}N_{10}O_{13}Li^+$	-0.28	fg – H_2O
991.48632	991.48608	$C_{49}H_{64}N_{10}O_{12}Li^+$	0.24	gi – O
989.47026	989.47043	$C_{49}H_{62}N_{10}O_{12}Li^+$	-0.17	gi – H_2O
977.47016	977.47042	$C_{48}H_{62}N_{10}O_{12}Li^+$	-0.27	gi – CH_2O
962.45939	962.45953	$C_{48}H_{61}N_9O_{12}Li^+$	-0.15	ej
934.46445	934.46461	$C_{47}H_{61}N_9O_{11}Li^+$	-0.17	ek – H_2
920.44857	920.44896	$C_{46}H_{59}N_9O_{11}Li^+$	-0.42	ek – CH_2
863.39095	863.39110	$C_{43}H_{52}N_8O_{11}Li^+$	-0.17	el – H_2
▲871.56566	871.56565	$(D\text{-}Arg)_5$	-	-
849.37557	849.37545	$C_{42}H_{50}N_8O_{11}Li^+$	0.14	el – CH_4
837.41167	837.41183	$C_{42}H_{54}N_8O_{10}Li^+$	-0.19	em
821.38036	821.38053	$C_{41}H_{50}N_8O_{10}Li^+$	-0.21	em – CH_4
809.38043	809.38045	$C_{40}H_{54}N_8O_{10}Li^+$	-0.02	mn
805.38546	805.38562	$C_{41}H_{50}N_8O_9Li^+$	-0.20	em – CH_2 –H_2O
788.35900	788.35907	$C_{41}H_{47}N_7O_9Li^+$	-0.09	em – CH_4 –NH_3
780.35383	780.35390	$C_{39}H_{47}N_7O_{10}Li^+$	-0.09	p
778.33790	778.33833	$C_{39}H_{45}N_7O_{10}Li^+$	-0.55	p – H_2
750.30692	750.30702	$C_{37}H_{41}N_7O_{10}Li^+$	-0.13	p – NH_3 –CH_3
736.36389	736.36415	$C_{38}H_{47}N_7O_8Li^+$	-0.35	q – H_2O
724.32762	724.32776	$C_{36}H_{43}N_7O_9Li^+$	-0.19	q – C_2H_4
722.31180	722.31211	$C_{36}H_{41}N_7O_9Li^+$	-0.43	q – C_2H_6 –H_2
717.32173	717.32195	$C_{38}H_{42}N_6O_8Li^+$	-0.31	q – H_2O –NH_3 –H_2
706.31717	706.31719	$C_{36}H_{41}N_7O_8Li^+$	-0.03	q – C_2H_6 –H_2O
▲697.45398	697.45398	$(D\text{-}Arg)_4$	-	-
679.26983	679.26990	$C_{34}H_{36}N_6O_9Li^+$	-0.10	ejrs – H_2
667.26977	667.26990	$C_{33}H_{36}N_6O_9Li^+$	-0.19	ejrs – CH_2
653.29010	-	unassigned	-	-
651.27458	651.27499	$C_{33}H_{36}N_6O_8Li^+$	-0.63	qtu – H_2
635.28002	635.28007	$C_{33}H_{36}N_6O_7Li^+$	-0.08	qtu – H_2O
633.26436	633.26442	$C_{33}H_{34}N_6O_7Li^+$	-0.09	qtu – H_2O –H_2
623.28000	623.28007	$C_{32}H_{36}N_6O_7Li^+$	-0.11	qvw

607.28505	607.28515	$C_{32}H_{36}N_6O_6Li^+$	-0.16	qrw
570.25342	570.25352	$C_{29}H_{33}N_5O_7Li^+$	-0.18	qtxy
568.23753	568.23787	$C_{29}H_{31}N_5O_7Li^+$	-0.60	qtxy – H_2
564.20648	564.20657	$C_{29}H_{27}N_5O_7Li^+$	-0.16	ejrz
556.23782	556.23786	$C_{28}H_{31}N_5O_7Li^+$	-0.07	qtxy – CH_2
554.22225	554.22221	$C_{28}H_{29}N_5O_7Li^+$	0.07	qtxy – CH_4
538.22719	538.22730	$C_{28}H_{29}N_5O_6Li^+$	-0.20	qtα – H_2O
536.21154	536.21165	$C_{28}H_{27}N_5O_6Li^+$	-0.21	qtα – H_2O –H_2
▲523.34230	523.34230	$(D\text{-}Arg)_3$	-	-
510.23233	510.23238	$C_{27}H_{29}N_5O_5Li^+$	-0.10	qtβ – H_2O
508.21661	508.21673	$C_{27}H_{27}N_5O_5Li^+$	-0.24	qtβ – H_2O –H_2
488.30526	488.30554	$C_{23}H_{39}N_5O_6Li^+$	-0.57	γ
465.13805	465.13814	$C_{24}H_{18}N_4O_6Li^+$	-0.19	elrz
457.16956	457.16944	$C_{23}H_{22}N_4O_6Li^+$	0.26	emrz + H_2
437.14318	437.14322	$C_{23}H_{18}N_4O_5Li^+$	-0.09	emvz
431.24762	-	unassigned	-	-
420.55755	-	ω_3	-	-
411.16390	-	unassigned	-	-
401.20068	-	unassigned	-	-
393.15332	-	unassigned	-	-
391.19925	-	unassigned	-	-
387.25785	387.25785	$C_{19}H_{32}N_4O_4Li^+$	0.00	δε
375.22142	375.22146	$C_{17}H_{28}N_4O_5Li^+$	-0.11	δε – C_2H_6
366.29170	-	unassigned	-	-
356.12171	-	unassigned	-	-
▲349.23063	349.23063	$(D\text{-}Arg)_2$	-	-
328.12681	-	unassigned	-	-
318.16359	318.16361	$C_{14}H_{21}N_3O_5Li^+$	-0.06	πσ
312.13562	-	unassigned	-	-
292.18436	292.18434	$C_{13}H_{23}N_3O_4Li^+$	0.07	πσ – CO_2
	Mean Absolute Average		**0.22**	
	Standard Deviation		**0.17**	

Appendix B

Appendix B contains the supplementary data tables for the analysis of ruthenium anticancer drug binding sites on peptides in chapter 4.

Table B-1: CAD Fragments of Angiotensin and AH076, where AH076 is denoted by Ru(bipy) through loss of chloride and arene ligands

Assignment	**Expt. *m/z***	**Theo. *m/z***	**Error (ppm)**
▲ y_2	263.13900	263.13900	-
▲ b_2	272.13530	272.13530	-
$[a_6 + Ru(bipy) - 2H^+]^+$	506.68988	506.68993	-0.10
▲ y_4	513.28196	513.28200	-
$[y_6 + Ru(bipy) - H^+]^{2+}$	516.18921	516.18923	-0.04
$[b_6 + Ru(bipy) - H^+]^{2+}$	520.68734	520.68739	-0.10
b_2	528.09273	528.09278	-0.13
unassigned	551.29358	-	-
$[b_3 + Ru(bipy) - 2H^+]^+$	627.16115	627.16119	-0.06
$[M + Ru(bipy) - H_2O]^{2+}$	642.74792	642.74798	-0.09
$[M + Ru(bipy)]^{2+}$	651.75324	651.75326	-0.03
unassigned	664.37777	-	-
y_5	676.34527	676.34530	-0.04
$[y_4 + Ru(bipy) - 2H^+]^+$	769.23941	769.23944	-0.04
▲ y_6	775.41371	775.41370	-
▲ b_6	784.41010	784.41000	-
$[y_6 + Ru(bipy) - 2H^+]^+$	1031.37099	1031.37118	-0.18
Mean Absolute Average			**-0.08**

Standard Deviation	**0.05**

Table B-2: CAD Fragments of Angiotensin and AH078, where AH078 is denoted by Ru(o-pda) through loss of chloride and arene ligands

Assignment	**Expt. *m/z***	**Theo. *m/z***	**Error (ppm)**
ω_3 of y_5	255.44939	-	-
a_2	244.14040	244.14040	0.00
$b_2 - NH_3$	255.10875	255.10880	-0.20
ω_3 of y6	258.47249	-	-
▲ y_2	263.13900	263.13900	-
▲ b_2	272.13530	272.13530	-
unassigned	341.30499	-	-
▲ b_3	371.20368	371.20370	-
$y_3 - H_2O$	382.18734	382.18737	-0.08
b_6^{2+}	392.70863	392.70866	-0.08
▲ y_3	400.19790	400.19790	-
YIH	414.21354	414.21358	-0.10
[DR-Ru(o-pda)-HPF]$^{2+}$ (-CON)	419.14632	419.14636	-0.10
$[a_2 - 2H\bullet - H_2O + Ru(o\text{-}pda) - 2H^+]^+$	433.07944	433.07947	-0.07
y_7^{2+}	466.26103	466.26106	-0.06
[D-R-Ru(o-pda)-H-P-F]$^{2+}$ (+COO)	441.64515	441.64519	-0.09
$[a_2 - 2H\bullet + Ru(o\text{-}pda) - 2H^+]^+$	450.08217	450.08221	-0.09
$[b_2 - 2H\bullet + Ru(o\text{-}pda) - 2H^+]^+$	478.07708	478.07749	-0.86
$[y_6 - 2H\bullet + Ru(o\text{-}pda) - H^+]^{2+}$	491.18141	491.18141	0.00
$[b_6 - 2H\bullet + Ru(o\text{-}pda) - H^+]^{2+}$	495.67953	495.67997	-0.91
a_4	506.27206	506.27216	-0.20

▲ y_4	513.28195	513.28200	-
$[y_7 – 3H• + Ru – H^+]^{2+}$	514.69360	514.69368	-0.16
$[M+2H]^{2+}$	523.77449	523.77453	-0.08
$[b_7 – 3H• + Ru – H^+]^{2+}$	528.69106	528.69113	-0.13
▲ b_4	534.26705	534.26710	-
unassigned	536.71398	-	-
unassigned	539.09031	-	-
$[M – 2H• – COOH + Ru]^{2+}$	550.21218	550.21223	-0.09
unassigned	557.10089	-	-
$[y_7 – 2H• + Ru(o\text{-}pda) – H^+]^{2+}$	569.23191	569.23196	-0.09
$[M – 2H• – C_7H_8O + Ru(o\text{-}pda)]^{2+}$	572.71536	572.71668	-2.30
$[b_3 – 2H• + Ru(o\text{-}pda) – 2H^+]^+$	577.14549	577.14601	-0.90
$[M – 2H• – COOH + Ru(o\text{-}pda)]^{2+}$	604.24657	604.24661	-0.07
unassigned	612.16288	-	-
$[M – 2H• – H_2O + Ru(o\text{-}pda)]^{2+}$	617.74000	617.74015	-0.24
▲ b_5	647.35114	647.35110	-
▲ y_5	676.34527	676.34530	-
$[y_4 – 2H• + Ru(o\text{-}pda) – 2H^+]^+$	719.22380	719.22448	-0.95
a_6	756.41497	756.41513	-0.21
▲ y_6	775.41373	775.41370	-
▲ b_6	784.41004	784.41000	-
x_6	801.39283	801.39300	-0.21
$[M+H]^+$	1046.54206	1046.54179	0.26
$[DR\text{-}Ru(o\text{-}pda)\text{-}HPF]^+$ (-CON)	837.28538	837.28545	-0.08
$[DR\text{-}Ru(o\text{-}pda)\text{-}HPF]^+$ (+COO)	881.27532	881.27527	0.06
$[y_6 – 2H• + Ru(o\text{-}pda) – 2H^+]^+$	981.35545	981.35646	-1.03
Mean Absolute Average			**0.32**

Standard Deviation	**0.48**

Table B-3: CAD Fragments of Bombesin and AH076 where AH076 denoted by Ru(bipy) through loss of the arene and chloride ligands

Assignment	**Expt. *m/z***	**Theo. *m/z***	**Error (ppm)**
y_2	262.15844	262.15837	0.27
b_3	396.19905	396.19910	-0.13
b_7^{2+}	404.70674	404.70665	0.22
$[y_6 + Ru(bipy) - H^+]^{2+}$	441.65461	441.65451	0.23
unassigned	474.73602	-	-
b_8^{2+}	497.74636	497.74631	0.10
b_4	509.28313	509.28310	0.06
$[b_{12} + Ru(bipy)]^{3+}$	538.88110	538.88108	0.04
$[a_{13} + Ru(bipy)]^{3+}$	567.24415	567.24413	0.04
$[b_{13} + Ru(bipy)]^{3+}$	576.57574	576.57577	-0.05
b_{10}^{2+}	582.79916	582.79907	0.15
$[M + Ru(bipy) - CONH_2 - SCH_4]^{3+}$	594.92310	594.92317	-0.12
$[M + Ru(bipy) - CONH_2]^{3+}$	611.25870	611.25875	-0.08
$[M + Ru(bipy) - NH_3]^{3+}$	620.25583	620.25593	-0.16
$[M + Ru(bipy) + H^+]^{3+}$	625.93131	625.93145	-0.22
a_{12}^{2+}	665.84187	665.84180	0.11
b_6	680.34753	680.34750	0.04
$[y_4 + Ru(bipy) - 2H^+]^+$	712.19625	712.19620	0.07
b_{13}^{2+}	736.38137	736.38129	0.11
unassigned	744.89462	-	-
$[a_{12} + Ru(bipy) - H^+]^{2+}$	793.82042	793.82053	-0.14
b_7	808.40609	808.40610	-0.01
$[y_5 + Ru(bipy) - 2H^+]^+$	811.26467	811.26461	0.07

$[b_{13} + Ru(bipy) - H^+]^{2+}$	864.35997	864.36002	-0.06
$[y_6 + Ru(bipy) - 2H^+]^+$	882.30182	882.30173	0.10
b_8	994.48541	994.48540	0.01
b_9	1065.52261	1065.52250	0.10
b_{10}	1164.59088	1164.59090	-0.02
b_{11}	1221.61229	1221.61240	-0.09
Mean Absolute Average			**0.10**
Standard Deviation			**0.07**

Table B-4: CAD Fragments of Bombesin and AH078 where AH078 is denoted by Ru(o-pda) through loss of chloride and arene ligands

Assignment	**Expt. *m/z***	**Theo. *m/z***	**Error (ppm)**
▲ y_2	262.15844	262.15837	-
$[y_4 - 2H\bullet + Ru(o\text{-}pda)\text{-}H^+]^{2+}$	331.59391	331.59392	-0.03
b_6^{2+}	340.67740	340.67736	0.12
y_5^{3+}	381.12800	381.12811	-0.29
$[y_5 - 2H\bullet + Ru(o\text{-}pda)\text{-}H^+]^{2+}$	381.12814	381.12812	0.05
$[b_6 + NH_3]^{2+}$	349.19065	349.19064	0.03
b_3	*396.19909*	396.19910	-0.03
b_7^{2+}	404.70667	404.70665	0.05
$[y_6 - 2H\bullet + Ru(o\text{-}pda)\text{-}H^+]^{2+}$	416.64670	416.64667	0.07
$[b_8 - C_8H_7N]^{2+}$	439.21739	439.21739	0.00
$[b_8 - N_2H_4CO]^{2+}$	466.72232	466.72230	0.04
$[y_2 - 2H\bullet + Ru(o\text{-}pda)\text{-}2H^+]^+$	468.10018	468.10018	0.00
$[b_9 - C_8H_7N]^{2+}$	474.73596	474.73594	0.04
$[b_8 - N_2H_4]^{2+}$	480.71978	480.71976	0.04
a_8^{2+}	483.74887	483.74885	0.04
$[b_8 - NH_2]^{2+}$	489.23305	489.23303	0.04

b_8^{2+}	497.74633	497.74631	0.04
▲ b_4	509.28322	509.28310	-
$[y_7 – 2H• + Ru(o\text{-}pda)\text{-}H^+]^{2+}$	509.68636	509.68634	0.04
$[a_{12} – 2H• + Ru(o\text{-}pda)]^{3+}$	512.87756	512.87756	0.00
$[b_{12} – 2H• + Ru(o\text{-}pda)]^{3+}$	522.20930	522.20959	-0.56
$[b_9 – NH_3]^{2+}$	524.75161	524.75159	0.04
b_9^{2+}	533.26489	533.26486	0.06
$[a_{13} – 2H• + Ru(o\text{-}pda)]^{3+}$	550.57224	550.57225	-0.02
$[b_{13} – 2H• + Ru(o\text{-}pda)]^{3+}$	559.90389	559.90389	0.00
▲ b_5	566.30453	566.30460	-
$[M + Ru + H^+]^{3+}$	573.90855	573.90854	0.02
b_{10}^{2+}	582.79912	582.79907	0.09
$[M – H• + Ru(o\text{-}pda) – NH_3]^{3+}$	603.58404	603.58448	-0.73
$[y_3 – 2H• + Ru(o\text{-}pda)\text{-}2H^+]^+$	605.15919	605.15960	-0.68
$[M – 2H• + Ru(o\text{-}pda)]^{3+}$	609.25932	609.25954	-0.36
$[M + Ru(C_{12}H_9) + H_2]^{3+}$	625.26777	625.26795	-0.29
$[y_4 – 2H• + Ru(o\text{-}pda) – NH_3\text{-}2H^+]^+$	645.15393	645.15401	-0.12
$[y_4 – 2H• + Ru(o\text{-}pda)\text{-}2H^+]^+$	662.18060	662.18110	-0.76
▲ b_6	680.34740	680.34750	-
$b_6 + NH_3$	697.37405	697.37400	0.07
$[y_6 – H• + Ru – 2H^+]^+$	725.22520	725.22516	0.06
b_{13}^{2+}	736.38128	736.38129	-0.01
$[y_5 – 2H• + Ru(o\text{-}pda) – H^+ - NH_3]^+$	744.22235	744.22241	-0.08
$[y_5 – 2H• + Ru(o\text{-}pda) – 2H^+]^+$	761.24890	761.24961	-0.93
$[a_{12} – 2H• + Ru(o\text{-}pda) – H^+]^{2+}$	768.81239	768.81328	-1.16
$[b_{12} – 2H• + Ru(o\text{-}pda) – H^+]^{2+}$	782.80987	782.81074	-1.11
$b_7 – NH_3$	791.37952	791.37948	0.05
▲ b_7	808.40568	808.40603	-
$[y_6 – 2H• + Ru(o\text{-}pda) – 2H^+ - NH_3]^+$	815.25957	815.25953	0.05

$[y_6 - 2H\bullet + Ru(o\text{-}pda) - 2H^+]^+$	832.28599	832.28677	-0.94
$[b_{13} - 2H\bullet + Ru(o\text{-}pda) - H^+]^{2+}$	839.35170	839.35281	-1.32
$b_8 - C_9H_7N$	865.42757	865.42749	0.09
$b_8 - C_8H_7N$	877.42745	877.42804	-0.67
$b_8 + H_2O - C_6H_7N$	919.43826	919.43805	0.23
$b_8 + H_2O - C_6H_4N$	936.46466	936.46460	0.06
a_8	966.49059	966.49042	0.18
$b_8 - NH_3$	977.45891	977.45879	0.12
▲ b_8	994.48557	994.48540	-
$[y_7 - 2H\bullet + Ru(o\text{-}pda) - 2H^+]^+$	1018.36529	1018.36627	-0.96
a_9	1037.52807	1037.52754	0.51
$b_9 - NH_3$	1048.49631	1048.49590	0.39
▲ b_9	1065.52258	1065.52247	-
▲ b_{10}	1164.59094	1164.59087	-
b_{11}	1221.61251	1221.61237	0.15
Mean Absolute Average			**0.27**
Standard Deviation			**0.36**

Table B-5: ECD Fragments of Bombesin and AH076 where AH076 is denoted by Ru(bipy) through loss of chloride and arene ligands

Assignment	**Expt. *m/z***	**Theo. *m/z***	**Error (ppm)**
▲ c_3	413.22555	413.22554	-
▲ c_4	526.30963	526.30961	-
▲ c_5	583.33107	583.33107	-
$[M - H\bullet + Ru(bipy) + H^+]^{3+}$	625.93145	625.93145	0.00
$[M - H\bullet + Ru(bipy) + H^+ + C_2H_3N]^{3+}$	639.60684	639.60696	-0.19
$[M - H\bullet + Ru(bipy) + H^+ + C_4H_6N_2]^{3+}$	653.28249	653.28248	0.02
unassigned	655.51197	-	-

$[x_3 + Ru(bipy)]^+$	683.16965	683.16965	0.00
▲ c_6	697.37399	697.37410	-
$[a_{12} + Ru(bipy) – H^+]^{2+}$	794.32418	794.32444	-0.33
$[b_{12} + Ru(bipy) – H^+]^{2+}$	808.32163	808.32190	-0.33
$[z_{12} + Ru(bipy)]^{2+\bullet}$	810.83853	810.83888	-0.43
$[z_{13} + Ru(bipy)]^{2+\bullet}$	874.86795	874.86817	-0.25
$[M + Ru(bipy) – NH_3]^{2+}$	930.38383	930.38418	-0.38
$[M – H\bullet + Ru(bipy) + H^+]^{2+\bullet}$	938.89717	938.89745	0.30
▲ c_8	1011.51218	1011.51189	-
a_{11}	1193.61768	1193.61742	0.22
▲ c_{11}	1238.63912	1238.63890	-
a_{12}	1330.67666	1330.67633	0.25
a_{13}	1443.76082	1443.76039	0.30
▲ c_{13}	1488.78182	1488.78190	-
$[c_{11} + Ru(bipy) – 2H^+]^+$	1494.59633	1494.59633	0.00
$[a_{12} + Ru(bipy)]^+$	1588.64974	1588.64943	0.20
$[b_{12} + Ru(bipy) – 2H^+]^+$	1614.62893	1614.62870	0.14
$[z_{12} + Ru(bipy)]^{+\bullet}$	1621.67852	1621.67830	0.14
$[c_{13} + Ru(bipy) – 2H^+]^+$	1744.74078	1744.73931	0.84
$[z_{13} + Ru(bipy)]^{+\bullet}$	1749.73638	1749.73688	-0.29
$[M + Ru(bipy) – H^+]^+$	1875.78163	1875.77981	0.97
Mean Absolute Average			**0.28**
Standard Deviation			**0.24**

Table B-6: ECD Fragments of Bombesin and AH078 where AH078 is denoted by Ru(o-pda) through loss of chloride and arene ligands

Assignment	**Expt. *m/z***	**Theo. *m/z***	**Error (ppm)**
▲ c_3	413.22555	413.22554	-

▲ c_4	526.30960	526.30961	-
▲ c_5	583.33116	583.33107	
$[M - 2H^{\bullet} + Ru(o\text{-}pda) + H^+]^{3+}$	609.25942	609.25938	-0.08
$[M - 2H^{\bullet} + Ru(o\text{-}pda) + H^+ + C_2H_3N]^{3+}$	622.93486	622.93491	-0.05
$[M - 2H^{\bullet} + Ru(o\text{-}pda) + H^+ + C_4H_6N_2]^{3+}$	636.61039	636.61042	-0.06
▲ c_6	697.37406	697.37410	-
$[z_{12} - 2H^{\bullet} + Ru(o\text{-}pda)]^{2+\bullet}$	785.83076	785.83105	-0.37
▲ c_7	825.43258	825.43258	-
$[c_{13} - 2H^{\bullet} + Ru(o\text{-}pda) - NH_3]^{2+}$	839.85571	839.85611	-0.48
$[z_{13} - 2H^{\bullet} + Ru(o\text{-}pda)]^{2+\bullet}$	849.86003	849.86034	-0.36
$[M + Ru - H^+]^{2+}$	859.85525	859.85526	-0.01
$[M - 2H^{\bullet} + Ru(o\text{-}pda) + H^+]^{2+\bullet}$	913.88976	913.88963	0.14
$[M + Ru(C_{12}H_9) + H_2]^{2+}$	937.90184	937.90221	-0.39
▲ c_8	1011.51194	1011.51189	-
▲ c_9	1082.54915	1082.54900	-
▲ c_{10}	1181.61770	1181.61750	-
▲ c_{11}	1238.63897	1238.63888	-
a_{12}	1330.67623	1330.67640	-0.13
$[c_{11} + Ru - 2H^+]^+$	1338.52736	1338.52758	-0.16
c_{12}	1375.69779	1375.69790	-0.08
$[c_{12} + Ru - 2H^+ - NH_3]^+$	1458.55971	1458.55955	0.11
$[c_{13} + Ru - 2H^+]^+$	1587.66101	1587.66274	-1.09
$[M + Ru - C_7H_{13}ON]^+$	1593.62114	1593.61917	1.24
$[M + Ru - C_7H_8O]^+$	1610.64742	1610.64572	1.06
$[M + Ru - 2H^+ - CONH_2]^+$	1674.68968	1674.69069	-0.60
$[M + Ru - 2H^+ - NH_2]^+$	1702.68529	1702.68561	-0.19
$[M + Ru - H^+]^+$	1719.71248	1719.71161	0.51
Mean Absolute Average			**0.37**
Standard Deviation			**0.34**

Table B-7: CAD Fragments of Angiotensin and AH076 where AH076 denoted by (bip)Ru(bipy) through loss of chloride ligand only

Assignment	Expt. *m/z*	Theo. *m/z*	Error (ppm)
$[y_2 + (bip)Ru(bipy) - H^+]^{2+}$	337.09092	337.09100	-0.24
$[y_2 + Ru - 2H^+]^+$	363.02763	363.02772	-0.25
a_6^{2+}	378.71112	378.71121	-0.24
unassigned	370.19785	-	-
b_6^{2+}	392.70858	392.70866	-0.20
$[y_7 + (bip)Ru(bipy) - H^+]^{2+}$	396.49553	396.49562	-0.23
y_3	400.19786	400.19790	-0.10
$[(bip)Ru(bipy) - H^+]^+$	411.04290	411.04297	-0.17
$[M + (bip)Ru(bipy) + H^+]^{3+}$	434.83784	434.83793	-0.21
$[y_7 + (bip)Ru(bipy)]^{3+}$	447.85495	447.85503	-0.18
$[b_7 + H_2O]^{2+}$	450.24029	450.24033	-0.09
y_7^{2+}	466.26101	466.26106	-0.11
$[M + 2H^+ - COOH]^{2+}$	500.77176	500.77179	-0.06
$[a_6 + (bip)Ru(bipy) - H^+]^{2+}$	506.68991	506.68993	-0.04
▲ y_4	513.28198	513.28199	-
$[M + 2H^+]^{2+}$	523.77446	523.77453	-0.13
▲b_4	534.26712	534.26707	-
$[F + (bip)Ru(bipy) - H^+]^+$	576.12194	576.12195	-0.02
a_5	619.35618	619.35620	-0.03
$[b_3 + (bip)Ru(bipy) - 2H^+]^+$	627.16126	627.16119	0.11
▲ b_5	647.35099	647.35110	-
$[y_3 + (bip)Ru(bipy) - 2H^+]^+$	656.15544	656.15538	0.09
▲ y_5	676.34538	676.34530	-
a_6	756.41522	756.41510	0.16
$[y_4 + (bip)Ru(bipy) - 2H^+]^+$	769.23960	769.23944	0.21

▲ y_6	775.41379	775.41379	-
▲ b_6	784.40999	784.41000	-
$[M + H^+]^+$	1046.54224	1046.54179	0.43
Mean Absolute Average			**0.16**
Standard Deviation			**0.10**

Table B-8: CAD Fragments of Bombesin and AH076 where AH076 denoted by (bip)Ru(bipy) through loss of chloride ligand only

Assignment	**Expt. *m/z***	**Theo. *m/z***	**Error (ppm)**
b_6^{2+}	340.67740	340.67736	0.12
$[b_6 + NH_3]^{2+}$	349.19067	349.19064	0.09
$[y_4 + Ru(bipy) – H^+]^{2+}$	356.60175	356.60174	0.03
$[y_8 + Ru(bipy) – H_2O, H]^{3+}$	393.48122	393.48120	0.05
▲b_3	396.19902	396.19910	-
▲ y_3	399.21735	399.21728	-
b_7^{2+}	404.70669	404.70665	0.10
$[(bip)Ru(bipy) – H^+]^+$	411.04302	411.04297	0.12
unassigned	425.82002	-	-
$[y_6 + Ru(bipy) – NH_3 - H^+]^{2+}$	433.14131	433.14123	0.18
$[y_6 + Ru(bipy) – H^+]^{2+}$	441.65457	441.65450	0.16
$[(bip)Ru(bipy) + SCH_4 – H^+]^+$	459.04640	459.04635	0.11
unassigned	466.72238	-	-
b_8^{2+}	497.74637	497.74631	0.12
▲ b_4	509.28308	509.28310	-
$[M + 3H^+ - SCH_4]^{3+}$	524.61123	524.61117	0.11
$[y_7 + Ru(bipy) – H^+]^{2+}$	534.69425	534.69416	0.17
▲ y_5	555.30456	555.30716	-
▲ b_5	566.30456	566.30460	-

$[y_8 + Ru(bipy) – NH_3 - H^+]^{2+}$	590.21024	590.221017	0.12
unassigned	621.15075	-	-
▲ y_6	626.34433	626.34427	-
$[y_9 + Ru(bipy) – H^+]^{2+}$	655.74496	655.74491	0.08
a_{12}^{2+}	665.84191	665.84180	0.17
$[y_{10} + Ru(bipy) – NH_3 - H^+]^{2+}$	675.74235	675.74237	-0.03
b_{12}^{2+}	679.83929	679.83926	0.04
▲ b_6	680.34746	680.34750	-
$[y_{10} + Ru(bipy) – H^+]^{2+}$	684.25564	684.25564	0.00
y_{12}^{2+}	690.86962	690.86951	0.16
$b_6 + NH_3$	697.37410	697.37400	0.14
$[y_4 + Ru(bipy) – 2H^+]^+$	712.19629	712.19620	0.13
a_{13}^{2+}	722.38391	722.38383	0.11
b_{13}^{2+}	736.38127	736.38129	-0.03
$[M + 2H^+ - NH_3]^{2+}$	801.90156	801.90153	0.04
▲ b_7	808.40604	808.40610	-
$[M + 2H^+]^{2+}$	810.41468	810.41481	-0.16
$[y_6 + Ru(bipy) – 2H^+]^+$	882.30179	882.30173	0.07
$b_8 – NH_3$	977.45885	977.45879	0.06
▲ b_8	994.48539	994.48534	-
$b_9 – NH_3$	1048.49604	1048.49590	0.13
b_9	1065.52247	1065.52250	-0.03
$b_{10} – NH_3$	1147.56452	1147.56432	0.17
b_{10}	1164.59087	1164.59090	-0.03
b_{11}	1221.61241	1221.61240	0.01
Mean Absolute Average			**0.10**
Standard Deviation			**0.05**

Table B-9: CAD Fragments of Insulin and AH076

Assignment	Expt. *m/z*	Theo. *m/z*	Error (ppm)
▲y_3	315.20270	315.20270	-
b_4	399.22384	399.22380	0.10
▲y_4	416.25039	416.25040	-
B b_5	489.24587	489.24560	0.55
b_5	527.28240	527.28240	0.00
unassigned	534.25590	-	-
y_9^{2+}	543.79021	543.79018	0.06
$y_5 - H_2O$	561.30310	561.30312	-0.04
y_5	579.31369	579.31369	0.00
y_{10}^{2+}	608.31157	608.31148	0.15
B b_{11}^{2+}	618.80072	618.80076	-0.06
B b_5	626.30446	626.30450	-0.06
$[y_{11} - H_2O]^{2+}$	627.81698	627.81693	0.08
unassigned	631.27219	-	-
y_{11}^{2+}	636.82221	636.82221	0.00
unassigned	648.29877	-	-
$[A\ y_4 + B\ y_{13}]^{3+}$	662.29398	662.29419	-0.32
B b_{12}^{2+}	668.33507	668.33496	0.16
$[y_{12} - SH]^{2+}$	671.33309	671.33294	0.22
$[y_{12} - H_2O]^{2+}$	679.32184	679.32152	0.47
y_{12}^{2+}	688.32681	688.32681	0.00
$[A\ y_4 + B\ y_{14}]^{3+}$	699.98883	699.98888	-0.07
$[B\ y_2\text{-}y_{12} + A\ Cys_{20}]^{2+}$	704.31284	704.31284	0.00
$y_6 - H_2O$	708.37138	708.37150	-0.17
A y_{12}^{2+}	716.31266	716.31150	1.62
▲y_6	726.38206	726.38210	-0.06
B b_{13}^{2+}	732.85636	732.85626	0.14

y_{13}^{2+}	737.86093	737.86101	-0.11
B b_6	739.38881	739.38859	0.30
[A y_6 + B y_{13}]$^{3+}$	743.00302	743.00308	-0.08
[B y_2-y_{13} + A Cys_{20}]$^{2+}$	753.84712	753.84705	0.09
B b_{14}^{2+}	768.37482	768.37482	0.00
[A y_6 + B y_{14}]$^{3+}$	781.03214	781.03224	-0.13
y_{14}^{2+}	794.40328	794.40304	0.30
[A y_2 + B y_{12}]$^{2+}$	804.85025	804.85032	-0.09
[B y_2-y_{14} + A Cys_{20}]$^{2+}$	810.38918	810.38908	0.12
[A y_7 + B y_{14}]$^{3+}$	817.38041	817.38044	-0.04
B b_{15}^{2+}	824.91687	824.91685	0.02
[A y_8 + B y_{13}]$^{3+}$	840.04377	840.04372	0.06
[A y_2 + B y_{13}]$^{2+}$	854.38456	854.38452	0.05
[A y_7 + B y_{15} – H_2O, NH_3]$^{3+}$	866.05936	866.05937	-0.01
[A y_7 + B y_{15} – H_2O]$^{3+}$	871.73467	871.73488	-0.24
[A y_7 + B y_{15}]$^{3+}$	877.73840	877.73840	0.00
[A y_3 + B y_{12}]$^{2+}$	886.38192	886.38198	-0.07
[B b_{14} -2H• + Ru(bipy) – H^+]$^{2+}$	895.34547	895.34573	-0.29
unassigned	906.44857	-	-
[A y_2 + B y_{14}]$^{2+}$	910.92645	910.92656	-0.12
▲ y_8	930.47193	930.47198	-0.05
[A y_8 + B y_{15}]$^{3+}$	932.09276	932.09285	-0.10
[A y_4 + B y_{12}– NH_3]$^{3+}$	934.88991	934.89017	-0.28
[A y_4 + B y_{12}]$^{3+}$	943.40331	943.40345	-0.15
[M + Ru(bipy) + $4H^+$ -F -L]$^{6+}$	952.91048	952.90942	1.11
[GERGFFYT – H_2O]$^+$	958.44161	958.44174	-0.14
B b_{17}^{2+}	962.99048	962.99055	-0.07
[M + Ru(bipy) + $4H^+$ -F –H_2O]$^{6+}$	971.75740	971.75676	0.66
[M + Ru(bipy) + $4H^+$ -N]$^{6+}$	976.92629	976.92587	0.43

[M + Ru(bipy) + $4H^+$ -L]$^{6+}$	980.25467	980.25461	0.06
[A y_3 + B y_{14}]$^{2+}$	983.45268	983.45294	-0.26
[A y_3 + B y_{14} + H_2O]$^{2+}$	992.45807	992.45822	-0.15
[M + Ru(bipy) + $4H^+$ –H_2O]$^{6+}$	996.26600	996.10019	0.34
[M + Ru(bipy) + $4H^+$]$^{6+}$	999.10180	999.10195	-0.15
unassigned	1021.41070	-	-
[A b_{13} + B b_{15} + Ru(bipy) – H^+]$^{3+}$	1027.74804	1027.74757	0.46
[B b_{16} -2H• + Ru(bipy) – H^+]$^{2+}$	1033.41930	1033.41942	-0.12
[A y_4 + B y_{14}– NH_3]$^{2+}$	1040.96644	1040.96641	0.03
[A y_4 + B y_{14}]$^{2+}$	1049.47965	1049.47968	-0.03
[A b_{11} + B b_{16} + Ru(bipy) – H^+]$^{3+}$	1053.09243	1053.09134	1.04
[A y_5 + B y_{13}]$^{2+}$	1057.45872	1057.45895	-0.22
[A y_6 + B y_{12}]$^{2+}$	1064.46700	1064.46677	0.22
[A b_{12} + B b_{16} + Ru(bipy) – H^+]$^{3+}$	1082.10260	1082.10202	0.54
[B b_{17} – 2H• + Ru(bipy) – H^+]$^{2+}$	1089.96239	1089.96146	0.85
[B b_{18} -2H• + Ru(bipy) – A – H^+]$^{2+}$	1105.98968	1105.99051	-0.75
[A y_5 + B y_{14}]$^{2+}$	1114.00128	1114.00098	0.27
[A b_{13} + B b_{16} + Ru(bipy) – H^+]$^{3+}$	1119.79767	1119.79670	0.87
[M + Ru(bipy) + $3H^+$ -F-V-L –H_2O]$^{5+}$	1123.67784	1123.67772	0.11
[A y_7 + B y_{12}]$^{2+}$	1128.49695	1128.49606	0.79
unassigned	1129.88079	-	-
[A y_4 + B y_{15}]$^{2+}$	1131.01188	1131.01135	0.47
[M + Ru(bipy) + $3H^+$ -A-L-L –H_2O]$^{5+}$	1136.08193	1136.08182	0.10
[M + Ru(bipy) + $3H^+$ -F-V-L]$^{5+}$	1139.68657	1139.68393	2.32
[M + Ru(bipy) + $3H^+$ -F -L]$^{5+}$	1143.49202	1143.49141	0.53
[M + Ru(bipy) + $3H^+$ -F -V]$^{5+}$	1149.69270	1149.69605	-2.91
[M + Ru(bipy) + $3H^+$ -F –V – H_2O]$^{5+}$	1152.48591	1152.48768	-1.54
[M + Ru(bipy) + $3H^+$ -F -V]$^{5+}$	1156.08979	1156.08979	0.00
[M + Ru(bipy) + $3H^+$ -Y]$^{5+}$	1166.10800	1166.10919	-1.02

$[A\ y_6 + B\ y_{14}]^{2+}$	1170.54283	1170.54301	-0.15
$[M + Ru(bipy) + 3H^+ - N]^{5+}$	1172.10963	1172.10959	0.03
$[M + Ru(bipy) + 3H^+ - L]^{5+}$	1175.70260	1175.70095	1.40
$[M + Ru(bipy) + 3H^+ - V]^{5+}$	1178.70504	1178.70660	-1.32
$[A\ b_{16} + B\ b_{15} + Ru(bipy) - H^+]^{3+}$	1200.51093	1200.51353	-2.17
$[A\ y_8 + B\ y_{12}]^{2+}$	1201.51344	1201.51445	-0.84
$[A\ y_8 + B\ y_{12}]^{2+}$	1210.02719	1210.02773	-0.45
$[A\ b_{15} + B\ b_{16} + Ru(bipy) - H^+]^{3+}$	1216.83749	1216.83734	0.12
$[A\ y_7 + B\ y_{14} - NH_3]^{2+}$	1226.05943	1226.05903	0.33
$[A\ y_7 + B\ y_{12}]^{2+}$	1234.57256	1234.57230	0.21
$[A\ b_{17} + B\ b_{15} + Ru(bipy) - H^+]^{3+}$	1243.19400	1243.19178	1.79
$[A\ y_6 + B\ y_{15}]^{2+}$	1252.07390	1252.07468	-0.62
$[A\ b_{15} + B\ b_{17} + Ru(bipy) - H^+]^{3+}$	1254.53246	1254.53203	0.34
$[A\ y_8 + B\ y_{13}]^{2+}$	1259.56057	1259.56193	-1.08
$[A\ chain + B\ b_{23} + Ru(bipy) + H^+]^{4+}$	1280.03684	1280.03656	0.22
$[A\ b_{16} + B\ b_{17} + Ru(bipy) - H^+]^{3+}$	1292.22625	1292.22671	-0.36
$[A\ b_{17} + B\ b_{16} + Ru(bipy) - H^+]^{3+}$	1297.88087	1297.88217	-1.00
$[A\ y_8 + B\ y_{14} - NH_3]^{2+}$	1307.59052	1307.59069	-0.13
$[A\ y_8 + B\ y_{14}]^{2+}$	1316.10365	1316.10397	-0.24
$[A\ b_{18} + B\ b_{17} + Ru(bipy) - H^+]^{3+}$	1335.55997	1335.56053	-0.42
$[A\ chain + B\ b_{25} + Ru(bipy) + H^+]^{4+}$	1353.57192	1353.57391	-1.55
$[A\ b_{18} + B\ b_{17} + Ru(bipy) - H^+]^{3+}$	1373.25487	1373.25522	-0.25
$[A\ b_{19} + B\ b_{16} + Ru(bipy) - H^+]^{3+}$	1389.91565	1389.91565	0.00
▲$B\ b_{15}^+$	1648.82659	1648.82600	0.36
$[A\ b_{13} + B\ b_{16} + Ru(bipy) - 2H^+]^{2+}$	1679.19237	1679.19142	0.57
Mean Absolute Average			**0.08**
Standard Deviation			**0.68**

Table B-10: CAD Fragments of Oxidised Insulin B-chain and AH076

Assignment	Expt. *m/z*	Theo. *m/z*	Error (ppm)
y_2	218.14977	218.14990	-0.60
noise	226.15481	-	-
noise	265.89283	-	-
▲ y_3	315.20271	315.20270	-
b_3	361.18705	361.18700	-
unassigned	412.18673	-	-
y_4	*416.25037*	416.25036	0.02
unassigned	*494.16640*	-	-
y_9^{2+}	543.79021	543.79018	0.06
unassigned	561.30316	-	-
▲ y_5	579.31370	579.31370	-
unassigned	601.30368	-	-
y_{10}^{2+}	608.31150	608.31148	0.03
▲ b_5	626.30458	626.30450	-
y_{11}^{2+}	636.82221	636.82221	0.00
unassigned	655.34499	-	-
unassigned	699.22225	-	-
$y_6 - H_2O$	708.37132	708.37154	-0.31
y_{12}^{2+}	712.31909	712.31918	-0.13
$[b_{10} - H\bullet + Ru(bipy) - H^+]^{2+}$	713.72573	713.72592	-0.27
▲ y_6	726.38205	726.38210	-
▲ b_6	739.38852	739.38860	-
y_{13}^{2+}	761.85338	761.85338	0.00
y_{14}^{2+}	818.39537	818.39542	-0.06
$[b_{12} + Ru(bipy) - H^+]^{2+}$	820.30626	820.30607	0.23
▲y_7	873.45051	873.45050	-
$[b_{13} + Ru(bipy) - H^+]^{2+}$	884.82757	884.82737	0.23

y_{15}^{2+}	899.92705	899.92708	-0.03
unassigned	907.89279	-	-
unassigned	913.13762	-	-
$[M + Ru(bipy) + 2H^{+} - H_2O – CH_3 – NH_3]^{4+}$	926.14440	926.14321	1.28
y_8	930.47184	930.47198	-0.15
$[b_{14} + Ru(bipy) – H^{+}]^{2+}$	920.34510	920.34592	-0.89
$[y_{22} - 3H• + Ru(bipy)]^{3+}$	934.73555	934.73532	0.25
y_{16}^{2+}	956.46880	956.46911	-0.32
$[b_{15} – H• + Ru(bipy) – H^{+}]^{2+}$	976.88658	976.88571	0.89
$[a_{24} + Ru(bipy)]^{3+}$	999.74924	999.74952	-0.28
$[b_{24} + Ru(bipy)]^{3+}$	1009.41595	1009.41711	-1.15
unassigned	1038.91884	-	-
y_{18}^{2+}	1056.50832	1056.50896	-0.61
$[b_{16} - H• + Ru(bipy) – H^{+}]^{2+}$	1057.91506	1057.91571	-0.61
y_9	1086.57323	1086.57310	0.12
y_{19}^{2+}	1106.04297	1106.04317	-0.18
$[b_{26} -H• + Ru(bipy)]^{3+}$	1112.45942	1112.45898	0.40
$[b_{17} -H• + Ru(bipy) – H^{+}]^{2+}$	1114.96023	1114.95941	0.74
$[b_{27} – H• + Ru(bipy) – H_2O]^{3+}$	1140.13817	1140.13804	0.11
$[b_{27} – H• + Ru(bipy)]^{3+}$	1146.14131	1146.14156	-0.22
$[y_{20} – H_2O]^{2+}$	1153.58038	1153.57992	0.40
$[b_{18} -H• + Ru(bipy) – H^{+}]^{2+}$	1164.49414	1164.49362	0.45
y_{20}^{2+}	1162.58498	1162.58520	-0.19
unassigned	1194.48649	-	-
unassigned	1220.54028	-	-
$[b_{19} - H• + Ru(bipy) – H^{+}]^{2+}$	1239.99060	1239.99059	0.01
unassigned	1244.50987	-	-
ALYLVCGERGF	1257.59302	1257.59323	-0.17
▲ y_{11}	1272.63720	1272.63710	-

unassigned	1303.57739	-	-
unassigned	1383.60369	-	-
[EALYLVCGERGF – H_2O]$^+$	1386.63546	1386.63583	-0.27
▲y_{12}	1423.63060	1423.63100	-
[b_{23} + Ru(bipy) – H^+]$^{2+}$	1440.08826	1440.08781	0.31
unassigned	1466.64051	-	-
unassigned	1484.65119	-	-
[b_{24} + Ru(bipy) – H^+]$^{2+}$	1513.62217	1513.62202	0.10
y_{13}	1522.69902	1522.69940	-0.25
[b_{25} + Ru(bipy) – H^+]$^{2+}$	1587.15656	1587.15622	0.21
unassigned	1598.78783	-	-
EALYLVCGERGFFY	1696.76653	1696.76757	-0.61
EALYLVCGERGFFYT	1797.81361	1797.81525	-0.91
Mean Absolute Average			**0.34**
Standard Deviation			**0.32**

Appendix C

Appendix C contains the list of compounds assigned in the selected mass region for the genuine and counterfeit vodka samples in chapter 5, as well as the principal component scores calculated and plotted in the PCA analysis.

Table C-1: Assigned peaks in the (-) ESI mass spectra of genuine and counterfeit samples. ▲ indicates a peak used for internal calibration

Theo. *m/z*	Proposed molecular formula
▲101.06080	$C_5H_{10}O_2$
▲115.07645	$C_6H_{12}O_2$
121.02950	$C_7H_6O_2$
▲143.10775	$C_8H_{16}O_2$
145.12340	$C_8H_{18}O_2$
149.02442	$C_8H_6O_3$
151.04007	$C_8H_8O_3$
153.03240	$C_5H_{10}O_3$
155.00176	$C_4H_4N_2O$
155.07137	$C_8H_{12}O_3$
155.10775	$C_9H_{16}O_2$
157.08702	$C_8H_{14}O_3$
▲157.12340	$C_9H_{18}O_2$
159.10267	$C_8H_{16}O_3$
161.08193	$C_7H_{14}O_4$
163.04007	$C_9H_8O_3$
164.98382	$C_8H_6S_2$

165.01933	$C_8H_6O_4$
166.95752	$C_4H_4O_3S$
166.99390	$C_5H_8O_2S$
168.97317	$C_4H_6O_3S$
169.08702	$C_9H_{14}O_3$
171.10267	$C_9H_{16}O_3$
▲171.13905	$C1_0H_{20}O_2$
173.00666	$C_{10}H_6OS$
175.09758	$C_8H_{16}O_4$
176.98382	$C_9H_6S_2$
177.05572	$C_{10}H_{10}O_3$
179.03498	$C_9H_8O_4$
179.05611	$C_6H_{12}O_6$
182.98882	$C_5H_8O_3S$
182.99438	$C_8H_8OS_2$
183.03306	$C_8H_8N_2O$
183.10267	$C_{10}H_{16}O_3$
184.96808	$C_4H_6O_4S$
▲185.15470	$C_{11}H_{22}O_2$
187.06120	$C_8H_{12}O_5S$
187.09758	$C_9H_{16}O_4$
187.13397	$C_{10}H_{20}O_3$
188.99938	$C_4H_{10}O_4S$
189.11323	$C_9H_{18}O_4$
191.01973	$C_6H_8O_7$
191.12888	$C_9H_{20}O_4$
192.97873	$C_9H_6OS_2$
194.95799	$C_8H_3O_2S_2$
197.00447	$C_6H_{10}O_3S$
197.04555	$C_9H_{10}O_5$

197.15470	$C_{12}H_{22}O_2$
198.98373	$C_5H_8O_4S$
▲199.17035	$C_{12}H_{24}O_2$
200.94524	$C_4H_6O_3S_2$
201.11323	$C_{10}H_{18}O_4$
202.92450	$C_3H_4O_4S_2$
205.15979	$C_{14}H_{22}O$
207.08741	$C_8H_{16}O_6$
209.09500	$C_8H_{18}O_3$
212.99938	$C_6H_{10}O_4S$
213.18600	$C_{13}H_{26}O_2$
214.93006	$C_7H_4O_2S_3$
215.03279	$C_6H_{12}O_6$
219.17544	$C_{15}H_{24}O$
221.08193	$C_{12}H_{14}O_4$
225.06159	$C_7H_{14}O_8$
225.08991	$C_9H_{18}O_4$
225.18600	$C_{14}H_{26}O_2$
226.97865	$C_6H_8O_5S$
227.09250	$C_{11}H_{16}O_5$
▲227.20165	$C_{14}H_{28}O_2$
229.14453	$C_{12}H_{22}O_4$
235.17035	$C_{15}H_{24}O_2$
239.07724	$C_8H_{16}O_8$
239.12888	$C_{13}H_{20}O_4$
239.16527	$C_{14}H_{24}O_3$
240.99430	$C_7H_{10}O_5S$
▲241.21730	$C_{15}H_{30}O_2$
242.97356	$C_6H_8O_6S$
245.02779	$C_{13}H_{10}O_3S$

248.96049	$C_{12}H_6S_2$
249.15300	$C_{12}H_{26}O_3S$
250.14487	$C_{14}H_{21}NO_3$
250.93976	$C_{11}H_4OS_2$
253.21730	$C_{16}H_{30}O_2$
255.00995	$C_8H_{12}O_5S$
255.10048	$C_{10}H_{20}O_5$
255.16018	$C_{14}H_{24}O_4$
▲255.23295	$C_{16}H_{32}O_2$
256.93256	$C_{10}H_6S_3$
256.98921	$C_7H_{10}O_6S$
257.17583	$C_{14}H_{26}O_4$
263.03835	$C_{13}H_{12}O_4S$
264.16052	$C_{15}H_{23}NO_3$
264.95541	$C_{12}H_6OS_2$
265.14790	$C_{12}H_{26}O_4S$
267.08741	$C_{13}H_{16}O_6$
267.12717	$C_{11}H_{24}O_5S$
267.16018	$C_{15}H_{24}O_4$
269.17583	$C_{15}H_{26}O_4$
▲269.24860	$C_{17}H_{34}O_2$
270.91183	$C_{10}H_4OS_3$
271.00486	$C_8H_{12}O_6S$
278.97106	$C_{13}H_8OS_2$
280.98671	$C_{13}H_{10}OS_2$
281.24860	$C_{18}H_{34}O_2$
▲283.26425	$C_{18}H_{36}O_2$
286.90674	$C_{10}H_4O_2S_3$
293.13945	C16H22O5
293.17583	$C_{17}H_{26}O_4$

295.00236	$C_{14}H_{12}OS_2$
301.23843	$C_{17}H_{34}O_4$
303.13686	$C_{15}H_{24}O_4$
305.06448	$C_9H_{18}O_9$
307.21261	$C_{15}H_{32}O_6$
310.99727	$C_{14}H_{12}O_2S_2$
311.16864	$C_{17}H_{28}O_3S$
314.93804	$C_{12}H_8O_2S_3$
317.28499	$C_{22}H_{38}O$
319.08013	$C_{10}H_{20}O_9$
325.18429	$C_{18}H_{30}O_3S$
329.26973	$C_{19}H_{38}O_4$
339.19994	$C_{19}H_{32}O_3S$
340.97145	$C_{14}H_{10}O_4S_2$
341.10894	$C_{12}H_{22}O_{11}$
354.98710	$C_{15}H_{12}O_4S_2$
357.30103	$C_{21}H_{42}O_4$
359.11950	$C_{12}H_{24}O_{12}$
363.09078	$C_{18}H_{20}O_6S$
365.24641	$C_{19}H_{38}O_4$
369.00275	$C_{16}H_{14}O_4S_2$
373.09876	$C_{12}H_{22}O_{13}$
373.25956	$C_{20}H_{38}O_6$
373.34759	$C_{26}H_{46}O$
374.10677	$C_{19}H_{21}NO_5S$
377.08561	$C_{12}H_{22}O_{11}$
387.11441	$C_{13}H_{24}O_{13}$
393.27771	$C_{21}H_{42}O_4$
401.13006	$C_{14}H_{26}O_{13}$
401.29086	$C_{22}H_{42}O_6$

403.30651	$C_{22}H_{44}O_6$
415.14571	$C_{15}H_{28}O_{13}$
417.32216	$C_{23}H_{46}O_6$
421.04978	$C_{24}H_{10}N_4O_2$
683.22515	$C_{24}H_{44}O_{22}$

Table C-2: Principal component scores calculated for each vodka sample using the intensities for the *m/z* values listed in Table C-1; gen = genuine product, CF = counterfeit product

Vodka	PC1	PC2
Smirnoff (gen)	-7.771	1.028
Stoilichnaya (gen)	-13.475	0.262
Soviet (gen)	4.120	0.406
Aros (gen)	-0.490	4.635
Dannoff (gen)	4.480	4.760
Luxury Blk (gen)	0.146	3.250
Vladivar (gen)	4.914	4.073
Wyborowka (gen)	3.677	3.158
Noble Russian (gen)	-14.329	-0.093
Russian Std (gen)	-14.550	-0.182
Glens (gen)	2.179	2.449
Troika (gen)	14.284	5.424
Soviet 541 (CF)	7.928	1.299
Smirnoff 648 (CF)	-13.448	-0.232
Smirnoff 818 (CF)	-13.343	0.206
Arctic Ice 815 (CF)	7.261	5.006
Arctic Ice 886 (CF)	7.027	1.568
Chekov (CF)	1.303	-1.175
Vodka (CF)	7.492	3.418

Drop (CF)	0.867	-0.787
BB07520 (CF)	6.148	-9.982
BB07682 (CF)	-14.335	-0.522
BB02537 (CF)	5.346	-6.812
BB04539 (CF)	9.786	-8.955
BB07813 (CF)	1.543	-4.676
T15737 (CF)	3.238	-7.525

Appendix D

Appendix D contains the supplementary information for chapter 6 – the use of carbon nanotubes as an alternative to a matrix in MALDI analysis.

Table D-1: Assignment of peaks detected in MALDI-TOF spectrum of PEG-1000 plus 2,5-DHB matrix

Assignment	*m/z*
unassigned	176.9284
unassigned	198.8956
unassigned	268.1576
unassigned	338.9832
unassigned	354.9451
unassigned	360.9660
unassigned	521.0155
unassigned	683.0485
unassigned)	699.0276
unassigned	701.3885
unassigned	715.0002
$C_{34}H_{70}O_{18}Na$	789.4453
$C_{36}H_{74}O_{19}Na$	833.4740
$C_{38}H_{78}O_{20}Na$	877.4977
$C_{40}H_{82}O_{21}Na$	921.5255
$C_{42}H_{86}O_{22}Na$	965.5503
$C_{44}H_{90}O_{23}Na$	1009.5786
$C_{46}H_{94}O_{24}Na$	1053.6045
$C_{48}H_{98}O_{25}Na$	1097.6295
$C_{50}H_{102}O_{26}Na$	1141.6560
$C_{52}H_{106}O_{27}Na$	1185.6782

$C_{54}H_{110}O_{28}Na$	1229.7060
$C_{56}H_{114}O_{29}Na$	1273.7342
$C_{58}H_{118}O_{30}Na$	1317.7544
$C_{60}H_{122}O_{31}Na$	1361.7866
$C_{62}H_{126}O_{32}Na$	1405.8080
$C_{64}H_{130}O_{33}Na$	1449.8346
$C_{66}H_{134}O_{34}Na$	1493.8674
$C_{38}H_{138}O_{18}Na$	1537.8931

Table D-2: Assignment of peaks detected in MALDI-TOF spectrum of substance P plus 2,5-DHB

Assignment	*m/z*
unassigned	339.0004
unassigned	359.9880
unassigned	360.9842
unassigned	537.0264
unassigned	698.0636
unassigned	699.0625
unassigned	700.0627
unassigned	1037.1111
$[M+H]^+$	1347.8166
$[M+Na]^+$	1369.7984